University of Nebraska Medical Center
BREAKTHROUGHS FOR LIFE

University of Nebraska Medical Center
DigitalCommons@UNMC

Theses & Dissertations

Graduate Studies

Spring 5-9-2020

Novel Detection and Treatment Strategies for Pancreatic Ductal Adenocarcinoma

Joseph Carmicheal
University of Nebraska Medical Center

Tell us how you used this information in this short survey.

Follow this and additional works at: https://digitalcommons.unmc.edu/etd

Part of the Diagnosis Commons, and the Therapeutics Commons

Recommended Citation

Carmicheal, Joseph, "Novel Detection and Treatment Strategies for Pancreatic Ductal Adenocarcinoma" (2020). *Theses & Dissertations*. 429.
https://digitalcommons.unmc.edu/etd/429

This Dissertation is brought to you for free and open access by the Graduate Studies at DigitalCommons@UNMC. It has been accepted for inclusion in Theses & Dissertations by an authorized administrator of DigitalCommons@UNMC. For more information, please contact digitalcommons@unmc.edu.

Novel Detection and Treatment Strategies for Pancreatic Ductal Adenocarcinoma

By
Joseph J. Carmicheal
A DISSERTATION

Presented to the Faculty of
the University of Nebraska Graduate College
in Partial Fulfillment of the Requirements
for the Degree of Doctor of Philosophy

Biochemistry and Molecular Biology Graduate Program

Under the Supervision of Professor Dr. Surinder K. Batra

University of Nebraska Medical Center
Omaha, Nebraska

March 2020

Supervisory Committee:

Jason Foster M.D.

Sukhwinder Kaur Ph.D.

Chi Lin M.D. Ph.D.

David Lyden M.D. Ph.D.

Michel Ouellette Ph.D.

Novel Detection and Treatment Strategies for Pancreatic Ductal Adenocarcinoma

Joseph Carmicheal, Ph.D.

University of Nebraska Medical Center, 2020

Advisor: Surinder K. Batra

Pancreatic ductal adenocarcinoma (PDAC) is one of the most lethal malignancies with an estimated 5-year survival rate of less than 9%. The high lethality of PDAC is due to two primary reasons: the discovery of PDAC at later stages, with locally invasive or metastatic disease present at the time of initial diagnosis as well as the lack of efficacious therapeutic interventions that significantly impact survival. In this dissertation, we sought to discover and test novel detection and treatment strategies for PDAC. Firstly, serum EVs were investigated as potential non-invasive liquid biopsy biomarkers, to serve as a means of early cancer detection. Secondly, a recently discovered form of cell death, ferroptosis, was investigated as a means of potentiating radiation therapy.

The investigation into the potential of extracellular vesicles (EVs) as circulating biomarkers began with a label-free analysis of EVs *via* surface-enhanced Raman Spectroscopy (SERS) and principal component discriminant function analysis (PC-DFA), to identify tumor-specific spectral signatures. This method differentiated EVs originating from PDAC or normal pancreatic epithelial cell lines with 90% overall accuracy. The proof-of-concept application of this method to EVs purified from patient serum exhibited up to 87% and 90% predictive accuracy for healthy control and early PDAC individual samples, respectively. The specific EV surface proteins that may contribute to the observed SERS differences were investigated *via* surface shaving LC-MS/MS. This analysis provided protein targets that were selected and validated with a combination of

bioinformatics, western blot, and immunogold labeling techniques. The first target protein selected for assessment *via* ELISA, EPHA2, showed elevated expression in complete cancer patient serum as compared to benign controls. Further, EV specific EPHA2 expression was capable of predicting cancer status in 25% (5/20) of the patient samples with 100% specificity. These data suggest a potential role of EV surface profiling for the early detection of PDAC. However, further work is required to increase the overall accuracy.

Additionally, we sought to investigate the involvement of ferroptosis, in radiation-induced cell death. Ferroptosis is a non-apoptotic form of cell death that requires labile ferrous iron (Fe^{2+}) and is caused by the reactive oxygen species (ROS) mediated build-up of lipid hydroperoxides. Further, we tested if the pharmaceutical induction of ferroptosis *via* the small molecule Erastin can potentiate the lethal effects of radiation *in vitro* and *in vivo*. We observed that radiation produces an increase in ROS and free Fe^{2+} leading to lipid hydroperoxidation, which was enhanced with the addition of Erastin culminating in the likely induction of ferroptosis. The combination of radiation and Erastin synergistically increased cell death in monocultures and patient-derived organoids as well as significantly reduced tumor size in xenograft mouse models. These findings suggest the potential of ferroptosis induction to improve radiation therapy, though specific mechanistic components require further evaluation. Therefore, further studies must be conducted to elucidate the specific role of ferroptosis in radiation-induced cell death.

The combination of early detection and novel therapeutic intervention strategies offers a means of improving the survival of those with this dreaded disease.

Table of Contents

Table of Contents 4

List of Figures 10

List of Tables 14

Abbreviations 15

Acknowledgments 19

Chapter 1: Introduction - Pancreatic Ductal Adenocarcinoma 22

1.1 Statistics and demographics 22

1.2 High-risk groups 27

1.2.1 Family history 28

1.2.2 Inherited genetic alterations and syndromes 29

1.2.2.1 Familial Atypical Multiple Mole Melanoma (FAMMM) Syndrome 29

1.2.2.2 Hereditary Nonpolyposis Colorectal Cancer (HNPCC)/Lynch Syndrome 30

1.2.2.3 Peutz-Jeghers Syndrome 30

1.2.2.4 Hereditary Pancreatitis 31

1.2.3 Precursor lesions 32

1.2.3.1 Pancreatic Intraepithelial Neoplasia (PanINs) 32

1.2.3.2 Pancreatic Cystic Lesions 33

A Serous Cystic Neoplasms 37

B Mucinous Cystic Lesions 38

C Other Pancreatic Cystic Lesions 41

1.3 Genetic and molecular mechanisms of PDAC oncogenesis and progression 42

1.4 Detection methods 46

1.4.1 Imaging 46

1.4.2 Cytology 47

1.4.3 CA19.9 and CEA 48

1. 5 Therapeutic strategy 50

1.5.1 Surgery 50

1.5.2 Adjuvant therapy 50

1.5.3 Neo-adjuvant therapy 52

1.6 Conclusions and perspective 54

Chapter 2: Methods 61
2.1 Cell Culture 61
2.2 Immunoblotting 61
2.3 Statistical Methods 62

2A Extracellular vesicle surfaceome characterization for the early detection of pancreatic ductal adenocarcinoma 62
2A.1 EV isolation from cell medium and serum 62
2A.2 FiberCell 63
2A.3 Transmission Electron Microscopy (TEM) 66
2A.4 Immunogold 66
2A.5 Atomic Force Microscopy (AFM) 69
2A.6 Nanoparticle Tracking Analysis (NTA) 72
2A.7 SERS Measurement 72
2A.8 SERS spectra processing and Principal Component –Discriminant Function 73
Analysis 73
2A.9 EV surface proteomics 73
2A.10 Bioinformatics Pipeline 74
2A.11 Sandwich enzyme-linked immunosorbent assay (ELISA) 75
2A.12 Lectin array 75
2A.13 Isolation of genomic DNA from EVs 76
2A.14 Mutation detection by digital droplet polymerase chain reaction (ddPCR) 76

2B Radiation Potentiation *via* Ferroptosis for the improved treatment of pancreatic ductal adenocarcinoma 77
2B.1 Bioinformatics 77
2B.2 MTT 78
2B.3 *In vitro* cell migration assay 78
2B.4 Immunohistochemical staining of human tissues 78
2B.5 siRNA knockdown and transient transfection 79
2B.6 *In vitro* irradiation 80
2B.7 *In vitro* radiation response determination 80
2B.8 Combenefit analysis 81
2B.9 Patient-derived organoids 81
2B.10 Patient derived organoid radiation response determination 82

2B.11 *In vivo* orthotopic xenograft model 83
2B.12 Treatment plan and experimental design 83
2B.13 Glutathione assay 84
2B.14 Measurement of reactive oxygen species production 84
2B.15 Intracellular free iron (Fe^{2+}) assessment *via* FeRhoNox™-1 87
2B.16 *In vitro* assessment of lipid peroxidation *via* BODIPY™ 581/591 C11 87
2B.17 Thiobarbituric acid reactive substances (TBARS) assay 88

Chapter 3: Overview of the extracellular vesicle surfaceome and its implications in cancer 90
3.1 Biogenesis 90
3.2 General Contents and Functions 94
3.3 Surface-based Isolation Methods 98
3.3.1 Traditional EV Isolation Techniques 99
3.3.2 Surface-based techniques for EV isolation 100
3.3.2.1 Immunoaffinity 101
3.3.2.2 Heparin isolation techniques 102
3.3.2.3 Lipid nanoprobes 103
3.4 Surface-based characterization techniques 105
3.4.1 Mass spectrometry 106
3.4.2 Microfluidics 109
3.4.3 Flow cytometry 110
3.4.4 Surface plasmon resonance 112
3.4.5 Surface-enhanced Raman spectroscopy 113
3.4.6 Nanoprobes 114
3.4.7 Biosensors 116
3.5 Cancer Biology 117
3.5.1 Signaling and crosstalk 117
3.5.2 Extracellular matrix remodeling 120
3.5.3 Metastasis 121
3.5.4 Immune Impact 122
3.6 Biomarkers 123
3.6.1 Proteins 124
3.6.2 Carbohydrates 126
3.6.3 Lipids 127
3.6.4 Label-free 127

3.7 Therapy 128
3.7.1 The endogenous EV surface 129
3.7.2 Functionalized the EV surface 129
3.7.3 Targeting the EV surface 131
3.8 Conclusion and perspective 131

Chapter 4: Extracellular vesicle surfaceome characterization for the early detection of pancreatic ductal adenocarcinoma 134

4A Label-free characterization of extracellular vesicles *via* Raman spectroscopy 134
4A.1 Synopsis 134
4A.2 Background and Rationale 134
4A.3 Results 138
4.3.1 EVs of appropriate size can be isolated from cell line conditioned media 138
4.3.2 Isolated EVs maintain morphological characteristics 141
4.3.3 EV consensus marker validation and substrate distribution assessment 141
4.3.4 Surface-enhanced Raman spectroscopy (SERS) spectral shifts from EVs are predicated on the cell type of origin. 146
4.3.5 EV SERS spectra are highly reproducible 149
4.3.6 Principal Component - Discriminant Function Analyses can discriminate between PDAC and normal cell line EV SERS spectra with high accuracy 152
4.3.7 EVs can be isolated from patient sera and are elevated in cancer patient samples compared to benign controls 159
4.3.8 The cell line trained PC-DFA algorithm can be applied to SERS spectra of serum EVs to predict patient cancer status 159
4.4 Discussion 164
4.5 Conclusions and future directions 168

4B: Biomarker discovery *via* extracellular vesicle surface profiling 170
4B.1 Synopsis 170
4B.2 Background and rationale 170
4B.3 Results 172
4B.3.1 LC-MS/MS EV surface proteomic profiling identifies proteins of interest pool 172
4B.3.2 Bioinformatics discernment of eight specific target EV surface proteins 177
4B.3.2.1 Proteins of interest gene expression in adjacent normal and PDAC tissues 177
4B.3.2.2 Target genes are correlated in two distinct datasets 177
4B.3.2.3 Target protein genes have high diagnostic accuracy 180

4B.3.3 All target proteins are present in greater concentrations in EVs from PDAC cell lines compared to those from HPDE 185
4B.3.4 EPHA2, ECM1, CD151, and HSPB1 are verifiably present on the EV surface 190
4B.3.5 EPHA2, ECM1, CD151, and HSPB1 expression in TCGA and effects on survival 190
4B.3.6 EPHA2 is present on CD63 positive EVs and is reliably detected with ELISA 195
4B.3.7 EPHA2 is increased on EVs originating from PDAC cell lines compared to HPDE cells 200
4B.3.8 Complete PDAC patient serum has a greater concentration of EPHA2 compared to healthy controls 200
4B.3.9 EV surface EPHA2 evaluation is more specific than complete serum EPHA2 levels for predicting patient cancer status 205
4B.4 Discussion 205
4B.5 Conclusions and future directions 209

Chapter 5: Radiation potentiation *via* ferroptosis for the improved treatment of pancreatic ductal adenocarcinoma 217
5.1 Synopsis 217
5.2 Background and rationale 218
5.3 Results 222
5.3.1 GPX4 and SLC7A11 are differentially expressed in pancreas cancer 222
5.3.2 SLC7A11 protein expression is increased in the majority of PDAC cell lines compared to HPDE 227
5.3.3 Most PDAC cell lines are more sensitive to Erastin than HPDE 232
5.3.4 Erastin inhibits cellular migration 237
5.3.5 Erastin treatment decreases intracellular GSH 237
5.3.6 Radiation promotes GPX4, SLC7A11 expression and the phosphorylation of NRF2 *in vitro* 242
5.3.7 SLC7A11 is increased in PDAC and radiated patient tissues 243
5.3.8 SLC7A11 gene expression is significantly correlated with survival in radiated patients 243
5.3.9 GPX4 knockdown sensitizes cells to radiation-induced cell death *in vitro* 250
5.3.10 Erastin and radiation synergistically induce cell death 250
5.3.11 Combination radiation and erastin treatment-induced cell death is mitigated with the addition of Ferrostatin-1 258
5.3.12 Erastin potentiates radiation-induced cell death in patient-derived organoids 261
5.3.13 Erastin potentiates radiation treatment *in vivo* 264
5.3.14 Radiation increases intracellular reactive oxygen species (ROS) 264

5.3.15 Combination treatment causes lipid peroxidation *in vitro* 269
5.3.16 Radiation increases intracellular free iron (Fe^{2+}) 269
5.3.17 Lipid peroxidation can be measured in radiated PDAC patient serum samples 276
5.4 Discussion 281
5.5 Conclusions and future directions 284

Chapter 6: General conclusions and future directions 286

Chapter 7: References 302

List of Figures

Chapter 1

Figure 1. 1 SEER database overall survival for PDAC patients from 1992-2016..... 23

Figure 1. 2 Organ system distribution of new cancer incidences and deaths in 2019. 25

Figure 1. 3 Chart depiction of pancreatic cystic lesion types. 35

Figure 1. 4 Survival of SEER patients (1992-2016) treated with currently available therapies. 56

Chapter 2

Figure 2A. 1 Isolation of EVs *via* density gradient ultracentrifugation..... 64

Figure 2A. 2 FiberCell Systems® high-density hollow-fiber bioreactor system. 67

Figure 2A. 3 Schematic of the immunogold TEM staining protocol..... 70

Figure 2B. 1 Small animal radiation machine and treatment planning..... 85

Chapter 3

Figure 3. 1 Mechanisms of EV biogenesis and secretion 91

Figure 3. 2 EV surface and intravesicular content 95

Chapter 4

Figure 4A. 1 Nanoparticle Tracking Analysis of cell line EVs 139

Figure 4A. 2 TEM images of EVs isolated from conditioned media 142

Figure 4A. 3 EV surface marker validation and substrate distribution verification 144

Figure 4A. 4 SERS spectra of cell line EVs 147

Figure 4A. 5 Repeated SERS spectra collections from cell line EVs and gold nanoparticles 150

Figure 4A. 6 Principal component analysis of cell line SERS spectra 153

Figure 4A. 7 Discriminant functional analysis of SERS generated principal components 155

Figure 4A. 8 Serum isolated EV quantification *via* protein concentration 160

Figure 4A. 9 Morphological validation of EVs isolated from patient serum 162

Figure 4B. 1 Gene ontology pathway analysis of EV surface proteins 173

Figure 4B. 2 Identification of cancer EV surface proteins of interest 175

Figure 4B. 3 Gene expression profiles for EV proteins of interest 178

Figure 4B. 4 Correlation of target proteins in two distinct datasets 181

Figure 4B. 5 Receiver operator characteristics curve of the eight target protein genes 183

Figure 4B. 6 Evaluation of consensus EV markers *via* western blot analysis 186

Figure 4B. 7 Evaluation of EV surface target proteins *via* western blot 188

Figure 4B. 8 Immunogold staining of EV surface proteins 191

Figure 4B. 9 EPHA2, ECM1, CD151, and HSPB1 expression in TCGA and effects on survival 193

Figure 4B. 10 EPHA2 expression in cancer vs. normal tissue across major cancer types 196

Figure 4B. 11 EPHA2 ELISA of CD63 positive EVs 198

Figure 4B. 12 EPHA2 ELISA of PDAC and HPDE cell lines 201

Figure 4B. 13 EPHA2 ELISA of complete patient serum samples 203

Figure 4B. 14 EPHA2 ELISA of patient seromic EVs 206

Figure 4B. 15 Preliminary lectin array of CD18/HPAF and HPDE EVs 211

Figure 4B. 16 Digital droplet PCR analysis of cell line EVs 213

Chapter 5

Figure 5. 1 Schematic of Erastin induced ferroptosis 220

Figure 5. 2 GPX4 expression in pancreas cancer compared to normal and relative to cancers of various origin 223

Figure 5. 3 SLC7A11 expression in pancreas cancer compared to normal and relative to cancers of various origin 225

Figure 5. 4 GPX4 and SLC7A11 expression and survival in the TCGA PDAC cohort 228

Figure 5. 5 GPX4 and SLC7A11 protein expression in PDAC cell lines 230

Figure 5. 6 Project DRIVE analysis of RNAi SLC7A11 knockdown in PDAC cell lines 233

Figure 5. 7 Erastin MTT survival curves in PDAC cell lines and HPDE 235

Figure 5. 8 Erastin impact on CD18/HPAF migration 238

Figure 5. 9 Erastin depletion of glutathione 240

Figure 5. 10 mRNA and protein analysis of PDAC cell lines after radiation 244

Figure 5. 11 GPX4 and SLC7A11 protein expression in patient tissue samples 246

Figure 5. 12 SLC7A11 survival of radiated PDAC patients in TCGA 248

Figure 5. 13 Impact of GPX4 knockdown on CD18/HPAF and Panc1 survival in the setting of radiation 251

Figure 5. 14 Response of CD18/HPAF and Panc1 to combination radiation and Erastin treatment 254

Figure 5. 15 Direct comparison between CD18/HPAF and Panc1 of response to 1 μM and 2 μM Erastin with 5Gy radiation treatment 256

Figure 5. 16 the lethal effects of radiation and Erastin combination are synergistic 259

Figure 5. 17 Effect of combination treatment in the setting of apoptosis, necroptosis, or ferroptosis inhibition 262

Figure 5. 18 Response of patient-derived organoids to combination treatment 265

Figure 5. 19 Effect of Erastin and radiation in an orthotopic PDAC murine model 267

Figure 5. 20 Radiation production of reactive oxygen species (ROS)..... 270

Figure 5. 21 Effect of combination therapy on lipid peroxidation in CD18/HPAF cells 272

Figure 5. 22 Effect of combination therapy on lipid peroxidation in Panc1 cells 274

Figure 5. 23 Effect of treatment on intracellular free iron (Fe^{2+})..... 277

Figure 5. 24 Malondialdehyde (MDA) assessment in radiation patient samples 279

Figure 5. 25 Schematic of the proposed mechanism for Erastin potentiation of radiation *via* ferroptosis..... 282

List of Tables

Chapter 4

Table 4A. 1 Prediction of cell line cancer status *via* SERS PC-DFA 157

Table 4A. 2 Application of cell line PC-DFA algorithm on SERS of EVs isolated from patient serum 165

Abbreviations

5-FU 5-Fluorouracil

AF4 asymmetric flow field-flow fractionation

AFM – Atomic Force Microscopy

ASCO – American Society of Clinical Oncology

AUC - Area Under Curve

AuNPs – Gold Nanoparticles

BSA - Bovine Serum Albumin

CEA – Carcinoembryonic Antigen

CT – Computerized Tomography

D/I - Death to Incidence Ratio

DNA – Deoxyribonucleic Acid

EBRT – External Beam Radiation Therapy

ECM – Extracellular Matrix

ESCRT – Endosomal Complex Responsible for Transport

EUS – Endoscopic Ultrasound

EV – Extracellular Vesicle

FBS – Fetal Bovine Serum

FNA – Fine Needle Aspirate

GLC - Gas Liquid Chromatography

GPX4- Glutathione Peroxidase 4

GSH - Glutathione

Gy - Gray

HA - Hyaluronic Acid

HFBR - Hollow Fiber Bioreactor

hFC - High-Resolution Flow Cytometry

HSPG – Heparin Sulfate Proteoglycan

IHC - Immunohistochemistry

ILV – Intraluminal Vesicle

IPMN – Intraductal Papillary Mucinous Neoplasm

kDA - kilo Dalton

KO - knock out

LC-MS/MS – Liquid Chromatography-Tandem Mass Spectrometry

LEC - Lymphoendothelial Cysts

mAB monoclonal antibodies

MCN – Mucinous Cystic Neoplasm

MDA - Malondialdehyde

miRNA - MicroRNA

MRI – Magnetic Resonance Imaging

mRNA – Messenger RNA

MSI - Microsatellite Instability

MTT - 3-(4,5-Dimethylthiazol-2-yl)-2,5-diphenyltetrazolium bromide

MVB – Multivesicular Body

NCCN – Nation Clinical Cancer Network

NTA – Nanoparticle Tracking Analysis

PanIN – Pancreatic Intraepithelial Neoplasia

PBA - Proximity Dependent Barcoding Assay

PBS – Phosphate Buffered Saline

PCA – Principal Component Analysis

PD-DFA – Principal Component Discriminant Function Analysis

PCL – Pancreatic Cystic Lesion

PCR – Polymerase Chain Reaction

PDAC – Pancreatic Ductal Adenocarcinoma

PJS - Peutz Jeghers Syndrome

PNEN – Pancreatic Neuroendocrine Neoplasms

PS - Phosphatidyl Serine

RIPA - Radio immunoprecipitation Assay Buffer

RNA – Ribonucleic Acid

ROS – Reactive Oxygen Species

RT - Room Temperature

SBRT – Stereotactic Body Radiation Therapy

SCA - Serous Cystadenomas

SCN – Serous Cystic Neoplasm

SEC - Size Exclusion Chromatography

SEM – Scanning Electron Microscopy

SERS – Surface-Enhanced Raman Spectroscopy

SMA - Serous microcystic Adenoma

SPR – Surface Plasmon Resonance

TBARS - Thiobarbituric Acid Reactive Substances

TEM – Transmission Electron Microscopy

TLC - Thin layer chromatography

TME – Tumor Microenvironment

UC - Ultracentrifugation

Acknowledgments

I would like to thank my Ph.D. mentor Dr. Surinder K. Batra for his mentorship, guidance, and coaching throughout the duration of my training. When I initially inquired into joining his lab he accepted me with unwavering support. He gave me a chance that few others would have and for that, I am extremely grateful. He has allowed me to test hypotheses of my own design and has supported me the entirety of the way. His ever-present encouragement and unrelenting determinism for fellowship applications and paper submission have been invaluable to my success. Above all, his concern for my welfare outside of the lab was deeply moving and provided me with the confidence that he will make every effort to do what is best for me and my future.

I would also like to thank Dr. Sukhwinder Kaur for her day-to-day mentorship and for serving on my supervisory committee. She was always available whenever a technical or theoretical issue needed to be addressed and provided her years of expertise in biomarker research to my studies. She was always present when I needed help in navigating the world of science, publications, and presentations. For that and many other reasons, I thank her.

I would also like to thank the other members of my supervisory committee Dr. Jason Foster, Dr. Chi Lin, Dr. David Lyden, and Dr. Michel Ouellette for their suggestions, criticisms, and encouragement throughout this process.

I would like to extend my appreciation to all the members of the Batra lab, past and present, with whom I have had daily interactions and shared a workspace. These interactions helped shape my science and I learned a great deal from the other students, postdocs, instructors, and professors. Specifically, I would like to thank Dr. Alexey Krasnoslobodtsev, Dr. Maneesh Jain, Dr. Moorthy P. Ponnusamy, Dr. Sushil Kumar, Dr.

Parthasarathy Seshacharyulu, Dr. Satyanarayana Rachagani, and Dr. Imayavaramban Lakshmanan for their willingness and ability to offer guidance and help when asked. My sincere thanks also go to Dr. Wade Junker, Dr. Prakash Kshirsagar, Dr. Abhijit Aithal, Dr. Shailendra Gotham, Dr. Sakthivel, Dr. Samy Ponnusamy, Dr. Rakesh Bhatia, Dr. Jawed Siddiqui, Dr. Raghupathy Vengoji, Dr. Sanjib Chaudhary, Dr. Ramesh Pothuraju, and Dr. Ashu Shah for giving advice and suggestion over this period. My warm thanks and gratitude go to Karen, Amy, Jeanette, Coleen, and April for all their help and support they provided during my graduate training.

I would like to extend a special thank you to the friends I have made during my time in graduate school. Specifically Andrew Cannon, Christopher Thompson, Rahat Jahan, Koelina Ganguly, and Pranita Atri. These are the people with whom I have interacted with the most and have put up with my antics daily. The life of a graduate student is tough and without individuals helping you get through it, the chances of success are greatly diminished. They have been integral to the completion of my degree and provided a stress outlet through comedy, banter, and theoretical whimsy.

I am indebted to my parents, Mark and Tamara Carmicheal, whose sacrifices and parenting made it possible for me to even contemplate this career path, let alone see it through to fruition. Them, along with my siblings Cory, Talia, and Laura have always been there to support me in every stage of life. I have never given up on myself because they have never given up on me. Finally, my wife Cassandra is my partner in life and best friend. Without her, none of this would be possible. Her patience, strength, resilience, and grace are the cause of me being where I am today. For that, I will be eternally grateful and will strive to do the same for her.

Chapter 1: Introduction

Pancreatic Ductal Adenocarcinoma

Portions of the content covered in this chapter are the subject of a published article in *Biochim Biophys Acta Rev Cancer* by Carmicheal et al. [1].

Chapter 1: Introduction - Pancreatic Ductal Adenocarcinoma

1.1 Statistics and demographics

Pancreatic ductal adenocarcinoma (PDAC) is a devastatingly lethal disease with a five-year survival of 9% [2]. The patients in the SEER database (1992-2016) have even worse mortality ranging from 28.2% of patients remaining alive one year after diagnosis down to only 6.2% at the five-year time-point (**Figure 1.1**). It is currently the third leading cause of cancer-related death and is projected to replace colon cancer as the second leading cause within the next decade [3]. In fact, the mortality rate of PDAC is one of the highest out of all major cancer types including those with the greatest number of total patient deaths such as lung, colorectal, breast, and prostate [2]. While the incidence of PDAC is not as high as many of the other major cancer types at 56,770 in 2019, the number of deaths occurring during this same time totaled 45,750, leading to a shockingly high death to incidence (D/I) ratio. Where lung, colorectal, breast, and prostate cancers have D/I ratios of 0.63, 0.51, 0.16, and 0.18 respectively, the ratio associated with PDAC is the worst at 0.81 [2] (**Figure 1.2**).

Unfortunately, the early stages of PDAC typically are asymptomatic in nature. Further confounding diagnosis of this disease is the fact that when symptoms are present, they are often transient or intermittent, as well as frequently mild and quite ambiguous. For example, nausea, lethargy, and abdominal pain [4]. When patients do start to experience more serious symptoms including jaundice, weight loss (cachexia), and migratory phlebitis the disease has often advanced to later (and more lethal) stages. Later stage presentation with greater disease burden comes with an inherent increase in the probability of local invasion at the primary site preventing surgical resection (currently the only means of curative

Figure 1. 1 SEER database overall survival for PDAC patients from 1992-2016

The overall survival trend observed within the SEER database for the PDAC population who underwent surgery and chemotherapy treatments was 28.2% at one year, 13.1% at two years, 9.0% at three years, 7.2% at four years, and 6.2% at 5 years.

Figure 1.1

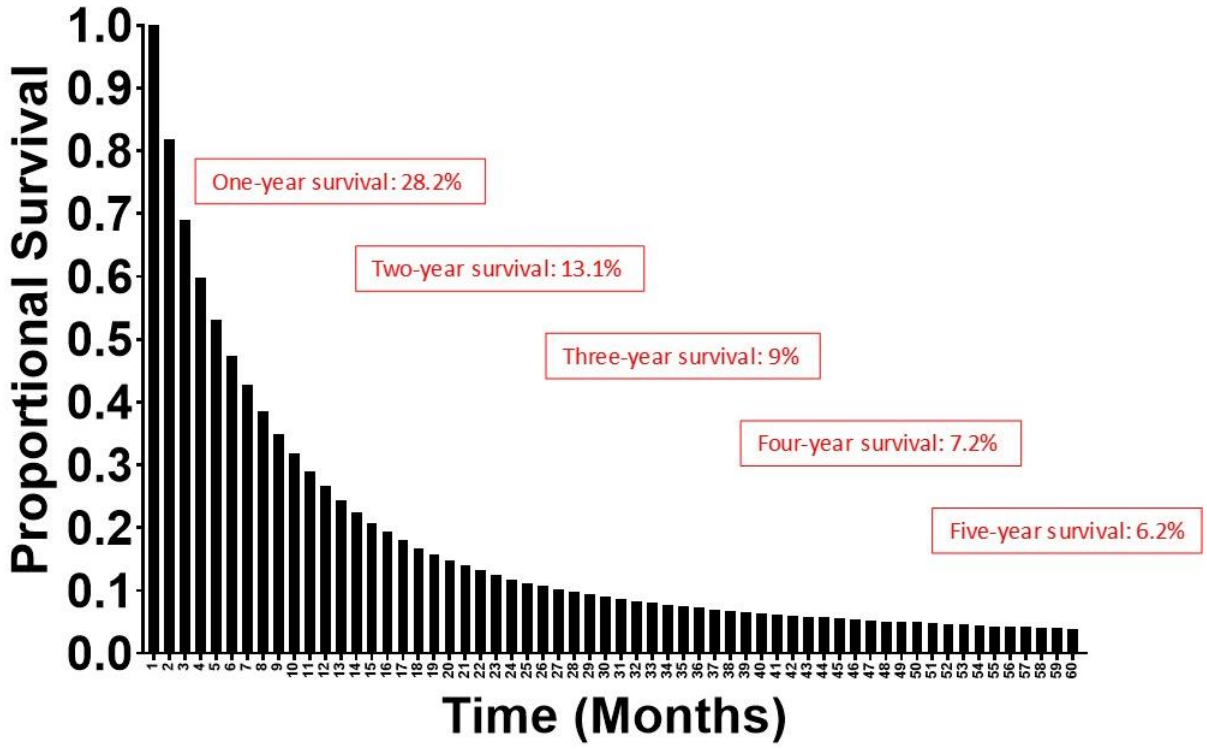
Proportional Survival
1.0
0.9
0.8
0.7
0.6
0.5
0.4
0.3
0.2
0.1
0.0
One-year survival: 28.2%
Two-year survival: 13.1%
Three-year survival: 9%
Four-year survival: 7.2%
Five-year survival: 6.2%
Time (Months)

Figure 1. 2 Organ system distribution of new cancer incidences and deaths in 2019.

A. Estimated incidences of major cancer types along with the estimated number of deaths caused by that cancer during the same one year time period. The death to incidence ratio is presented in panel **B.** Notably, PDAC has the worst overall ratio among all the cancers. (Numbers sourced from Siegel RL, Miller KD, Jemal A. Cancer statistics, 2019. CA Cancer J Clin. 2019;69(1):7-34.).

Figure 1.2

A

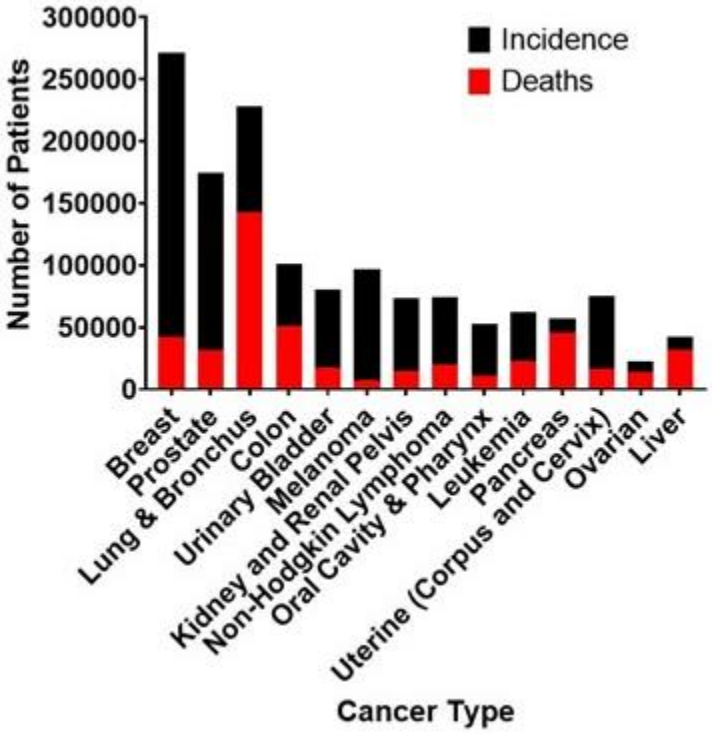
Incidence
Deaths
Number of Patients
300000
250000
200000
150000
100000
50000
0
Breast
Prostate
Lung & Bronchus
Colon
Urinary Bladder
Melanoma
Kidney and Renal Pelvis
Non-Hodgkin Lymphoma
Oral Cavity & Pharynx
Leukemia
Pancreas
Uterine (Corpus and Cervix)
Ovarian
Liver
Cancer Type

B

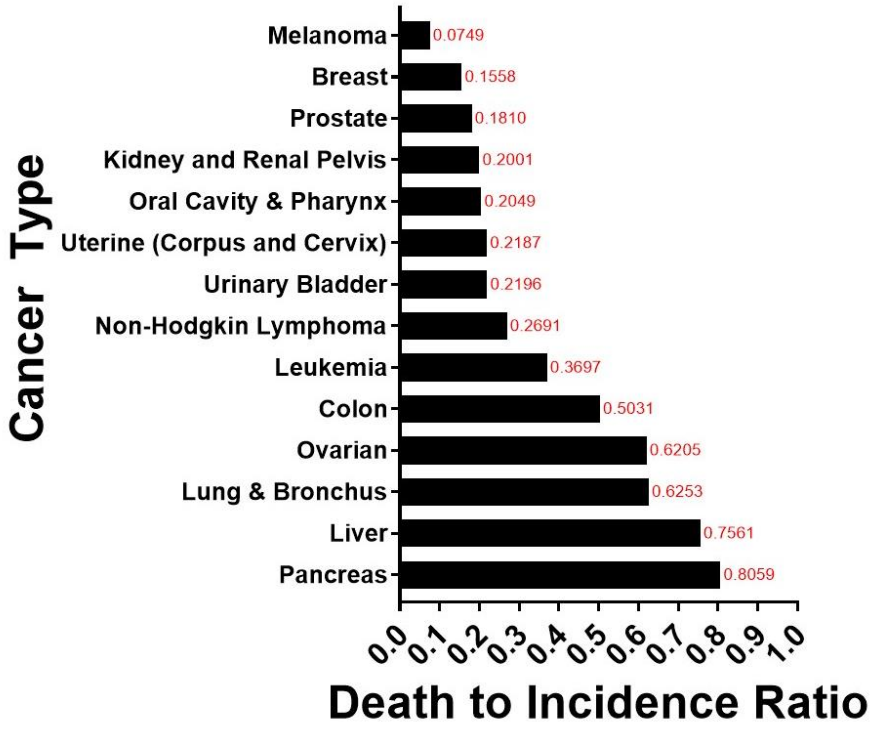
Cancer Type
Melanoma 0.0749
Breast 0.1558
Prostate 0.1810
Kidney and Renal Pelvis 0.2001
Oral Cavity & Pharynx 0.2049
Uterine (Corpus and Cervix) 0.2187
Urinary Bladder 0.2196
Non-Hodgkin Lymphoma 0.2691
Leukemia 0.3697
Colon 0.5031
Ovarian 0.6205
Lung & Bronchus 0.6253
Liver 0.7561
Pancreas 0.8059
0.0 0.1 0.2 0.3 0.4 0.5 0.6 0.7 0.8 0.9 1.0
Death to Incidence Ratio

therapy available) as well as the prevalence of metastasis. Further, it confers a diminished probability that adjuvant treatment options, such as chemotherapy, will be efficacious.

1.2 High-risk groups

Like many other cancers, the general risk of developing pancreatic cancer depends on a variety of controllable and non-controllable factors. Some of the controllable clinical factors which confer an increased risk of PDAC include tobacco use, being overweight, long-standing Diabetes Mellitus Type II, and chronic pancreatitis arising from poor diet and/or heavy alcohol use [5-9]. Conversely, many uncontrollable factors are present such as age, gender, race, chronic pancreatitis resulting from a genetic abnormality, family history, inherited genetic syndrome, and those with pancreatic cancer precursor lesions [10]. However, it is worth noting that the sudden onset of diabetes after the age of 50 is highly correlated with the presence of PDAC and not merely an increase in risk [11].

Only some of these groups confer an increased level of risk large enough, relative to the extremely low incidence of PDAC in the general population, to merit identification as a high-risk group; that is, only those groups of patients with a greater than 5% lifetime risk, or an increased relative risk >5, are considered high-risk as suggested by the International Cancer of the Pancreas Screening (CAPS) consortium meeting [12]. Along with that, the American College of Gastroenterology has recently published clinical guidelines regarding the classification of high-risk groups, which ones require continuous surveillance, and exactly what that surveillance entails [13]. The six recommendations pertaining to PDAC screening and continual surveillance are summarized as follows: 1. Warranted for hereditary syndromes associated with PDAC; 2. Should be conducted at an experienced center with a multidisciplinary approach; 3. It should be conducted *via* EUS

or MRI and not CT; 4. Begin at 50 years of age or 10 years prior to the earliest age of familial onset; 5. Cystic lesions require evaluation at the center with expertise in the area of high-risk patients; 6. Surgical intervention decisions must be individualized and made *via* multidisciplinary approach [13]. The high-risk groups that will be discussed herein are those fitting the criteria of both of these expert panels. They are those with a family history, inherited genetic syndromes, and history or current diagnosis of pancreatic cystic lesions (a clinically identifiable cancer precursor) [14].

1.2.1 Family history

The individuals comprising this group have at least two first-degree relatives (or 3 relatives of any degree) diagnosed with pancreas cancer but do not fulfill the criteria set for a specific genetic syndrome [15]. The overall risk for these individuals to get PDAC is 6.4% for those with two first-degree relatives affected and climbs to 32% if three first-degree relatives are diagnoses [16, 17]. Aside from the increase in general probability, this population tends to be diagnosed 10 years earlier than the previous generation [18], which is valuable information required for timely monitoring. Congruently, many of these patients are diagnosed before the age of fifty compared to those diagnosed without a family history [19].

Though a unifying germline mutation or genetic signature is not known for a strong hereditary pattern of PDAC (in the absence of a known genetic syndrome), recent studies have discovered some genetic germline perturbations present in small subsets of the population. One such mutation is in the PALB2 gene which has been detected in around 3% of those with familial PDAC [20]. Other gene mutations and their respective prevalence in familial cases of PDAC include BRCA1 at 1.2%, BRCA2 at 3.7%, and CDKN2A at

2.5% according to a study by Zhen et al. [21]. Incredibly, germline mutations in these genes, along with PALB2, were present in over 10% of those with familial PDAC [21]. Roberts et al. corroborated these findings in another study incorporating whole-genome sequencings of familial PDAC [22]. The importance of BRCA1 and 2 is also highlighted by the fact that a family's strong family history of breast and ovarian cancer associated with germline mutations in one of the two BRCA family members also confers an increased risk of developing PDAC [23]. Even though they represent a small subset of the total group, the discovery of these novel tumor susceptibility genes suggests a possible role for genetic testing in the monitoring of this cohort, along with the current imaging and laboratory modalities.

1.2.2 Inherited genetic alterations and syndromes

Many inherited genetic alterations and syndromes have been acknowledged that confer an increased risk of developing PDAC to a level that required screening intervention, as per the CAPS consortium recommendation. These include familial atypical multiple mole melanoma (FAMMM), hereditary nonpolyposis colorectal cancer (HNPCC)/Lynch Syndrome, hereditary pancreatitis, and Peutz-Jeghers Syndrome. These syndromes along with their associated mutation and relative percent increase in the probability of PDAC are listed in this section.

1.2.2.1 Familial Atypical Multiple Mole Melanoma (FAMMM) Syndrome

A germline mutation in the gene that encodes p16/CDKN2A is responsible for Familial Atypical Multiple Mole Melanoma (FAMMM) [24]. Notably, p16/CDKN2A has known tumor suppressor functions and somatic mutations and/or loss of function are associated with the progression of early precursor lesions, PanINs, to invasive PDAC and

are found in the majority of patients [25]. However, p16/CDKN2A germline mutations were originally only associated with the occurrence of melanoma and the formation of various benign nevi and it was only later when it was found to be implicated in multiple other types including sarcoma, breast, lung, and pancreatic cancers [26]. These patients harbor a 16% lifetime risk of developing PDAC [26].

1.2.2.2 Hereditary Nonpolyposis Colorectal Cancer (HNPCC)/Lynch Syndrome

As indicated by the name, hereditary nonpolyposis colorectal cancer or Lynch Syndrome is more often associated with colorectal cancer than the pancreas. It arises due to alterations in the mismatch repair genes MLH1, MSH2 & 6, and PMS2, or germline mutation of EpCAM which silences the transcription of MSH2 by epigenetic modification [27, 28]. Usually, one of the alleles is deleted followed by a second mutational hit to the remaining allele, thus causing a loss of function and an inability to efficiently repair DNA. Many of these patients are identified by high-levels of tumoral microsatellite instability (MSI) *via* polymerase chain reaction (PCR) and/or DNA mismatch repair deficiencies *via* immunohistochemical (IHC) staining [29]. While many of these patients are in fact characterized by early-onset colorectal cancer, HNPCC also confers an 8.6 fold cumulative lifetime risk of developing PDAC compared to the general population [30].

1.2.2.3 Peutz-Jeghers Syndrome

A germline STK11/LKB1 mutation, which encodes a member of the serine/threonine kinase family and regulates cell polarity, is autosomal dominant and leads to the Peutz-Jeghers Syndrome (PJS) phenotype. This is a syndrome characterized by hyperpigmentation of mucocutaneous areas as well as the formation of harmartomatous polyps throughout the gastrointestinal tract [31]. PJS leads to an incredibly high risk of

developing a myriad of cancers including esophageal, lung, breast, uterus, ovary, stomach, colon, and pancreas [32]. Specifically, PJS confers the largest cumulative lifetime risk of developing PDAC out of all the familial syndromes at 36% by age 65 [33], thus routine surveillance is warranted in this population.

1.2.2.4 Hereditary Pancreatitis

Hereditary Pancreatitis presents as recurrent bouts of acute pancreatitis manifesting with sudden onset of severe epigastric abdominal pain that radiates to the back often with concurrent nausea and vomiting [34]. This presentation is much like other etiologies of pancreatitis (i.e. alcohol/diet-induced and idiopathic) yet differs in a number of key ways. One of which is that symptoms often present themselves at far younger ages than other forms of pancreatitis (as young as ten-years-old in one study) [35]. The hereditary form of pancreatitis is thought to occur because of mutations that alter the homeostatic balance between secreted proteases and inhibitors, thus leading to autodigestion of the pancreas itself and inflammation [36].

The overwhelming majority of these cases (80%) are caused by an autosomal dominant mutation in PRSS1, which is a gene that encodes cationic trypsin [37]. The normal physiological function of cationic trypsin is the conversion of zymogens into active forms when excreted into the duodenum to digest food. PRSS1 mutations likely facilitate the premature conversion of trypsinogen (the inactive form of trypsin) into trypsin prior to excretion, thus causing autodigestion and the associated symptoms of pancreatitis [37]. The other known mutation that causes hereditary pancreatitis is SPINK1, which has the same result as PRSS1 mutations, i.e. trypsin over activation and autodigestion of the pancreas parenchyma, except *via* a slightly different mechanism. SPINK1 encodes a trypsin

inhibitor, thus mutations which result in a loss of function or expression of SPINK1 protein, cause an over activation of trypsin leading to autodigestion [38, 39]. Importantly, hereditary pancreatitis, regardless of the mutation that causes it, confers a dramatically increased risk of PDAC. Specifically, the cumulative risk by the age of 70 was found to be 40% for all patients and up to 75% for those with paternally inheritance [40]. Another study corroborated this finding and found a 44% cumulative risk by age 70 [41].

1.2.3 Precursor lesions

1.2.3.1 Pancreatic Intraepithelial Neoplasia (PanINs)

Pancreatic Intraepithelial Neoplasia (PanINs) are asymptomatic lesions < 0.5 cm in diameter found inside the intralobular ducts of the pancreas and consist of neoplastic proliferation of intraluminal columnar and cuboidal cells [42, 43]. These cells often produce mucin and have different proportions of cytological and architectural atypia leading to the formation of papillary structures [44]. PanINs are classified into three distinct grades that are predicated on histological characterization with the unifying feature that none of them are invasive. PanIN-1A (flat) and 1B (papillary) possess little atypia and are minimally dysplastic (low-grade). Progression to PanIN-2 involves mild to moderate nuclear atypia and cytoarchitectural changes and these are classified as intermediate-grade lesions. Finally, high-grade lesions with extreme mitotic atypia, cribriform structures, and possible necrosis comprise PanIN-3 lesions [45]. Progression through the PanIN stages to invasive cancer is considered the canonical route of pancreatic oncogenesis [46]. Notably, almost all high-grade PanIN lesions have been reported with concomitant infiltrating PDAC [47]. However, a recent study has highlighted cases of rare high-grade PanINs in the absence of PDAC, which can infiltrate the lumen causing upstream duct dilation [48].

Immunohistochemical staining of PanIN lesions displays an elevated expression of mucin proteins MUC1 and MUC5AC with a concomitant decrease in the level of MUC6 [49, 50].

PanIN progression is posited to be caused/accompanied by the accumulation of sequential genetic alterations that culminate in the formation of malignancy [51] (these chronological genetic changes that are associated with the formation of PDAC are discussed subsequent sections in this thesis). Those that harbor these precursor lesions theoretically represent a high-risk patient population that could be identified prior to the formation of cancer. Yet, these lesions are not able to be detected by modern radiological assessment methods including cross-sectional imaging [Computerized tomography (CT), magnetic resonance imaging (MRI)] and endoscopic ultrasound (EUS). Additionally, as mentioned prior, it is only possible to speculate the incidence within the general population because almost all of the high-grade PanINs heretofore identified are with concomitant PDAC with rare exceptions. Unfortunately, these facts, combined with the asymptomatic nature of PanIN lesions, prevent this cohort from being a screenable population from a biomarker perspective.

1.2.3.2 Pancreatic Cystic Lesions

The group that consists of the patients perhaps most amenable to early detection among the determined high-risk groups are those with a current or previous diagnosis of a pancreatic cystic lesion (PCL) [52]. Importantly, this is an identifiable cohort because, unlike PanINs, PCLs are clinically observable lesions (*via* imaging) that can provide a means of identification and thus, will be expounded on in this section. Patients harboring a cystic lesion are more likely to progress to cancer than even those with a family history of PDAC [53] making them a prime target population for screening and surveillance modalities.

However, complexities arise because PCLs present a variable risk for malignant progression: while some PCLs carry up to a threefold increased risk of developing PDAC [54, 55], others present with a marginal risk or low probability of developing into PDAC [56] (**Figure 1.3**). Thus, PCL patients represent one of the ideal populations to screen for PDAC.

It is estimated that 0.7-2.6% of the general asymptomatic population harbors some form of PCLs [57]. The prevalence of these lesions increases with age; autopsies of 70 to 79-year-old patients revealed that 25% harbor a pancreatic cyst, increasing to 37% for patients older than 80 [58-60]. These proportions extrapolate to an estimated 3.5 million people with cystic lesions in the U.S. alone. The transformation potential of all cysts is minimal and an investigation utilizing the SEER database found that 33.2 per 100,000 pancreatic cysts will progress to PDAC [61].

Though screening and intervention are warranted in this high-risk group, the pervasiveness of PCLs leads to thousands of unnecessary medical and surgical interventions per year. These high-risk procedures carry great comorbidity, especially for the elderly. Even if surgery is not required, immense amounts of time and resources are utilized to monitor patients for years following initial discovery [62]. This monitoring is multimodal and can involve expensive sequential imaging methods along with invasive procedures such as repeat Endoscopic Ultrasound-guided Fine Needle Aspiration (EUS-FNA), culminating in eventual excision. This leads to an increased economic burden on the health care system. Importantly, the anxiety and stress imparted on the patient after a PCL diagnosis cannot be understated, and the ability to ameliorate this burden would be immensely impactful [63].

Figure 1. 3 Chart depiction of pancreatic cystic lesion types.

All PCLs are divided into three main types, inflammatory, serous and mucinous. Those grouped under the "Other" heading are rare cyst types that include pseudopapillary tumors (SPT), lymphoendothelial cysts (LEC), and pancreatic neuroendocrine neoplasia (PNEN). The inflammatory type is predominately comprised of pseudocysts. Importantly, serous type cysts are rarely malignant. Mucinous cysts, however, divided into intraductal pancreatic mucinous neoplasms (IPMN) and mucinous cystic neoplasms (MCN), harbor a greater potential for malignancy. Thus, this is the primary PCL population that undergoes surgical resection. The prevalence of IPMN types (branch, main, and mixed duct), as well as sub-classifications (gastric, intestinal, pancreaticobiliary, and oncocytic), are shown along with their respective proportions that harbor concurrent malignancy. (Carmicheal J et al. Elevating pancreatic cystic lesion stratification: Current and future pancreatic cancer biomarker(s). Biochim Biophys Acta Rev Cancer. 2020;1873(1):188318).

Figure 1.3

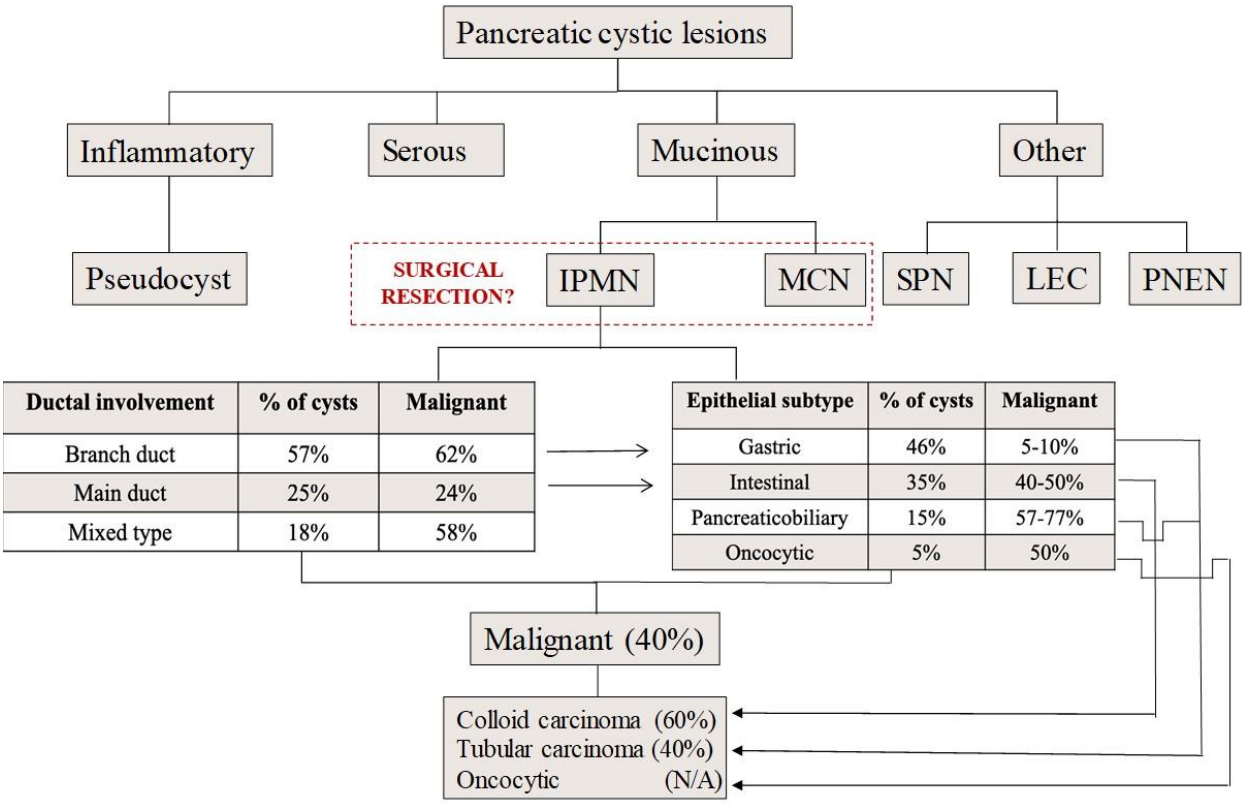
Pancreatic cystic lesions
Inflammatory
Serous
Mucinous
Other
Pseudocyst
SURGICAL RESECTION?
IPMN
MCN
SPN
LEC
PNEN
Ductal involvement | % of cysts | Malignant
Branch duct | 57% | 62%
Main duct | 25% | 24%
Mixed type | 18% | 58%
Epithelial subtype | % of cysts | Malignant
Gastric | 46% | 5-10%
Intestinal | 35% | 40-50%
Pancreaticobiliary | 15% | 57-77%
Oncocytic | 5% | 50%
Malignant (40%)
Colloid carcinoma (60%)
Tubular carcinoma (40%)
Oncocytic (N/A)

As per WHO classification (2000) [64-66] PCL's can be divided into; A. Serous tumors- including serous cystadenoma and serous cystadenocarcinoma B. Mucinous tumors- including mucinous cystadenoma, mucinous cystadenocarcinoma, intraductal papillary-mucinous adenoma and intraductal papillary-mucinous adenocarcinoma C. Solid pseudopapillary tumors.

A Serous Cystic Neoplasms

Serous cystadenomas/Serious cystic neoplasms (SCAs/SCNs) are benign tumors that can be sub-divided into serous microcystic adenoma (SMA) and serous oligocystic adenoma [64]. SMAs have a proclivity towards body or tail in 50-75% of cases while the rest involve the head of the pancreas [67, 68]. SMAs account for 1-2% of all exocrine pancreatic tumors. Females (70%) are affected more than males with a mean age of 66 years (range 34-91 years) at presentation. SOAs are far less common than SMA with no sex predilection and are located mainly in the head and body of the pancreas [69, 70]. On cross-sectional imaging with computed tomography (CT) or magnetic resonance imaging (MRI), SCAs are often multilocular with a honeycomb-like appearance and contain a central stellate scar [71]. This characteristic appearance can often lead to a definitive diagnosis *via* imaging. Histologically, the cysts are lined with glycogen-rich simple cuboidal epithelium, which is positive on periodic acid-Schiff stain without diastase digestion [72]. If imaging results are inconclusive, EUS/FNA of cystic fluid can also be done but has low sensitivity though the addition of cytobrushing can improve the sensitivity of EUS-FNA [73, 74]. SCNs have relatively lower carcinoembryonic antigen (CEA) levels than other PCL types with a higher risk of malignant progression [71]. However, there is no concrete evidence to support a direct correlation between CEA levels and the risk of malignant progression [75].

SCAs are considered benign lesions that do not communicate with the pancreatic ducts [76]. Their progression to serous cystadenocarcinoma is exceedingly rare, with an incidence rate of less than 1%, including the largest series that reported three cases of cystadenocarcinoma out of 2622 patients [77]. For this reason, the clinical recommendation is to observe serous cystadenomas, with or without serial imaging, to check on the growth rate of the tumor. Resection is warranted only if mass effect symptoms are present such as abdominal pain, nausea, jaundice, or rapid cystic growth. Palliative resection can also be considered if the lesion transforms into a serous cystadenocarcinoma and becomes malignant [78].

B Mucinous Cystic Lesions

B.1 Mucinous Cystic Neoplasms

Mucinous cystic neoplasms (MCNs) represent 2-5% of all exocrine pancreatic tumors [69]. The mean age at diagnosis is 49 years (20-82 years) and these lesions are predominantly found in women (F: M > 20:1) [69, 79]. MCNs are mainly located in the body and tail of the pancreas and if present in the head of the pancreas, they are highly suspicious for mucinous adenocarcinoma [80, 81]. MCN's are typically a single lesion, that can be unilocular or multilocular, which does not communicate with the pancreatic duct [82]. Morphologically, MCNs are characterized by a large, solitary, septated, thick-walled cyst with a pseudo-capsule containing either mucin or mixture of mucin and hemorrhagic material [83]. Histological analysis can reveal ovarian-like stroma in addition to columnar cells with abundant mucin production [84]. As per international consensus in 2004, the histological presence of unique ovarian-type stroma was necessary to confirm the diagnosis of MCNs [85]. In contrast to the aforementioned serous cystic lesions, MCNs have an

increased propensity to be malignant or progress to a malignant state. The incidence rate of mucinous adenocarcinoma varies between 6-36% [86]. If the lesion is multilocular, contains papillary projections, and/or contains mural nodules the risk of malignancy drastically increases [87]. The spectrum of differentiation in terms of histology ranges from normal-appearing columnar epithelium to the atypical epithelium. Tumors can be classified as MCN with low/intermediate grade dysplasia, MCN with high-grade dysplasia, or MCN with an associated invasive carcinoma [88].

In an analysis of 163 patients with resected MCNs, the prevalence of adenocarcinoma was reported to be 17.5% by Crippa et al. [89]. The older patients with invasive adenocarcinoma in this cohort suggested a progression from adenoma to carcinoma. Thus, this group stated that resection should be considered in patients with high-risk MCNs and patients with low-risk MCNs, defined as size less than 4 cm and no nodules, can be considered for non-radical resections [89].

B.2 Intraductal papillary-mucinous neoplasms

Intraductal papillary-mucinous neoplasms (IPMNs) are mucin-producing tumors arising from the main pancreatic duct or its branches [90]. These lesions are characterized by a dilation of the pancreatic duct resulting from immense mucus production and papillary growth of ductal epithelium. IPMNs comprise 1-3% of exocrine pancreatic neoplasms, with an incidence rate of 1 per 100,000 per year [59, 91, 92] and their frequency is higher in males than in females with a median age of diagnosis in the 6-7th decade [82, 93]. IPMNs can be divided into low-risk and high-risk, with the latter defined as dilated main pancreatic duct >5 mm or the presence of a mural nodule. The pooled cumulative incidence of high-grade dysplasia or pancreatic cancer for low-risk IPMNs is 0.02%, 3.12% and 7.77% at 1

year, 5, and 10 years, respectively. While that for high-risk IPMNs is 1.95%, 9.77% and 24.68 % at 1 year, 5 and 10 years, respectively [94]. IPMNs can involve the main duct (MD-IPMN) or side branches (BD-IPMN) or both, which are known as mixed IPMN. BD-IPMNs are not only the most common IPMNs but also the most common pancreatic cyst. MD-IPMNs carry a higher risk of malignancy than BD-IPMN, with 38-68% of the resected specimens of MD-IPMNs showing high-grade dysplasia or cancer [95]. The relative risk of malignant transformation for multifocal IPMNs is not at higher risk as compared to a single cystic lesion [96]. Mixed-type IPMNs contain features of both, yet behave most similarly to MD-IPMNs in terms of progression and malignant potential and are clinically treated as such. Differentiating IPMNs that are malignant/invasive from those that are benign is a persistent and important problem to address.

Based on the cytoarchitectural features and mucin immunohistochemistry (i.e. MUC1, MUC2, and MUC5AC), IPMNs have been classified into four histopathological types; gastric (49-63%), intestinal (18-36%), pancreaticobiliary (7-18%), and oncocytic (1-8%) [96-98]. Recent investigations showed benign EUS findings (cyst size < 5mm and the absence of a mural nodule) are associated with gastric type IPMN [99]. Corroborating this finding, Furukawa et al. found prognostic relevance to IPMN classification, where patients with gastric type had a better prognosis than patients with intestinal-type IPMNs [100]. Gastric type is associated with the more indolent BD-IPMN, whereas intestinal type is often associated with MD-IPMN [101]. The pancreaticobiliary type has been regarded by some as a high-grade version of the gastric type. These lesions are uncommon, not well characterized, and the invasive carcinoma associated with this type is more aggressive [102, 103]. Oncocytic type is relatively uncommon, tends to be large lesions with obscure

intraductal appearance, and is less invasive [104]. A retrospective study of patients with cystic lesion type verified on pathology found that even though gastric type IPMN had a better prognosis than intestinal type, those with the gastric type who developed invasive disease had worse outcomes when compared to those with progression arising from intestinal-type [100]. The reason for this phenomenon was that gastric IPMNs had the potential to develop a more aggressive tubular (ductal) carcinoma as opposed to the colloid (mucinous) carcinoma arising from intestinal IPMNs [100].

C Other Pancreatic Cystic Lesions

Other cystic lesions of the pancreas include solid pseudopapillary tumors (SPT), lymphoendothelial cysts (LEC), and neuroendocrine neoplasms (PNENs). SPT is a rare tumor seen most frequently in young women in their 20's. Less than 10% of SPT's have aggressive tumor behavior pathologically with a 5- year disease-specific survival of over 98% [105]. The tumor is considered indolent given the high survival rates of patients even when metastases are present [106]. The diagnostic accuracy of preoperative imaging for SPT is high with a sensitivity of 95% [107]. LECs are extremely rare complex lesions that are often round and exophytic that predominately occur in males [108]. They are often anechoic or hypoechoic on EUS and can present with elevated CEA and amylase levels in the cyst fluid aspirate [108]. While these lesions can harbor malignancy, their rarity has prevented adequate pathological characterization [109]. PNENs are also rare and may be solid, cystic, or mixed in morphology. They are usually non-functioning and may occur sporadically or in individuals with multiple endocrine neoplasia type 1 (MEN1) and/or Von Hippel-Lindau (VHL) [110]. They usually present in the sixth decade and have equal gender predisposition.

Unlike SPTs, the diagnostic accuracy of preoperative imaging for PNEN is low (sensitivity of 53.3%) [107]. However, EUS-FNA of PNENs has a 90% diagnostic accuracy [111].

Inflammatory pseudocysts are non-malignant fluid-filled sacs often filled with necrotic and hemorrhagic material along with pancreatic enzymes [112]. These are not true cysts as they do not have an epithelial lining. In the absence of any clinical symptoms, they can be monitored with imaging while symptomatic lesions can be effectively treated with steroids and/or surgical drainage [113]. Notably, pseudocysts are often associated with a history of chronic and/or acute pancreatitis [114], alcoholic pancreatitis [115], or autoimmune pancreatitis [116]. These studies found that 42-56% of pancreatitis patients harbor pseudocysts [114, 115]. Unfortunately, some cystic neoplasms, including those with malignant potential, can initially present with pancreatitis or even cause recurrent bouts of pancreatitis [63, 117]. Along with this, serum amylase and lipase levels, the standard metrics by which pancreatitis is assessed in clinics, are unable to differentiate between MCNs and pancreatitis without supplemental imaging and invasive procedures [118]. Up to 15% of IPMN patients present with pancreatitis [119] as well as 9% of those with MCNs [89] and some IPMNs can elicit an immune response thus inducing autoimmune pancreatitis [120]. BD-IPMNs, in particular, can be difficult to differentiate from pseudocysts in the setting of pancreatitis and thus, many pseudocysts are often mismanaged as IPMNs [63]. It has been reported that 10-15% of cystic lesions discovered with a background of pancreatitis can be malignant [116, 121]. Large cyst size and poor response to steroids increase the likelihood of the presence of malignancy [116, 121].

1.3 Genetic and molecular mechanisms of PDAC oncogenesis and progression

Recent comprehensive genomic analyses have built upon this foundation and have yielded influential insights regarding the genetic alterations associated with pancreatic tumorigenesis [122-124]. These whole-exome/genome sequencing studies have confirmed the importance of traditional somatic oncogenic driver genes but have also elucidated a number of less frequently mutated driver genes as well as uncovered germline tumor susceptibility genes in PDAC patients without a family history or genetic syndrome [125]. Though these are important and impactful findings (e.g. National Comprehensive Cancer Network (NCCN) guidelines no recommend germline testing for all confirmed PDAC cases), they lie outside the purview of this section and the traditional genetic progression model will be the focus in this section.

The first characterized mutation in PDAC was in a cancer cell line (T3M4) in codon 61 of KRAS (Glu-His) [126]. This study initiated the search and eventual discovery of myriad genes determined to be involved in various aspects of PDAC including initiation, development, and progression. These include oncogene activation/overexpression such as KRAS [127] and tumor suppressor gene inactivation/downregulation such as DPC4/SMAD4 [128], TP53 [127], and p16/CDKN2A [25]. Concurrent telomere dysfunction and shortening have also been proven to be a component of PDAC formation [129]. These studies culminated in the current generally accepted progression model proposed by Hruban and colleagues in 2000 [51].

Among the earliest events associated with progression to PDAC are alterations in the KRAS oncogene, telomeric shortening, and CpG island hypermethylation [130]. KRAS encodes for a RAS GTP-binding protein family member that dictates cellular proliferation and survival [131]. Activated KRAS initiates many different pro-survival signaling

mechanisms including RAF-MAPK and PI3K pathways [132]. KRAS mutations are one of the earliest genetic abnormalities in the PDAC progression model and have been well characterized as driver mutations the pathogenesis of pancreatic cancer [133] [134, 135]. The most common activating point mutations (most often residing in codons 12 and 13) produce a constitutively active protein resulting in unrestricted growth signaling [136, 137]. Alterations in KRAS are thought to be an early event in IPMN and PanIN biogenesis as it is found in all types without significant differences [138, 139].

Another one of the earliest events in PanIN formation and progression to PDAC is telomeric shortening. Telomeres protect the end of chromosomes preventing unwanted chromosomal fusion events and telomere shortening can lead to aberrant chromosomal fusion resulting in unstable chromosome structures and subsequent DNA fragmentation [129, 140]. Loss of telomere protection can also lead to the accumulation of chromosomal amplification and/or deletions causing aberrant protein expression profiles [141]. Along with KRAS, this telomeric shortening is considered integral to the initiation of PanIN lesions formation and the subsequent trajectory towards PDAC.

CpG island methylation within a gene promoter region is an epigenetic modification that leads to a silencing of gene transcription under normal physiological circumstances [142]. However, hypermethylation of a number of genes (namely tumor suppressors) has been observed in the setting of PDAC [143, 144]. Additionally, CpG island hypermethylation has been observed in low-grade PanIN lesions, thus implicating its role in initiation [145]. Some of the important tumor suppressor genes that are affected, and most relevant to PDAC progression, include p16/CDKN2A, TP53, and DPC4/SMAD4 [42].

p16/CDKN2A inactivation has been observed in later PanIN 1. The influence of p16/CDKN2A as a tumor suppressor (as a function of cell cycle regulation at G1 phase) is highlighted by the fact that homozygous deletion of 9p21 locus (location of p16/CDKN2A) is seen in up to 40% of PDAC cases and loss of function is seen in 90% of patients (40% homozygous deletion, 40% single allele loss with concomitant mutation, and 10% hypermethylation silencing) [25]. TP53 is mutated in 50-75% of all PDAC patients, and this is usually an allelic loss followed by a concomitant missense mutation in the remaining allele [146]. It functions as a tumor suppressor facilitating and maintaining G2/M arrest as well as induces apoptosis, thus the mutations occurring in the gene encoding for this protein results in cell cycle and cell death deregulation [147]. With this, DPC4/SMAD4 controls growth *via* the transformation growth factor β (TGF-β) pathway and the regulation of pro-growth genes [128, 148] and loss of this gene leads to a decrease in growth inhibitory signaling. In contrast to p16/CDKN2A, TP53 and DPC4/SMAD4 loss seem to arise only at the PanIN-3 stage and continue through PDAC, thus emphasizing their functions as key molecules preventing malignant transformation to an invasive phenotype [149].

Many other somatic mutations in oncogenes have been implicated in PDAC progression involving a wide array of signaling pathways. These include G-protein signaling (cAMP production) *via* GNAS [150], transcriptional regulation *via* MYC (chromosome 8q24 amplification) [123], and EGFR signaling *via* ERBB2 [151] and EGFR [152]. Additionally, many other tumor suppressor gene mutations have been brought to light including RNF4 [124]. The continual discovery of genes along with their diverse mechanisms of action, emphasizes the intense complexity associated with PDAC initiation, development, and progression.

1.4 Detection methods

The decades-old challenge still remains to identify the high-risk patients harboring early malignancy or precursor lesions that will eventually progress to PDAC. The incredibly low incidence of PDAC in the general population prevents wide use of conventional screening modalities as the quantities of false positives leading to erroneous procedures would eclipse the number of detected cancers [153]. Therefore, the high-risk groups previously discussed (those with greater than 5% lifetime risk of developing PDAC) are the only populations for which screening and possible early detection is recommended. Current detection methods used in the clinic are threefold: Imaging, EUS-FNA cytology, and the use of molecular markers CA19.9 and carcinoembryonic antigen (CEA).

1.4.1 Imaging

Various imaging methods including computerized tomography (CT), magnetic resonance imaging (MRI), magnetic resonance cholangiopancreatography (MRCP), and abdominal ultrasound are integral to the monitoring of high-risk individuals, presenting symptomatic patients, and lesion differentiation [154-156]. Guidelines regarding surveillance of patients with a family history of PDAC, hereditary pancreatitis, genetic syndromes, and PCLs all incorporate the use of sequential imaging with EUS and/or pancreas MRI as the initial means of patient screening [13, 14]. However, the level of clarity proffered by these myriad imaging modalities is not adequate for the actual diagnosis of PDAC. Conventional imaging does not have the resolution to detect PanIN lesions at any stage and nowhere is this problem of ambiguous imagining results more apparent than with the PCL population. The overall prevalence of all PCL types in the general population has increased in recent years due to the ubiquitous use of cross-sectional imaging modalities. According to the

American Gastroenterological Association (AGA), the proportion of incidental PCL discoveries in patients who undergo magnetic resonance imaging (MRI) for an unrelated reason is 15% [157].

Any abnormalities found on imaging require further investigation *via* tissue biopsy, laboratory testing, and more invasive/expensive imaging modalities including and endoscopic ultrasound (EUS), endoscopic retrograde cholangiopancreatography (ERCP), and positron emission tomography (PET). So while imaging is an incredibly important component of monitoring those at high-risk and assessing symptomatic patients, it is in no way definitive. Inherently this increases the total number of patients that require continual monitoring (image-guided) or even subjected to more invasive testing. Imaging will always be a mainstay for high-risk patient monitoring and its diagnostic shortcomings will need to be reduced. With this in mind, efforts are currently underway to increase the diagnostic efficacy of imaging for PDAC including but not limited to radiomics [158], FDG-PET/CT [159], and molecular imaging facilitated by mAB conjugated nanoparticles [160].

1.4.2 Cytology

Historically, cystic fluid has been collected and assessed for markers for two primary reasons; discerning between mucinous and serious cysts, and differentiating benign from malignant lesions. Coupled with EUS imaging, fine-needle aspiration (EUS-FNA) is a procedure used to obtain cystic fluid for analysis. This fluid can be assessed for the presence of dysplastic cells. Patients harboring cysts with worrisome features, or those greater than 3 cm, are recommended to undergo EUS. Each cyst subtype has discreet characteristic cellular typology, morphology, and immunohistochemical staining. Pseudocysts demonstrate inflammatory cells while serous mucinous neoplasms

demonstrate glycogen-containing cells [76]. Mucinous cystadenocarcinomas demonstrate cells with malignant features (increased nuclear/cytoplasmic ratio, pleomorphism, anaplasia, hyperchromatism, prominent nucleoli, and mitoses) nearly 50% of the time, but the yield is usually low [161]. MUC2 and CDX2 are indicative of intestinal differentiation and can be used as immunohistochemical markers to identify intestinal-type IPMN [103, 162]. A meta-analysis by Suzuki et al. showed a sensitivity and specificity of EUS-FNA cytology to be 65% and 91%, respectively, for distinguishing malignant and benign IPMNs [163]. There has always been a concern with peritoneal seeding secondary to EUS/FNA; however, a study found no significant increase in metastatic disease secondary to the procedure in patients with IPMNs who underwent EUS/FNA [164].

While cystic fluid cytology can help differentiate between various cyst types and can be highly specific, the cellular yield is often too low to be diagnostically useful thereby greatly diminishing the sensitivity. In the Cooperative Pancreatic Cyst study (CPC study) that involved 341 patients with PCLs, the sensitivity of cyst fluid cytology for diagnosing mucinous cysts was only 34% because of the low number of cells found in cystic fluid [165]. In conjunction, a multiloculated cystic lesion leads to the compartmentalization of fluid species, thus, FNA may not be representative of the lesion's gestalt.

1.4.3 CA19.9 and CEA

CA19.9 is a Sialyl Lewis A glycan present on multiple glycoproteins and is currently used in the clinic to monitor patients for PDAC progression and/or evaluation after surgical resection. It is often elevated in PDAC making it one of the most clinically useful markers to date [107]. Carcinoembryonic antigen (CEA) is a secreted glycoprotein involved in cell adhesion and has been used as a biomarker for various gastrointestinal

malignancies [166, 167]. It is one of the most clinically useful cystic fluid biomarkers for PCLs and the prediction of malignancy. These proteins are often aberrantly expressed and detectable in cystic fluid and serum, and much research has been conducted to discern their respective diagnostic and prognostic significance.

Cystic fluid CEA and CA19.9 levels have also been shown to be higher in malignant compared to benign cysts [168]. In this study, the sensitivity/specificity for CEA and CA19.9 for predicting malignancy were 92%/64% and 81%/69%, respectively [168]. A meta-analysis looking at the ability of serum CA19.9 and CEA to identify invasive and malignant IPMNs found CA19.9 had a pooled sensitivity of 52% and 40% and specificity of 88% and 89%, respectively while CEA has a pooled sensitivity of 18% for both invasive and malignant IPMNs and a specificity of 95% and 93%, respectively [169]. A combination of serum CA19.9 and CEA was used to determine the presence of malignancy in resected IPMNs [170]. CA19.9 alone had a sensitivity/specificity of 74%/86%, CEA had a sensitivity/specificity of 40%/92%, and a combination of CA19.9 (cutoff >37U/mL) and CEA (cutoff >5 g/mL) had a sensitivity/specificity of 80%/82% [170].

While these two markers are the current gold standards and prove beneficial for therapeutic monitoring and recurrence detection, they do not exhibit the required sensitivity nor specificity levels required for screening purposes. CA19.9 is limited in its diagnostic utility as Le(a^-b^-) patients do not have the necessary fucosyltransferase enzyme to produce it and also, this phenotype is highly variable among different ethnic groups: Asian (7%), European (8%), African (19%) [171]. CEA can be expressed in serum resulting from other diseases including lung fibrosis, Alzheimer's disease, and a variety of other cancers [172]. Further, neither of these proteins has been capable of adequately differentiating benign vs

malignant disease in cystic fluid specimens nor serum. With this, these studies demonstrate that clinically used cystic fluid and serum markers are variable in their diagnostic potential and that more accurate biomarkers are needed to determine the presence of malignancy.

1. 5 Therapeutic strategy

1.5.1 Surgery

Surgical resection is the mainstay of treatment for PDAC as it is the only curative treatment option available [173]. This can be accomplished with distal or total pancreatectomy, or a pancreaticoduodenectomy (Whipple) procedure, depending on the location of the tumor [174]. Unfortunately, surgery alone is necessary but not sufficient as >80% of patients relapse and succumb to the disease if no other therapy is administered [175]. Further, the overwhelming majority of patients (80-85%) present at a time when surgery is no longer a viable option due to the presence of locally advanced and/or metastatic disease [176]. Thus, while surgery is the cornerstone of PDAC therapy, improvements on outcomes have been reliant upon adjuvant and neo-adjuvant administration of systemic and/or localized therapies to further improve survival as well as decreased tumor volumes to sizes capable of being resected. Current guidelines American Society for Clinical Oncology (ASCO) and NCCN guidelines recommend the addition of adjuvant chemotherapy for all patients that have undergone surgical resection as well as neoadjuvant therapy for those with unresectable tumors [177, 178].

1.5.2 Adjuvant therapy

One of the earliest studies investigating the possible role of adjuvant therapy for PDAC discovered a significant increase in overall survival from 11 months to 20 months with the administration of 5-Fluorouracil (5-FU) after resection compared to resection

alone [179]. This study also formed the basis for the current opinion that adjuvant radiation is not beneficial in terms of survival outcomes as no difference was observed between the chemotherapy alone and chemoradiation therapy arms. This was a finding corroborated by the ESPAC-1 trial where chemoradiation was reported to provide no additional benefit to chemotherapy alone [180]. Following this a seminal study, CONKO-001, was conducted decades later in which adjuvant gemcitabine was found to be equally as effective as 5-FU, but with less toxicity [181]. Gemcitabine efficacy was found to be potentiated with the addition of capecitabine in the ESPAC-4 trial published in 2017, resulting in 5-year survival of 30% for patients undergoing combination treatment following surgery [182]. This trial set the new standard for PDAC therapy. With these results, this is the recommended therapeutic regimen provided by the current ASCO guidelines [177].

The combination treatment regimen of folinic acid, fluorouracil, irinotecan, and oxaliplatin (FOLFIRINOX) has been used to treat metastatic and recurrent PDAC patients with favorable impacts on survival compared to gemcitabine [183]. Results of a recent clinical trial (NCT01526135) investigating the use of adjuvant FOLFIRINOX compared to gemcitabine showed an impressive increase in median overall survival between the two groups increasing from 35.0 months in the gemcitabine arm to 54.4 months in the FOLFIRINOX arm [184]. Additionally, the 3-year overall survival percentage was 39.7% and 21.4% in the FOLFIRINOX and gemcitabine groups, respectively. Of note, this study used a modified version of FOLFIRINOX (decreased doses of the constituent drugs) to try and mitigate the associated toxicities, yet 75.9% of patients still experienced high-grade toxicities and many had to discontinue treatment [184]. This result has led the NCCN to add FOLFIRINOX as a consideration for patients that can tolerate the therapy [178].

1.5.3 Neo-adjuvant therapy

Even with the substantial benefit offered by adjuvant therapy up to 75% of patients relapse with disseminated disease [185]. Neo-adjuvant therapy could eliminate micro metastasis and shrink the primary tumors and thus diminish the probability of disease recurrence [186]. The NEOPA trial looked at the potential benefits of chemotherapy and radiation therapy prior to surgical resection and found that neo-adjuvant combination gemcitabine and external beam radiation provided a 12% increase in overall survival compared to surgery alone [187]. PREOPANC-1 trial is currently underway that aims to further expound the role of neoadjuvant therapy in the setting of resectable disease [188].

As described previously, the majority of patients present at a borderline or locally advanced stage, when surgery is complicated or not possible. Borderline resectable disease is often defined as confined to the pancreatic bed with limited involvement of the adjacent vasculature where vascular reconstruction is possible [189]. Locally advanced disease is often defined as involvement of the celiac artery (CA) or $>180^{o}$ encasement of the superior mesenteric artery (SMA) and/or superior mesenteric vein (SMV) or portal vein (PV) [190]. The mean 30-month survival of those with locally advanced disease has been reported as low as 8% [191]. These two groups of patients comprise 30-40% of initial presentations and represent a group of patients that stand to benefit from neo-adjuvant therapy [175, 192].

FOLFIRINOX has begun to emerge as an excellent neo-adjuvant chemotherapeutic agent in recent studies [193]One study found FOLFIRINOX treatment of locally advanced PDAC facilitated the eventual surgery of 61% of patients involved in the study [194]. Along with this, a meta-analysis incorporating data from 253 patients found this strategy to cause 43% of those treated to become resectable [195]. However, a different study found

FOLFIRINOX treatment in locally advanced PDAC to facilitate surgery in only 29% and a large proportion of participants (86%) had to discontinue or modify the chemotherapy regimen due to toxicity (Of note, total sample size was small at 14 and did not have a control group comparison) [196]. Interestingly, the addition of chemoradiation (25Gy in 5 fractions and capecitabine) with FOLFIRINOX for patients with borderline resectable disease lead to an impressive 67% resection rate (all but one of those had pathologically negative margins (R0)) and a median overall survival of 37.7 months [197]. Congruently, a meta-analysis incorporating 19 studies involving borderline resectable or locally advanced disease found that neo-adjuvant treatment (76.9% involving radiation and 74.4% involving chemoradiation) facilitated resection in 40.2% of patients [186].

One of the most prevalent neo-adjuvant therapeutic modalities is the administration of external beam radiation therapy (EBRT), in dose ranges from 25-50 Gray (Gy) typically in 2Gy fractions, with or without concurrent chemotherapy [198]. There have been many studies that have reported the benefit of incorporating EBRT into therapeutic regimens and these have reported resection rates up to 85% [199-201]. Along with this, a greater portion of those who are able to undergo surgery after EBRT achieve R0 resections reaching 100% in one study [202] and many reported increases in overall survival compared to non-radiated control groups [198].

In contrast to EBRT, stereotactic body RT (SBRT) is a highly conformational technique capable of delivering large radiation doses in a small number of fractions (hypo fractionated) with concurrent image guidance, thus limiting radiation delivery to surrounding tissues thereby abrogating toxicity and facilitating local ablation of the tumor [203, 204]. The benefits associated with SBRT has caused it to become heavily studies in

conjunction with traditional chemotherapeutic agents [205]. One study even found hypo fractionated SBRT spared lymphocytes from radiation-induced cell death compared to EBRT with conventional fractionation in PDAC patients [206]. A trial utilizing SBRT to deliver 33Gy in 5 fractions (6.6Gy/fraction) achieved a one-year overall survival rate of 59% with extremely low toxicities [207]. Additionally, the high-conformational ability of SBRT can be taken advantage of to deliver high-doses along the contours of vasculature adjacent to the tumors in borderline resectable and locally advanced patients. For example, one trial delivered 30Gy in 5 fractions to the entire tumor and 40Gy in 5 fractions (with concomitant gemcitabine) to the tumoral surface abutting the vasculature to increase shrinkage [207]. Importantly, 51% of borderline resectable patients went on to receive surgical treatment and 96% of those achieve an R0 (negative surgical margins) resection [207]. Even with these high doses administered *via* hypo fractionated, in-field recurrence has been found to still occur in 26.1% of patients, which highlights the problem of radiation resistance in PDAC [208].

1.6 Conclusions and perspective

The ability to determine the need and level of intervention in high-risk populations depends upon an accurate diagnosis. This must be achieved prior to the onset of symptoms as these do not often occur until later-stage disease. Initial presentation to the clinic is most often at stages III and IV [209]. Importantly, only stage I and II patients even have a possibility of being resected predicated on the structures involved. While tissue-based classification can be incredibly accurate and allow for true histological

analysis and verification of disease by a pathologist, sample acquisition can carry significant comorbidities due to the invasive nature of the procedure.

Further, single-site biopsies do not account for the entirety of the lesion, thus increasing the possibility of missing malignant disease. Conversely, the use of imaging for classification is non-invasive and can take into account the holistic state of the lesion. Unfortunately, current imaging modalities are expensive, are susceptible to observer variation, cannot visual extremely early malignancy, and have limited accuracy in differentiating malignant vs non-malignant cysts. Cystic fluid (*via* EUS/FNA) and serum (*via* blood draw) offer a less invasive means of analysis than biopsy. Yet many FNA samples have scant cellularity leading to inconclusive results and the current serum-based biomarkers are inadequate for detection.

An intense investigation into biomarkers for the noninvasive characterization of high-risk patients is required and these biomarkers must be able to consider the diversity in the genetic origins of PDAC [210]. Biomarkers should be used in conjunction with the current consensus for imaging guidelines to determine the potential of malignancy. In effect, the task remains to identify the most at-risk patients within the high-risk populations. These include options such as the assessment of circulating endothelial cells [211], cell-free DNA measurements [212], improved imaging/biopsy modalities [165], and extracellular vesicle (EV) analysis [213, 214]. EVs are an especially attractive target as a means of detecting PDAC and further analysis of the intravesicular and surface contents may lead to the discovery of unique circulating biomarkers.

Once detected, medicine must be able to offer a treatment that provides a meaningful extension of life to the patients suffering from this dreaded disease. Surgical

Figure 1. 4 Survival of SEER patients (1992-2016) treated with currently available therapies.

The 5-year survival of all patients within the SEER database is relatively unchanged regardless of therapeutic modality. The addition of chemotherapy and/or radiation to surgery marginally improves survival at the one-year and two-year time points but does not confer any survival advantage at later time points.

Figure 1.4

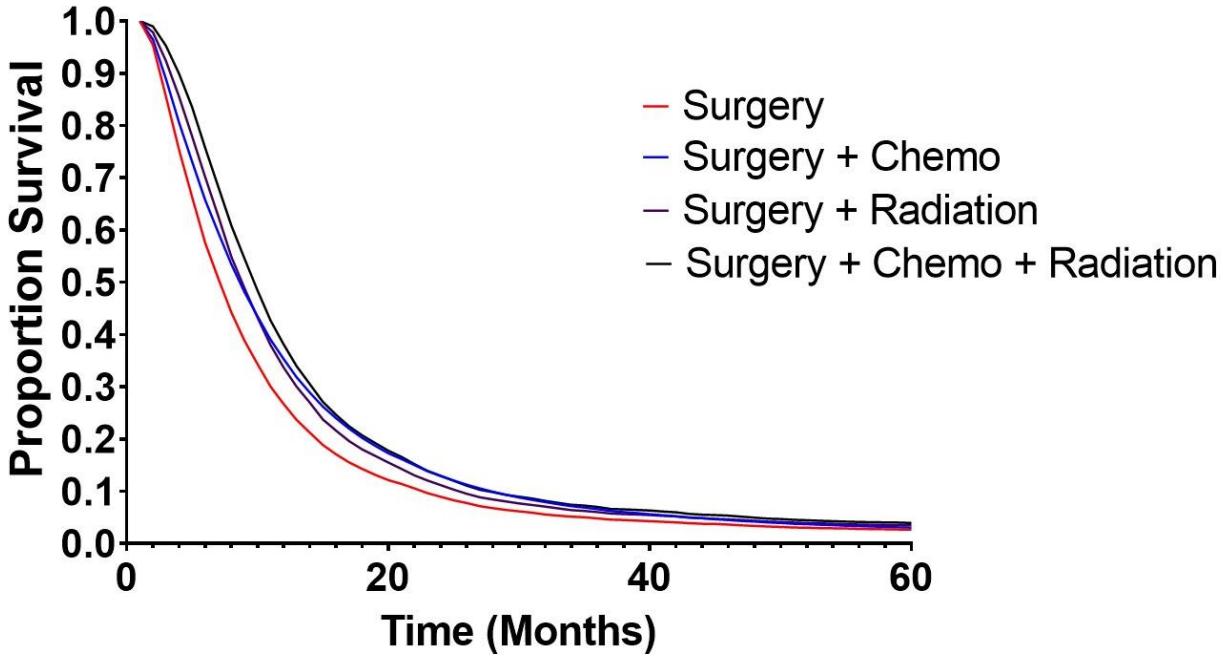
Proportion Survival
1.0
0.9
0.8
0.7
0.6
0.5
0.4
0.3
0.2
0.1
0.0
0
20
40
60
Time (Months)
Surgery
Surgery + Chemo
Surgery + Radiation
Surgery + Chemo + Radiation

resection of the primary tumor remains the only curative option for pancreas cancer. Only marginal increases in the life span of PDAC patients by just a couple of months have been achieved over the last 30 years [215]. While the current therapeutic strategies (i.e. surgery, chemotherapy, and radiation therapy) do confer an improvement in outcomes compared to no treatment, the 5-year survival of PDAC patients in the SEER database (1992-2016) is still incredibly low, even with combination regimens (**Figure 1.5**). Traditional mild chemotherapeutic options such as gemcitabine and paclitaxel offer very little benefit in overall survival and conversely, very few patients are eligible or capable of undergoing more effective treatments such as FOLFIRINOX due to intense chemo-toxicities. Along with this, many PDAC patients are refractory to radiation treatment and thus, this has not been a traditional first-line therapy.

There exists a fervent need to improve the therapeutic armamentarium when it comes to PDAC. One that may take into consideration some of the unique aspects of this disease and prevent some of the toxicities associated with pan-cytotoxic chemotherapies. With the advent of SBRT, site-directed radiation treatment is possible, at higher doses that the past with limited off-target toxicities. Additionally, it was shown capable of reducing the volume of non-resectable PDAC tumors, to a size amenable to resection. Unfortunately, there remains a portion of the patient population that remains resistant to radiation therapy. A means of potentiating this site-specific and targeted therapy would prove highly advantages in the fight against this horrible malignancy [216].

The high lethality of PDAC is due to two primary reasons: 1. the discovery of PDAC at later stages, with metastatic disease present at the time of initial diagnosis [177]. 2. The lack of efficacious therapeutic interventions. In a time when average survival for most

cancers is climbing, PDAC continues to remain stagnant [2]. The goal of this thesis is to develop novel detection and treatment strategies for PDAC. Firstly, serum EVs will be investigated as potential non-invasive liquid biopsy biomarkers, to serve as a means of early cancer detection. Secondly, a recently discovered form of cell death, ferroptosis, will be investigated as a means of potentiating radiation therapy.

Chapter 2: Methods

2A: Extracellular vesicle surfaceome characterization for the early detection of pancreatic ductal adenocarcinoma

2B: Radiation potentiation *via* ferroptosis for the improved treatment of pancreatic ductal adenocarcinoma

Chapter 2: Methods

2.1 Cell Culture

MiaPaCa, CD18/HPAF, T3M4, BxPC3, Panc1, Colo357, AsPC1, and Capan1 (pancreatic ductal adenocarcinoma) cell lines were cultured in Dulbecco's modified Eagle's high glucose medium (Hyclone, South Logan, UT, USA) with 10% FBS and 1% streptomycin at 37ºC in a humidified atmosphere containing 5% CO_2. HPDE (human pancreatic ductal epithelium) cell line was cultured in keratinocyte serum-free medium supplemented with epidermal growth factor (EGF) and bovine pituitary extract (Invitrogen, Carlsbad, CA, USA) with 10% FBS and 1% streptomycin at 37˚C in a humidified atmosphere containing 5% CO_2. (Note: This is a nonmalignant pancreatic ductal epithelial cell line immortalized from a normal human specimen *via* retroviral transduction of HPV16 E6/E7. Neither oncogenic mutations nor neoplastic morphological changes are present in this cell line.) At 70-80% confluence the plates were washed with PBS and serum-free medium was added. The cells were cultured in serum-free medium for 48 hours followed by the collection of medium for the EV isolation experiments.

2.2 Immunoblotting

Protein was extracted from purified EVs using ice-cold RIPA (50mM Tris-HCl, 150mM NaCl, 1% NP-40, 0.5% sodium deoxycholate and 0.1% SDS) containing protease (1mM phenyl-methyl sulphonyl fluoride, 1mg/ml aprotinin, 1mg/ml leupeptin) and phosphatase inhibitors. EV lysates were spun at 13,000 RPM for 30 minutes at 4ºC, the pellet was discarded the supernatant collected. Proteins were resolved using acrylamide; bisacrylamide gels and transferred to a PVDF membrane. The membranes were then

blocked with 5% milk, probed with primary antibodies overnight at 4°C. Membranes were washed (3 x 8min) with phosphate-buffered saline and .01% Tween 20 (PBST) at room temperature and subsequently probed with 1:3000 dilution of horseradish peroxidase-conjugated anti-mouse or anti-rabbit secondary antibodies (Thermo Fisher Scientific, Waltham, Mass, USA). After secondary antibody incubation for one hour, the membrane was again washed (4 x 8min) with PBST and the protein of interest was visualized by enhanced chemiluminescence detection (Thermo Fisher Scientific, Waltham, MA, USA) and exposed on an X-ray film for signal detection.

2.3 Statistical Methods

Statistical analysis was conducted using JMP Pro software with either student T-test, or Mann-Whitney-U and Wilcoxon rank test for non-parametric testing of groups that did not meet the normal distribution assumption. Survival curves were evaluated *via a* log-rank test with $p \leq 0.05$ considered statistically significant.

2A Extracellular vesicle surfaceome characterization for the early detection of pancreatic ductal adenocarcinoma

2A.1 EV isolation from cell medium and serum

Three hundred ml of cell medium was centrifuged in 50 ml aliquots at 11200G for ten minutes at 4°C to remove dead cells and cellular debris. The supernatant was then filtered and concentrated with a 100kDA centrifugal filtration to a total of 10ml. The six solutions used of different quantities of sucrose by weight% in PBS with respective relative densities (g/ml) are as follows: 5% - 1.0178, 15% - 1.0596, 30% - 1.1270, 40% - 1.1765, 50% - 1.2295, 60% - 1.2884. 500 µl of each mixture was layered into 4 ml ultracentrifuge tubes with the highest densities added first. The concentrated cell line supernatant was

deposited on top of the sucrose density gradient and the EVs were isolated *via* sequential ultracentrifugation as detailed earlier [217]. Notably, the target EV population density ranges from 1.15 – 1.19 g/ml. thus the expected population should settle in the 30 and 40% layers (i.e. fractions 3 and 4). A flow diagram of this protocol and isolated EVs can be seen in **Figure 2A.1.** The purified particles were washed using 10mM Borate Buffer, suspended in 50ul of buffer and stored at -20°C.

EVs were isolated from benign control patients and pancreatic cancer patients with early-stage (IA-IIB) disease (IRB # 517-15-EP). For the isolation of EVs from serum, a modified version of the cell line supernatant isolation protocol was used. One ml of patient serum was added to 1.5 ml PBS and centrifuged at 500G for 10 minutes at 4°C. The supernatant was collected and then centrifuged at 12000G for 20 minutes at 4°C. Again, the supernatant was collected and centrifuged at 100000G for six hours at 4°C. The pellet that formed was suspended with 3 ml PBS and centrifuged for the final time at 100000G for two hours at 4^{o}C. From here the EV pellet was treated with the same density gradient steps as described for isolation from cell medium. The particles from each fraction were suspended in 50ul of PBS and stored at -20°C.

2A.2 FiberCell

Though density gradient ultracentrifugation is the currently used gold standard method of isolation, it is incredibly time-consuming and few particles are isolated from high volumes of conditioned media. In an effort to streamline this process, a High-density hollow-fiber bioreactor from FiberCell Systems® (**Figure 2A.2**) was acquired for the large-scale production of EVs to decrease the time spent and increase the yield for experiments. Cells grow in high densities on the external portion of the hollow fibers in the

Figure 2A. 1 Isolation of EVs *via* density gradient ultracentrifugation.

Flow diagram depiction of the sequential steps required for EV isolation from the cell-conditioned media beginning with 150 ml of media and finally ending up with concentrated EV samples. The relative densities of the target EV population and the sucrose solutions are presented on the right side of the figure along with an image showing isolated EVs within the third sucrose layer inside a 4 ml ultracentrifuge tube.

Figure 2A.1

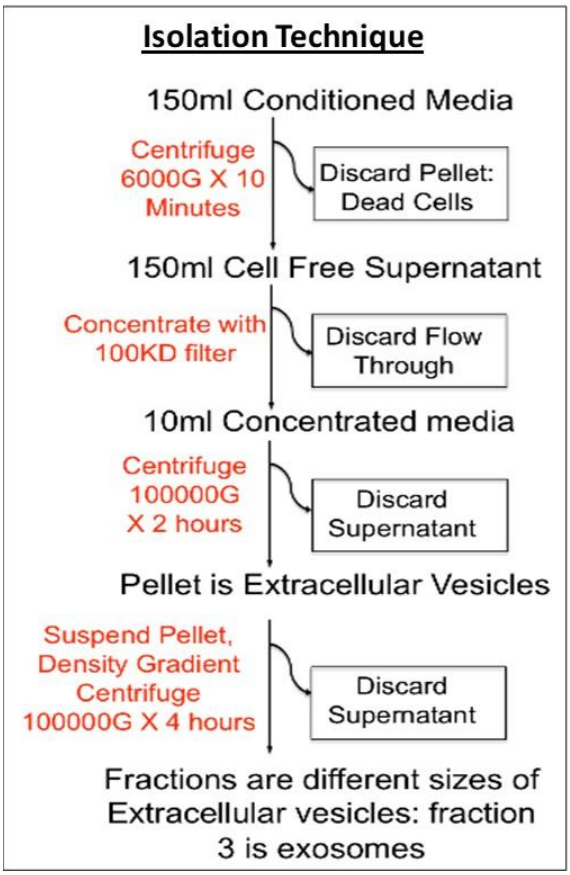

Sucrose Density:
1.12-1.18 g/ml

Target EV Density:
1.15-1.19 g/ml

Cushion effect captures EVs and separates high density contaminating proteins

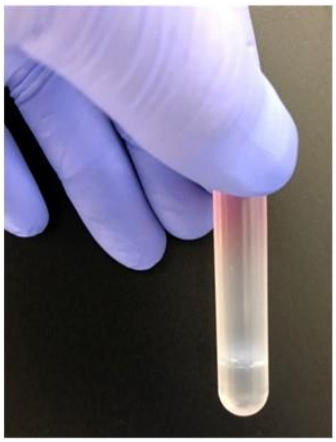

bioreactor cartridge, while the media is retained on the inside of these fibers. This prevents the contamination of cell-line exosomes by bovine exosomes present in fetal bovine serum (FBS), allowing complete media to be used during production. This has major advantages including 1) no longer requiring serum starvation of cells to prevent FBS contamination which is the current method used in the field, 2) nutrient and waste exchange through the pores resultant from the constant flow-through of fresh media, and 3) constant production and vast increases in the number of exosomes produced compared to standard multi-plate cultures. In one week, the equivalent number of EVs as would result from 80 to 100, 145mm cell culture dishes at 80% cellular confluence may be produced. The yield of EVs ranged from 24-26 µg/ml with the use of the FiberCell system and only 8-12 µg/ml when using the conventional isolation method (**Figure 2A.2**).

2A.3 Transmission Electron Microscopy (TEM)

Formvar coated copper grids were glow discharged for two minutes to facilitate EV binding and even distribution upon deposition. 6 µL of purified EVs were loaded onto each grid and allowed to dry for three minutes followed by removal of the excess sample. Nanovan vanadium negative stain (6 µL) was then added to the grid and allowed to rest for one minute when excess was removed and the grids were then incubated for five minutes at room temperature (RT). Samples were then analyzed by a Tecnai G2 Spirit transmission electron microscope (FEI Inc., Hillsboro, Oregon, USA)

2A.4 Immunogold

EVs were deposited onto a formvar coated copper grid after glow discharge with excess removed after 3 minutes and allowed to incubate at RT for 7 minutes. All washing, blocking, antibody treatments, and gold nanoparticles binding steps were performed by

Figure 2A. 2 FiberCell Systems® high-density hollow-fiber bioreactor system

The picture is of the FiberCell® unit purchased and utilized for some EV experiments in this thesis. The close-looped system allows for cells located on the external surface of the capillaries to produce EVs that remain uncontaminated from complete medium flowing through the internal aspect of the capillaries. The 3-D architecture, release from the requirement of serum-free media, and continual culture all allow for the production of EVs far superior to conventional methods. Indeed, FiberCell can produce 2-4 times the quantity of EVs as compared to conventional isolation *via* ultracentrifugation.

Figure 2A.2

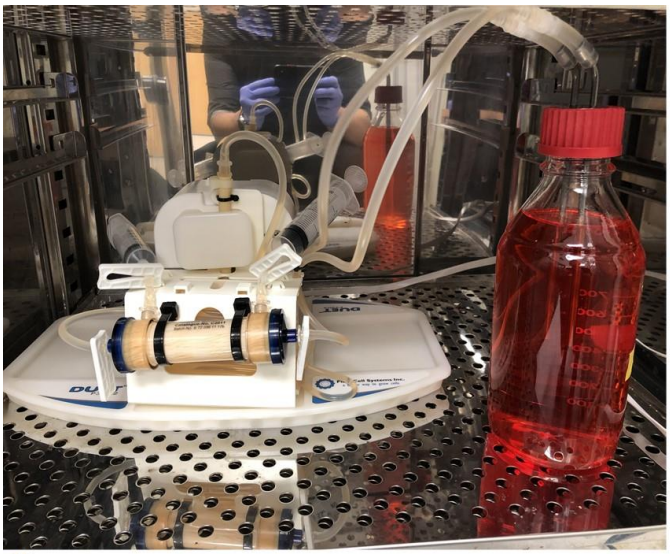

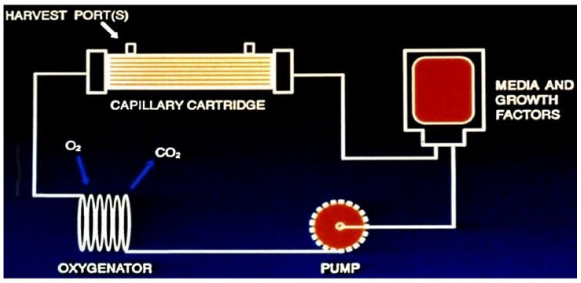

Isolation	µg yield/ml
Conventional	8-12
FiberCell	24-46

floating the grids containing EV samples on 100 µl droplets of the solution with the side containing sample facing the surface of the droplet at RT. Briefly, the grids were washed with PBS 2min X 3 and blocked with 3% goat serum for 30min. They were next washed 2min X 3 in 0.1% BSA-c then transferred to an antibody droplet and allowed to incubate for 1 hour at RT while covered to prevent evaporation (antibodies dilutions made in 0.1% BSA-c with specific dilution concentrations predicated on target of interest. Isotype control species antibodies or no primary antibody deposition served as controls for all immunogold experiments). Grids were again washed with .01% BSA-c 2min X 6. They were next incubated with Protein-A conjugated 10 nm gold nanoparticles (AuNPs) (Nanocs GP10-PA-1) at a 1:25 dilution in 0.1% BSA-c for 1 hour. They were washed with 0.1% BSA-c 2min X 6 and then with PBS 2min X 3. Antibody and protein-A binding were fixed with 2% glutaraldehyde for 5min, washed with deionized water 2min X 6, and subsequently were prepared for TEM analysis as described above (**Figure 2A.3**).

2A.5 Atomic Force Microscopy (AFM)

The overall negative charge of EVs was exploited for depositing them on positively charged mica substrate modified with aminopropylsilatrane (APS) and prepared as described in previous publications [218]. EV samples (5 µL) were left to incubate for a total of 2 min. Excess samples were washed with DI water and dried under argon flow. AFM images were acquired using a MultiMode AFM NanoScope IV system (Bruker Instruments, Santa Barbara, CA, USA) operating in tapping mode with a 1.5 Hz scanning rate using a TESPA-300 probe from Bruker with a resonance frequency of 320 kHz and a spring constant of about 40N/m. Images were processed using the FemtoScan Online software package (Advanced Technologies Center, Moscow, Russia).

Figure 2A. 3 Schematic of the immunogold TEM staining protocol

Figure 2A.3

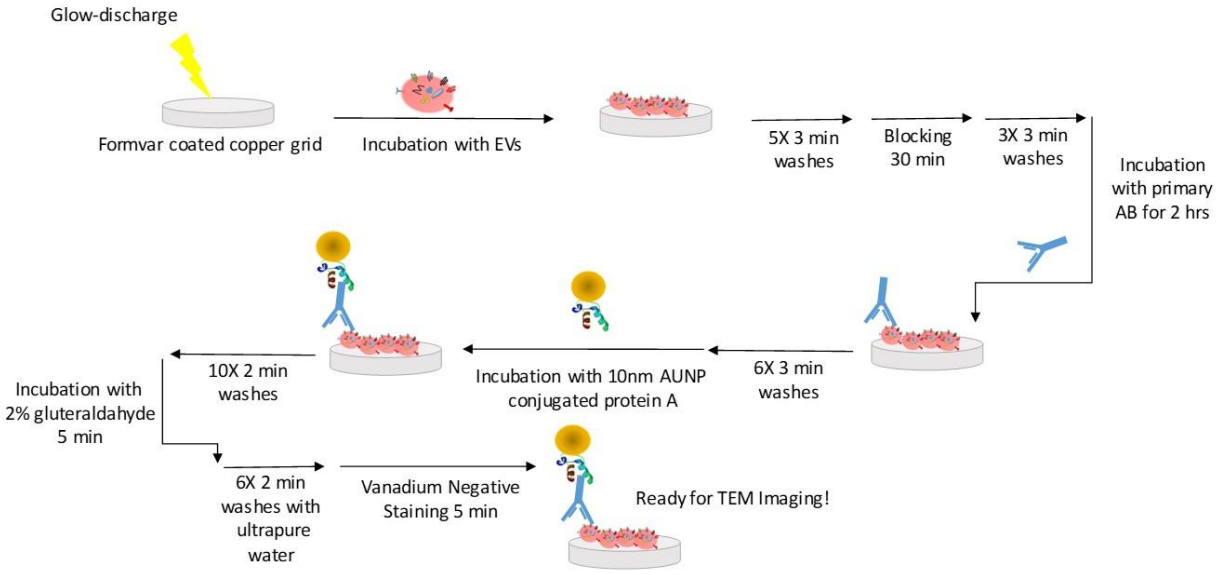
Glow-discharge
Formvar coated copper grid
Incubation with EVs
5X 3 min washes
Blocking 30 min
3X 3 min washes
Incubation with primary AB for 2 hrs
6X 3 min washes
Incubation with 10nm AUNP conjugated protein A
10X 2 min washes
Incubation with 2% gluteraldahyde 5 min
6X 2 min washes with ultrapure water
Vanadium Negative Staining 5 min
Ready for TEM Imaging!

2A.6 Nanoparticle Tracking Analysis (NTA)

The concentration, size, and size distribution of the purified EV samples were measured with a NanoSight LM10 Nanoparticle Analysis System and processed with NTA 2.3 Analytical Software (Amesbury, Wiltshire, UK). The purified samples were diluted at 1:200 in PBS. A 1 mL syringe was used to inject the particle chamber with the diluted sample for NanoSight LM10 readings. For all samples, 60-second videos were recorded with the shutter speed set to 250 and gain at 680, and subsequently analyzed.

2A.7 SERS Measurement

Ti/Au 40 nm/100 nm coated 25mmx75mmx1.1mm microscope slides were purchased from Deposition Research Lab Inc. (St. Charles, MO, USA) 10 nm AuNPs coated with Branched Polyethyleneimine (BPEI) were purchased from nanoComposix, Inc. (San Diego, CA USA). A 250 uL amount of 10-nm-diameter Au nanoparticles were centrifuged at 5500RPM for 10 minutes and the supernatant subsequently removed. The pellet was suspended with 250 uL of 2 mM Borate Buffer and this mixture was spun at 5500 RPM for 10 minutes. The supernatant was again removed and the pellet was suspended in 250 uL of 2 mM Borate Buffer. EVs from each cell line were then added to the mixture in a 1:1 ratio. These samples (5 µL each) were dropped onto the gold slides and allowed to incubate overnight at room temperature. They were allowed to dry completely and then stored at 4°C prior to SERS measurement.

The SERS measurements were conducted using a commercial microscope (Renishaw InVia Reflection, Wotton-under-Edge, United Kingdom) with 785-nm diode laser excitation. The laser power was set to be 10 mW. The laser beam was focused by a

50×microscope objective with a numerical aperture of 0.75 (Leica n PLAN EPI 50×/0.75. Buffalo Grove, IL, USA) to a spot size of around 1 μm in diameter. They were recorded with an acquisition time of 1s and accumulated 10 times.

2A.8 SERS spectra processing and Principal Component –Discriminant Function Analysis

The raw spectra were baseline corrected *via* the Vancouver Raman algorithm with 5-point boxcar smoothing along with fifth-order polynomial fit. Normalization of spectra was conducted *via* the standard normal variant method thus removing multiplicative error while maintaining the same level of contribution to the measurement for each spectrum [219]. The preprocessed spectra were then analyzed by the PC-DFA method utilizing the "mixOmics" package in R software. The PCA reduced the dimensionality of the SERS spectrum from 1004 variables (from 719 cm^{-1} to 1800 cm^{-1}) to 20 PCs. These 20 PCs were further analyzed by DFA for the development of a classification model. Classification efficacy was evaluated by cross-validation and external validation for the cell lines and patient serum samples, respectively.

2A.9 EV surface proteomics

EV surface protein profiling of the EV proteins was conducted through an outside partner, System Biosciences Inc (SBI). EVs isolated from four pancreatic cancer cell lines, CD18/HPAF, MiaPaCa, T3M4, and Capan1 as well as EVs isolated from an immortalized normal human pancreatic ductal epithelium cell lines, HPDE were used for these experiments. Briefly, 100 μg of purified EVs were treated with proteinase-A to cleave the surface proteins from the external surface of the EV membranes and the EVs were separated from the cleaved proteins *via* size exclusion chromatography. The cleaved

surface proteins were treated with trypsin to facilitate proteolytic cleavage into peptides at lysine and arginine residues. Purified peptide samples were analyzed *via* liquid chromatography-tandem mass spectrometry (LC-MS/MS). Given the possibility of ultralow concentrations of proteins present on the EV surfaces, two peptides were set as the determiner cutoff for the presence a protein, in an effort widen the size of the initial pool utilized for subsequent analyses. Of note, EVs isolated from the Capan1 cell line were excluded from further analyses due to Golgi-marker 130 (GM-130) protein being present, which is not found in EVs and is a marker of cellular contamination.

2A.10 Bioinformatics Pipeline

Surface proteins identified by LC-MS/MS from HPDE EVs were compared to the pooled protein population found on all cancer cell line EVs. Proteins shared between the two populations were subtracted from being possible targets. Remaining proteins within the cancer population that were expressed on the surface of two or three of the cancer EV populations were considered for further analysis. The expression level of the genes encoding each protein was compared between PDAC tissue and adjacent normal tissue from 45 individual patients in the publicly available GSE28735 dataset. The genes with the greatest difference between the two tissues were further paired down by determining which were able to make a Receivers Operator Characteristics (ROC) curve with the largest AUC using The Cancer Genome Atlas (TCGA) dataset. The target genes were then assessed for cancer stage-based expression level, correlations, and impact on survival as well as pathway analysis in both datasets. Further, GO analysis was performed on the EV surface proteins to determine their functional implications [220].

2A.11 Sandwich enzyme-linked immunosorbent assay (ELISA)

The in-house ELISA assay was produced as previously described [221]. Briefly, a 96-well microplate was coated with .25ug/well of capture antibody against an EV target protein (i.e. CD63, EPHA2, TSG101) diluted in carbonate buffer (0.05M, pH 9.2). The microplate was allowed to incubate overnight at RT then washed X 3 with phosphate-buffered saline and 0.1% Tween-20 (PBS-T) in an automated plate-washer. The plates underwent blocking with 3% filtered bovine serum albumin (BSA) in PBS for 3 hours at 37^{o}C and again washed 3 times. EVs purified from cell lines or patient serum samples were diluted with 1% BSA, added to each well (in duplicates), allowed to incubate overnight at 4^{o}C, and again washed 3 times. A mixture of biotinylated anti-CD63 and ant-CD9 antibodies diluted 1:2500 in 1% BSA served as the detection cocktail and incubated at 37^{o}C for 2 hours. After washing, Pierce Streptavidin conjugated Poly-HRP (Thermo Scientific) was added to each well, covered, and allowed to incubate for 30 minutes at RT, then washed the final 3 times. 3,3′,5,5′-Tetramethylbenzidine (TMB) solution was deposited into each well and allowed to react in the dark for 20 minutes at RT. 1M sulfuric acid was used to stop the reaction and absorbance at 450 and 650 nm was measured. Further EPHA2 measurement in cell line EVs, patient serum, and patient serum EVs was conducted with a commercial kit (RayBio®).

2A.12 Lectin array

A 40-lectin array (RayBiotech) was used to investigate possible cancer-specific EV glycan patterns. EVs isolated from HPDE and CD18/HPAF were used to discriminate possible targets. Amines and azides inhibit the biotinylation reaction thus EV samples were dialyzed in PBS (pH 8.0) using a floating rack, dialysis tubes provided, and a stir plate.

The first dialysis period was 3 hours, fresh buffer was added, and continued overnight at 4ºC. BCA protein analysis was then completed and 30µg of sample was biotinylated with the reagents provided according to the manufacturer's recommendations. The glass slide containing the lectin array was blocked for 2 hours, blocking solution decanted away, and 10 µg of biotinylated sample added and to each well and incubated overnight at 4ºC. The slide was washed and incubated with Cy3 equivalent dye-streptavidin for one hour at room temperature. The slide was washed, dried with compressed N_2, and sent to the manufacturer for fluorescence measurement.

2A.13 Isolation of genomic DNA from EVs

DNA was extracted from HPDE and Panc1 EVs using QIAamp DNA Micro Kit (Qiagen) according to the manufacturer's instructions. DNA was quantified with a NanoDrop One spectrophotometer (Thermo Scientific). 130ng of EV DNA was subsequently utilized for KRAS G12D and *TP53* R273H mutation analysis by digital PCR.

2A.14 Mutation detection by digital droplet polymerase chain reaction (ddPCR)

Two probe-based mutation detection assays were conducted for KRAS G12D and TP53 R273H mutants in genomic DNA isolated from HPDE and Panc1 EVs: respective probe sequence COSMIC_ID and unique assay ID are as follows: KRAS G12D - COSM521, dHsaMDV2510596; TP53 R273H – COSM10660, dHsaMDV2010109. Mutant target and WT assays are provided mixed together, with FAM conjugated to the probe for the mutant allele and HEX attached to the probe for the WT allele. The reaction mixture was made containing 10µl probe supermix, 1µl probe, 1µl restriction enzyme, and 130ng EV DNA diluted in 10µl nfH_20 (22µl total). (Of note, sample DNA was able to be

digested directly in each ddPCR reaction with 5 units of HaeIII restriction enzyme diluted in 1µl of dilution buffer at room temperature prior to thermocycling). Sample mixture and 70µl of droplet generation oil were added to a DG8 cartridge and droplets generated with the QX200 automatic droplet generator. After droplet generation, samples were carefully transferred to a 96-well ddPCR plate, sealed, and underwent thermocycling with the following conditions: Enzyme activation at 95°C for ten minutes – 1 cycle, denaturation at 94°C for 30 s followed by annealing/extension at 55°C for 1 minute – 40 cycles, enzyme deactivation at 98°C for 10 minutes – 1 cycle, and held at 4°C indefinitely. All cycles were conducted with a 2°C ramp rate. QX200 ddPCR droplet reader and QuantaSoft Software were used for data acquisition and analysis.

2B Radiation potentiation *via* ferroptosis for the improved treatment of pancreatic ductal adenocarcinoma

2B.1 Bioinformatics

The expression levels of genes of interest were analyzed in publicly available RNA sequencing data from PDAC patients within The Cancer Genome Atlas (TCGA) acquired from the UCSC Xena portal (http://xena.ucsc.edu) as well as in the GSE2783 (preprocessed with R-preprocessing and affy package version 1.50.0) microarray dataset. TCGA was additionally used for elucidation of genes of interest effects on survival. Further, MiPanda [222] and Gepia [223] webserver tools were used to investigate the expression of GPX4 and SLC7A11 with a merged dataset containing TCGA data and GTEx cell lines sequencing data. The protein-protein interaction information was extracted with the Biological General Repository for Interaction Datasets (BioGRID) *homo sapiens* database [224]. Along with this,

Project DRIVE (a database built to uncover cancer genetic dependencies with large scale deep RNAi screening) was used to investigate the effects of SLC7A11 inhibition in the setting of PDAC [225].

2B.2 MTT

The cytotoxic effect of Erastin treatment was assessed using a 3-(4, 5-dimethylthiazol-2-yl)-2, 5-diphenyl tetrazolium bromide (MTT) assay. 2,500 cells were seeded per well in a 96-well plate and allowed to adhere and proliferate for 24 hours. Two plates were treated with Erastin at various concentrations (100 nM – 10 μM) for 24 and 48 hours. Subsequently, 10ul of MTT (5mg/ml PBS) was added to each well and incubated for 3-5 hours at 37^{o}C. The media was aspirated out of each well and replaced with 100 μl DMSO and mixed vigorously to release the intracellular contents. Cytotoxicity values were measured with a Spectramax 190 (Molecular Devices) microplate reader at a wavelength of 520 nm.

2B.3 *In vitro* cell migration assay

The ability of Erastin to inhibit CD18/HPAF cell migration was tested using a wound-healing assay. Cells were seeded in each well of a six-well plate and allowed to gain 80-90% confluence. A 1-ml pipet tip was used to make cross-pattern scratches in the cell cultures at which point fresh media with different concentrations (0, 1, 5, and 10 μM) of Erastin were deposited into three wells for technical replication. Pictures of the cruciform scratch were taken at 0, 24, 48, and 72 hours and the percent wound closure recorded at each time point.

2B.4 Immunohistochemical staining of human tissues

Formalin-fixed normal pancreas, PDAC, and irradiated PDAC tissues were embedded in paraffin and sectioned at 5 µm thickness. Slides were incubated overnight at 58^{o}C and deparaffinization of tissue sections was facilitated 10 min X 4 incubations in xylene with subsequent rehydration *via* sequential graded ethanol (20-100%). A solution of 3% hydrogen peroxide and methanol was used for 30 minutes to quench endogenous peroxidases. Then, sections were deposited into 90^{O}C 0.01% citrate buffer (pH 6.0) for 15 minutes for antigen retrieval. Once the samples cooled to room temperature, they were washed with PBS and blocked with horse serum for 2 hours (IMMPRESS kit; Vector Labs). The sections were incubated overnight in primary antibody (either anti-GPX4 at 1:500 dilution in PBS or anti-SLC7A11 at 1:500 dilution in PBS). They were washed in PBS for 10 minutes x 4 and incubated with universal anti-rabbit/anti-mouse peroxidase-labeled secondary antibody (IMMPRESS kit; Vector Labs) for 1 hour at room temperature. Slides were again washed and developed *via* DAB as a substrate. Hematoxylin counterstain was applied and slides were washed with tap water. Subsequently, they underwent dehydration with decreasing ethanol concentration (100-20%) and finally incubated in xylene for 5 minutes. The slides were mounted with permount mounting medium (Fisher Scientific) and photographed using an EVOS FL Auto Microscope (Life Technologies). Slides were graded by a licensed pathologist and H-scores were obtained by application of the formula: 3 x percentage of cells with strong staining + 2 x percentage of cells with moderate staining + percentage of cells with weak staining resulting in a range of 0-300.

2B.5 siRNA knockdown and transient transfection

Glutathione peroxidase 4 (GPX4) siRNA was purchased from Ambion with sequences as follows; sense: GGCAAGACCGAAGUAACUtt; antisense:

AGUUUACUUCGGUCUUGCCtc. Cells were seeded in a six-well plate 24 hours prior to transfection. They underwent serum starvation for 4 hours when Lipofectamine 2000 reagent (Invitrogen) was used for transient transfection as per the manufacturer's protocol. Six hours following transfection, serum-containing media was added to the wells. Proteins were collected or all experiments (i.e. colony-forming assays) were performed 48hours post-transfection to allow for optimal GPX4 KD.

2B.6 *In vitro* irradiation

Cells were plated in T75 flasks and allowed to become 50-60% confluent. A linear accelerator in the Radiation Oncology Department at the University of Nebraska Medical Center was utilized to irradiate the cells. Flasks were placed onto the LINAC couch within a 40 cm^2 radiation field on the top of a 10 cm solid water block (a material used for radiation beam calibration). X-rays were delivered with 6MV at 2.73 Gy min^{-1} through the bottom of the flask (aspect containing the cell monolayer) which was located 100cm from the X-ray target. Cell lysates were collected at 6, 12, 24, 48, and 72 hours post-radiation exposure.

2B.7 *In vitro* radiation response determination

Colony survival assay was used to determine the effect of radiation and the ability of Erastin (Tocris) to act as a potentiator. Briefly, 500 cells/well were seeded in triplicates in separate 6-well plates and treated with various concentrations of Erastin (0.0, 0.1, 0.5, 1.0, and 2.0 μM). The separate plates were exposed to different dosages of radiation (0, 1, 3, 5, and 7 Gy) and allowed to proliferate until the no treatment control colonies were in close proximity to each other and were near to merging. Cells were washed, fixed in MeOH, and stained with 0.4% crystal violet in 25% MeOH. Colonies (defined as >50 cells) were counted for each well separately and the numbers associated with each technical

replicate (same radiation and Erastin doses) were averaged. The colony numbers from each experimental condition were divided by the total colonies in the no treatment control to yield proportional survival. The log of the proportional surviving fraction was plotted against radiation dose. The linear-quadratic model used to fit the clonogenic survival curve for each experimental condition was $\boldsymbol{Y=e\text{^}-[\alpha*X+\beta*X^2]}$. Where α and β were calculated according to the Fertil method [226], which was also used to determine the radiation enhancement ratio (ER) (i.e. the area under the curve) for each Erastin concentration. The ER was calculated as the ratio of the mean inactivation dose without any drug divided by the mean inactivation dose under various experimental conditions such as Erastin treatment and differing cell lines) where values >1 are indicative of radiation sensitization. This was plotted using GraphPad Prism (GraphPad Software Inc., La Jolla, CA, USA).

2B.8 Combenefit analysis

Erastin synergistic and/or additive effect on radiation-induced cell death was determined with the publicly available Combenefit web server [227]. This free software analyzed the colony survival assay data with three known synergy assessment methods: Highest single agent (HSA) [228], BLISS [229], and Loewe [230] models. The interpretation of synergy scores can be assumed as follows: < -10 is considered likely antagonism, -10 to 10 is considered likely additivity, and >10 is considered likely synergism. The Combenefit package offers myriad graphical representations of the survival and synergy scores and from these, the contour and matrix views are presented herein.

2B.9 Patient-derived organoids

Patient derived organoids graciously supplied by Dr. Michael Bouvet from the University of San Diego were revived and maintained in complete DMEM/F12 medium supplemented with HEPES [Invitrogen], Glutamax [Invitrogen], penicillin/streptomycin [Invitrogen], B27 , Primocin [1 mg/ml, InvivoGen], N-acetyl-L-cysteine [1 mM, Sigma Aldrich], mouse recombinant Wnt3a [100ng/ml, EMD Milipore], human recombinant RSpondin1 [1µg/ml, PeproTech], Noggin[0.1 mg/ml, PeproTech], epidermal growth factor [EGF, 50 ng/ml, PeproTech], Gastrin [10 nM, Sigma], fibroblast growth factor 10 [FGF10, 100 ng/ml, PreproTech], Nicotinamide [10 mM, Sigma], and A83- 01 (0.5 mM, Tocris Biosciences). Once healthy and proliferating the organoids were seeded into 4-wells each (8 total) of two black walled 96-well plates.

2B.10 Patient derived organoid radiation response determination

After seeding, both plates of organoids were allowed to grow for 48 hours at which point one well on each plate was treated with various concentrations of Erastin (0.0, 1, 2.5, and 5 µM). One of the plates was irradiated with 5Gy radiation using a linear accelerator in the University of Nebraska Medical Center Department of Radiation Oncology (as described above) 24 hours after the initiation of Erastin treatment, and the other plate remained radiation free. Organoids were then allowed to proliferate for 4 days and pictures of each experimental condition were taken with an EVOS FL Auto Microscope (Life Technologies) at 24, 48, 72, and 96-hour time points. At 4 days post-radiation treatment, CellTiterGlo® 3D cell viability assay (Promega) to detect the presence and quantity of ATP as an assessment of overall organoid survival. The assay was conducted according to the manufacturer's recommendations and luminescence measurements were taken with a SynegyNeo2 Multimode Reader (BioTek). The relative luminescence was compared

between the no treatment control and the various experimental conditions and plotted using GraphPad Prism (GraphPad Software Inc., La Jolla, CA, USA).

2B.11 *In vivo* orthotopic xenograft model

Eight-week-old nude mice were used for orthotopic implantation of CD18/HPAF-L luciferase transfected cells. Mice were anesthetized by intraperitoneal injection of xylazine (10mg kg^{-1}) and ketamine (100mg kg^{-1}) and a laparotomy performed on the left lateral flank to expose the head of the pancreas. 2.5 X 10^5 CD18/HPAF-L cells were suspended in 50 µl of PBS and injected into the head of the pancreas and the incision closed. Monitoring of tumor growth was performed *via in vivo* bioluminescence imaging using the Xenogen IVIS-100 (Xenogen Corporation) after intraperitoneal injection of D-luciferin (150 mg kg^{-1}) while mice were anesthetized with isoflurane.

2B.12 Treatment plan and experimental design

On day 10 post-implantation, the mice were randomized into four groups of five mice each, based on luminescence intensity on IVIS imaging. Group 1: no treatment control, Group 2: Radiation only, Group 3: Erastin (SelleckChem) only, and Group 4: Radiation plus Erastin. A total of 42 Gy of radiation was administered to groups 2 and 4 in six fractions over the course of six sequential days in a Strahl Small Animal Radiation Research Platform (SAARRP). This unit provides onboard 3D volumetric image guidance *via* high-resolution cone beam-CT for target localization and dose delivery. In addition, the precision beam radiation source can be arced around the animal, thus conferring conformal dose distributions in three dimensions with limited off-target dose spillage. The tumor and other tissue contouring, isocenter, beam arrangements, and dose calculations were conducted with MuriPlan Software (**Figure 2B.1**). Beginning post-implantation day 14

(radiation day 4) groups 3 and 4 received intraperitoneal injections of Erastin (25 mg kg^{-1}) for 6 consecutive days. IVIS monitoring was conducted again at days 18 and 26 at which point it was determined the no treatment group tumors were getting to a size that required sacrifice. On post-implantation day 29, all animals were sacrificed and the tumors harvested and weighed. The University of Nebraska Medical Center Institutional Care and Use Committee approved the procedures for all experiments performed with mice.

2B.13 Glutathione assay

A GSH/GSSG ratio and detection assay kit (Fluorometric – Green, Abcam) was used to determine the total glutathione (GSH) present in cells after treatment with Erastin and radiation exposure as per the manufacturer's protocol. Briefly, Panc1 and CD18/HPAF cell lines were treated with Erastin and irradiated and cells were collected and lysed after 24 hours. These lysates were next deproteinated with 4M perchloric acid (PCA) and subsequently neutralized with 2M KOH to prevent enzymatic degradation of cellular GSH. Total glutathione was measured with a provided dye that fluoresces only in the presence of GSH. Fluorescence was measured at excitation/emission wavelengths of 490/520 nm using a SynegyNeo2 Multimode Reader (BioTek) and has been reported in this thesis as the relative proportional fluorescence of Erastin and radiation treatment groups compared to no-treatment controls.

2B.14 Measurement of reactive oxygen species production

Cells undergoing ROS evaluation were first washed with PBS and a 10 μM solution of H_2DCFDA in HBSS was added to each well of a 96-well plate and allowed to incubate

Figure 2B. 1 Small animal radiation machine and treatment planning

A. Still image captured from a video of the Strahl Small Animal Radiation Research Platform (SAARRP). This image displays the ability of the radiation source to circumnavigate the treatment couch where the mouse is positioned to provide increased dose delivery to the tumor while limiting off-target delivery. **B.** A screenshot of the MuriPlan software displaying the capability of the real-time CT imaging and determination of the dose isocenter relative to tumor location. Importantly, the software also allows the user to visualize the percentage of the prescribed dose (in our case 7Gy) received within the colored contours. For example in the image provided, the tumor is falling within the red-colored line and thus is receiving the entire 7Gy prescribed dose.

Figure 2B.1

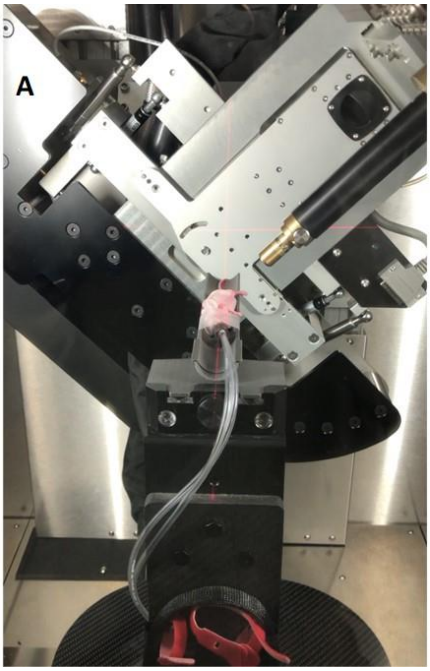

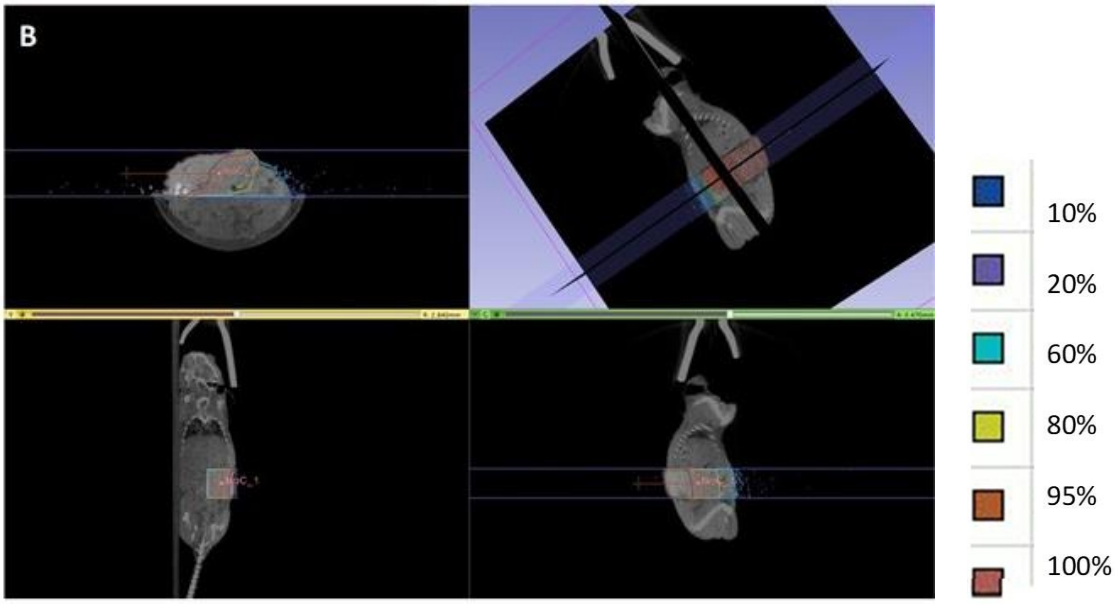

for 30 minutes at room 37°C in the dark. Non-fluorescent H_2DCFDA is cleaved by endogenous esterases into the DCF which is trapped inside the cell and is oxidatively sensitive. When DCF interacts with ROS it gets oxidized into the fluorescent dye fluorescein. The fluorescence was visualized using the Cy3 filter with an EVOS FL Auto Microscope (Life Technologies) and the intensity was assessed at an excitation/emission of 480/529 using a SynegyNeo2 Multimode Reader (BioTek).

2B.15 Intracellular free iron (Fe^{2+}) assessment *via* FeRhoNox™-1

The effect of radiation and Erastin treatment on the level of unbound catalytically active iron (Fe^{2+}) was determined *via* assessment with FeRhoNox™-1 (Goryo Chemical) as per the manufacturer's protocol. Briefly, the solid dye was reconstituted with 109 µl of DMSO to make a 1mM stock solution. This was diluted with Hank's Balanced Salt Solution (HBSS) to make a 5 µM working solution. Cells under the previously described experimental conditions were washed twice with HBSS and 100 µl of the 5µM FheRhoNox solution per well was added and allowed to incubate at 37°C for 1 hour. The fluorescence was measured at excitation/emission of 520/570 nm using a SynergyNeo2 Multimode Reader (BioTek).

2B.16 *In vitro* assessment of lipid peroxidation *via* BODIPY™ 581/591 C11

Lipid peroxidation was determined by measuring the alteration in the fluorescence of C11-BODIPY 581/591 from red to green [231]. Cells were seeded on slide coverslips at the bottom of a 12-well plate. They were treated with 1 µM or 2 µM Erastin, 5Gy radiation, or both, and lipid peroxidation was assessed at 12 and 24-hour time points. 10µM of C11-BODIPY dye (Invitrogen) was added to the cells (diluted in DMEM) and they were allowed to incubate for 30 minutes at 37°C. They were then washed with PBS and nuclei

stained with DAPI mounting media and mounted onto slides. Cells were imaged with a 710 Confocal Laser Scanning Microscope (Zeiss) and dye fluorescence analyzed *via* Zen software (Zeiss). Determinations regarding the red/green ratio are the result of three independent location measurements in each sample.

2B.17 Thiobarbituric acid reactive substances (TBARS) assay

When lipid peroxidation cannot be directly visualized (i.e. when the system being evaluated is a cancer patient), byproducts of peroxidation such as malondialdehyde (MDA) can be used as a surrogate marker to estimate the relative level of lipid peroxidation. A commonly used method of doing so is with a thiobarbituric acid reactive substances (TBARS) assay[232]. When TBA and MDA interact, they form an adduct that can be measured in a colorimetric or fluorometric manner. A TBARS assay was purchased and used according to the manufacturer's protocol (Caymen Chemical). For the experiments in this thesis, 100µl of irradiated patient serum samples were pipetted in sealable 5 ml vials and the equivalent volume of SDS solution was added then mixed. 4 ml of the provided TBARS reagent was added to each vial, which was subsequently placed in a styrofoam floating rack and boiled in water for one hour, then incubated on ice for 10 minutes. After incubation, the samples were centrifuged for at 1,600G at 4^{o}C for 10 minutes then allowed to come to room temperature. 150 µl from each vial was loaded in duplicates into a 96-well black-walled plate for fluorometric evaluation. Fluorescence was measured at excitation/emission wavelengths of 530/550 nm with a SynegyNeo2 Multimode Reader (BioTek).

Chapter 3: Overview of Extracellular Vesicle Surfaceome and its Implications in Cancer

Chapter 3: Overview of the extracellular vesicle surfaceome and its implications in cancer

3.1 Biogenesis

All mammalian cells and human tissues secrete membranous-organelles nanometers in diameter which are collectively classified as extracellular vesicles (EVs) [233]. This group is comprised of two primary vesicle populations, exosomes (50-150 nm) and microvesicles (100-1000 nm), distinguished by separate mechanisms of biogenesis. EVs begin as the inward budding of late endosomes to create a multi-vesicular body (MVB) harboring intraluminal vesicles (ILVs). The MVB is trafficked to and fuses with the plasma membrane, releasing its ILV content into the extracellular space where these vesicles are referred to as EVs [234] (**Figure 3.1**). Conversely, microvesicles are the results of direct plasma membrane budding into the extracellular space and subsequent release [235]. Traditionally, size-based classifications for EVs and microvesicles were utilized in studies. However, a preponderance of evidence has shown that overlap in sizes can lead to the assumption of homogeny in an incredibly heterogeneous vesicle population in relation to biogenesis [236], vesicular content [237], and biological functions [238].

While the author recognizes that these categorical differences are important, biologically pertinent, and warrant further investigation, they lie outside the purview of this thesis. Along with this, many studies specifically investigating "exosomes" were doing so in the setting of size-based categorization which may inadvertently yet incorrectly muddle the differences between attributable vesicle subpopulation contents and functions. Vesicles of different origin with synonymous size ranges harbor synonymous biophysical attributes including size, density, and membrane orientation making disparate populations difficult to differentiate [239]. Thus, the reference of "extracellular vesicles" will be used as

Figure 3. 1 Mechanisms of EV biogenesis and secretion

The EV population of interest for this thesis is comprised of exosomes and microvesicles and each arises from separate mechanisms of creation. Where exosomes result from the inward budding of the late endosomal membrane facilitated by ESCRT proteins and subsequent trafficking and fusion with the plasma membrane with aid of Rab GTPases, microvesicles form from direct outward budding of the plasma membrane. While these biogenesis pathways differ, they produce a heterogeneous population of EVs that contain a variety of nucleic acids and proteins. Many of the proteins involved in these biogenesis pathways have become the accepted EV markers in the field including Rabs, TSG101, ALIX, and various tetraspanins including CD9, CD63, and CD81.

Figure 3.1

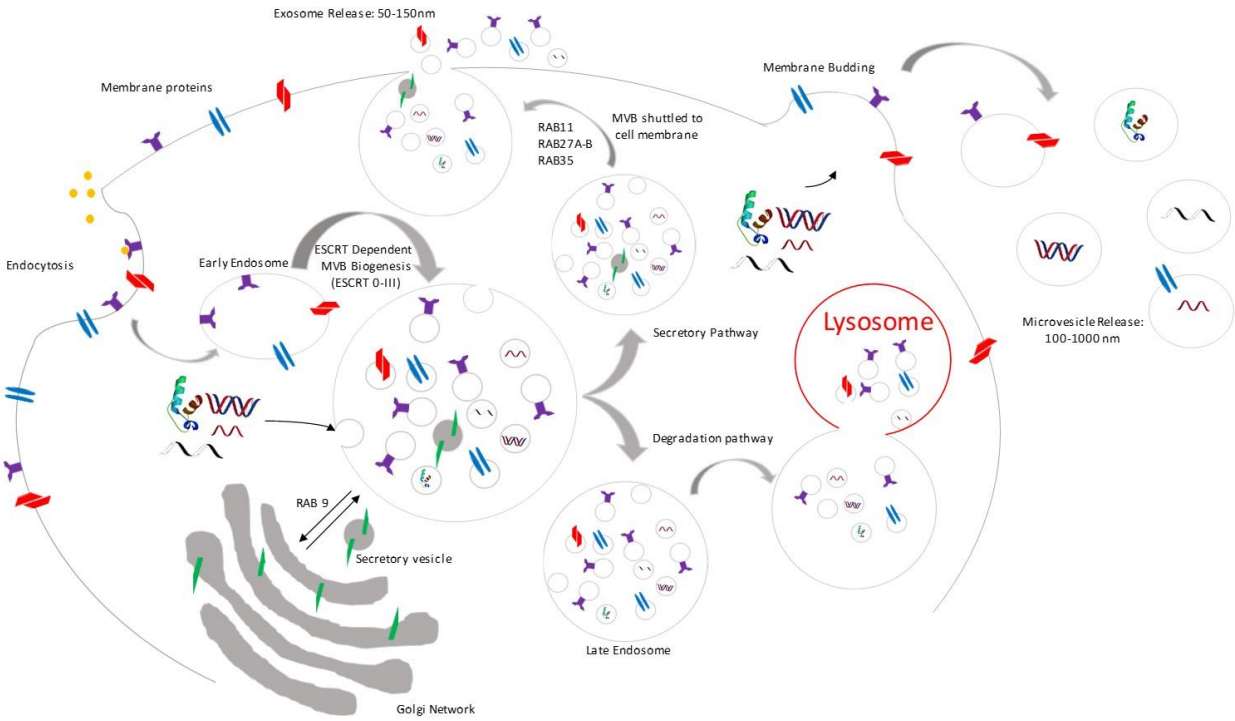
Exosome Release: 50-150nm
Membrane proteins
Membrane Budding
RAB11
RAB27A-B
RAB35
MVB shuttled to
cell membrane
Endocytosis
Early Endosome
ESCRT Dependent
MVB Biogenesis
(ESCRT 0-III)
Secretory Pathway
Lysosome
Microvesicle Release:
100-1000 nm
Degradation pathway
RAB 9
Secretory vesicle
Late Endosome
Golgi Network

an all-encompassing nomenclatural designation, unless otherwise specified throughout the manuscript.

One of the best-studied mechanisms of EV biogenesis is the endosomal sorting complex required for transport (ESCRT) family of proteins (ESCRT 0-III) [240]. The ESCRTs, along with other proteins including tumor susceptibility gene 101 (TSG101) and ALIX, are required for cargo sorting and the formation of ILVs within the MVB (**Figure 3.1**) [234]. For years these proteins were used as EV specific markers, however, all of these complexes are required for other vesicular formation events and are not exclusive to EV biogenesis [240, 241]. Additionally, tetraspanins, such as CD9, CD63, and CD81 have also been shown to impact EV cargo packaging as well as MVB formation [242-244]. Of note, these are the consensus markers and most frequently used metrics by which the presence of EVs is assessed. After ILV formation, transport of MVBs throughout the cell, as well as to the plasma membrane, is facilitated by Rab GTPases [245] including Rab35 [246] and Rab27a/b [247]. Finally, Rab11 [248] and soluble N-ethyl-maleimide-sensitive fusion attachment protein receptors (SNAREs) [249] facilitate MVB membrane fusion with the plasma membrane.

Conversely, ESCRT independent EV biogenesis has also been reported. Trajkovic et al. found that vesicular contents form separate subdomains on the membrane of the late-endosome and observed that the molecular cargo present within these subdomains required the sphingolipid ceramide for transport into vesicles, sans the requirement of ESCRT [250]. Along with ceramide, further implicating the role of lipids in EV biogenesis is the enriched of a variety of other lipid species in EV membranes, as compared to their cell of origin, including phosphatidylserine (notably often with reverse orientation) [251], sphingomyelin [252], phosphatidyl inositides [253], and cholesterol [254]. Indeed, the presence and orientation of

specific lipid moieties are shown to be required for vesicular biogenesis. For example, syndecan/syntenin complex-mediated phosphatidic acid manipulation, which requires phospholipase D (PLD2), is required for ILV formation (again, independent of ESCRT) [255]. Congruently, ARF6, a small G protein that activates PLD2, mediates microvesicle formation and shedding from the plasma membrane [235]. Finally, Cholesterol and sphingomyelin interaction with ostreolysin A (OlyA), a cholesterol/sphingomyelin nanodomain binding protein, which is required for the formation of MVs [256]. Notably, many of the aforementioned sorting machinery, mechanisms, and molecular species are shared between exosome and microvesicle biogenesis [257].

3.2 General Contents and Functions

EVs were originally thought to have only one function, which was providing a means of cellular waste disposal and the removal of contaminants [258]. However, it was discovered decades later that these entities harbor a variety of molecular species that impact recipient cell functions. Some of the initial examples of this were antigen presentation and the associated molecules including MHC Class I [259] and MHC Class II [260] from monocytes and B lymphocytes, respectively. Understanding of EV content continued to evolve when it was discovered that they contain deliverable mRNA and miRNA that remain functional when delivered to target cells [261]. Since the time of these important initial findings, EVs have been found to contain many deliverable biologically impactful molecules including proteins [262], nucleic acids [263], and lipids [264] (**Figure 3.2**).

EV mechanisms of creation and selective cargo sorting necessitates that their components reflect the cell of origin and produce vesicles with shared intrinsic properties. Some of the specific EV protein contents include adhesion molecules, such as integrins,

Figure 3. 2 EV surface and intravesicular content

The surface of EVs is decorated with a wide array of proteins including the aforementioned tetraspanin markers, immunoregulatory molecules such as PDL-1 and MHCs, annexins, and adhesion proteins such as integrins. However much of the research to date has been completed on the intravesicular content of EVs and its implications in cancer. EVs can harbor metabolically active enzymes, a variety of nucleic acid species including DNA, mRNA, miRNA, and lncRNA, biogenesis molecules ALIX and TSG101, and many proteins with chaperone functions or signaling capabilities.

Figure 3.2

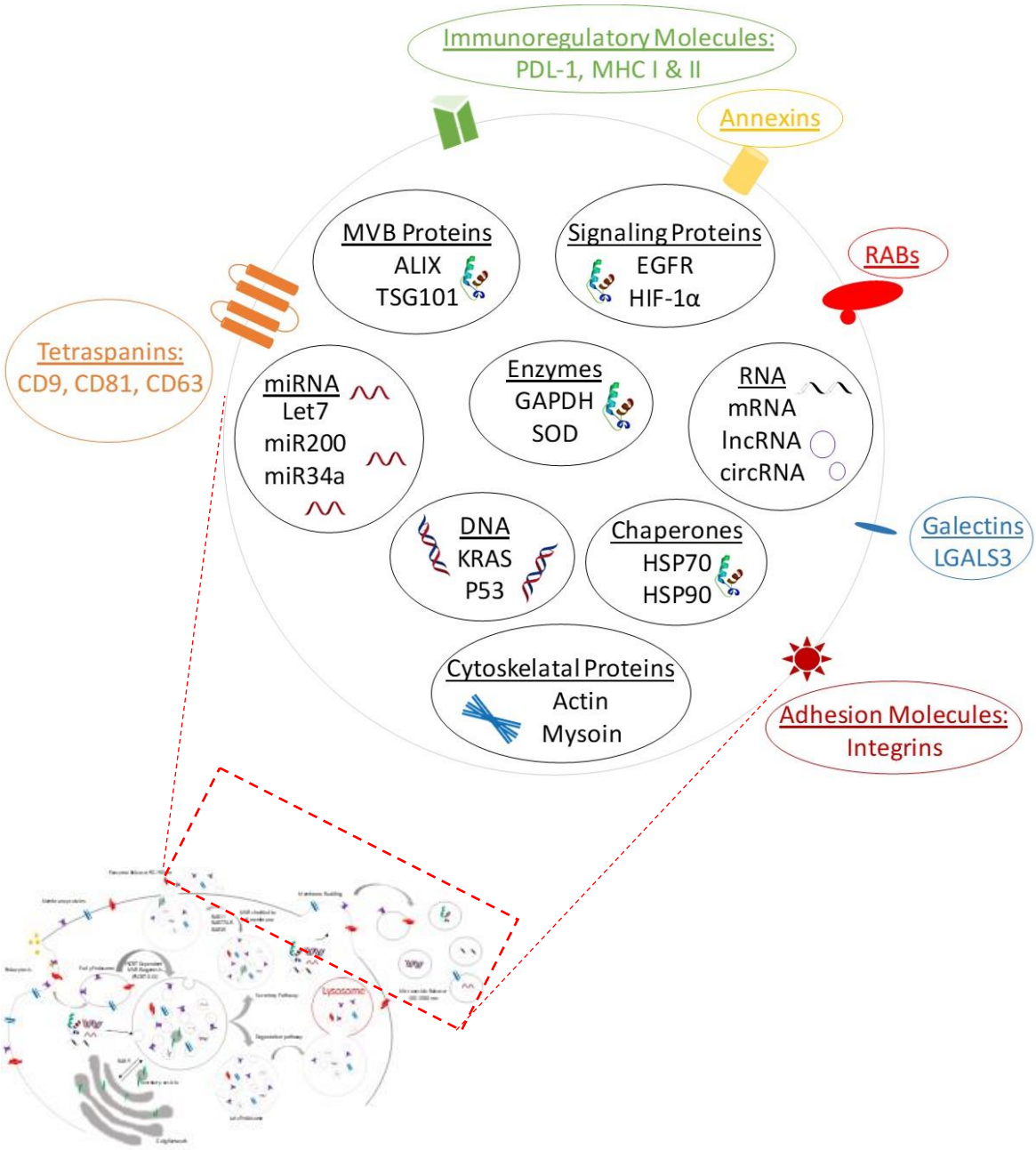
Immunoregulatory Molecules:
PDL-1, MHC I & II
Annexins
MVB Proteins
ALIX
TSG101
Signaling Proteins
EGFR
HIF-1α
RABs
Tetraspanins:
CD9, CD81, CD63
miRNA
Let7
miR200
miR34a
Enzymes
GAPDH
SOD
RNA
mRNA
lncRNA
circRNA
Galectins
LGALS3
DNA
KRAS
P53
Chaperones
HSP70
HSP90
Cytoskelatal Proteins
Actin
Mysoin
Adhesion Molecules:
Integrins
Lysosome

which are present in many EV subpopulations [237]. Mentioned previously, as a result of their biogenesis, these vesicles harbor various tetraspanin markers, namely CD9, CD63, and CD81 [243], which have become the consensus markers for EVs throughout the field. Other proteins involved in ILV formation, cargo sorting, and trafficking are found including Rab GTPases [245], TSG101, and ALIX [265]. Additionally, membrane-binding proteins such as annexins [266] and carbohydrate-binding proteins such as galectins [267], are also present in EVs. Along with these, heat-shock proteins, including HSP70 and HSP90, are often observed [268]. Signaling molecules are also often present such as EGFR [269] and HIF-1α [270].

Along with proteins, a variety of nucleic acid molecules are frequently present within EVs. These include microRNA (miRNA) [271], messenger RNA (mRNA), long non-coding RNA (lncRNA), and circular RNA (circRNA) [272]. The deposition of the different RNA types into the recipient cells (either by receptor-mediated endocytosis of the EVs or direct membrane fusion) can alter endogenous gene expression patterns [261]. Along with these, single-stranded DNA (ssDNA) and double-stranded DNA (dsDNA), [273] from genomic and mitochondrial sources have also been found in vesicles [274]. Kahlert et al. found EVs to contain genomic DNA spanning all 23 chromosomes as well as harbor identifiable mutant (mt) KRAS and mtP53 DNA [275]. One of the primary roles that EVs fill includes cell-to-cell communication [276]. An elegant experiment by Lai et al. utilized fluorescent-tagged mRNA within a donor cell being packaged into EVs, the fluorescent EVs subsequently were observed in the tumor microenvironment (TME) and were taken up by recipient cells, where the fluorescent-tagged mRNA was still able to be detected [277].

While many of the EV constituents' functional implications have not yet been fully appreciated they have attributions to cellular homeostasis [278]. EV components have proven capable of altering recipient cell functionality *via* delivery of their cargo [279], target cell signaling initiation [280], and propagation of disease process [281]. With these discoveries, EV implications in cancer progression [282], metastasis [283, 284], and drug resistance [285] have become an incredibly ubiquitous and highly informative area of research. Many of these EV functions are influenced or are directly facilitated by the vesicle surface and its necessary interaction with a target cell [286]. However, heretofore, a preponderance of studies and reviews have focused on the functional implications of cancer EVs ascribed to intravesicular cargo transfer [287, 288]. Further, traditional methods of EV assessment have often neglected to segregate the intravesicular vs. surface constituents. With this dissertation, I aim to highlight the recent investigations into the EV surfaceome in the setting of cancer and subsequent elucidation of EV surface-specific isolation techniques, characterization techniques, surfaceome effects on cancer biology, EV biomarkers, and therapeutic implications.

3.3 Surface-based Isolation Methods

The recognition that EVs possess cancer-associated surface characteristics has led to the emergence of myriad novel surface profiling techniques. These methods often exploit surface features such as the presence of specific target proteins, lipid composition, and carbohydrate moieties for EV isolation, characterization, or a combination thereof. Some of these are the simple product of the new application of old technology to EVs while others have been fabricated and engineered from the bottom-up. This section will give examples of the EV surface profiling methods heretofore attempted.

3.3.1 Traditional EV Isolation Techniques

One of the most commonly utilized EV isolation methods is sequential ultracentrifugation (UC), first outlined by Théry where conditioned media or biological fluid specimens are subjected to multiple centrifuge steps that increase in speed and relative gravitational force [289]. This method first removes unwanted cellular contaminants from the vesicle population (i.e. cell membrane particles, apoptotic bodies, etc.) and then vesicles are pelleted at very high rotation speeds topping 100,000G. A sucrose gradient can be utilized to further differentiate the vesicle population predicated on size and relative density [289]. This is the most frequently used isolation method for EVs and is considered the current gold standard. However, this method is incredibly time-consuming, expensive, requires large starting samples volumes, and special equipment. The ultracentrifugation process can also lead to EV clustering upon pelleting under such force, thus making it difficult to suspend the individual vesicles in solution. This clumping can diminish overall EV yield as well as hinder downstream analyses (e.g. flow cytometry, ELISA, SERS) and functional studies (e.g. target cell uptake) [290].

Another frequently used method is commercial EV isolation kits that utilize polymer-based precipitation and subsequent column isolation, which facilitates high-throughput and facile EV isolation from conditioned media as well as biological fluid samples [291]. However, these commercially available kits, while efficient at removing EVs from solution, can be contaminated by various non-EV debris including apoptotic bodies and cellular plasma membranes, protein aggregates (e.g. bovine serum albumin (BSA) from media [292], albumen and lipoproteins from serum [293], Tamm-Horsfall protein in urine [294], lipids from non-vesicular sources, and extra-vesicular nucleic acids.

Another traditional method involves the incorporation of isolation predicated on size through modification of various techniques including size exclusion chromatography (SEC) [295], ultra-filtration [296], and microfluidics. For example, the application of microfluidics to an obstacle array can be utilized for vesicle isolation with a specific size cutoff [297]. The combination of microfluidics and size exclusion filters is also able to efficiently separate EVs based on the size as well as decrease exogenous protein contamination within the sample [298]. A new technique pioneered by the Lyden group uses asymmetric flow field-flow fractionation (AF4) for size-based EV isolation [238, 299]. Interestingly, this method yielded a new subpopulation of EV (< 50 nm in diameter), which has been termed an "exomere" [238]. Two main problems persist when considering size-based isolation methods: 1. size is not mutually exclusive to a specific subpopulation (i.e. size overlap between exosomes and microvesicles). 2. an inherent lack of site-specificity, which is important when considering EV use as biomarkers or as vehicles for therapeutic delivery.

3.3.2 Surface-based techniques for EV isolation

Other methods have begun to take advantage of various EV surface characteristics including protein content, lipid composition, and surface charge. Importantly, the exposed EV surface is amenable to interaction with lipid probes, antibodies, lectins, heparin-binding proteins, and aptamers. In addition, these vesicles often harbor a negative surface charge (as measured by ζ-potential), thus making them behave in a predictable manner when interacting with an electric field or charged particle. All of these features allow for the incorporation of EV surface features into novel isolation techniques with increased specificity and the capability of direct isolation from biofluids without the need for prior UC.

3.3.2.1 Immunoaffinity

The EV surface proteome has become one of the primary methods by which vesicles are isolated from various biofluids and/or cell culture supernatant. The majority of these techniques utilize immunoaffinity capture methods in some manner. Usually, these involve surfaces functionalized with antibodies against EV surface proteins including printed antibody arrays on various substrates (e.g. glass or metal slides), antibody decorated magnetic beads, and antibody decorated latex beads. Samples containing EVs (i.e. biofluids or conditioned media) can be directly deposited onto the antibody decorated substrates, or beads can be added directly into the solution. The antibodies can then be pulled out of solution *via* centrifugation or a magnet. Aside from the obvious time saving and simplicity of direct isolation, another primary benefit of these surface isolation techniques as compared to conventional ultracentrifugation is that individual EV's can be chemically released from the antibody functionalized substrate/beads with minimal morphological or structural changes and subsequently utilized for functional experiments.

Many of the first attempts at EV surface protein-based isolation techniques utilized the consensus tetraspanin markers including CD9, CD63, and CD81 for vesicle sequestration. Specifically, magnetic beads decorated with antibodies against these three proteins have proven capable of separating EVs from solution. Isolation and release of EVs by magnetic beads were determined to be superior to that of conventional techniques including ultracentrifugation and polymerization kits, as determined *via* flow cytometry, immunogold TEM, and western blot [300]. While this technique allows for facile and immediate isolation from fluids, it still requires a release step where some EVs may be lost or damaged, and EVs must undergo an additional processing step for further analyses, i.e.

rebinding to latex beads for flow cytometry assessment. A slightly different approach involved EVs isolated from conditioned media directly with anti-CD9, anti-CD63, and anti-CD81 functionalized latex beads with these vesicles able to be directly assessed by flow cytometry [301].

The same direct assessment capabilities have been demonstrated with other EV specific proteins. For example, anti-epithelial cell adhesion molecule (EpCAM), another known EV protein, coated beads have successfully isolated EVs [302]. Also, vesicle capture with anti-EpCAM on a solid substrate, in combination with microfluidics, has also proven capable of adequate EV isolation and can facilitate further vesicle characterization by SEM, AFM, and SERS [303]. Along these same lines, a synthetic peptide capable of binding canonical heat-shock proteins (venceremin, Vn) also proved capable of adequately isolating EVs directly from samples and was multiparametricly validated [304]. Though quite promising and a needed step towards facile EV isolation, immunoaffinity capture with a single antibody (our few antibodies) may be too selective and will prevent the acquisition of EVs which lack the known surface protein. In conjunction, large scale isolation can be difficult and large antibody cocktails are quite cumbersome and diminish reproducibility.

3.3.2.2 Heparin isolation techniques

One of the alternatives to immunoaffinity EV capture that has recently been brought to light takes advantage of studies interpreting the effect of heparin sulfate proteoglycans (HSPGs) on vesicular uptake in target cells. HSPGs are known cell-surface receptors whith structural homology to heparin [305]. It has been shown that ligand binding to HSPG on the cell surface can be blocked by the addition of heparin. The addition of heparin has proven capable of preventing the uptake of labeled EVs into target cells [306] and further, mitigate

EV mediated migration of cancer cells when added contemporaneously with EVs [307]. Congruently, HSPG expression on the surface of cells was found to be required for recipient cell uptake of EVs [308]. These findings led Balaj et al. to investigate if heparinized agarose beads can bind to vesicles for large scale and facile isolation [309]. Indeed, EVs from conditioned media as well as human serum could bind to and be isolated by heparin beads with 60% efficiency compared to conventional UC. This binding was prevented when beads were pre-washed with a heparinase solution. They validated these findings *via* western blot, TEM, and RNA yield/quality. Further, the isolated EVs were subsequently labeled with red fluorescent lipid dye and their internalization was not hindered by this isolation process [309]. Thus, heparin isolation provides a platform for the investigation of all EVs from a sample, agnostic of protein expression.

3.3.2.3 Lipid nanoprobes

Another surface-based isolation method seeks to exploit the enrichment and altered orientation of lipid species in EVs as compared to parental cells. Lipid probes, which tightly intercalate with EV phospholipid bilayers, can be conjugated to a variety of species including magnetic beads or biotin to facilitate isolation. One such probe used a biotin-conjugated 1, 2-di-stearoyl-sn-glycero-3-phosphoethanolamine-poly (ethylene glycol) (DSPE-PEG) probe which tagged EVs from serum-free cell culture supernatant as well as human serum [310]. NeutrAvidin coated magnetic particles were added to the solution and were able to bind to the biotin-conjugated lipid probes and separate EVs from the media/serum. This lipid nanoprobe was able to rapidly and efficiently isolation EVs with a dramatic reduction in the procedure time (as compared to UC) to only 15 minutes [310].

Microfluidics, in conjunction with lipid probes conjugated to a substrate with a silica nanostructured surface, has proven capable of efficient vesicle isolation [311]. This method was able to isolate EVs and characterize the intravesicular DNA content (measured by KRAS point mutations) directly from pancreatic cancer patient serum samples [311]. Along the same lines, another group was able to immobilize individual EVs on PEG-lipid "brushes" conjugated to a silica surface [312]. Another interesting microfluidics-lipid-based assay is ExoChip®, a commercial product from the company BioTEK, and is marketed as an on-chip isolation method that is capable of both quantifying and characterizing circulating EVs. It accomplishes this by targeting exposed phosphatidylserine (PS) on the surface of EVS (a lipid species that is normally on the intracellular leaflet of a plasma membrane unless undergoing apoptosis [313]) with the PS specific protein, annexin V [314]. A unique aspect of this design is the simple procedure for the release of EVs from annexin V with Ca^{2+} chelation. While this assay was capable of isolating 90% of cancerous EVs (and a larger total quantity than an anti-CD63-functionalized system), it also isolated 38% of healthy EVs, thus limiting its use for diagnostic and functional assessment of cancerous vesicles [314]. Importantly, Annexin V functionalized beads have been utilized for flow cytometry analyses [315] as well as another PS specific protein Tim4 [316].

All of the surface-based isolation techniques heretofore discussed have proven to be simple tools for easy and timely EV isolation in vitro as well as from human biofluids. Efficient yield, minimal impact on surface features, and maintenance of a vesicular structure, coupled with ease of release and vesicle recovery, allows the EVs isolated with these methods to be utilized for subsequent analyses. Congruently, surface-based isolation allows for the preservation of EV functional characteristics, organ specificity, and

propensity to interact with target cells, which are required for EV use as therapeutic delivery systems (discussed later in the text). These combined advantages are causing surface isolation and characterization methods to become preferred over traditional means and as such, they are becoming more ubiquitous throughout the field. What remains to be seen is if these isolation methods are specific enough to be viable separation methods for research as well as in the clinic. Immunoaffinity based assays are limited by the fact that only a certain number of EVs express the target proteins and those that do express them have variations in the quantity. Thus, immunoaffinity can yield a heterogeneous EV population in regard to biogenesis, tissue/cell of origin, or pathological involvement. While the lipid composition is different in EVs as compared to parental cells, these lipid species are not mutually exclusive to EVs, thus allowing for the possibility of diminished assay specificity.

3.4 Surface-based characterization techniques

Given the promise of the surface-based isolation techniques described in the previous section, many have been mingled with existing technologies to yield more efficient, lower cost, timely, and specific profiling assays. Specific techniques include; mass spectroscopy (MS), which has been able to elucidate a vast array of protein, glycan, and lipid targets for EV isolations and/or profiling. Microfluidics, which has provided an excellent means of increasing sample volumes tested and increases the ability of multimarker assessment within a single sample. Surface plasmon resonance (SPR), flow cytometry, and labeled-nanoprobe studies, which have improved quantitative analysis of specific EV proteins in total populations as well as on individual vesicles. Surface-enhanced Raman spectroscopy (SERS), which has proven capable of assessing the EV

surface in a labeled (antibody-mediated) or label-free manner. Finally, various electro kinetic and impedance-based biosensors, which have been able to semi-quantitatively assess EVs in a facile and reproducible manner.

The remainder of this section will describe some of these methods used to profile the EV surfaceome. The discussed studies are not an exclusive or exhaustive list, yet seek to emphasize some of the key examples of techniques utilized for surface-based characterization of EVs. Further, many of these techniques are used to determine EV associated cancer biomarkers, which will be further highlighted within that section.

3.4.1 Mass spectrometry

Mass spectrometry (MS) has been in existence and utilized for many years for the discernment of protein components within a sample. This sensitive technique has successfully been applied to extracellular vesicles in an effort to determine their general (internal and external) protein content [317]. These studies have shown that EV proteins are dramatically altered predicated on the conditions under which the originating cell exists including stress [318], immune-inflammatory state [319], and pathological state such as cancer [320]. These differences have thus provided valuable insight into disease processes including oncogenesis, tumor progression, and metastasis as well as provided novel targets for EV based biomarkers.

Though few in number, recent studies have utilized LC-MS/MS to determine the surface proteomic profile of EV populations. These studies have provided valuable insight into the morphology as well as possible functions of EVs after cellular uptake. One such study utilized a triple proteomic profiling method that combined LC-MS/MS of *in vitro*

purified EVs analyzed directly, after proteinase K surface protein separation, and after biotinylation with trypsin digestion followed by subsequent column-based separation [321]. Notably, luminal proteins are not affected by enzymatic digestion due to the protection from the vesicle membrane, thus this method allowed for the identification of proteins expressed on the vesicular membrane as well as presumptions about the membrane location of these proteins (luminal or external surface). They found a distinct population of proteins on the vesicle surface relative to the intravesicular contents. Interestingly, they found that some of these proteins could have a "reverse topology" where the cytosolic domains were located on the superficial aspect of the vesicle surface. Unexpectedly, surface proteins were enriched in nucleic acid binding proteins and nuclear proteins (i.e. histones). These MS/MS findings were further verified *via* flow cytometry and fluorescent microscopy [321] and this was one of the first studies to elucidate the luminal and external proteomic differences.

Surface-specific proteomic profiling of EVs isolated from a variety of biofluids have also been conducted. MS/MS analysis of serum EV surfaces have yielded specific proteomic signatures used to isolate cancer-specific vesicles from patient samples [322]. Urinary EV surface proteomes have also been investigated and it has been found that at-least forty-nine proteins are unique to the urinary vesicle surface [323]. Further, these results corroborated the aforementioned Cvjetkovic et al. findings that vesicular surface proteins may have an inverted topology compared to expected cellular membrane orientation. The majority of these surface proteins were glycosylated, much like cell-surface proteins, implying similar protein-protein interactions and functional mechanisms [323]. Thus providing another aspect of surface profiling that may be elucidated *via* mass spectroscopy, that of glycosylation status.

With the realization that one of the primary topographical constituents of EV membranes are carbohydrate moieties, it stands to reason to investigate and characterize their glycosylation profiles. One such study outlined and utilized an approach with MALDI MS to measure the number and quantity of N-glycans of urine EVs after enzymatic digestion and permethylation [324]. They found Paucimannosidic, high-mannose, and complex type glycans in the EV samples and further structural details of *N*- as well as *O*-glycans were assessed *via* LC-MS/MS [324]. A materials engineering approach taken by another group allowed for further clarification of their MS/MS illuminated glycoproteome associated with EVs by utilizing a hydrazide thermosensitive polymer that selectively binds to N-glycans [325]. The polymer couples with oxidized glycoproteins present in solution and self-assembles into large aggregates that fall out of solution at room temperature and may be pelleted *via* centrifugation. These polymer chains decouple and again become soluble when heated. Thus, facilitating the selective enrichment of the N-glycans present within the mixture. This technique was applied to EVs isolated from healthy and glioma patient serum samples by with a commercial isolation kit and found that 26 N-glycoproteins to be significantly different between the two populations [325].

Another application of mass spectroscopy that has proved advantageous for EV surface characterization is lipid constituent assessment. Many studies have found differential lipid compositions in EVs relative to parental cells [252, 254]. Ratiometric increases in the relative amounts of many lipid species have been realized between parental cell membranes and EVs including cholesterol, sphingomyelin, ceramide, phosphatidylserine, and phosphatidylethanolamine [326, 327]. Lipid species differences have also been observed between vesicle subpopulations such as exosomes (enriched in glycolipids and free fatty

acids) and microvesicles (enriched in ceramides and sphingomyelins) [328]. Importantly, several studies have profiled the lipid content of EVs isolated from human biofluids including urine and found differences between cancer and healthy cohorts [329]. Of note, co-isolation of lipid droplets and lipoproteins present a problem for many of these MS techniques and as such, require further laboratory validation.

The majority of these LC-MS/MS EV studies conducted to date have focused on the presence of proteins and glycosylations, agnostic as to their location. The select few that have chosen to focus on the surface proteome/glycome and EV membrane lipidome have proven the capability of this global technique to identify unique surface features linked to specific EV populations, both *in vitro* as well as in patient samples. Increased application of mass spectroscopy could provide novel insight into the proteomic, glycomic, and lipidomic differences observed in EVs isolated from various biofluids and in different pathological settings, including cancer. This, in turn, could identify novel biomarkers, improve isolation capabilities, help discern EV functions in target cells, and aid in the understanding of how EVs interact with their surroundings. One must remain cognizant that MS data can be muddled and much uncertainty persists upon data collection. Any result found with these methods must be further experimentally validated.

3.4.2 Microfluidics

Microfluidics platforms have become integral to EV isolation and content assessment. When combined with antibodies, lectins, or aptamers microfluidic platforms offer an easy and high-throughput method of profiling the EV surface. Importantly, this technique can be combined with various electrochemical analyses to improve overall sensitivity and population characterization. One study utilized immunoelectrophoresis to

detect EV bound antibodies *via* alterations in surface ζ-potential, without the requirement of fluorescent labeling [330]. Additionally, microfluidics facilitates ease in multiplexed analyses within a single sample involving the quantitative detection of specific markers. Vaidyanathan et al. used a tunable alternating current electrohydrodynamic method to detect multiple cancer-associated molecules including epidermal growth factor receptor 2 (HER2) and prostate-specific antigen (PSA) [331]. Concurrently, He et al. has produced a microfluidics platform for the concurrent analysis of EV surface and internal contents [332]. The design incorporates an integrated cascading circuit of analytical procedures including immunoisolation (surface protein profiling), EV lysis, protein immunoprecipitation (intravesicular protein profiling), and chemifluorescent sandwich assays. They were able to apply this technology for the direct assessment of EVs in patient plasma samples, accurately characterize EV subpopulations based on surface proteins, and determine Insulin-like growth factor 1 receptor (IGF-1R) phosphorylation status [332].

3.4.3 Flow cytometry

Flow cytometry is an ideal candidate for individual vesicle analyses with the simple yet impactful caveat that EVs are too small to be accurately assessed. Therefore, many different methods have been proposed to increase the accuracy and reproducibility of flow cytometry analysis [333, 334]. Many of these methods evolve directly from the antibody functionalized beads used for EV isolation by flow cytometry [301, 302, 335]. In these instances, EVs can be isolated directly from the media or patient sample with EV consensus proteins and subsequently profiled with a second probe antibody/antibodies against a protein(s) of interest. A profile of protein expression on EV populations can be compiled specifically for discriminating the tissue of origin and/or pathological involvement (i.e. cancerous vs

non-cancerous). However, due to the possibility of multiple EVs binding onto a single bead, or not harboring both distinct analytes for antibody binding, this method is considered to be only semi-quantitative.

Evolving from this notion, Yoshioka et al. produced an assay coined "ExoScreen", whereby EV specific antibodies on two distinct photosensitizer beads are combined to produce a fast and facile profiling technique [336]. Briefly, streptavidin-conjugated donor beads are bound to a biotinylated antibody against an EV protein of interest. A second bead-antibody conjugate for the same EV specific protein will act as an acceptor bead. The first bead (donor) is excited with a laser, which releases oxygen causing the excitation of the second bead (acceptor) when in close proximity (within 200nm). This proximity requirement is a benefit, particularly when one is hoping to assess smaller EV populations such as exosomes and smaller microvesicles, and improve the accuracy of quantitative assessment [336].

Another evolution from standard bead-based flow cytometry is the recent development of high-resolution flow cytometry (hr-FC). This is a technique with great potential in profiling EV surfaces because it is a mass through-put method capable of analyzing individual EV in a multiparametric fashion. Perhaps most importantly, hr-FC has a dynamic range of size assessment within the EV range (50-1000nm), thus abrogating the requirement of bead conjugation a priori [337]. Unfortunately, the reproducibility of EV characterization *via* hr-FC is minimal and attempts are still being made and standardizing fluorescent labeling methods and inter-instrumental variations [338]. For instance, highly concentrated samples can cause an underestimation of particle number [339]. Never-the-less, with the inherent benefits hr-FC possesses, along with the potential of combining with

affinity-based methods, this is a technique that holds great promise in the future of individual EV surfaceome analysis.

3.4.4 Surface plasmon resonance

Surface plasmon resonance (SPR) is a long-known method for the sensitive detection of molecular components within a sample. Importantly, SPR sensors can be functionalized with antibodies against a protein of interest [340], lectins for carbohydrate moieties [341], or aptamers reactive to particular nucleotide sequences [342]. Given the potential it has of specifically identifying and quantifying a wide array of biological molecules, coupled with its long-time use for sensitive detection, SPR has recently been used to characterize EV surfaces [343, 344]. For example, Gool et al. found that SPR analysis was capable of detecting far more antibody-EV pairs compared to flow cytometry, due primarily to high blank and isotype control signals in the latter technique [345].

Recently, localized SPR (LSPR, where light is incident with metal nanostructures thus producing an extremely high electromagnetic field in the local environment which can be detected with an interferometer [346]) has been highlighted as an ultrasensitive technique that is an excellent method of assessing EV surfaces with aptamer conjugated metal nanoparticles [347] or with nanostructured metal surfaces [348]. Interestingly, one group was able to optically differentiate *via* LSPR, exosomes from microvesicles, without the requirement of a functionalized antibody using a self-assembled monolayer of gold nanoislands (SAM-AuNIs) [349]. Conversely, Wang et al. were able to use labeled LSPR (i.e. aptamer reactive to CD63 for capture and conjugated gold nanoparticles AuNPs) to isolate and characterize EVs with AuNP proximity ligation (*via* aptamer interaction) signal amplification [350].

3.4.5 Surface-enhanced Raman spectroscopy

Surface-enhanced Raman spectroscopy (SERS) is another ultrasensitive technique predicated on vibrational patterns of molecules present within a sample producing inelastic photonic scattering that is amplified by the presence of surface plasmon on a noble metal surface [351]. Scattered photons are identifiable to the molecular species with which they interact, thus yielding a highly specific spectral shift [352]. In the label-free SERS approach, Raman shifts are measured from endogenous molecules present within the EV samples. While these spectra necessarily depend on the vibrational patterns of the molecules present, the abundance of molecular species and heterogeneity of the system produce an intensely complex pattern. A myriad of statistical methods have been applied to deduce EV population-specific patterns such as principal component analysis (PCA) [353] and partial least squares discriminant analysis (PLS-DA) [354], within the Raman spectra. Nanoparticle alterations (i.e. silver-shelled AuNPs) have been produced that increase the specificity of label-free signals thus facilitating accurate population discrimination [355]. Conversely, the labeled SERS approach uses mAB conjugated metal nanoparticles to increase assay specificity when a specific marker is known [356]. This comes with the obvious requirement of knowing the molecule that you looking for, and in the case of cancer-associated species, remains quite elusive.

Recent progress in the SERS field has allowed for the analysis of individual vesicles, rather than the bulk EV solution. Many of these use optical tweezers to trap vesicles and conduct SERS measurements on each distinct vesicle [357]. This technique was able to further categorize $CD9^+$ EVs into subpopulations based on Raman shifts as a function of differences in surface molecules including proteins, lipids, and nucleic acids

[358]. One of the primary benefits that may be attributed to individual vesicle analysis is increasing the discriminatory potential between distinct populations, whether that is within the same biological sample or within the same sample grouping such as serum from healthy donors or cancer patients.

3.4.6 Nanoprobes

One of the most prevalent of these techniques involves brute force investigation of EV surfaces by large numbers of antibody arrays. In a large study involving 431 lung cancer patient samples and 150 healthy controls, an antibody array consisting of 49 different mABs was used to capture EVs from serum samples [359]. The arrays were then probed with detection antibodies against the consensus EV markers CD9, CD63, and CD81 and surface proteins were identified that separated cancer patients from controls based on area under curve (AUC); CD151: AUC = 0.68; CD171: AUC = 0.60; and tetraspanin 8 (TSPAN8): AUC = .60) [359].

Yang et al. engineered a surface profiling method called Exosome-Oriented Aptamer Nanoprobe-Enabled Surface Proteins Profiling and Detection (ExoAPP) [360]. EVs are immobilized onto surfaces of aldehyde sulfate beads and treated with the ExoAPP nanoprobes, which are linked to quenching graphene oxide (GO) surfaces conjugated to fluorescent aptamers. When aptamers come into proximity with EVs they preferentially bind the proteins of interest thus restoring fluorescence. Once the signal is measured, DNase can be used to digest the aptamers thereby facilitating repeat probing for different targets in the same EV population. This sequence can then be repeated with different aptamers thereby facilitating multi-marker profiling and delineation of patterns between disparate populations (i.e. healthy vs cancer). This has allowed for ultrasensitive protein

marker detection and profiling (as few as 1.6 x 10^5 vesicles) [360]. Similarly, another group combined microfluidic size separation with γ-DNA/aptamers protein assessment and machine learning, to yield a profiling assay predicated on EV EpCAM and Her2 expression [361].

In an effort to detect ultralow quantities of proteins on individual vesicles, Wu et al. composed a proximity-dependent barcoding assay (PBA) to sensitively assess the EV surface proteome [362]. They selected 38 protein targets which are converted to DNA sequences by antibodies conjugated to DNA. The bound oligonucleotide conjugates polymerize with rolling circle amplified (RCA) protein tags and amplified by PCR. The amplified RCA-PBA complex is decoded with next-generation sequencing (NGS), which identifies the specific proteins present within the sample [362]. This elegant fusion of immunoaffinity and barcoding techniques was able to discern distinct surface protein patterns predicated on cells of origin, even at ultralow quantities as determined by the percentage of the total sample. The group posited this assay could improve EV characterization studies by first identifying the tissue from whence the vesicle originated and isolating the population of interest from the myriad others within a biofluid sample.

Some researchers have begun to utilize lectin arrays to profile the surface glycome of EVs [363]. In an evolution from the traditional lectin array method, one study again took advantage of RCA mediated conversion of EV surface molecules into DNA mediated fluorescent detection moieties, but this time with lectin profiling of surface glycans [364]. Briefly, EVs were isolated *via* UC and deposited in hydrophilic wells. These EVs were probed with various lectin-oligonucleotide conjugates (i.e. sialic acid, fucose, and truncated O-glycans) and in situ RCA was performed for glycan signal DNA conversion

and amplification. They validated these findings with sialidase treatment and subsequent re-analysis as well as flow cytometry. They were able to improve the limit of detection (LOD) from traditional lectin array performance. The assay was able to distinguish between vesicles arising from different cell sources (HeLa and Panc1 cell lines) based on glycan signaling intensities (i.e. Siaα2-6Gal/GalNac and truncated O-glycans) as well as differences between EVs and parental cell lectin affinities (i.e. Jacalin, PNA, & HPA) [364]. Thus, providing a novel method by which EV glycans can be monitored and their functional impact investigated.

3.4.7 Biosensors

An increasingly wide variety of other biosensors take advantage of electrochemical and physics principals to efficiently segregate and characterize EV surfaces. A representative sample of some of these innovative and novel technologies including electro kinetics, electro generated chemiluminescence, and thermophoretics are described thusly.

Electro kinetic microarrays combine alternating AC current dielectrophoretic separation with aptamer/mAB capture for surfaceome profiling of vesicle subpopulations requiring ultralow quantities of patient fluid [365, 366]. Electro generated chemiluminescence (ECL, materials/chemicals capable of emitting light in the presence of electro generated redox reactants) combined with mAB functionalized electrode surfaces has also been applied for the successful characterization of EV surfaces [367]. Astoundingly, this group has reported an ultrasensitive limit of detection (LOD) of 125 particles μL^{-1} with an in-house ECL nanoprobe produced from Ti3C2 MXenes nanosheets [367].

Finally, thermophoresis is a phenomenon found in mixtures of distinct and movable particles, where particle subpopulations behave differently in response to gradation in

temperature. In an elegant study, Liu et al. took advantage of this property of physics and thermophoretically enriched from patient plasma samples and subsequently profiled their surface with aptamers [368]. These various biosensor technologies have been briefly discussed herein to provide insight into some of the newer technologies that have the potential to play a greater role in EV surface profiling in the near future.

3.5 Cancer Biology

Many studies have uncovered the role of EVs in cancer [287, 369]. Unfortunately, most of these neglect to differentiate between the intravesicular and surface contents of EVs leading to a relative paucity in surface-specific studies relative to the compendium of EV research. However, interactions that take place at the EV surface and cell surface interface are critical in cancer biology as these are the initial events that dictate EV-cell binding resulting in the eventual intake of vesicular contents or signal transduction [370]. Conversely, some of the surface molecules themselves are biologically active and thus can interact with and affect the tumor microenvironment (TME) as well as augment the surrounding stroma. This section will discuss some of the EV associated impacts on cancer biology that have been attributed to the vesicle surface.

3.5.1 Signaling and crosstalk

EVs can directly interact with cell surface receptors without the need to deliver their intravesicular cargo [371]. The same holds true in cancer. HSP90α on the surface of breast cancer EVs interacts with low-density lipoprotein receptor-related protein-1 (LRP-1) receptor in an autocrine manner (of note, these EVs have a paracrine function and interact with the surrounding stroma as well but will not be included in the crosstalk subsection) [372]. Conversely, EVs can also carry molecules on their surface which initialize

pro-tumorigenic signaling after internalization. Case in point, a highly-glycosylated form of extracellular matrix metalloproteinase inducer (EMMPRIN) on EV surfaces initiates p38/MAPK signaling after internalization [373]. One of the most interesting aspects of this particular study is that the putitive primary function of EMMPRIN is to induce MMPs in the tumor microenvironment [374], yet the form found on the EV surfaces only had an effect once internalized into cancer cells and did not induce MMP degradation of the TME [374].

Much of the cancerous phenotype including tumor initiation and progression is propagated by crosstalk between the cancer cells themselves as well as between the malignant cells and the surrounding tumor milieu [375, 376]. EVs have a substantial role in cellular crosstalk and the initiation of signaling events throughout normal homeostasis and just as integral, if not to an even greater extent, in the setting of cancer [377, 378]. There is a paucity of studies regarding specifically the surfaceome yet some groups have begun to investigate its impact on cellular communication. For example, heparin sulfate proteoglycans (HSPGs) residing on the surface of tumor-associated EVs and recipient cells have been found to be integral for EV uptake across different cell types [379]. Christianson et al. corroborated this finding and observed that HSPGs on the surface of EV are necessary for both internalization and functional delivery of cargos including signaling molecules, metabolites, and RNA [308]. This led the authors to posit that HSPG could be a novel therapeutic target for the treatment of cancer.

Another example of tumor EV crosstalk with the tumor microenvironment (TME) is TGFβ-1 bound to the surface of tumor-associated EVs induced a migratory phenotype in surrounding mesenchymal stem cells (MSCs) [380]. Further, EV-TGFβ-1, which gets trafficked into the cell and remains in the endocytic compartment, induced this phenotype

via SMAD dependent signaling for a longer period of time compared to free TGFβ-1 [380]. In the same direction, a separate study uncovered that fibroblasts within the TME can gain malignant characteristics including resistance to cell death and invasive properties (through the FAK pathway) when exposed to tissue transglutaminase (tTG) cross-linked fibronectin (FN) on the surface of EVs from breast cancer and glioma cell lines [381]. Endothelial cells can also be affected by tumor-associated EVs. E-cadherin on the surface of ovarian tumor EVs has been shown to heterodimerize with vascular E-cadherin on the surface of endothelial cells thus activating β-catenin and NFκB mediated angiogenesis [382].

Of course, cellular communication within the TME also occurs in the other direction, from the surrounding stromal cells to the cancer cells. One study found that EVs arising from senescent cells within the TME push breast cancer cells to a more aggressive phenotype *via* EphA2 mediated interaction with ephrin-A1 at the surface interphase. Ephrin-1 activation initiates reverse signaling through the Erk pathway leading to cell proliferation [383]. Congruently, glioma-associated stem cells (GASCs) release vesicles that produce an invasive and migratory phenotype in glioma cells through the presence of Semaphorin7A (SEMA7A) on the EV surface [384]. This effect was mediated by SEMA7A interaction with integrinβ-1 and activation of the focal adhesion kinase (FAK) pathway leading to the increase in cell motility [384]. Finally, EVs from cancer-associated fibroblasts (CAFs) contain fibronectin which facilitates invasion and promotes anchorage-independent growth of cancer cells [385]. Interestingly, the promotion of invasion was not accomplished when fibronectin was located inside vesicles but only when it was on the surface *via* direct interaction with its receptor, integrin α5β1, thereby initiating the FAK and Src family kinase pathways [385].

The TME is not the sole origin of EVs that interact with and affect cancer cells in patients. Shtam et al. conducted a study with interesting implications. They found that plasma EVs, isolated from healthy donors, were able to stimulate breast cancer aggressiveness, again *via* FAK [386]. By combining enzymatic EV surface modification (trypsinization) with mass spectrometry, they deduced that this signaling was mediated by EV surface proteins that had previously been shown to be involved in FAK signaling including extracellular matrix protein 1 (ECM1), fibrinogen (FGA), and fibronectin (FN1) to name a few [386]. This study has far-reaching implications regarding the effects of normal EVs on cancer cells, thus warranting further investigation.

3.5.2 Extracellular matrix remodeling

Augmentation and refinement of the extracellular matrix (ECM) surrounding a tumor are required for migration, invasion, and metastasis [387]. A few studies have shown how the EV surfaceome facilitates some of the manipulations of the ECM compartment. Proteases and glycosidases have been observed on the surface of EVs providing direct implications of ECM remodeling [388]. Slightly more nuanced is $CD44^+$ EVs released by tumors that can bind with hyaluronic acid (HA) and accumulate at the invadopodia, thereby effecting stroma and increasing the ability of cancer cells to invade [389]. EVs harboring CD151 and Tspan8 on their surfaces have been shown to support matrix degradation and activate the stromal cells to release a variety of cytokines and proteases that propagate an invasive phenotype [390].

The ECM remodeling capability of EVs can be modified/enhanced with the introduction of chemotherapy. Bandari et al. found that heparinase on the surface of EVs collected from myeloma cells was impressively elevated after the administration of various

standard chemotherapies. The surface localization was a requirement to allow for heparinase mediated degradation of heparin sulfate found in the ECM. Further, they found that uptake of these EVs by untreated cells activated ERK signaling and caused a concomitant increase in heparinase loaded EVs as well as enhanced shedding of the heparin sulfate proteoglycan syndecan-1 (SDC1) [391]. This is an incredibly informative finding with huge implications in possible therapeutic resistance and/or disease recurrence.

3.5.3 Metastasis

One of the initial studies to delineate EV implications in cancer metastasis involved the formation of a premetastatic niche by EVs released from pancreatic cancer cells in the liver [392]. This study, while not concerned specifically with the EV surface, was a seminal finding in the field and ignited an explosion of research revolving around EVs in metastasis. Following this, the same group discovered that integrins on the EV surface are responsible for metastatic organ tropism [393]. They showed that EVs from specific organ-tropic tumor cells are selectively up taken by or cells within that organ to form a premetastatic niche. Further, they were able to change the tropism of cancer by pretreating with EVs from a different organ-tropic cancer (i.e. bone-tropic to lung-tropic), specifically integrins $\alpha_6\beta_1$ and $\alpha_6\beta_4$ facilitate lung metastasis and integrin $\alpha_v\beta_5$ is correlated with metastasis to the liver [393].

An addition to the EV integrin story was provided by Zhao et al. when they investigated the role of two tetraspanins located on the EV surface previously implicated in metastasis: Tspan8 and CD151 [394]. They found that metastasis was drastically reduced in an MCA tumor induced in a $Tspn8^{-/-}$ and $CD151^{-/-}$ knock out (KO) murine model. $Tspn8^{-/-}/CD151^{-/-}$ EVs interactions with integrins, CAMs, and selectins were inhibited and cancer

cell migration and invasion were diminished. Along with this, no change in the growth rate and survival of the primary tumor was observed. This resulted in the conclusion that Tspan8 and CD151 mediate their metastatic enhancement *via* EV-Tspan8/CD151-integrin/CAM interactions [394]. Another group corroborated the notion that EVs facilitate cellular adhesion and found that small EVs harbor extracellular matrix and adhesion proteins [395]. They went one step farther and observed that tumor cells that were deposited onto surfaces coated with EVs showed and improved adhesion, thus displaying the functional relevance of their findings [395].

3.5.4 Immune Impact

Seemingly contrarian to the majority of EV studies conducted in recent years, a much larger proportion of research investigating the role of EVs on the immune system specifically involves their surface. EV surfaces have been shown to contain immunologically impactful molecules such as complement [396], MCH class I & class II [397], and bioactive lipids [398], as well as act as damage-associated molecular patterns (DAMPS) themselves [399]. Conversely, responses mediated by immune cells can be mediated by EV surfaces including PMN release of EV-neutrophil elastase (NE) [400], macrophage release of EV-histones that activate toll-like receptor 4 (TLR4) [401], and myeloid-derived suppressor cell (MDSC) chemotaxis facilitated by MDSC release of EV-CD47, TSP1, and SIRPα [402].

With the prevalence of EV surface-mediated immune effects, it is natural to investigate some of these in the setting of cancer. Indeed, the EV consensus markers, CD9 and CD81, along with other tetraspanins including CD151, CD53, CD37, and Tssc6 seem to have a defining role in antitumor immunity [403]. B-cell surface antigens including CD19, CD20, CD24, CD37, and HLA-DR are on the surface of EVs from B-cell lymphoma cell

lines, which could feasibly diminish the efficacy of immunotherapy [404]. An incredibly impactful finding was made in the field of EV immunology when it was discovered that tumor-associated EV surface expression of PD-L1 contributes directly to tumor mediated immune suppression in melanoma [405]. It was also observed that EV-PD-L1 surface expression was positively correlated with IFN-γ and modulates the effect of anti-PD-L1 therapies. Further, EV-PD-L1 expression can also be used as a predictor of response to anti-PD-L1 therapy [405]. This result was corroborated by the findings by separate groups [406, 407].

Another impactful study by Muller et al. found that the regulation of regulatory T-cell (Tregs) functions mediated by tumor-associated EVs was facilitated by interactions at the EV surface Cell surface interface and did not require EV uptake [408]. Interestingly, other immune cell types including B-cells, NK cells, and monocytes internalized many of the EV originating from cancer cells but Tregs did not. This surface interaction sustained Ca^{2+} influx into Treg cells which translated increased conversion of extracellular ATP to inosine by the Treg, thus suggesting functional consequences of the interaction [408].

3.6 Biomarkers

Liquid biopsy-based biomarkers for the successful detection of cancer in a less/non-invasive manner has become a subject of increasing interest [409, 410]. EVs hold many advantages for use as liquid-based biomarkers. They are expressed by every tissue/cell in the body and are present in almost all biofluids including serum/plasma [411], urine [412], breast milk [413], semen [414], ascites [415] and bronchiolar lavage [416], and can even cross the blood-brain barrier (BBB) [417]. EVs also contain proteins, carbohydrates, lipids, and RNA/DNA molecules that reflect their cell of origin and have a measure of tissue specificity [418]. This

feature can be taken advantage of to provide a means for the peripheral assessment of residing cancer. Importantly, many of these molecules can be found on the surface of EV, which has led to the use of surface profiling and characterization for the diagnosis and prognosis of cancer.

3.6.1 Proteins

A preponderance of the studies attempting to evaluate the potential of EVs as biomarkers do so by characterization the surface proteome. Predefined antibody microarrays are widely used for experimental biomarker discovery. An array of 49 antibodies against EV proteins found that NY-ESO-1, EGFR, PLAP, EpCAM, and ALIX were able to prognosticate non-small cell lung cancer (NSCLC) patient survival [419]. Another prognostication study was able to accurately predict High-grade and low-grade glioma patients using an array identified EV protein, syndecan-1 (SDC1), with a 71% sensitivity (SN), 91% specificity (SP), and an area under ROC curve (AUC) of 0.81 (30679164). Another study used an antibody array on cancer cell line EVs [LIM1215-colon cancer, MEC1- B-cell chronic lymphocytic leukemia (CLL)] to select protein targets used to probe EVs isolated from CLL patient serum. A subset of the targeted proteins including an assortment of tetraspanin markers and HLA molecules were expressed at high-levels on the surface of CLL patient EVs and not expressed at all on those of healthy individuals [420].

As eluded to in the profiling and characterization section found herein, mass spectrometry can also be used as a global approach to identify EV surface proteins capable of serving as biomarkers. However, special requirements are necessary, such as proteinase K treatments and size exclusion chromatography to compare with untreated EVs, in order

to assure an external EV membrane location. For example, Castillo et al. used proteomics to identify multiple pancreatic cancer EV markers: CLDN4, EpCAM, CD151, LGALS3BP, HIST2H2BE, and HIST2H2BF. They were able to use antibodies against these surface proteins to selectively isolate cancer-associated EVs from patient plasma, as determined by the enrichment of detectable KRAS mutations [322]. Glypican-1 is another pancreatic cancer EV surface marker that was discovered by MS proteomics and verified by flow-cytometry [421]. Along with pancreas cancer, EV surface proteins identified by MS and have also been able to facilitate target identification in gliomas (with surface location validation conducted by proximity extension assays) [422] and colorectal cancer [423]. Of note, much more mass spectrometry proteomic assessment has been conducted on EVs but almost all of them have been concerned with the complete vesicle proteome and the proteins identified are unable to be specifically attributed to the EV surface.

Other protein profiling techniques have been utilized as well. Logozzi et al. used an enzyme-linked immunosorbent assay (ELISA) to assess the levels of specific proteins: CD63, Rab-5b, and caveolin-1 in EVs purified from melanoma patient serum. They found a consistent increase in the expression level of CD63 and caveolin-1, as well as an increase in the abundance of caveolin-1 within the $CD63^+$ population, in EVs from cancer patient serum as a comparison to healthy controls [424]. High-sensitivity flow-cytometry is another technical approach that has also been adapted to help identify cancer-associated proteins on the surface of EVs. This study found CD147 expression to be significantly increased on the surface of EVs from colorectal cancer patients as compared to healthy donors [425]. Another group utilized plasmonic profiling EVs from pancreatic cancer patients, to find a five-marker signature able to predict patient cancer status with some accuracy. The assay

sensitivity of 86% and specificity of 81% offered produced higher accuracy than the current gold standard marker CA19-9 [426]. Congruently, Liang et al. were able to use labeled LSPR (i.e. anti-EphA2 mAB conjugated metal nanoparticles) to discriminate between healthy and pancreatic cancer patient serum requiring only 1uL of sample [427].

3.6.2 Carbohydrates

Aberrant glycosylation of cells and the extracellular matrix in the setting of cancer has been known for many years [428, 429] and the presence of glycans on the surface of EVs has been discussed in previous sections. With this, investigations into the presence and patterns of carbohydrate moieties on the surface of EVs have proven fruitful for use as cancer biomarkers [430]. For example, the presence of sialic acid on EV-CD133 isolated from ascitic fluid of pancreatic cancer patients was linked with a better prognosis in advanced-stage patients [431]. In a related experiment, a lectin array that focused on tumor-associated glycans such as sialic acids, fucose, and truncated O-glycans was able to determine differential expression of surface glycans between EVs and parental cervical and pancreas cancer cells [364].

Likewise, flow cytometry mediated lectin evaluation of melanoma EVs revealed an increase in the presence of fucose and complex N-glycans with bisecting GlcNAc [432]. Along with the serum-based studies, urine N-glycosylation status was found to be associated with EVs released in the setting of prostate cancer [433]. The majority of these studies are starting points of glycosylation-based biomarkers in cancer because just as with proteins, many more studies involving EV glycosylation status have been conducted without necessarily focusing on surface localization of the moieties.

3.6.3 Lipids

Lipids offer another means of EV population differentiation. Targeted lipidomic analysis of EVs isolated from non-tumorigenic prostate cells and prostate cancer cells elevation in the presence of fatty acids, glycerolipids and prenol lipids in the former while the latter harbored more sterol lipids, sphingolipids, and glycerolipids [327]. "Shotgun" lipidomic profiling of EVs isolated from a different cancer type, colorectal, corroborated these prostate cancer findings and found an increase in sphingolipids, sterol lipids, glycerolipids, and glycerophospholipids [434]. A final study applied lipid characterization to the actual diagnosis of prostate cancer patients. The abundance of nine lipid species was altered in urinary EVs isolated from healthy donors and prostate cancer patients. The two lipids with the most differential expression levels were phosphatidylserine (18:1/18:1) and lactosylceramide (d18:1/16:0), and when combined phosphatidylserine (18:0/18:2) were capable of predicting patient cancer status with 93% sensitivity and 100% specificity [329]. Importantly, the overlap in lipid species between these two individual studies, while not complete, reinforces the notion of selective lipid species incorporation into EVs and supports their use as possible biomarkers.

3.6.4 Label-free

An increasingly ubiquitous label-free method of treating the EV surface as a cancer biomarker is surface-enhanced Raman spectroscopy (SERS). This technique, in combination with a variety of statistic methods discussed previously in the profiling section, has allowed for the reproducible, non-destructive, and non-targeted assessment of EVs isolated from cancer cell supernatant and patient samples. Examples include SERS measurements and PCA analysis of EV surfaces isolated from NSCLC cells, which were

similar in pattern to SERS spectra of the EGFR protein. Thus, the authors concluded that much of the cancer EV spectra is conferred by the presence of EGFR on the surface of the EVs [435]. SERS was again applied to cell line EVs and proved capable of distinguishing between lung cancer and non-malignant origins with very high accuracy (95.3% sensitivity and 97.3% specificity) [436]. Another study took another step towards the application of SERS technology to patient samples and involved SERS-based analysis of pancreatic cancer cell line EVs that was used to train a PC-DFA (discriminant function analysis) algorithm, which was subsequently applied to SERS spectra collected from EVs isolated from patient samples. This method was able to predict patient status with up to 87% accuracy for healthy controls and up to 90% accuracy for early pancreatic cancer [353]. SERS characterization has also been successfully applied to EVs originating from breast cancer cells [437] as well as prostate cancer cells [438].

3.7 Therapy

A plethora of studies have investigated the use of EVs as a delivery vehicle for various therapeutic molecules including cytotoxic drugs and inhibitory RNA with a variety of loading techniques [439, 440]. EVs have many advantages which make them ideal candidates for cancer therapy including protection of intravesicular contents (i.e. prevention of RNA degradation), minimal immunogenicity (especially when of autologous origin), ability to be loaded with therapeutic cargo, and the capability of surface modification for selective targeting [441]. The methodology and effectiveness of these strategies lie much out of the purview of this thesis, with the exception of the role the EV surface may play in the facilitation of drug delivery or enhancement of vaccine potency.

3.7.1 The endogenous EV surface

Generally speaking, EV surface proteins are important for their pharmacokinetic profile. EVs treated with proteinase k which significantly lowered the volume of distribution as well as diminished EV lung localization, presumably through enzymatic cleavage of integrin α6β1 [442]. This study highlighted the importance of the EV surface on vesicle distribution and its use as a therapeutic delivery method. The distribution of tetraspanin expression on the surface of EVs is another factor that contributes to target selection and uptake [443]. Another observation that holds immense therapeutic importance is the fact that cancer cells seem to have a preference for the uptake of EVs originating from themselves, that is, they possess a degree of autologous tropism [444].

Some EV-based therapies take advantage of the importance of endogenous surface profiles. For example, Li et al. bound doxycycline loaded superparamagnetic iron oxide nanoparticles to the surface of EVs with antibodies against A33, a protein expressed in cells of origin as well as the EV surfaces. These duplex particles were preferentially up taken by the parental cells thereby facilitating delivery [445]. Another method is isolating EVs from a patient and loading them with various cargos using different methods including electroporation, sonication, and freeze-thaw cycles [446, 447]. Notably, some of the traditional isolation methods such as UC, polymer-based precipitation kits, and ultrafiltration can cause vesicle lysis, aggregation, and morphological changes [290] all of which, could be ameliorated by the surface-based isolation methods previously discussed herein.

3.7.2 Functionalized the EV surface

One of the most prevalent strategies is the use of surface modification to influence the tissue-tropism, stability, and/or cancer specificity of EVs. EV surfaces can be decorated

directly with myriad exogenous targeting molecules through biochemical engineering facilitated by linker molecules [448]. Some of the surface functionalization methods that have had success include deposition of tumor-specific antibodies [449] and aptamers [450]. Notably, the PEGylation of EV surfaces after modification can serve the dual purpose of preserving the conjugation as well as increase the stability and circulation time of EVs in the body [451].

A slightly more refined approach to increase EV tumor homing is a genetic vector transfection harboring construct coding for the expression of tumor-targeting molecules on the surface of EVs. For example, a vector coding for anti-EGFR nanobodies linked to glycosylphosphatidylinositol (GPI) was transfected into cells and their EVs subsequently isolated [452]. These EVs successfully displayed the nanobodies on their surface and resulted in selective internalization by EGFR overexpressing tumor cells [452]. Interestingly, a different surface modification made with RNA nanotechnology induction of folate expression on the EV surface did not necessarily increase the uptake of EVs in cancer cells but prevented their subsequent trapping in the endosomal compartment. This facilitated the EV delivery of functional siRNA which subsequently inhibited tumor cell growth [453].

Along with targeting cancer cells for improved therapeutic delivery, EV surface modifications can be conducted that facilitate targeting of antigen-presenting cells, thus improving antigen delivery as a vaccine [454]. Lactadherin binds to the external EV surface *via* interaction of its C1C2 domain with EV lipids [455]. Hartman et al. took advantage of this by constructing a vector expressing the extracellular domains of tumor-associated antigens (TAAs) linked with lactadherin. They found that indeed, this caused the TAAs to be located on the surface of EVs and further, that administration of these EVs provided a significant enhancement of the antigen-specific immune response *in vivo* [456]. Importantly, this study

suggested EV surfaces as a possible method of anti-cancer vaccine. Congruently, if the glycocalyx is modified on tumor-associated EVs to possess high-manno glycans, they are preferentially take up by dendritic cells and result in a higher degree of CD8+ T cell priming than compared to unmodified EVs [457].

3.7.3 Targeting the EV surface

Since EVs have been proven to facilitate cancer progression, invasion, and metastasis (see previous sections), some researchers have attempted to target the EVs themselves in an effort to slow disease progression. For example, targeting integrin $\alpha_3\beta_1$ expressed by EVs originating from ovarian cancer cells by peptide LXY30 reduced uptake into the parental cancer cells, thus demonstrating a possible use in therapy [458]. A functional application of this notion came when heparinoids added to EVs, bound to their surface and subsequently prevented uptake into cancer cells. Further, the cancer cells exposed to heparinoid treated EVs displayed inhibited migratory potential [307]. In a slightly different approach, EV surface molecules can be targeted to prevent undesired downstream signaling. For example, activated T-cells release EVs with Fas ligand (Fas-L) on their surface which induces T-cell apoptosis. Cai et al. showed that targeting FAS-L on the surface of EVs with a mAB prevents T-cell dying and mitigates the tumor growth rate [459]. Few studies have been conducted that investigate this notion of targeting EVs yet this is a novel concept with great potential that requires further exploration.

3.8 Conclusion and perspective

The biological implications of the EV surfaceome in the setting of cancer are just beginning to come to light. The mechanism of biogenesis for these particles provides a window into the cancer cell from whence they came and thus, is inherently is a close look

into the processes and mechanisms of tumor biology. Surface-based isolation and profiling techniques have proved invaluable in the study of these EVs and continue to provide information on tumor biology including initiation, progression, and metastasis as well as how they interact with target cells, affect the tumor microenvironment, alter the extracellular matrix, and impact immune cells. Additionally, the surface of these vesicles provides a platform for the discovery of liquid biopsy-based biomarkers to facilitate the early detection of cancer. They are ubiquitous in human biofluids and possess cancer-specific signatures. Finally, understanding the surface of EVs facilitates their utilization as drug delivery vehicles. Surfaces can also be modified to improve cellular uptake or increase target specificity. Thus, given these many attributes, further study involving the surface of EVs and its impact in all these areas is highly warranted, if not required.

Chapter 4: Extracellular vesicle surfaceome characterization for the early detection of pancreatic ductal adenocarcinoma

4A: Label-free characterization of extracellular vesicles *via* Raman spectroscopy

4B: Biomarker discovery *via* extracellular vesicle surface profiling

Portions of the content covered in this chapter are the subject of a published article in *Nanomedicine: Nanotechnology, Biology, and Medicine* by Carmicheal et al. [353]

Chapter 4: Extracellular vesicle surfaceome characterization for the early detection of pancreatic ductal adenocarcinoma

4A Label-free characterization of extracellular vesicles *via* Raman spectroscopy

4A.1 Synopsis

Pancreatic cancer is a highly lethal malignancy and early detection is key to improved survival. Lack of early diagnostic markers makes timely detection of pancreatic cancer a highly challenging endeavor. EVs have emerged as information-rich cancer-specific biomarkers. However, the characterization of tumor-specific EVs has been challenging. This study investigated the potential of extracellular vesicles (EVs) as circulating biomarkers for the detection of pancreatic cancer. Label-free analysis of EVs purified from normal and pancreatic cancer cell lines was performed using surface-enhanced Raman Spectroscopy (SERS) and principal component discriminant function analysis (PC-DFA), to identify tumor-specific spectral signatures. This method differentiated EVs originating from pancreatic cancer or normal pancreatic epithelial cell lines with 90% overall accuracy. The cell line trained PC-DFA algorithm was applied to SERS spectra of serum-purified EVs. SERS spectral signatures of circulating EVs, with PC-DFA analysis, exhibited up to 87% and 90% predictive accuracy for HC and EPC individual samples, respectively.

4A.2 Background and Rationale

Pancreatic cancer is characterized by insidious onset and relentless progression. According to the American Cancer Society (ACS), this disease is the third-leading cause of cancer death in both men and women, with an estimated 44,330 deaths in 2019 [2]. As per

ACS statistics, for all pancreatic cancer diagnoses, the five-year survival rate is 9% and falls to 3% when the diagnosis is made after metastasis has occurred [2].

The only curative option for this lethal malignancy is surgical resection. Surgical resection of the primary tumor, before it has given off metastases, confers the largest increase in overall patient survival [177]. Unfortunately, surgery is often not possible. At the time of initial discovery, primary tumors have often locally invaded to the point of being nonresectable and/or have produced metastases. The primary reason for this is the predominantly asymptomatic nature of early disease. Congruently, symptoms, when present, are mild and ambiguous such as nausea, malaise, and right upper quadrant pain [460]. Only in later stages do patients experience more dramatic clinical symptoms such as jaundice, cachexia, and migratory phlebitis. Thus, it is important to develop non-invasive and label-free tools for the early detection of pancreatic cancer. A liquid biopsy-based tumor biomarker for the screening and early diagnosis of pancreatic cancer is a promising area of research that could change the outcome of this lethal malignancy and improve patient survival.

Among a variety of serum-based cancer markers put forth as a possible means of pancreatic cancer detection [461], extracellular vesicles (EVs) are highly sought after and valuable targets. EV genesis begins as vesiculation of late endosomes. They are a product of the inward pinching of the endosomal membrane and subsequently are released to the extracellular space *via* direct fusion with the external cellular membrane [462]. Inherent in this mechanism of creation is that the intravesicular contents of EVs mirror the cell of origin. A variety of functions have been attributed to EVs including intercellular

communication [463], pathogen transmission [464], and immune response induction [465]. And recently, the functional capabilities of EVs have been extended to include a role in the progression and metastasis of various cancers [393], [466, 467]. Because of this, many investigators have begun to examine the potential of EVs as cancer markers [421, 468-470].

A portion of circulating RNA and DNA (extracellular nucleic acids found in serum) is located within these membrane-bound vesicles, and studies have focused on their genomic profiles [471, 472]. Further, these vesicles are easily accessible *via* non-invasive liquid biopsies involving saliva, blood, urine, breast milk, and ascitic fluid [473, 474]. Due to these myriad attributes, EV purification and characterization are imperative in the ongoing pursuit of liquid biopsy-based cancer biomarkers. New techniques are being investigated for better characterization and analysis of cancer-derived EVs to distinguish them from those of normal physiologic origin.

One technique that has unique attributes that make it a promising candidate for EV analysis is Raman spectroscopy [475, 476]. This is a vibrational technique that measures inelastically scattered photons after a sample interacts with incoming monochromatic laser light. These photons change their energy by exciting vibrational modes of molecules. The result is a Raman spectrum that corresponds with known vibrations of specific chemical groups. Such a spectrum can accurately identify the molecular composition of a sample.

Raman spectroscopy has several advantages making it ideal for EV characterization. Of great importance is that it is a label-free and a non-destructive technique. This holds a translational advantage in that immediate analysis of EVs is possible without undue risk for the patient nor long waiting periods. Raman scattering can

also provide a unique fingerprint signature based on the molecular composition of a sample. Hence, this method can differentiate EVs as a function of membrane lipid/protein content along with other various surface modifications. Finally, the Raman signal can be enhanced by several orders of magnitude by employing noble metal nanoparticles (Au/Ag) or rough nanostructures. As a result, only a small concentration of EVs in a sample is needed for detection and analysis.

The primary limitation of this method is weak Raman scattering efficiency (lower than 1 in 10^7 photons). In the presence of surface plasmon on metallic (usually Au or Ag) nanoparticles or nanostructured surfaces, Raman signals can be significantly enhanced. This phenomenon is called surface-enhanced Raman scattering and the technique is called surface-enhanced Raman spectroscopy (SERS) [477, 478]. This technology has been widely studied and applied for many years; however, it has only recently been employed to analyze EVs [436, 479]. When combined with multivariate analytical techniques that can condense a large amount of spectral information gathered, SERS can serve as a valuable tool to separate EV subpopulations and can potentially be utilized for the characterization of EVs for cancer diagnoses.

One method for the mathematical processing of SERS data is principal component discriminant function analysis (PC-DFA) [219]. With this technique, principal component analysis (PCA) is performed initially on SERS spectra. This reduces total variables considered and accentuates the amount of variation within a data set. In so doing, it allows for the determination of which combination of variables contributes the greatest to the overall variance measured between samples. PCA conducts a linear (orthogonal)

transformation on the SERS data, compressing a multitude of correlated variables (i.e. Raman shift peaks) into linearly uncorrelated variables known as principal components (PCs). PCs can then be used as input independent variables for discriminant function analysis (DFA). This applies yet another linear discriminant transformation to the SERS data that further differentiates EV subpopulations and provides classification efficacy *via* a cross-validation or external-validation method.

In this experiment, SERS and PC-DFA were utilized to characterize subpopulations of EVs from various cellular origins as well as patient sera. The SERS spectra of EVs derived from one healthy and two pancreatic cancer cell lines were successfully characterized and classified by a PC-DFA algorithm. Further, the PC-DFA algorithm trained from the three cell lines was applied to the SERS spectra of EVs isolated from pancreatic cancer patient serum samples to investigate the diagnostic efficacy of EV spectral signatures.

4A.3 Results

4.3.1 EVs of appropriate size can be isolated from cell line conditioned media

EVs were isolated from the cell culture supernatants of representative pancreatic cancer cell lines CD18/HPAF and MiaPaCa, as well as from the untransformed pancreatic epithelial cell line HPDE, by diffusion gradient ultracentrifugation as described in the methods section. Size distribution and concentration of the EV isolates were discerned through the use of nanoparticle tracking analysis (NTA) that revealed the CD18/HPAF cell line-derived EVs modal hydrodynamic size to be 132 nm, those from MiaPaCa to be 221 nm, and HPDE EVs to have a modal size of 261 nm (**Figure 4A.1**).

Figure 4A. 1 Nanoparticle tracking analysis of cell line EVs

EVs were purified *via* density gradient ultracentrifugation from cell line supernatant as described in the methods section. Nanoparticle tracking analysis (NTA) was conducted on EVs isolated from two pancreatic cancer cell lines, CD18/HPAF and MiaPaCa, as well as one normal human immortalized epithelial cell line, HPDE. The results showed size distributions within the expected range for heterogeneous EV isolation ranging from 50-500 nm in diameter. Importantly, the quantities of each EV population were sufficient to be used in subsequent experiments.

Figure 4A.1

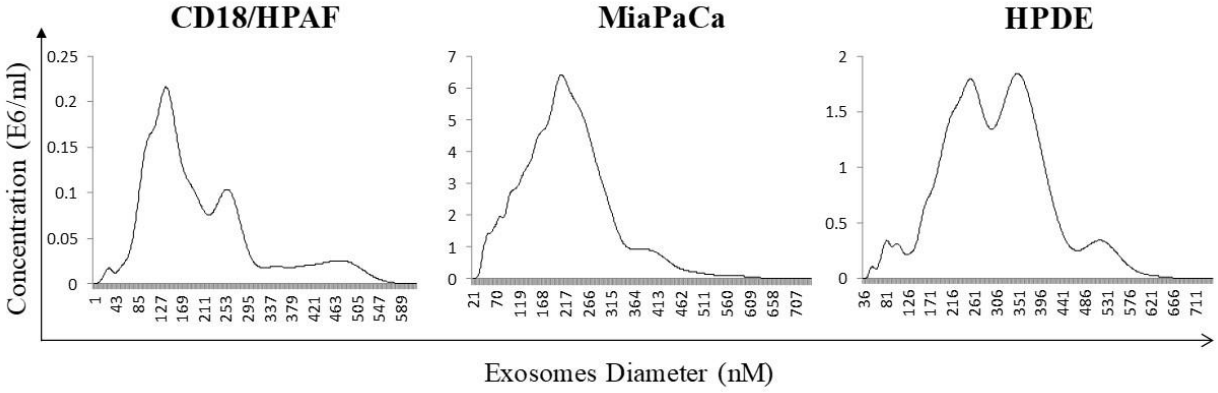
CD18/HPAF
MiaPaCa
HPDE
Concentration (E6/ml)
0.25
0.2
0.15
0.1
0.05
0
1 43 85 127 169 211 253 295 337 379 421 463 505 547 589
7
6
5
4
3
2
1
0
21 70 119 168 217 266 315 364 413 462 511 560 609 658 707
2
1.5
1
0.5
0
36 81 126 171 216 261 306 351 396 441 486 531 576 621 666 711
Exosomes Diameter (nM)

4.3.2 Isolated EVs maintain morphological characteristics

Morphology and size of the extracellular vesicles were visualized with transmission electron microscopy (TEM) (**Figure 4A.2**). Imaged EV isolated from all three cell line supernatants contained particles with diameters ranging from 40 nm to 200 nm as can be seen by the individual vesicle measurements on the TEM images. The mounting, fixing, and staining process required for TEM visualization of EVs results in dehydration creating a concavity in the center of the vesicles where vanadium negative stain can pool. This pooling increases the electron opacity at that location thereby conferring the characteristic "saucer shape" morphology [480]. Fewer EVs were noted in the HPDE isolates as compared to those isolated from the two cancer cell lines. Of note, the larger EV sizes measured *via* NTA can be attributed to the combination of possible vesicular agglomeration in NTA making them measured larger and/or the preparation of the samples required for TEM with the aforementioned dehydration and resultant shrinkage making them look smaller than their true hydrodynamic size.

4.3.3 EV consensus marker validation and substrate distribution assessment

Further characterization of the EVs was conducted *via* immunoblotting in order to validate the presence of the accepted EV markers as well as their increased concentration compared to the respective EV whole cell lysate (CD18/HPAF) (**Figure 4A.3A**). 10 µg of protein from each of the six fractions formed *via* the density gradient was utilized. The accepted tetraspanin protein markers, CD9 and CD63, along with the adhesion molecule EpCAM [420], were used as proof of the presence and increased concentration of EVs by the ultracentrifugation process. As seen in the figure, all three of these markers were prominent in sucrose layers three and four, denoting high EV concentration within these fractions.

Figure 4A. 2 TEM images of EVs isolated from conditioned media

TEM images of EVs isolated from CD18/HPAF, MiaPaCa, and HPDE, show spherical consistency and size homogeneity of each population. Notably, morphology is unaltered with the exception of the characteristic “cup” shape due to dehydration from the TEM mounting/staining procedure. These images prove the ability to efficiently isolate EVs from cell-conditioned media *via* density gradient ultracentrifugation.

Figure 4A.2

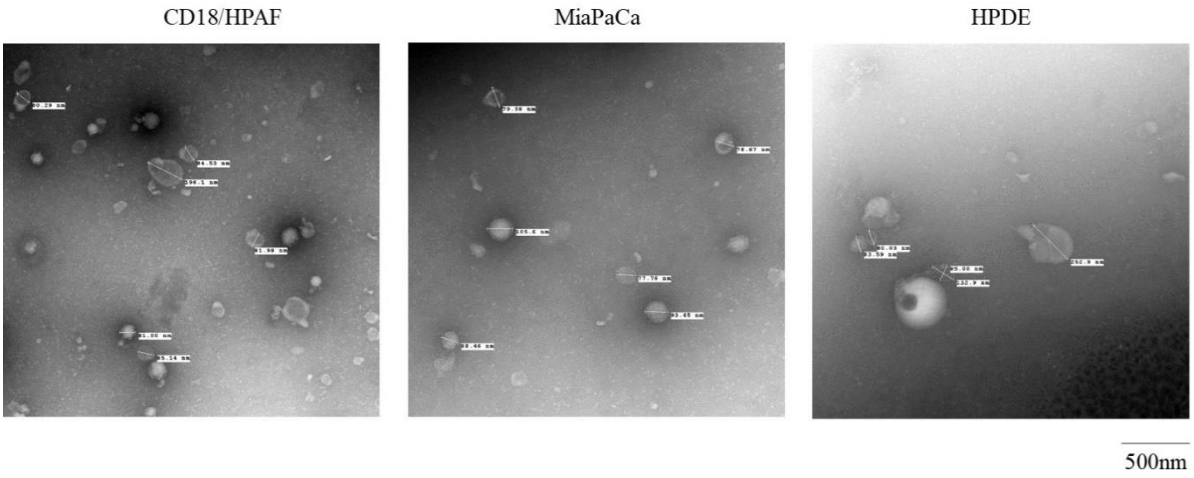

Figure 4A. 3 EV surface marker validation and substrate distribution verification

A. EV samples residing in the various layers/fractions of the sucrose density gradient were tested for the presence of known EV protein markers CD9, CD63, and EpCAM along with pancreatic cancer-associated molecule glypican-1 *via* western blot. The results showed the consensus markers along with glypican-1 settled in sucrose layers 3 and 4 (as predicted by comparable density with EVs, 1.15 – 1.19 g/ml). Thus, subsequent experiments were conducted on one EV population produced by the combination of EVs collected in fractions 3 and 4. **B.** Atomic force microscopy (AFM) of EVs isolated from CD18/HPAF verified that the ionic interactions between the EV surface and the gold substrate allowed for strong and efficient binding of EVs to the substrate surface which is required for eventual SERS analysis. Further, AFM provided verification that the EVs were adequately and evenly dispersed over the surface, which is another prerequisite for accurate SERS measurement.

Figure 4A.3

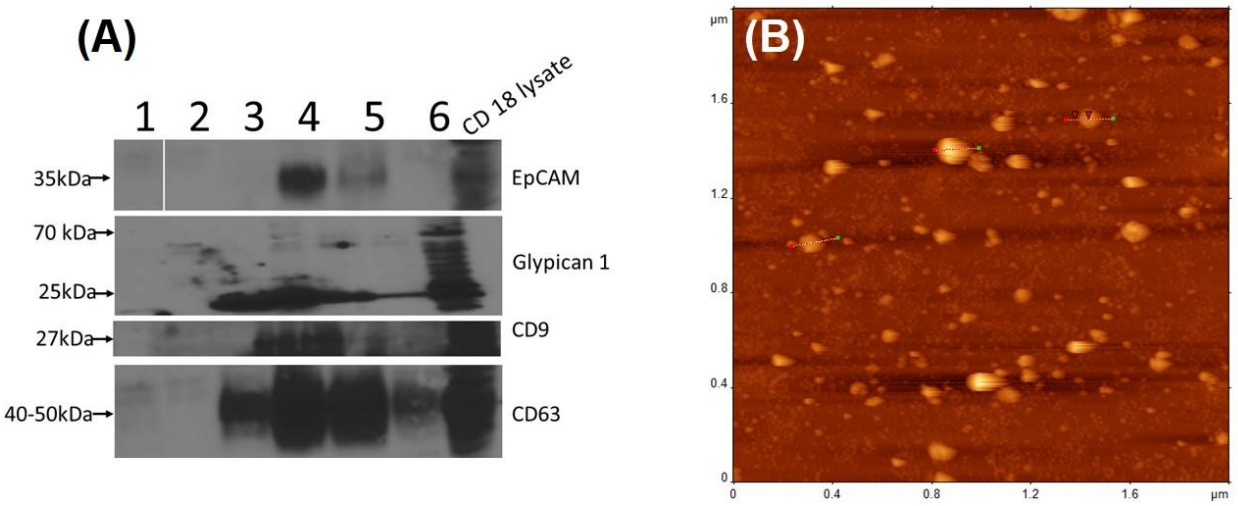
(A)
1 2 3 4 5 6 CD 18 lysate
35kDa
EpCAM
70 kDa
25kDa
Glypican 1
27kDa
CD9
40-50kDa
CD63
(B)
µm
1.6
1.2
0.8
0.4
0
0.4
0.8
1.2
1.6
µm

Thus, fractions three and four were merged and subsequently utilized in the SERS experiments. Interestingly, EVs from both CD18/HPAF as well as MiaPACa (data not shown) were positive for Glypican 1, a marker previously was shown to be 100% specific to pancreatic cancer [421], however, this specificity is currently a matter of some debate in the field.

Finally, the characterization of purified EVs was conducted *via* atomic force microscopy (**Figure 4A.3B**). The ionic interactions between the surface of the EVs and the gold substrate provide a strong enough electro attractive force to bind EVs to the surface of the gold. AFM confirmed that the EVs bind to the gold surface which is required for the SERS process. Further, AFM shows that the EVs adequately and evenly disperse over the gold surface giving the necessary spatial distribution required for accurate SERS measurement.

4.3.4 Surface-enhanced Raman spectroscopy (SERS) spectral shifts from EVs are predicated on the cell type of origin.

For characterizing SERS signatures of EVs, Raman shifts in the range of 719-1800 cm^{-1} were measured from 33 samples of EVs derived from CD18/HPAF, 31 samples from MiaPaCa, 35 samples from HPDE, and 22 from the control (AuNPs only) were obtained with the Raman shift range of 719-1800 cm^{-1}. Standard deviations associated with the means for each of the samples and control are shown in **Figure 4A.4A**. The individual SERS spectra were averaged for each EV population, as well as for the control (**Figure 4A.4B**). Interestingly, variations in peaks (amplitude and Raman shift value) were noted both between the control and EV populations and also between the EV population

Figure 4A. 4 SERS spectra of cell line EVs

For this experiment, 33 sample spectra of CD18/HPAF, 31 from MiaPaCa, 35 from HPDE, and 22 from the control were obtained and pre-processed. **A.** Individual SERS spectra collected from CD18/HPAF, MiaPaCa, and HPDE EVs in addition to gold nanoparticles (GN) only. **B.** The averages for all the technical replicate SERS spectra. The GN spectra serve as a control to elucidate what spectral features are associated with particles alone, and subsequently factored out of any variance observed in the spectra collected from the various EV populations. Differences in peak presence and amplitude are observed between all the EV groups. Amplitude does fluctuate over repeated measurements, as noted by the red dotted line representing the standard deviation but importantly the pattern does not change.

Figure 4A.4

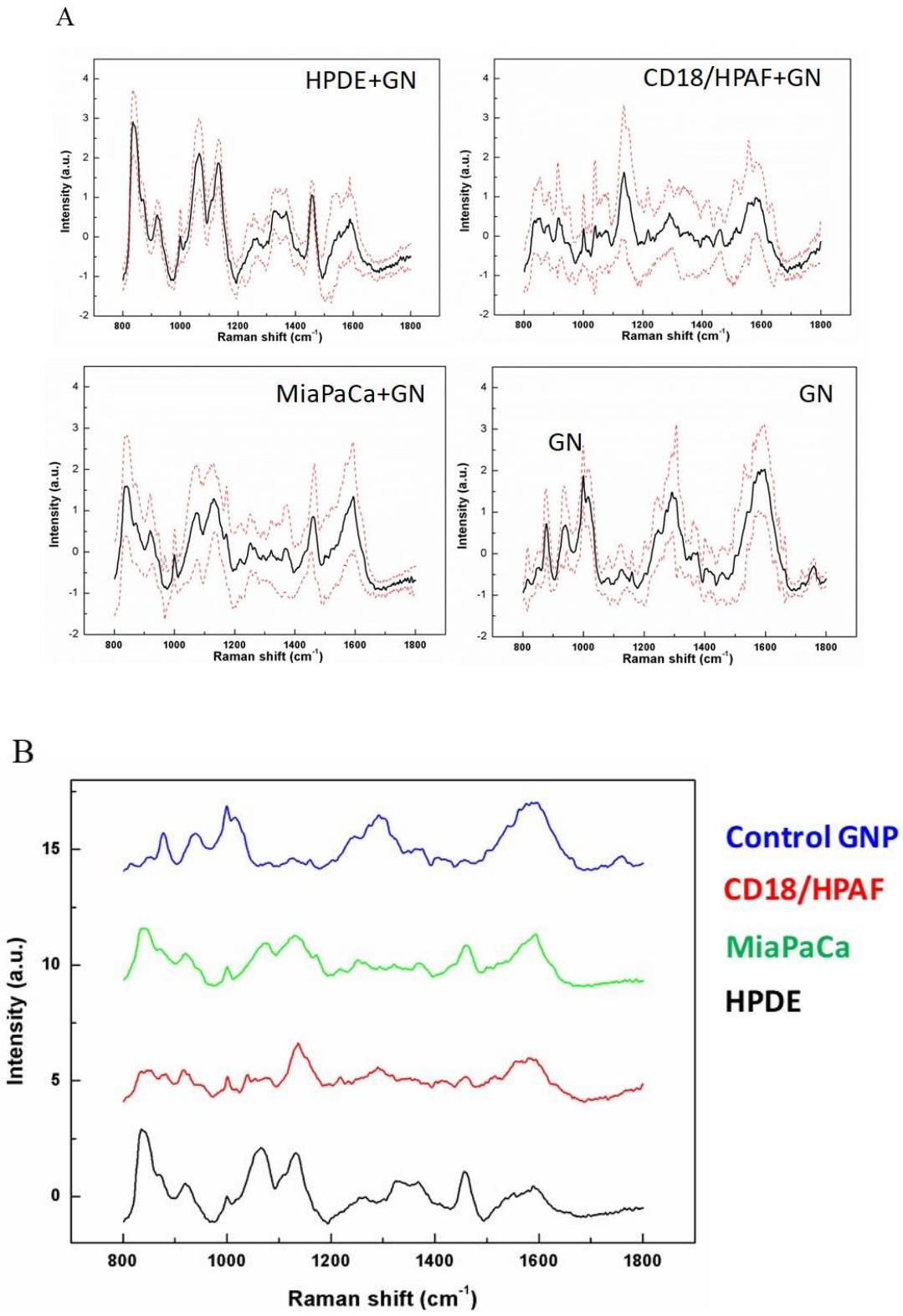
A
HPDE+GN
CD18/HPAF+GN
MiaPaCa+GN
GN
GN
Intensity (a.u.)
Raman shift (cm-1)
B
Control GNP
CD18/HPAF
MiaPaCa
HPDE
Intensity (a.u.)
Raman shift (cm-1)

samples themselves thus providing the foundation for differential characterization of the particles.

In the 719-1800 cm^{-1} region, spectra exhibited peaks characteristic of vibrations corresponding to lipids and proteins which are the major contributors of EV surface composition. For example, vibrations due to the C-C skeletal stretching appear as peaks at 1051 cm^{-1} and 1124 cm^{-1}. Another peak that can be clearly distinguished lies at 1450 cm^{-1} that is due to CH_2 bending vibration and is very typical of lipids [481]. The peaks in the 1300-1400 cm^{-1} region can be attributed to CH_2 twisting vibrations. An intense peak at 830 cm^{-1} is also observed corresponding to C-O-O vibration typical of phospholipids [475].

4.3.5 EV SERS spectra are highly reproducible

High reproducibility and consistency of SERS spectra were observed (**Figure 4A.5**) providing validity to each individual SERS peak as specific to that sample EV population and not merely arising from background noise. Although most repeated peaks of each group were identified, not every spectrum exhibited all of these specific peaks and not every specific peak was surface-enhanced. The possible reason for this variable peak enhancement could be the randomness in the interaction and subsequent bonding between gold nanoparticles and EVs. To address this issue, adequate spectral numbers and whole fingerprint spectral data were acquired for multivariate analysis. Of note, in addition to common spectral features across EV populations, distinct differences in peaks' profiles and intensities were observed in SERS. This observation highlights the ability of Raman spectroscopy to distinguish EVs by their lipid composition. To increase the SERS output, we have used gold nanoparticles as well as gold substrate as an improvement over the

Figure 4A. 5 Repeated SERS spectra collections from cell line EVs and gold nanoparticles

Repeated collections of SERS spectra are plotted for each experimental condition. Importantly, the spectral shifts arising from different EV populations are highly reproducible. Overlapping peaks are appreciated in each sample by a thickening of the black patternation, denoting spectral continuity and specific peaks unique to each population, which is required for eventual use as a means of differentiation.

Figure 4A.5

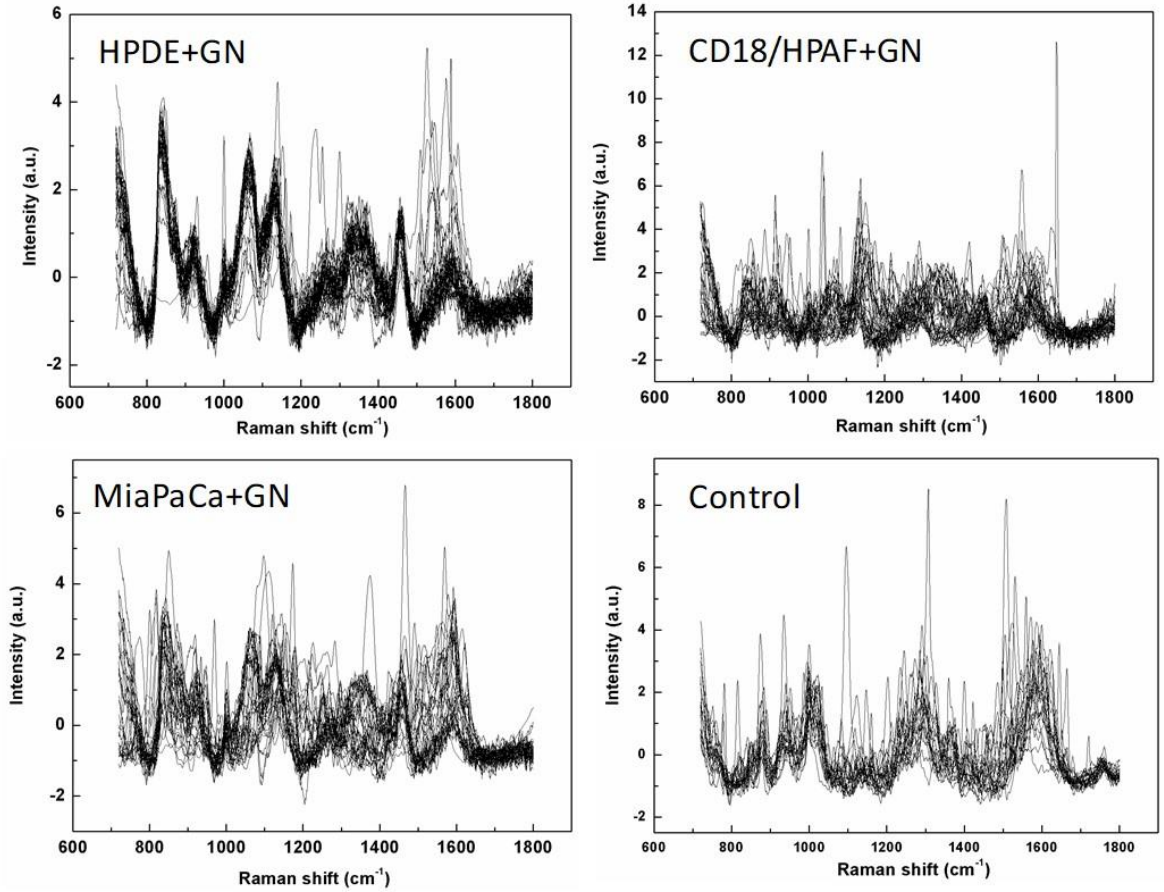
HPDE+GN
CD18/HPAF+GN
MiaPaCa+GN
Control
Intensity (a.u.)
Raman shift (cm-1)

previous design [420]. To identify differential peaks associated with pancreatic cancer, principal component, and discriminant function analyses were conducted on the collected SERS data.

4.3.6 Principal Component - Discriminant Function Analyses can discriminate between PDAC and normal cell line EV SERS spectra with high accuracy

After pre-processing of the raw SERS spectra, PCA was used to reduce the number of variables considered from 1004 variables to 20 PCs, which counted for 88.2% of the total variance. Principal Component #1(PC #1) contained the most important data with 35.4% of the total variance. The next two PC #2 and PC #3 represented 14.4% and 6.6% of the total variance, respectively. A three dimensional (3D) PCA plot for the first three PCs (PC #1, PC #2, and PC #3) is shown in **Figure 4A.6**. Although these three PCs contributed 56.4% of the total variance, it is still not enough for high-efficiency classification. Twenty PCs were chosen for the trade-off between low data dimensionality and high variance observed in samples.

The PC-DFA plots for the three discriminant function classifiers (DA1, DA2, and DA3) of the total 121 spectra from four groups (HPDE, CD18/HPAF, MiaPaCa, and Control) are shown in **Figure 4A.7**. The EV groups and control group are clearly separated by DA1 and DA2 (the two upper plots in **Fig. 4A.7**) due to the absence of EV peaks within the control group, leading to a distinct spectral pattern. The EV subpopulations formed discrete clusters and separated from each other by all the classifiers, as shown in the 3-dimensional PC-DFA plot (**lower right plot in Fig. 4A.7**). The classification accuracy was calculated *via* the cross-validation method and is shown in **Table 4A.1**. As shown, only one spectrum of healthy cell-derived EVs was misclassified as having a cancer cell origin.

Figure 4A. 6 Principal component analysis of cell line SERS spectra

Principle component analysis (PCA) was first conducted on raw SERS spectra from both normal human pancreatic ductal epithelial cell line (HPDE) and pancreatic cancer cell lines (CD18/HPAF, MiaPaCA) to reduce the dimensionality of the data from 1004 individual wavenumber variables (from 719 cm^{-1} to 1800 cm^{-1}) to 20 PCs. The 3D plot shows the SERS measurements segregated as a function of the first three PCs which account for 56% of the total spectral variance. Spectra collected from HPDE and GNs are beginning to efficiently cluster yet their remains widespread dissemination of cancer EV spectra dispersed throughout the area. Notably, this suggests a degree of similarity between the EVs isolated from cancer cell lines as compared to those from HPDE. To increase the population clustering the PCs were used as the input independent variables for DFA.

Figure 4A.6

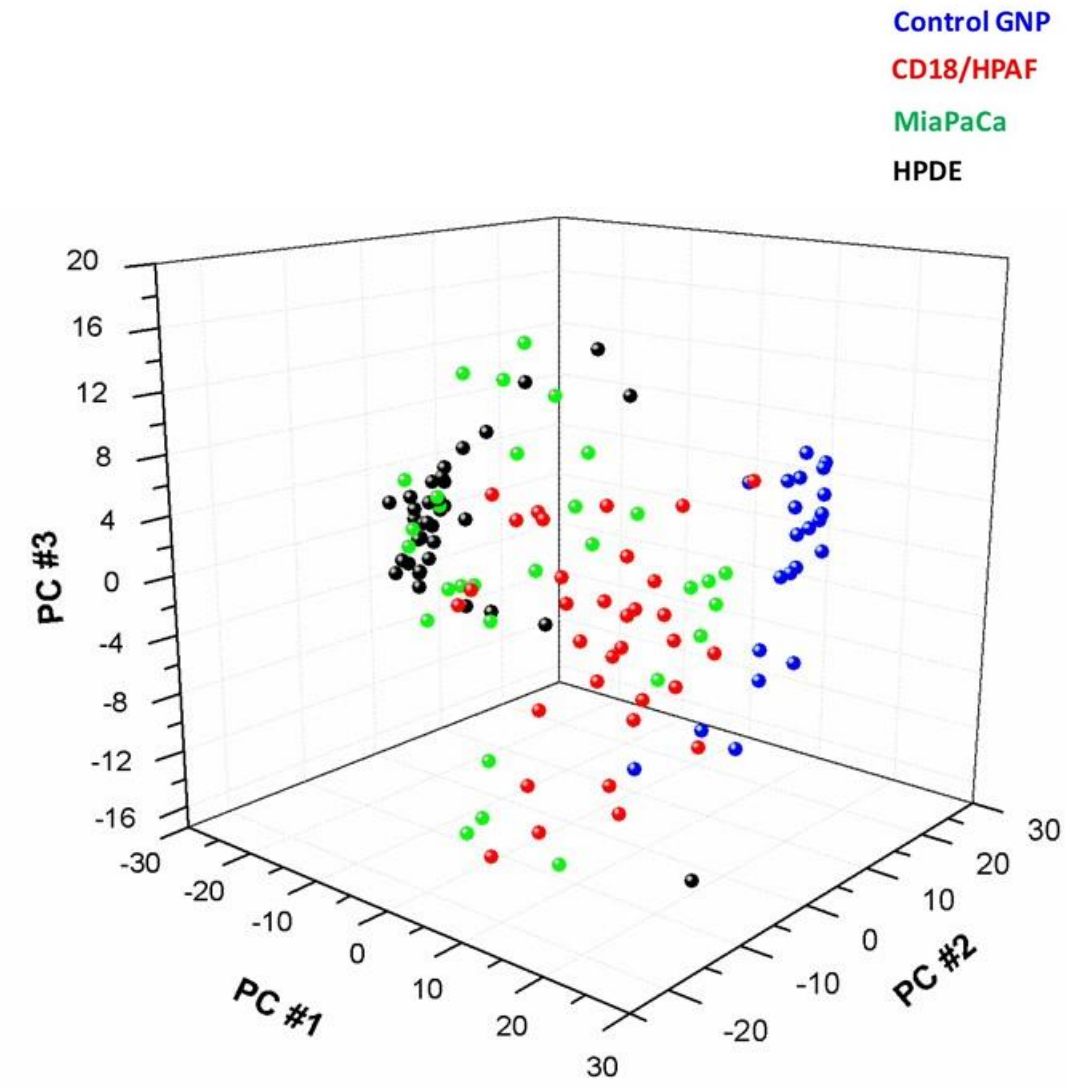
Control GNP
CD18/HPAF
MiaPaCa
HPDE
PC #3
PC #1
PC #2
20
16
12
8
4
0
-4
-8
-12
-16
-30
-20
-10
0
10
20
30
30
20
10
0
-10
-20

Figure 4A. 7 Discriminant function analysis of SERS generated principal components

The PCs were used as the input independent variables for the DFA. **A.** 2D DFA plot of DA1 vs. DA2. **B.** 2D DFA plot of DA1 vs. DA3. **C.** 2D PC-DFA plot of DA2 vs. DA3. **D.** 3D DFA plot of DA1 vs. DA2 vs. DA3. Especially in the last 3D plot it can be observed that all four EV populations have clustered into distinct areas predicated cell of origin. These graphical representations visually display the capability of the PC-DFA algorithm to efficiently separate differing EVsubpopulations based on SERS spectra.

Figure 4A.7

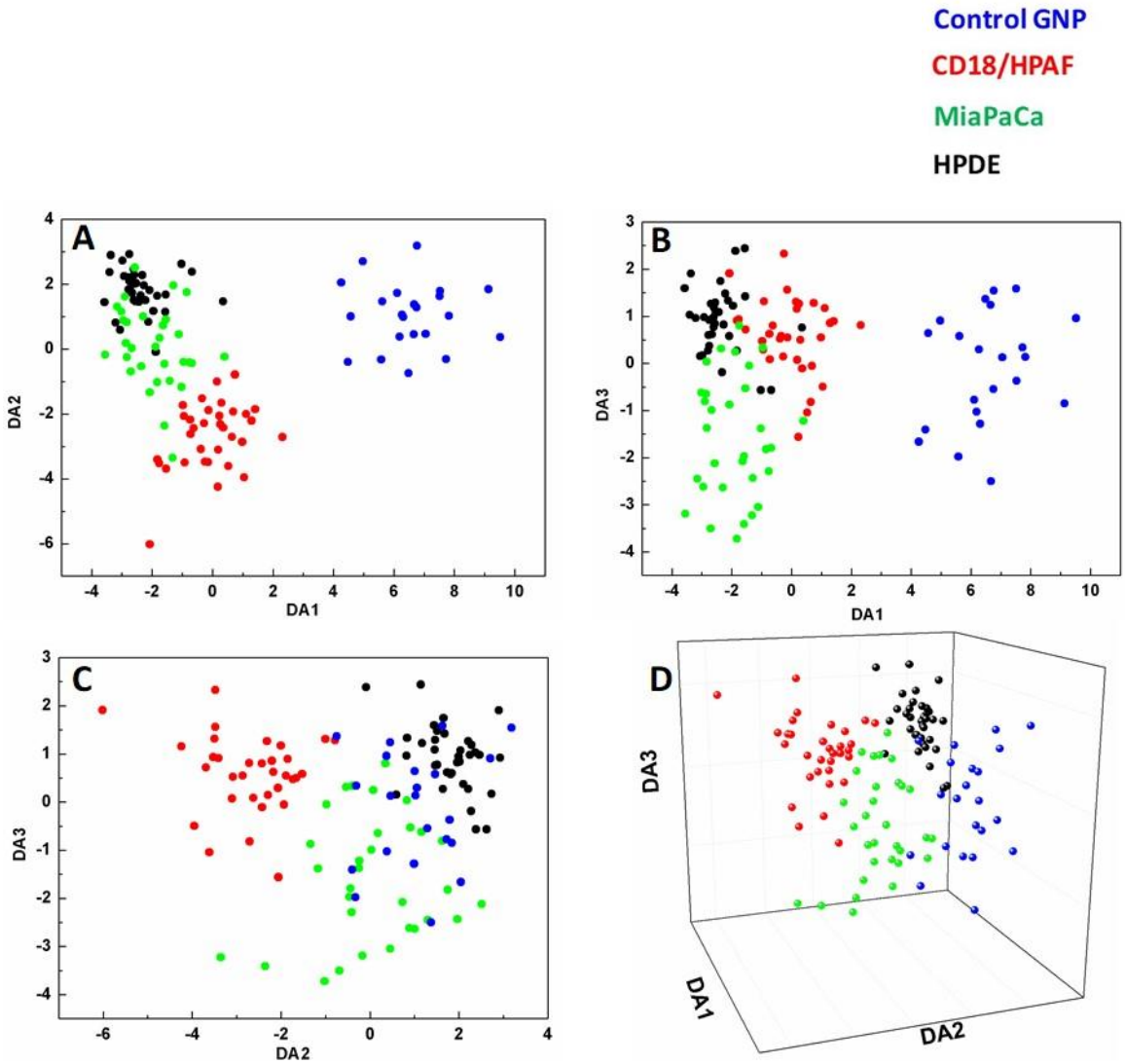
Control GNP
CD18/HPAF
MiaPaCa
HPDE
A
DA2
DA1
B
DA3
DA1
C
DA3
DA2
D
DA3
DA1
DA2

Table 4A. 1 Prediction of cell line cancer status *via* SERS PC-DFA

The table depicts the number of EV sample spectra taken from each cell population (in the two left columns) as well as the population with which each cell was clustered *via* PC-DFA. The number of spectra out of the total that was correctly classified as the EV population of origin is joined with the percent correct in parenthesis in each of the subsequent columns. The accuracy associated with classifying SERS spectra as arising from CD18/HPAF, MiaPaCa, HPDE, and GN control was 97%, 93%, 71%, and 100%, respectively.

Table 4A.1

	No. of spectra	Classified as CD18	Classified as MiaPaCa	Classifieds HDPE	Classified as Control
CD18/HPAF	35	34 (97%)	1	0	0
MiaPaCa	33	0	31 (93%)	2	0
HPDE	31	6	3	22 (71%)	0
Control (AuNPs only)	22	0	0	0	22 (100%)

Congruently, six spectra of cancer cell-derived EVs were misclassified as having a healthy cellular origin, with none of these being CD18/HPAF spectra (MiaPaCa spectra were classified as healthy six times, and as CD18/HPAF spectra 3 times). The overall accuracy of PC-DFA classification was 90.0% for the three cell lines and the control. Since CD18/HPAF and MiaPaCa are cancer cell lines and HDPE is a healthy cell line, the sensitivity and specificity are calculated to be 90.6% and 97.1% respectively, regardless of the control.

4.3.7 EVs can be isolated from patient sera and are elevated in cancer patient samples compared to benign controls

To investigate the potential diagnostic efficacy, EVs were isolated as described in the experimental section from the sera of ten healthy subjects and ten early-stage pancreatic cancer patients. The quantity of EV protein isolated from equivalent quantities of serum from each of the three groups can be seen in **Figure 4A.8**. Corroborating previous work, the quantity of EVs is significantly higher in early and late-stage PDAC patients as compared to healthy controls. The presence, size, and number of EVs in these samples were verified with NTA (**Fig. 4A.9A**). Though the size and concentration were less than what was measured for cell line-derived EVs, their presence was confirmed by direct visualization by TEM, where the vesicles exhibited the characteristic "cup shape" morphology (**Figure 4A.9B**). Adhesion to the gold substrate surface and adequate SERS address distribution was verified by AFM (**Figure 4A.9C**).

4.3.8 The cell line trained PC-DFA algorithm can be applied to SERS spectra of serum EVs to predict patient cancer status

Figure 4A. 8 Serum isolated EV quantification *via* protein concentration

The relative quantity of EVs present in 500 µl of human serum isolated *via* ultracentrifugation was estimated by protein concentration. While the median EV protein concentration of healthy individuals was below 0.2 mg/ml, and an equivalent volume of early-stage (I-IIB) and late-stage (III-IV) PDAC patient serum harbored EV protein concentrations above 0.7 and 0.6, respectively. This 3-4 fold increase in the setting of cancer is in line with previous findings and is important for the justification of utilizing seromic EVs as cancer-specific biomarkers.

Figure 4A.8

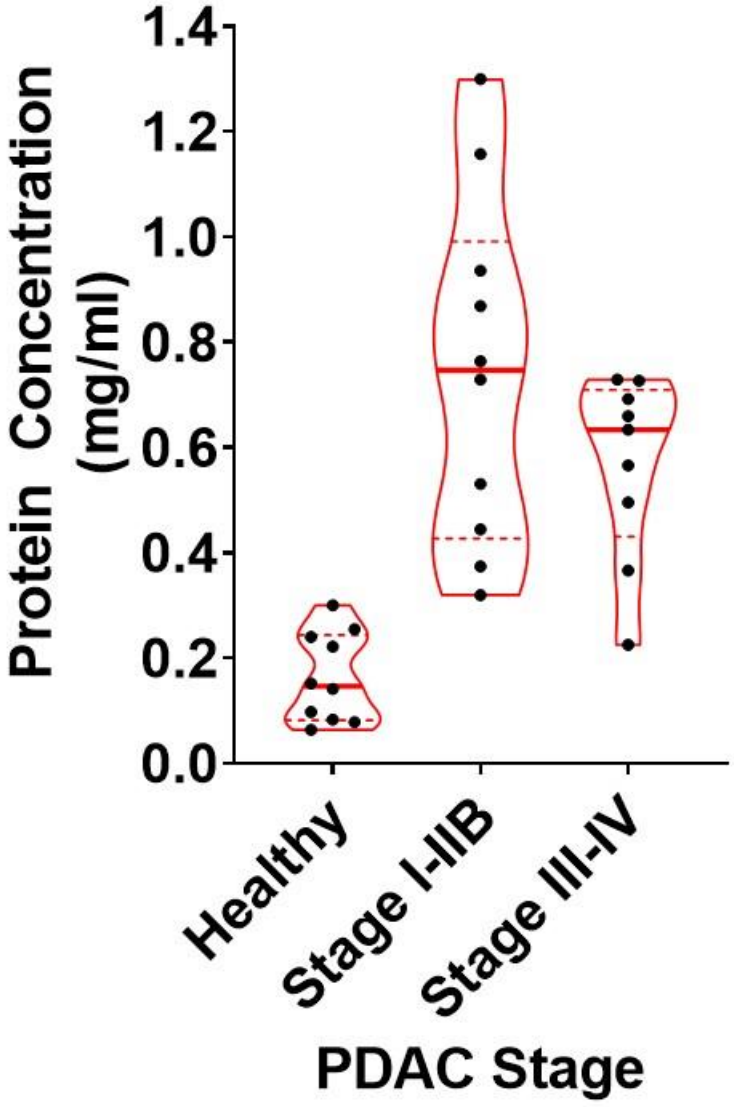
Protein Concentration (mg/ml)
1.4
1.2
1.0
0.8
0.6
0.4
0.2
0.0
Healthy
Stage I-IIB
Stage III-IV
PDAC Stage

Figure 4A. 9 Morphological validation of EVs isolated from patient serum

A. NTA showing size distribution and concentration of EVs purified from patient sera. The hydrodynamic size ranged from 50-200 nm in diameter, which is synonymous with those isolated from cell line supernatant. **B.** TEM showing spherical individual vesicle morphology purified from patient sera displaying the capability of ultracentrifugation to isolate EVs from serum without damage. **C.** AFM of the substrate surface (gold) displaying presence and adequate coverage of EVs for SERS.

Figure 4A.9

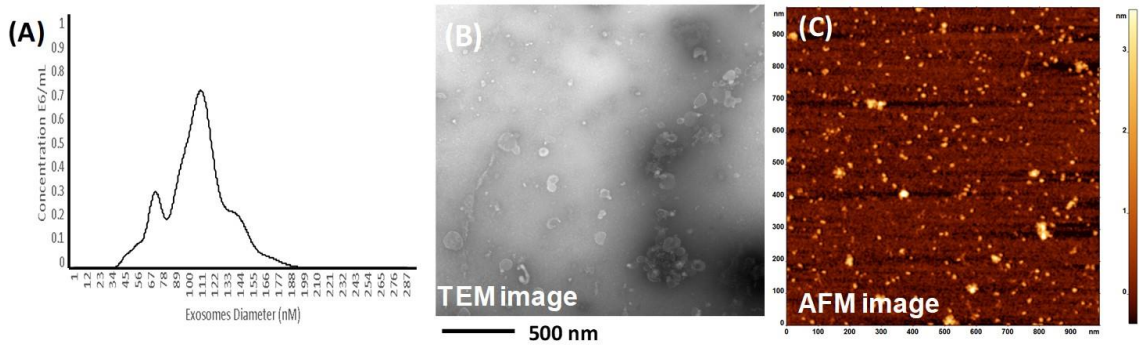
(A)
Concentration E6/mL
Exosomes Diameter (nM)
(B)
TEM image
500 nm
(C)
AFM image

For each of the twenty EV samples purified from sera, 10-20 SERS measurements were collected for external validation. The PC-DFA algorithm, trained from the previous SERS of cell line EVs, was applied to the SERS measurements of the patient sera EV samples. With the application of this algorithm, the SERS spectra measured from EVs derived from serum exhibited a range of predictive accuracies. HC samples ranged from 20-87% characterization efficiency while EPC sample characterization efficiency was from 30%-90% (**Table 4A.2**).

4.4 Discussion

Label-free technologies offer many advantages that are amenable to the characterization and utilization of liquid biopsies as diagnostic markers. Conventional methods such as immunohistochemistry, flow cytometry, PCR, and immunoblotting use known targets of interest which require predetermined markers or probes. This narrow focus inherently limits the possible information gathered from a given sample and precludes the possibility of discovery. Conversely, label-free modalities circumvent the requirement of predetermination, thereby offering a universal metric by which all species are measured and compared. Further, novel species characteristics can be elucidated that can be quantified and used as a biomarker metric.

Many investigators have recognized the value in label-free techniques and as such, a variety of methods have recently been evaluated. Surface plasmon resonance is used in the quantification and detection of multiple serum-based biomarkers by refractive index changes predicated on binding interactions [482]. Surface proteomics is a technique that involves "shaving" proteins off the surface of EVs [322]. Mass Spectrometry is then utilized to discern the identity of the shaved proteins that may subsequently be used as cancer-

Table 4A. 2 Application of cell line PC-DFA algorithm on SERS of EVs isolated from patient serum

The left part of the table shows the PC-DFA predicted cancer status of EVs isolated from the SERS of ten different healthy individual serum controls (HC) while the right part of the table shows the PC-DFA predicted cancer status from the SERS of EVs isolated from the serum of ten different early pancreatic cancer patients (EPC). Note: The number in parentheses in the population type column is the total number of SERS measurements taken from serum samples of each healthy individual or pancreatic cancer patient. The number in parentheses in the predicted columns is the number of SERS measurements with that predicted characterization. Individual assay efficiency ranged from 20%-87% and 30% to 90% for HC and EPC samples, respectively.

Table 4A.2

HC	Predicted as healthy	Predicted as cancer	EPC	Predicted as healthy	Predicted as cancer
HC 1 (15)	13	2	EPC 1 (12)	7	6
HC 2 (15)	4	11	EPC 2 (13)	4	9
HC 3 (15)	11	4	EPC 3 (15)	4	11
HC 4 (15)	12	3	EPC 4 (15)	3	12
Prediction accuracy is 66.7% and 67.3% for healthy patent serum controls (HC) and early pancreatic cancer patient (EPC), respectively.					

specific biomarkers. Also, species-specific impedance biosensors have been utilized in the pursuit of biomarkers [483]. This study utilizes the label-free technique of SERS which is uniquely suited for EV characterization due to its high sensitivity, molecular signature specificity, and ability to be amplified. This method can take advantage of the differing, yet unknown, characteristics of EVs and separate EVs predicated on spectral differences.

Though the specific molecules that contribute to the variance in SERS spectra are unknown at this time, the Raman spectral shifts offer an insight into possible species. Lipids and proteins are the primary molecules that comprise the EV surface. This surface composition is highly variable between cancer and normal EVs and is the reason behind SERS spectral variance. For example, peaks associated with C-C skeletal stretching and CH_2 bending are characteristic for the presence of lipids and a peak associated with C-O-O vibrations alluded to the presence of phospholipids. Changes in the relative amounts of these molecular species, or even species ratios, can confer a measurable and useful amount of spectral variance.

Previously, Park et al. conducted an elegant study that investigated the PCA of SERS and the ability to differentiate EVs originating from healthy cells vs. those originating from lung cancer cells [436]. Their work proved the utility of PCA of SERS to accurately characterize EVs originating from healthy or lung cancer cells. However, the study was unable to translate the findings from pure cell line EV populations to those purified from patient sera. Another study conducted by Stremersch et al. combined partial least squares discriminant analysis to SERS of EVs [354]. They showed that pure populations of EVs purified from melanoma or red blood cells could be accurately separated. Just as the previous group, their method was not applied to EVs from patient sera. The study put

forth in this paper is a proof-of-concept experiment, proving the power and potential for PC-DFA of EV SERS to serve as a means to diagnose pancreatic cancer at an early stage, when curative resection is still possible, that heretofore had not been successful.

Lower prediction efficacies were observed when the PC-DFA was applied to SERS of patient sera. This is a direct result of the diverse origin of EVs in patient serum. In addition, the sera from cancer patients, especially from those with early-stage disease, inherently have a larger portion of EVs arising from normal epithelium rather than tumor cells. This increases the complexity of the SERS spectra and therefore the difficulty of algorithmic determination increases significantly. Even so, this study opens the door to a novel cancer detection method. Congruently, the trend of multiple testing outcomes (i.e. characterization as HC or EPC) from a single patient could serve as a means of allying or increasing suspicion of cancer. The use of this technique in high-risk patients and/or those with high-risk features could give insight into the disease gestalt.

4.5 Conclusions and future directions

Surface-enhanced Raman spectroscopy, in conjunction with PC-DFA methodology, was applied for the classification of EVs derived from a healthy cell line and two pancreatic cancer cell lines *via* a cross-validation method in the present study. The sensitivity and specificity were 90.6% and 97.1%, respectively. Moreover, a proof-of-concept experiment was conducted to investigate the diagnostic efficacy of the SERS spectra of EVs collected from pancreatic cancer patient serum samples when the PC-DFA algorithm was applied. The present work demonstrates that EVs can be analyzed by SERS and combined with PC-DFA as a liquid biopsy-based detection of pancreatic cancer.

The practical use of this technology and lack of specificity can be ameliorated *via* multiple means and are possible future directions for the continuation of this research. The first will be to conduct and intragroup comparison between well-characterized and poorly characterized samples, as determined by the current PC-DFA algorithm. This will elucidate peaks or areas within the spectra that may be diminishing assay efficacy. Second, we will establish an EV SERS spectral library collected from a large sample set of healthy individuals and pancreatic cancer patients of various stages and use those for the basis of the PC-DFA predictive algorithm. The multiple spectra would then be utilized to enhance the accuracy and power of the data and further solidify what Raman shift peaks contribute the greatest to the overall variance between healthy and tumor purified EVs. Additionally, larger serum sample volumes may be used to increase the total amount of pancreatic cancer originating EVs. Further investigation is planned to discover if different metrics such as proteomics, metabolomics and RNA sequencing of EV contents, in combination with SERS, would improve on the aforementioned sensitivity and specificity. Isolation of EVs *via* ultracentrifugation is expensive and time-consuming. Alternative methods of purification include EV specific ELISA and magnetic bead isolation, to purify directly from serum. Implementing these methods would allow for more facile isolation. Finally, we plan to investigate other various biological sources of EVs, such as urine and ascites, and apply PC-DFA. This could uncover novel EV sources for noninvasive liquid-based biopsies.

4B: Biomarker discovery *via* extracellular vesicle surface profiling

4B.1 Synopsis

The experiments presented herein (Chapter 4B of this thesis) began with EV surface proteomic profiling using a novel "surface shaving" technique *via* proteinase-A trypsin digestion, size exclusion chromatography, and liquid chromatography-tandem mass spectrometry (LC-MS/MS), which allowed for the specific analysis of proteins exposed on the external membrane compartment. Clinical significance and reduction of potential biomarkers from the LC-MS/MS detected proteins were determined by bioinformatics assessment of The Cancer Genome Atlas (TCGA) and GSE28375 microarray datasets. Protein target presence was validated in cell lines and patient samples *via* western blot and their surface localization with immunogold TEM. The first target protein assessed *via* ELISA analysis, EPHA2, showed elevated expression in complete cancer patient serum as compared to benign controls. Further, EV specific EPHA2 expression was capable of predicting cancer status in 25% (5/20) of the patient samples with 100% specificity.

4B.2 Background and rationale

Experiments in Chapter 4A of this thesis utilized EVs from normal pancreatic ductal epithelial cells (HPDE) and two pancreatic cancer cell lines (MiaPaCa, CD18/HPAF) representing the wide mutational spectrum of PDAC were isolated *via* density gradient ultracentrifugation. Surface-enhanced Raman spectroscopy (SERS), in conjunction with principle component-discriminant function analysis (PC-DFA), was used to classify EVs originating from cells *in vitro* high overall accuracy. The proof-of-principal application of the cell line-derived PC-DFA algorithm to SERS spectra collected from EVs

isolated from patient serum samples proved the possibility of using EV surface differences as a biomarker for the early detection of PDAC.

However, the limited overall accuracy of the label-free SERS PC-DFA algorithm requires further investigation into the surface of EVs to discover specific molecular species that may be used as biomarkers. Many studies have illustrated the potential of discovering cancer-specific markers in EVs including proteins, miRNA, lncRNA, and genomic DNA [484]. However, the majority of these studies investigate the entirety of the EV contents without specific consideration of the EV surface. Studies that have investigated the EV surface per se are limited in number yet have provided valuable prospects for biomarker discovery. Much like the studies assessing EVs in their entirety, surface profiling has elucidated myriad cancer-associated molecular species including proteins, DNA, glycans, and lipids, many of which have been comprehensively discussed in Chapter 3 of this thesis.

Surface characterization of EVs has many benefits that make it an ideal method for the discovery of clinically useful biomarkers. Molecular species positioned on the exposed surface of the EV membrane are capable of being targeted by immunoaffinity techniques [485, 486] thereby providing a means of rapid isolation and characterization directly from patient samples. The presence of specific surface proteins can also provide clues into the organ tropism of particular cancer as in the case of integrin αvβ5 association with liver metastasis in the setting of PDAC [393]. Congruently, therapeutic efficacy can be surmised from the EV surfaceome as when the response to PD-L1 blockade predicted *via* the quantity of EV surface PD-L1 [487]. These attributes are in addition to the general EV advantages previously described including presence in all biofluids, the capability of use

as a non-invasive liquid-biopsy, present at higher concentrations in cancer patients, and contents mirroring the cell of origin.

Given the promising yet limited results of our SERS PC-DFA study, the dearth of surface-specific characterization studies, and the potential of EV surface biomarkers, we sought to profile the surface of PDAC cell line EVs in an effort to uncover a novel clinically useful biomarker.

4B.3 Results

4B.3.1 LC-MS/MS EV surface proteomic profiling identifies proteins of interest pool

EVs from four PDAC cell lines (CD18/HPAF, MiaPaCa, T3M4, and Capan1) and HPDE were isolated *via* density gradient ultracentrifugation and underwent surface proteomic profiling as described in the methods section. Notably, Capan1 EV proteins were withdrawn from subsequent analyses because of the presence of GM-130 protein, which is a Golgi marker that is not present in EVs and thus, is indicative of cellular contamination. Interestingly, gene ontology (GO) pathway analysis confirmed that the top upregulated pathways associated with the remaining proteins identified on the EV surface (other than those directly involved with EV biogenesis and transport) were involved in adhesion and binding (**Figure 4B.1**). This finding is in line with previous studies implicating EVs in cancer dissemination and metastasis [393, 488].

A total of 114 surface proteins were detected on HPDE EVs and a total of 229 on the surfaces of the pooled EV population comprised of the three remaining cancer EV populations. Of these, 101 proteins were shared between the two groups yielding a unique cancer-associated pool of 128 proteins of interest (**Figure 4B.2).** This total pool was further evaluated to find the proteins that were present on the surface of all three cancer EV

Figure 4B. 1 Gene ontology pathway analysis of EV surface proteins

GO pathway analysis showed that other than the expected presence of proteins associated with EV biogenesis and transport, the primary upregulated pathways involved cellular adhesion and binding. These pathways, including cell-substrate junction, focal adhesion, and cell adhesion molecule binding, have been highlighted with a red box in the figure.

Figure 4B.1

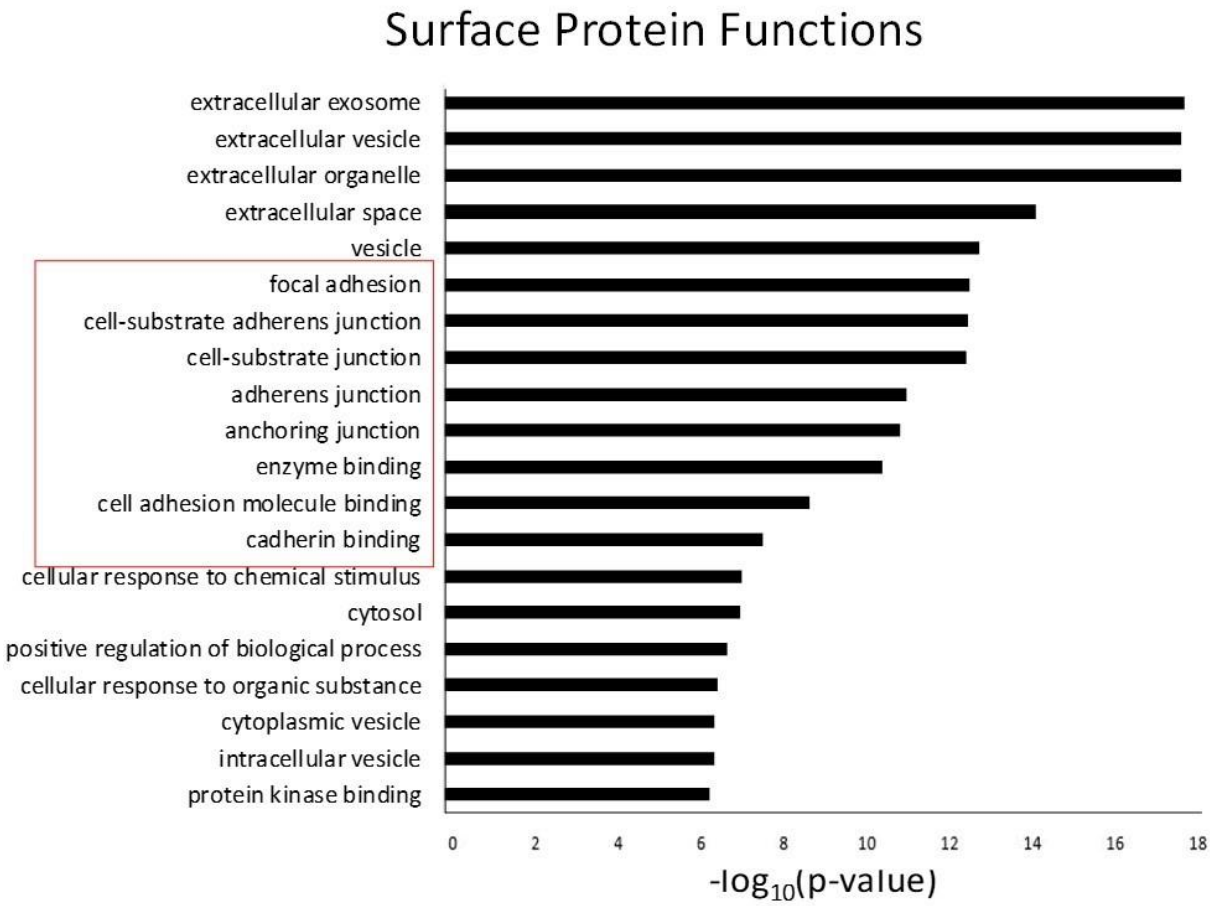
Surface Protein Functions
extracellular exosome
extracellular vesicle
extracellular organelle
extracellular space
vesicle
focal adhesion
cell-substrate adherens junction
cell-substrate junction
adherens junction
anchoring junction
enzyme binding
cell adhesion molecule binding
cadherin binding
cellular response to chemical stimulus
cytosol
positive regulation of biological process
cellular response to organic substance
cytoplasmic vesicle
intracellular vesicle
protein kinase binding
0
2
4
6
8
10
12
14
16
18
-log10(p-value)

Figure 4B. 2 Identification of cancer EV surface proteins of interest

Venn diagrams depict 114 proteins from the healthy (HPDE) EV population in light blue, the 239 pooled cancer EV protein group (all three PDAC cell lines) in purple, and the 204 from CD18/HPAF, the 135 from MiaPaCa, and the 104 from T3M4 in yellow, blue, and red, respectively. The overlap of 101 proteins between the healthy and cancer group was removed from subsequent analysis followed by identification of the proteins present on all three PDAC cell line EVs (n = 86) as well as those present on two of the three EV population surfaces. After factoring in redundancy in these four subgroups, a total of 30 proteins of interest proceeded to undergo bioinformatics analysis.

Figure 4B.2

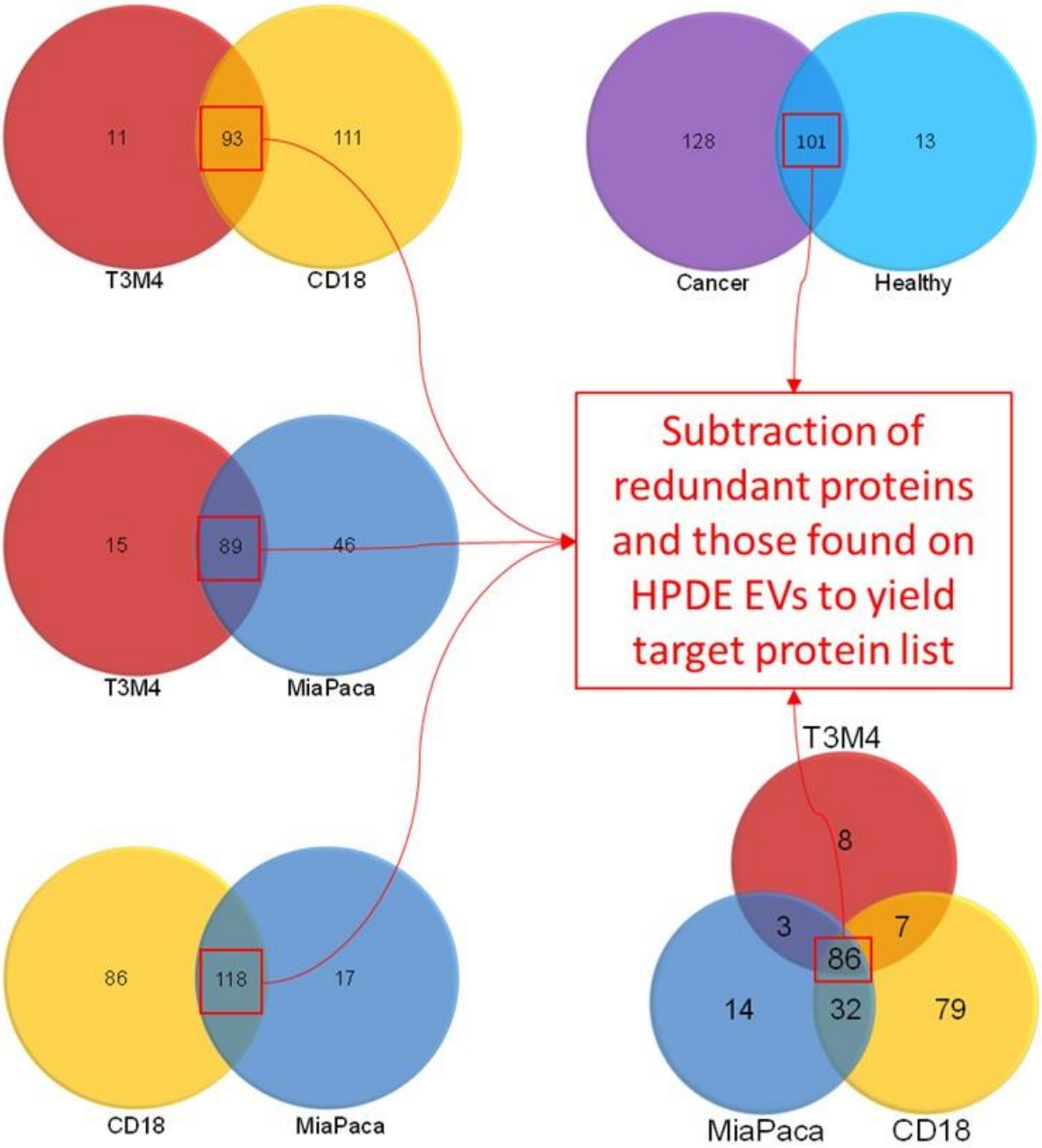
11
93
111
T3M4
CD18
128
101
13
Cancer
Healthy
15
89
46
T3M4
MiaPaca
86
118
17
CD18
MiaPaca
Subtraction of redundant proteins and those found on HPDE EVs to yield target protein list
T3M4
8
3
7
86
14
32
79
MiaPaca
CD18

populations individually as well as to find the proteins that were expressed on the surface of at least two of the individual cancer EV populations (**Figure 4B.2**). In the end, 30 surface proteins met all these criteria and underwent further bioinformatics evaluation.

4B.3.2 Bioinformatics discernment of eight specific target EV surface proteins

4B.3.2.1 Proteins of interest gene expression in adjacent normal and PDAC tissues

The GSE27385 microarray dataset was used to determine the relative expression levels of the 30 proteins of interest in the setting of PDAC. This dataset is comprised of 45 matching tumor and adjacent tumor samples, from the same patient, which provides a unique opportunity to assess what genes may be selectively upregulated or downregulated in PDAC utilizing an internal patient control. The gene expression for each of the proteins was internally normalized (i.e. each gene individually) and the z-scores were used to determine relative expression levels. Many of the genes associated with the LC-MS/MS identified proteins are upregulated in the setting of PDAC compared to adjacent normal tissue (**Figure 4B.3**). Among these, those with the most consistent pattern of increased expression were cluster of differentiation 151 (CD151), galectin-1 (LGALS1), cofilin (CFL1), tyrosine 3-monooxygenase/tryptophan 5-monooxygenase activation protein zeta (YWHAZ), extracellular matrix protein-1 (ECM1), ephrin A2 (EPHA2, integrin alpha 3 (ITGα3), and heat-shock protein family B (small) member-1 (HSPB1) (these have been identified by red boxes in **Figure 4B.3**).

4B.3.2.2 Target genes are correlated in two distinct datasets

In an attempt to further evaluate the potential of these eight markers to serve as clinically relevant biomarkers all 30 of the proteins of interest were correlated with one

Figure 4B. 3 Gene expression profiles for EV proteins of interest

Heat map representation of Z-scores of internally normalized (within gene normalization) genes coding for the 30 EV surface proteins of interest. Many of the selected genes were overexpressed in the setting of PDAC. Eight of the most consistently overexpressed targets in cancer tissue compared to adjacent normal tissue are CD151, LGALS1, CFL1, YWHAZ, ECM1, EPHA2, ITGα3, and HSPB1 and these are highlighted with red boxes in the figure.

Figure 4B.3

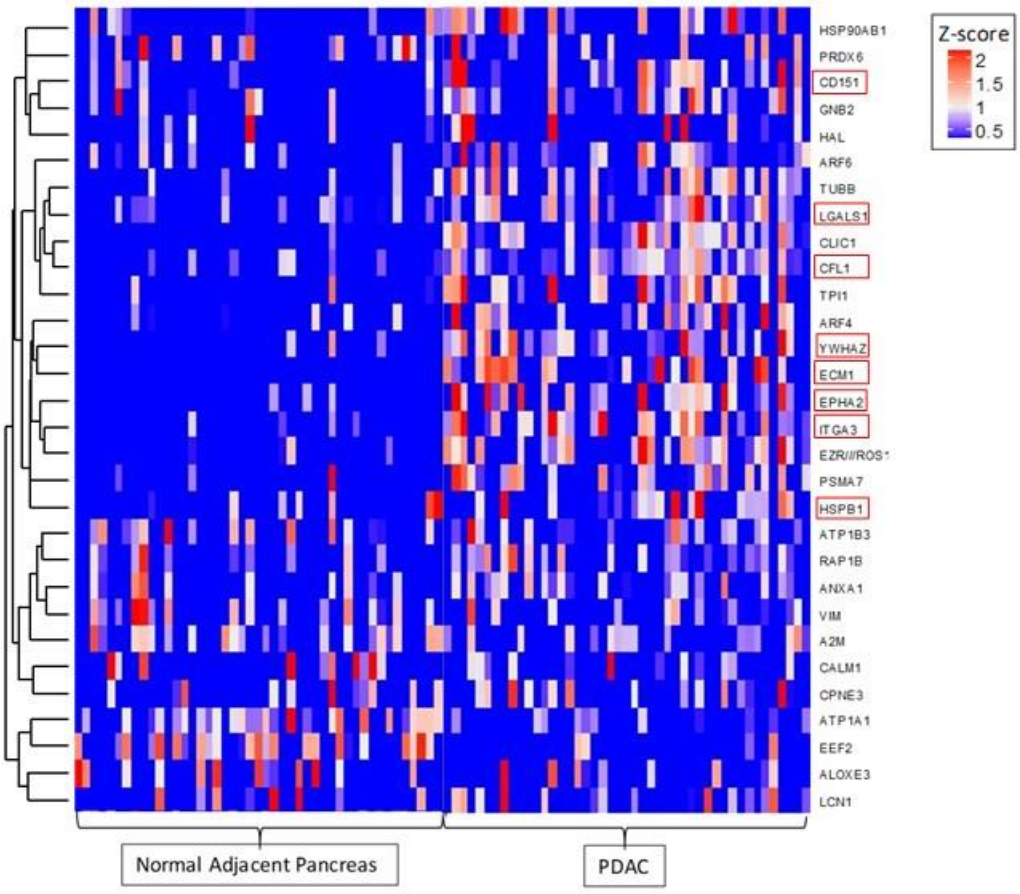
Z-score
2
1.5
1
0.5
HSP90AB1
PRDX6
CD151
GNB2
HAL
ARF6
TUBB
LGALS1
CLIC1
CFL1
TPI1
ARF4
YWHAZ
ECM1
EPHA2
ITGA3
EZR///ROS1
PSMA7
HSPB1
ATP1B3
RAP1B
ANXA1
VIM
A2M
CALM1
CPNE3
ATP1A1
EEF2
ALOXE3
LCN1
Normal Adjacent Pancreas
PDAC

another The Cancer Genome Atlas (TCGA) RNA sequencing dataset was analyzed along with the GSE23785 microarray dataset. TCGA was not used in the previous analyses because it contains only 3 samples from healthy pancreas tissue but can serve for evaluation of cancer patient expression levels. In both of these datasets CD151, LGALS1, CFL1, YWHAZ, ECM1, EPHA2, ITGα3, and HSPB1 proteins were among the most correlated genes with each other (**Figure 4B.4**). Additionally, they were highly correlated with the consensus EV marker, CD9 in both sets. The black boxes within the figure highlight the size and intensity of the blue circles for the target proteins. This suggests that the eight target proteins are upregulated in the setting of PDAC and could serve as an additive combinatorial biomarker platform.

4B.3.2.3 Target protein genes have high diagnostic accuracy

Finally, these target genes were also assessed for their ability to differentiate between normal and tumor samples in the GSE27385 dataset. Impressively, the combination of the tissue expression profiles of these eight genes identified by EV surface proteomics produces a receiver operator characteristics (ROC) curve with an area under the curve (AUC) of 0.9136 (**Figure 4B.5**). For reference, the current gold standard blood-based protein biomarker used in clinics, CA19.9, produces an AUC ranging from 0.66-0.836 [489-492]. Importantly, these results enhance the findings of our *in vitro* EV proteomics data by displaying the real-world validation of our target proteins. With this bioinformatics analysis, the target protein list was able to be efficiently narrowed down from 30 to eight which is a much more manageable and testable quantity.

Figure 4B. 4 Correlation of target proteins in two distinct datasets

Correlation plots of the genes coding for the targets of interest in GSE27385 microarray datasets and TCGA RNA sequencing dataset. A pattern emerged in both datasets of significant correlations between the eight target proteins: CD151, LGALS1, CFL1, YWHAZ, ECM1, EPHA2, ITGα3, and HSPB1. Additionally, these proteins were also correlated with the consensus EV marker, CD9. The eight target proteins, along with their correlations between themselves, are highlighted with black boxes.

Figure 4B.4

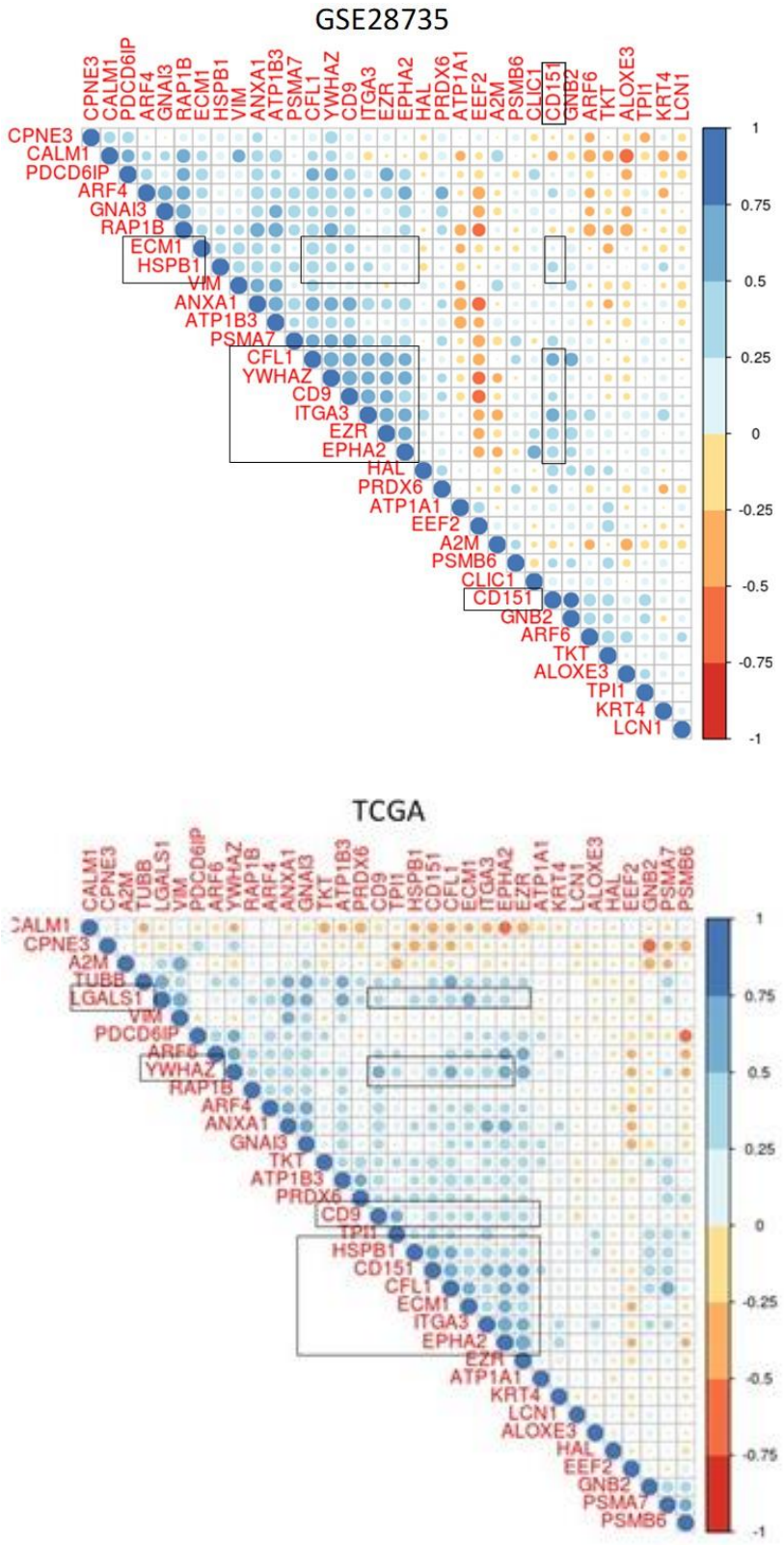
GSE28735
CPNE3
CALM1
PDCD6IP
ARF4
GNAI3
RAP1B
ECM1
HSPB1
VIM
ANXA1
ATP1B3
PSMA7
CFL1
YWHAZ
CD9
ITGA3
EZR
EPHA2
HAL
PRDX6
ATP1A1
EEF2
A2M
PSMB6
CLIC1
CD151
GNB2
ARF6
TKT
ALOXE3
TPI1
KRT4
LCN1
1
0.75
0.5
0.25
0
-0.25
-0.5
-0.75
-1
TCGA
CALM1
CPNE3
A2M
TUBB
LGALS1
VIM
PDCD6IP
ARF6
YWHAZ
RAP1B
ARF4
ANXA1
GNAI3
TKT
ATP1B3
PRDX6
CD9
TPI1
HSPB1
CD151
CFL1
ECM1
ITGA3
EPHA2
EZR
ATP1A1
KRT4
LCN1
ALOXE3
HAL
EEF2
GNB2
PSMA7
PSMB6
1
0.75
0.5
0.25
0
-0.25
-0.5
-0.75
-1

Figure 4B. 5 Receiver operator characteristics curve of the eight target protein genes

The ROC curve generated from the combination of the tissue expression profiles of CD151, HSPB1, CFL, LGALS1, YWHAZ, ECM1, ITGα3, EPHA2 results in an AUC of 0.9136.

Figure 4B.5

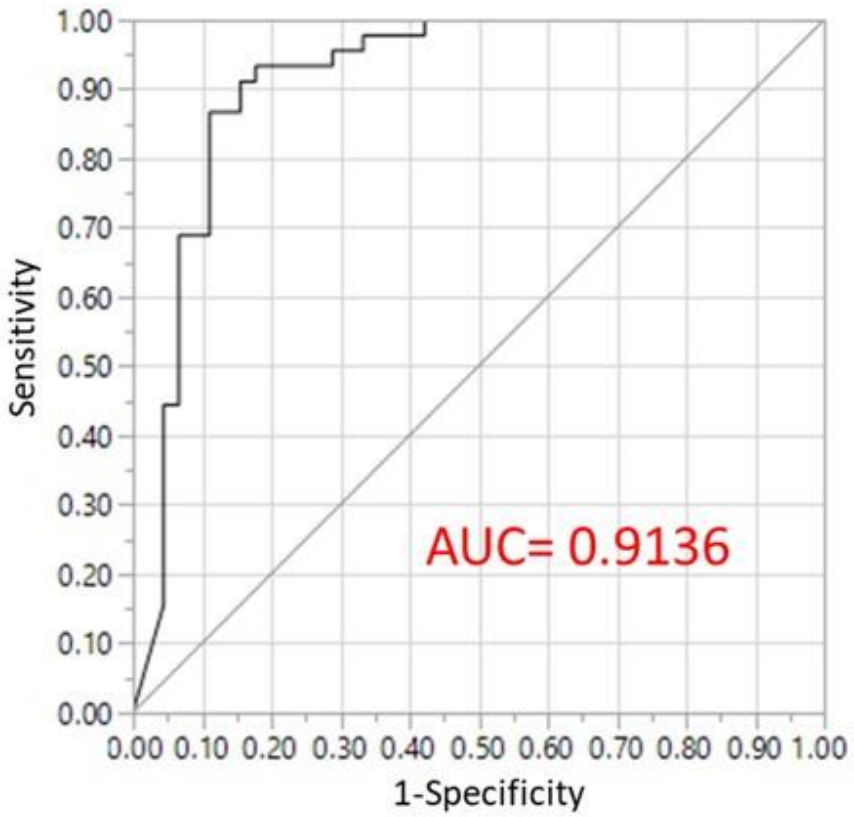

Gene components of ROC curve:
CD151, HSPB1, CFL, LGALS1,
YWHAZ, ECM1, ITGα3, EPHA2

4B.3.3 All target proteins are present in greater concentrations in EVs from PDAC cell lines compared to those from HPDE

EVs used for these experiments were isolated *via* density gradient ultracentrifugation as well as the FiberCell® hollow-fiber bioreactor system. Verification of EV enrichment was initially conducted by assessing the protein levels of a variety of consensus markers including CD9, CD63, and TSG101 (**Figure 4B.6**). These markers were markedly increased in the EV samples as compared to the paired whole cell lysates, regardless of the cell type of origin. Suggesting an adequate collection of EVs from both cancer and healthy cell lines. Importantly, calnexin, a chaperone protein found only in the endoplasmic reticulum, was absent in the EV samples and present in whole-cell lysates (**Figure 4B.6**). This served as a positive marker of lysate loading as well as making the possibility of cellular contamination in the EV samples is far less likely.

Next, the presence and amount of all eight of the target proteins were assessed *via* western blot analysis (**Figure 4B.7**). CD151 and HSPB1 were enriched in EVs from T3M4, MiaPaCa, and CD18/HPAF as compared to their matched whole cell lysates. Additionally, the expressions of CD151 and HSPB1 were greatly diminished in HPDE EVs, suggesting possible cancer specificity (**Figure 4B.7A-B**). Conversely, ITGα3 was expressed in EVs and cell lysates in the cancer cell lines as well as HPDE, although EVs from CD18/HPAF and MiaPaCa harbored a greater quantity. ECM1 is far more concentrated in cancer EVs than in lysate (**Figure 4B.7C**). EPHA2, CFLN, LGALS1, and YWHAZ seem to be virtually absent in HPDE EVs, which is an important feature for possible use as PDAC specific biomarkers (**Figure 4B.7D**).

Figure 4B. 6 Evaluation of consensus EV markers *via* western blot analysis

A-B. Isolated EV populations from T3M4, MiaPaCa, CD18/HPAF, and HPDE were verified with the consensus markers CD9 and CD63. Selective enrichment can be seen in the EV samples and is minimal/absent in equivalent quantity (10 µg/well) of cell lysate. **C.** Measurement of a third marker, TSG101, in EVs isolated *via* density gradient ultracentrifugation as well as with the FiberCell® system. **D.** Blot showing the absence of calnexin (a marker for cellular contamination) in isolated EV samples.

Figure 4B.6

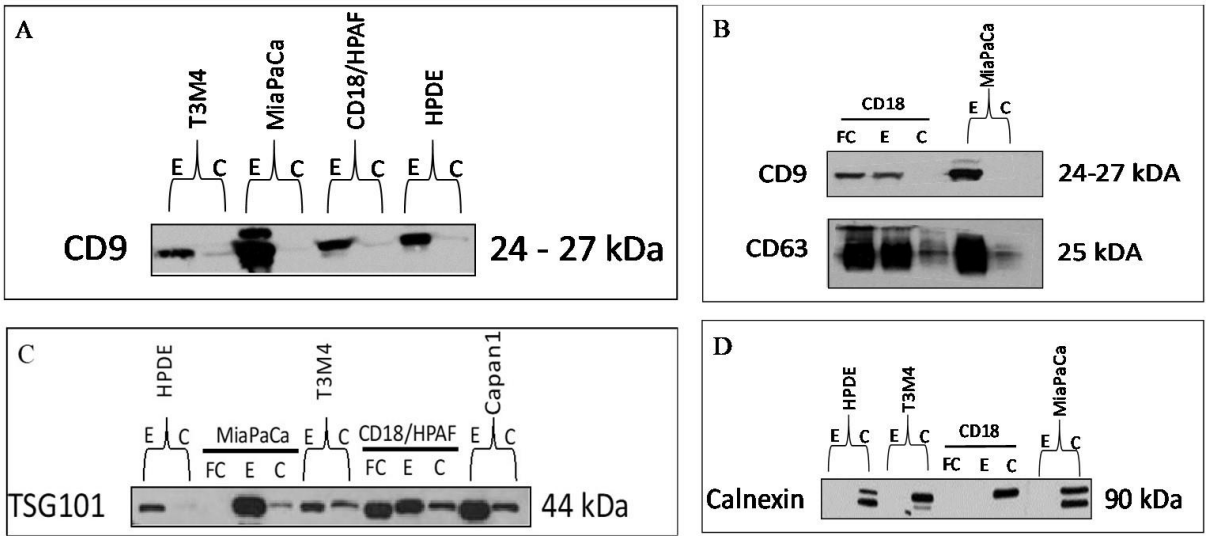
A
T3M4
MiaPaCa
CD18/HPAF
HPDE
E C E C E C E C
CD9
24 - 27 kDa
B
MiaPaCa
CD18
E C
FC E C
CD9
24-27 kDA
CD63
25 kDA
C
HPDE
T3M4
Capan1
E C
MiaPaCa
E C
CD18/HPAF
E C
FC E C
FC E C
TSG101
44 kDa
D
HPDE
T3M4
MiaPaCa
E C E C
CD18
E C
FC E C
Calnexin
90 kDa

Figure 4B. 7 Evaluation of EV surface target proteins *via* western blot

Equal protein concentrations (20 µg) of EV samples and cell lysates were loaded in each well. The relative expression of each protein was assessed between cancer EV samples and matched whole-cell lysates. Concurrently, the number of target proteins were compared between EVs isolated from cancer cells and EVs isolated from the normal HPDE cell line. Each panel displays a unique protein(s) as follows. **A.** CD151. **B.** HSPB1. **C.** ITGα3 and ECM1. **D.** EPHA2, CFLN, LGALS1, and YWHAZ.

Figure 4B.7

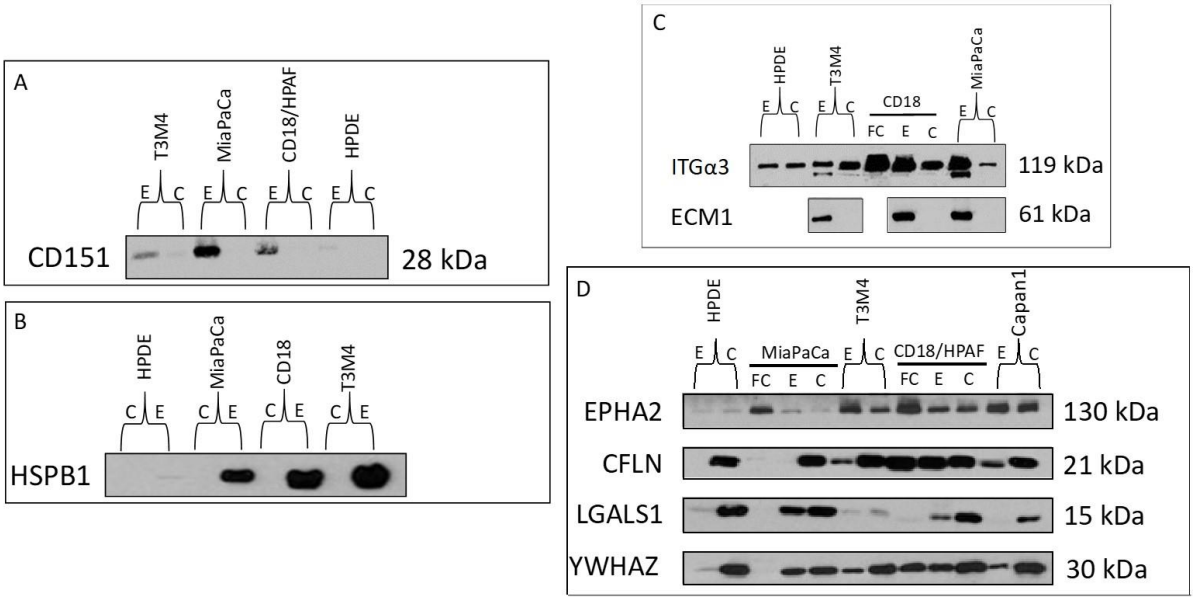
A
T3M4
MiaPaCa
CD18/HPAF
HPDE
E C E C E C E C
CD151
28 kDa
B
HPDE
MiaPaCa
CD18
T3M4
C E C E C E C E
HSPB1
C
HPDE
T3M4
MiaPaCa
E C E C CD18 E C
FC E C
ITGα3
119 kDa
ECM1
61 kDa
D
HPDE
T3M4
Capan1
E C MiaPaCa E C CD18/HPAF E C
FC E C FC E C
EPHA2
130 kDa
CFLN
21 kDa
LGALS1
15 kDa
YWHAZ
30 kDa

4B.3.4 EPHA2, ECM1, CD151, and HSPB1 are verifiably present on the EV surface

Vesicular rupture during EV isolation, sample preparation, surface shaving, and/or the LC-MS/MS procedure can contaminate the surface molecules with intravesicular contents. Thus, immunogold staining and TEM evaluation were conducted in order to verify the location and accessibility of the target proteins on the external aspect of the EV membrane outer leaflet. Briefly, protein-A conjugated gold nanoparticles 10 nm in size interact with primary antibodies bound to a protein of interest and appear as black spheres on the TEM image. This provides a means of directly visualizing the location of a protein within a sample. The immunogold protocol was first standardized with EV proteins known to be present on the EV membrane, CD63, and TSG101 in CD18/HPAF EVs (**Figure 4B. 8**). Next, the eight target proteins were evaluated with this method. Four out of the eight, EPHA2, ECM1, CD151, and HSPB1 were observed to be definitively located on the external surface of the EVs (**Figure 4B.8**).

4B.3.5 EPHA2, ECM1, CD151, and HSPB1 expression in TCGA and effects on survival

In an effort to discern which one of the targets would provide the most diagnostic and prognostic significance, stage-wise FPKM expression levels and survival analysis was conducted using the TCGA datasets on the proteins verified *via* immunogold staining to be present on the EV surface: EPHA2, ECM1, CD151, and HSPB1 (**Figure 4B.9**). The gene expression levels for CD151, ECM1, and EPHA2 were increased in cancer patients compared to healthy patient tissue samples, even in stage I disease. Notably, the increase in EPHA2 expression was greater than the other two targets. HSPB1 expression was not about the same between healthy samples and throughout tumor progression. Congruently,

Figure 4B. 8 Immunogold staining of EV surface proteins

TEM images of immunogold staining showing the surface localization of consensus EV protein markers CD63 and TSG101 as well as the four out of the eight target proteins: EPHA2, CD151, ECM1, and HSPB1. The black spheres in the images are protein-A conjugated 10 nm gold nanoparticles bound to the IgG primary antibodies against the target proteins in question. Importantly, the isotype control (mouse IgG not reactive with target proteins) is lacking the presence of black spheres around the EV surface, thus supporting the observed positive staining.

Figure 4B.8

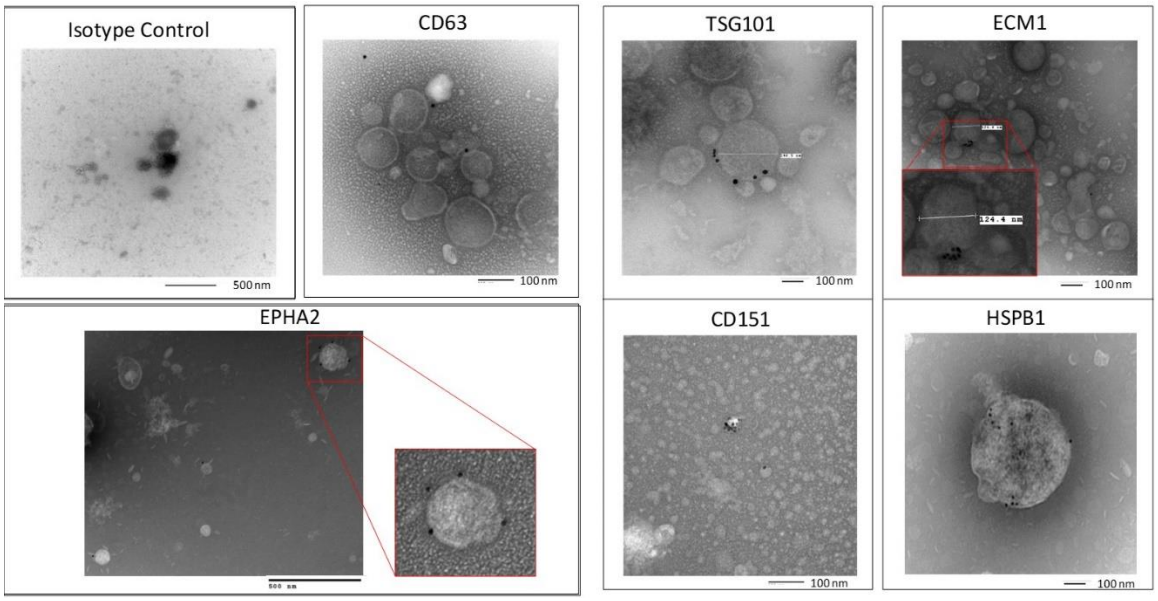
Isotype Control
500 nm
CD63
100 nm
TSG101
100 nm
ECM1
100 nm
EPHA2
CD151
100 nm
HSPB1
100 nm

Figure 4B. 9 EPHA2, ECM1, CD151, and HSPB1 expression in TCGA and effects on survival

TCGA stage-specific gene expression and survival curves were generated for the proteins that were verified to be on the EV surface: ECM1, HSPB1, CD151, and EPHA2. No difference in gene expression nor a significant impact on survival was observed for HSPB1. However, the other three proteins were differentially expressed in PDAC as compared to normal samples and all had a significant negative impact on survival. Notably, EPHA2 had the largest discernible difference in expression between the two groups and the associated survival curve was the most significant of all the proteins assessed (Log-Rank test $p = 0.0137$, Wilcoxon test $p = 0.0111$).

Figure 4B.9

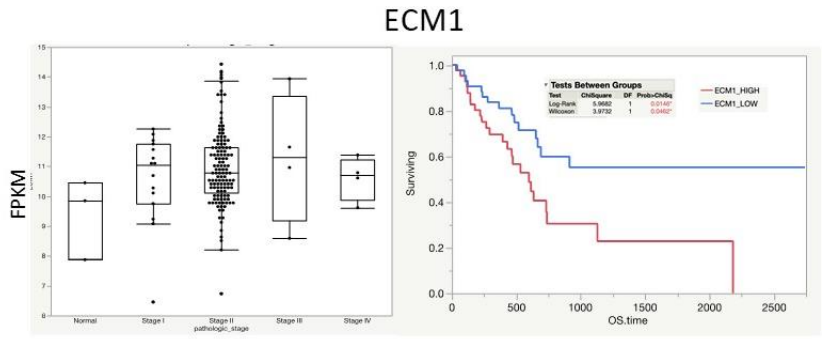
ECM1
FPKM
Normal
Stage I
Stage II
Stage III
Stage IV
pathologic_stage
Surviving
OS.time
Tests Between Groups
Test ChiSquare DF Prob>ChiSq
Log-Rank 5.9682 1 0.0146*
Wilcoxon 3.9732 1 0.0462*
ECM1_HIGH
ECM1_LOW

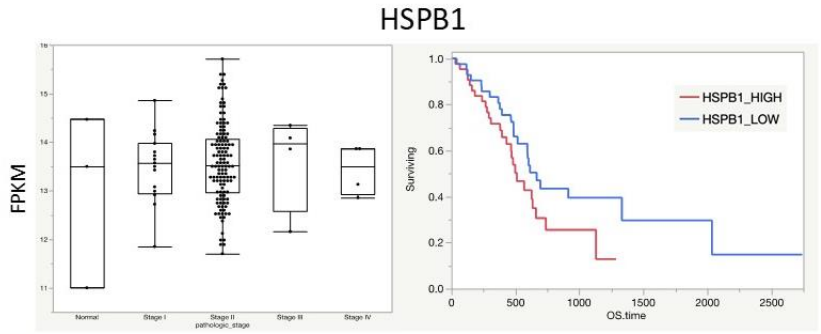
HSPB1
FPKM
Normal
Stage I
Stage II
Stage III
Stage IV
pathologic_stage
Surviving
OS.time
HSPB1_HIGH
HSPB1_LOW

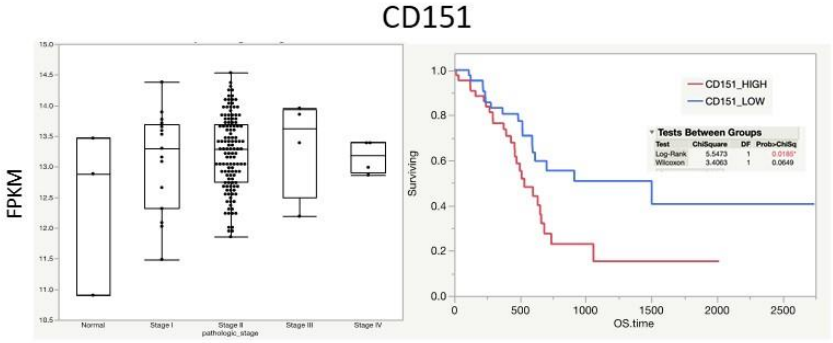
CD151
FPKM
Normal
Stage I
Stage II
Stage III
Stage IV
pathologic_stage
Surviving
OS.time
CD151_HIGH
CD151_LOW
Tests Between Groups
Test ChiSquare DF Prob>ChiSq
Log-Rank 5.5473 1 0.0185*
Wilcoxon 3.4063 1 0.0649

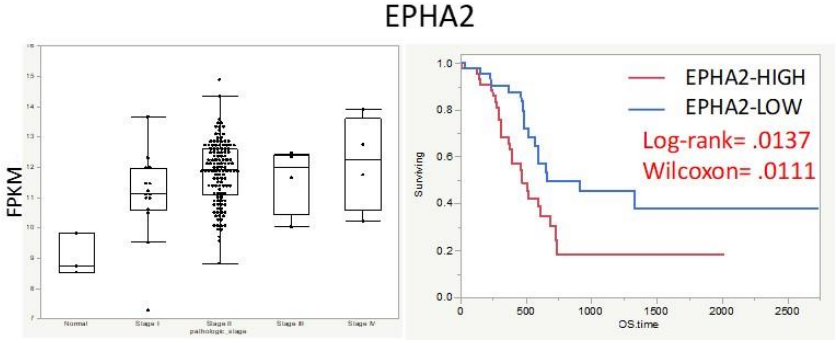
EPHA2
FPKM
Normal
Stage I
Stage II
Stage III
Stage IV
pathologic_stage
Surviving
OS.time
EPHA2-HIGH
EPHA2-LOW
Log-rank= .0137
Wilcoxon= .0111

the associated Kaplan-Meier curves for the three overexpressed proteins show that high expression of CD151, ECM1, and EPHA2 are significantly correlated with worse overall survival (**Figure 4B.9**). The most significant effect on survival was EPHA2, as determined by both Log-Rank test, p = 0.0137 as well as Wilcoxon test, p = .0111. These findings regarding the potential of EPHA2 were supported by results from the MiPanda Portal (a combination database containing both TCGA and GTEx datasets) where EPHA2 was found to be the most significantly upregulated in pancreas cancer ($p = 2.48\ e^{-36}$, relative to normal tissue) when compared to other major cancer types (**Figure 4B.10**).

4B.3.6 EPHA2 is present on CD63 positive EVs and is reliably detected with ELISA

With the verified surface location of the protein, differential gene expression, and prognostic capability EPHA2 became the first protein analyzed *via* ELISA. An in-house sandwich-based ELISA was produced (specifics on in-house ELISA production are presented in the method chapter of this thesis) utilizing an mAB antibody against EPHA2 (R&D Systems: MAB3036) to capture EVs and biotinylated CD63 (Abcam: ab134331) for the detection antibody [CD63 was chosen because of the high level of expression in EVs compared to the other consensus markers (CD9 and TSG101) in the previous western blot analysis]. As a positive control, another ELISA was developed using CD63 as both the capture and detection antibodies.

EVs isolated from the MiaPaCa cell line were deposited in duplicates into wells at serially diluted concentrations beginning at 100 µg/well and ending at 1.6 µg/well. EPHA2 capture was able to efficiently capture EVs as well as produce a concentration-dependent curve (**Figure 4B.11**). Interestingly, the signal intensities associated with EPHA2 capture and CD63 detection were far greater than those produced from CD63 capture and detection

Figure 4B. 10 EPHA2 expression in cancer vs. normal tissue across major cancer types

MiPanda portal was used to assess the relative level of EPHA2 expression in cancer vs. normal tissues and cells of various origins. EPHA2 is the most significantly upregulated in the setting of pancreas cancer ($p = 2.48\ e^{-36}$) compared to the other major cancer types.

Figure 4B.10

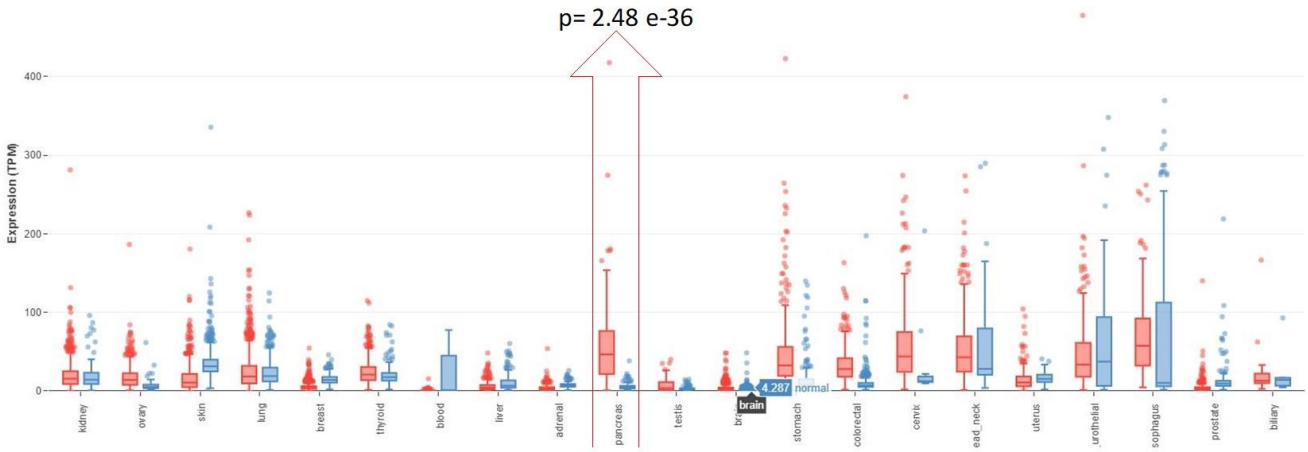
p= 2.48 e-36
Expression (TPM)
400
300
200
100
0
kidney
ovary
skin
lung
breast
thyroid
blood
liver
adrenal
pancreas
testis
brain
4.287
normal
stomach
colorectal
cervix
ead_neck
uterus
urothelial
sophagus
prostate
biliary

Figure 4B. 11 EPHA2 ELISA of CD63 positive EVs

A sandwich ELISA platform utilizing EPHA2 capture antibody and CD63 detection antibody proved efficacious for the quantification of EPHA2 on CD63 positive EVs isolated from CD18/HPAF supernatant. 100 µg of CD18/HPAF EVs were serially diluted down to 1.6 µg and produced a concentration-dependent curve. Interestingly, the signal amplitude achieved by EPHA2 capture and subsequent detection with CD63 was far greater than what was produced by CD63 capture and detection (red and black bars, respectively).

Figure 4B. 11

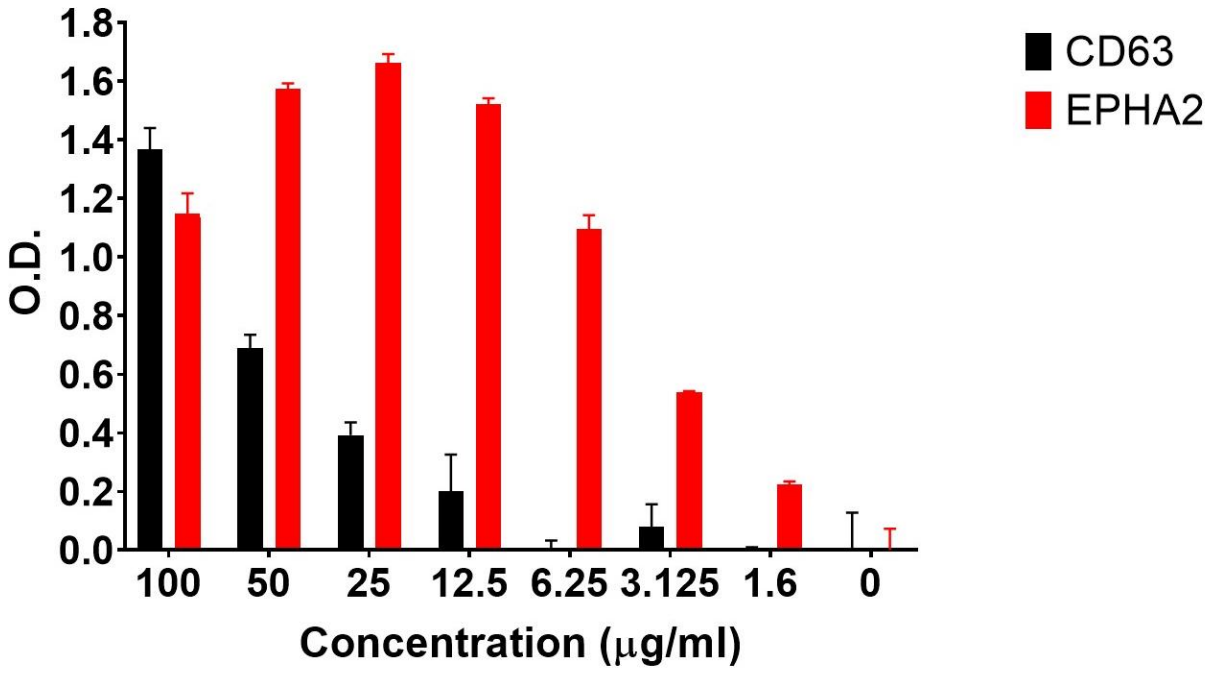
1.8
1.6
1.4
1.2
1.0
0.8
0.6
0.4
0.2
0.0
O.D.
100
50
25
12.5
6.25
3.125
1.6
0
Concentration (μg/ml)
CD63
EPHA2

(**Figure 4B.11**). Possible reasons for this unforeseen observation could that CD63 harbor a large quantity of surface EPHAS or conversely, CD63 is present in small numbers and thus is unavailable for detection antibody binding when utilized for capture.

4B.3.7 EPHA2 is increased on EVs originating from PDAC cell lines compared to HPDE cells

In order to minimize technical variation in the assay set up as well as to facilitate both capture and detection with EPHA2 antibodies, a commercial EPHA2 ELISA kit was purchased for subsequent experiments (RayBiotech). 50 μg/ml of EVs isolated from CD18/HPAF, MiaPaCa, and HPDE, along with the same quantity of matched respective whole cell lysates, were assayed in duplicates. Indeed, EPHA2 is enriched in EVs compared to cell lysates and further, EPHA2 enrichment is far greater in cancer EVs compared to EVs originating from HPDE (**Figure 4B.12**).

4B.3.8 Complete PDAC patient serum has a greater concentration of EPHA2 compared to healthy controls

39 completed patient serum samples from benign controls (comprised of chronic pancreatitis, cystic lesion, biliary obstruction, and family history patients, n =13), early-stage PDAC (I – IIB, n = 13), and late-stage PDAC (III-IV, n = 13) were diluted 1:1 in PBS and assessed with the EPHA2 ELISA kit. The median expression of EPHA2 in complete patient serum was 0.14 ng/ml for benign controls while the medians for early and late-stage PDAC patient serum was 0.53 ng/ml and 0.57 ng/ml, respectively (**Figure 4B.13**). Using a cutoff above the benign control median value of 0.15 ng/ml, the assay accuracy had a sensitivity of 76% and specificity of 62%. These data suggest a role for EPHA2 assessment for PDAC diagnosis and monitoring but requires further refinement.

Figure 4B. 12 EPHA2 ELISA of PDAC and HPDE cell lines

50 µg/ml of isolated EVs and matched whole cell lysates from CD18/HPAF, MiaPaCa, and HPDE cell lines were analyzed. EPHA2 was present in all whole cell lysate samples (black bars). However, HPDE EVs had far less concentration of EPHA2 that the EVs isolated from the two PDAC cell lines (red bars).

Figure 4B.12

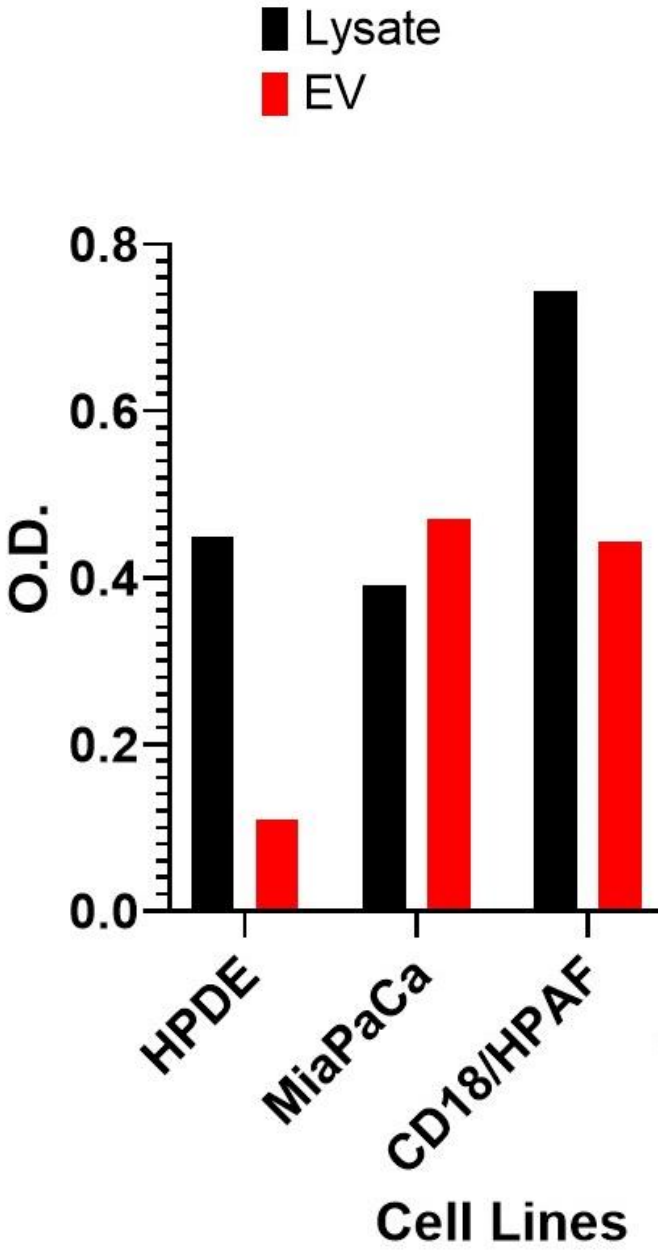

Figure 4B. 13 EPHA2 ELISA of complete patient serum samples

ELISA analysis of complete patient serum samples from 13 patients each in benign control, early-stage PDAC (I-IIB), and late-stage PDAC (III-IV) groups showed increased expression of EPHA2 in cancer patient serum samples as compared to benign control. The median for each cohort is denoted by the thick red bar in the middle of each violin plot and is 0.14 ng/ml, 0.53 ng/ml, and 0.57 ng/ml for benign control, early-stage, and late-stage PDAC, respectively.

Figure 4B.13

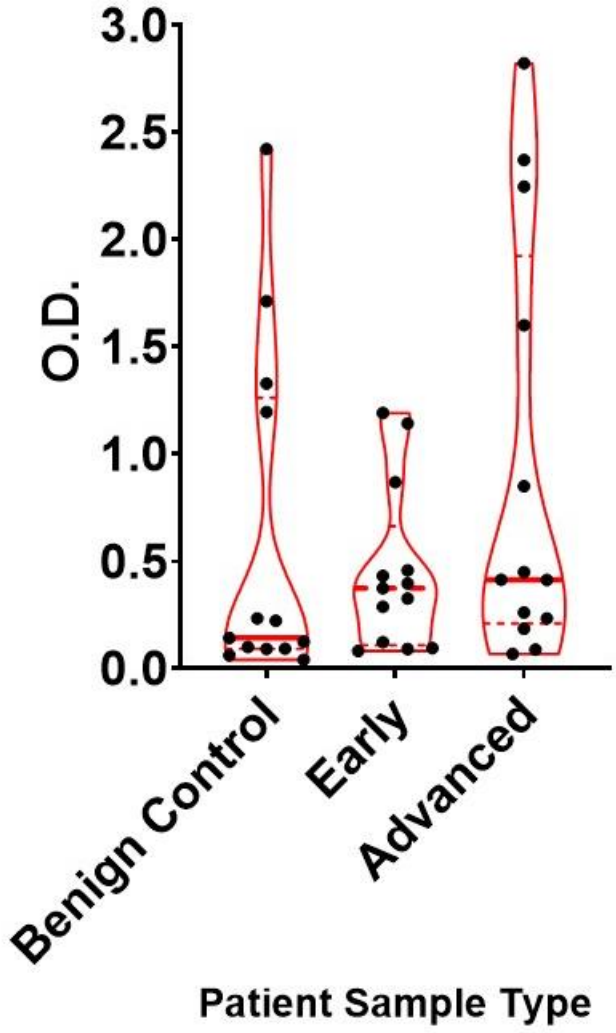
3.0
2.5
2.0
1.5
1.0
0.5
0.0
O.D.
Benign Control
Early
Advanced
Patient Sample Type

4B.3.9 EV surface EPHA2 evaluation is more specific than complete serum EPHA2 levels for predicting patient cancer status

In an effort to further refine the results of the complete serum analysis, ELISA was next conducted on patient seromic EVs. EVs were isolated from ten patient serum samples each from the benign control, early-stage PDAC, and late-stage PDAC groups to total 30 individual EV samples. Just as with complete serum, the levels of EV specific EPHA2 were higher in both cancer cohorts as compared to benign controls (**Figure 4B.14**). However, the assessment of EPHA2 only on the EV surface facilitated a dramatic shift in EPHA2 sensitivity and specificity as a PDAC diagnostic marker. Notably, the majority of the EV samples from benign controls produced zero or negative (after blank subtraction) O.D. values with only two samples achieving detection above the level of the blank. When an O.D. cutoff was applied just above the highest benign control sample reading at 0.0036 to ensure 100% specificity, five out of the 20 (25%) PDAC EV samples were able to correctly predict cancer status. (Of note, one of the O.D. values in the early stage cohort is not shown on that graph because of a comparatively high reading relative to other samples at 0.45).

4B.4 Discussion

Ever since the discovery that EVs are more than a simple mechanism to eliminate intracellular waste and harbor functional molecules within their vesicular cargo, attempts have been made to take advantage of them for a variety of purposes, including for use as cancer-specific biomarkers [493]. EVs hold myriad advantages for use as biomarkers including being present in all biofluids, ease of collection, present at higher concentrations in cancer patients, and mirroring their cell of origin. Recent studies have underscored

Figure 4B. 14 EPHA2 ELISA of patient seromic EVs

EPHA2 expression was increased in EVs isolated from both cancer cohorts as compared to benign controls. Only two O.D. values in the benign control group achieved a level of detection above blank. The median of each group is demarcated by the thick red line in the center of each violin plot. Of note, one of the O.D. values in the early stage cohort is not shown on that graph because of a comparatively high reading relative to other samples at 0.45.

Figure 4B.14

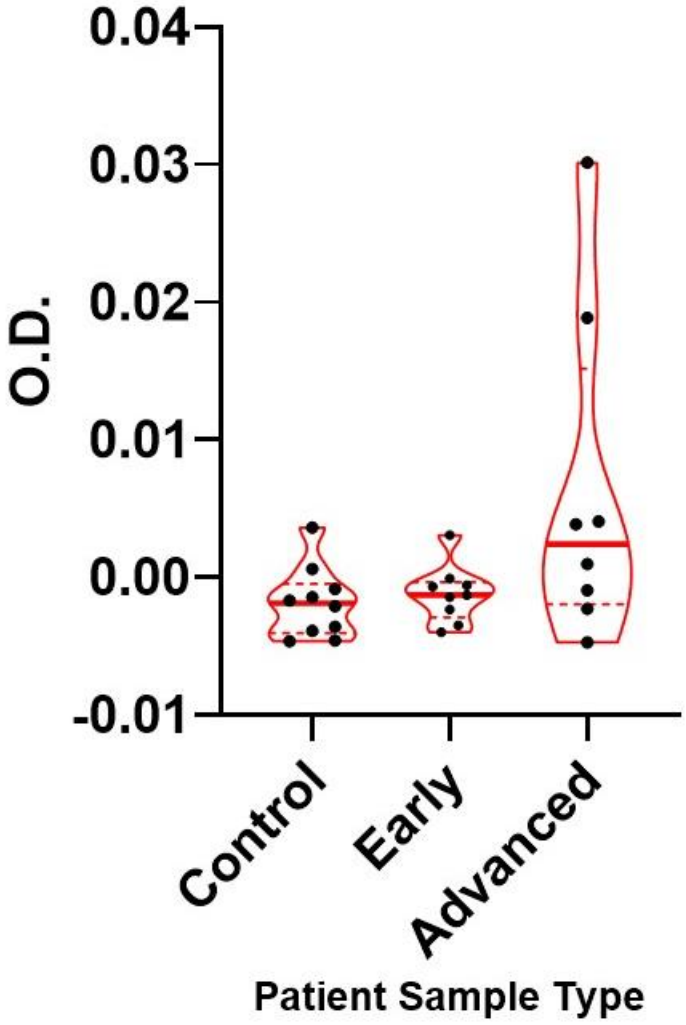
0.04
0.03
0.02
0.01
0.00
-0.01
O.D.
Control
Early
Advanced
Patient Sample Type

this potential of EVs to serve as non-invasive liquid biopsy-based biomarkers in the setting of cancer [484]. However, the majority of these studies to date have investigated the complete EV contents for this purpose.

Specifically focusing on the EV surface hold many advantages making it an ideal method for biomarker discovery. Identified targets are present on the external surface of the EVs and thus, can be targeted for cancer-specific EV isolation and/or profiling, as illustrated by previous studies. The preferred organ of metastasis can be predicted predicated on what integrin proteins are present on the surface of cancerous EVs [284]. Conversely, specific EV surface molecules can impact the efficacy of therapeutic modalities such as the case with PD-L1 [487].

EVs possess great potential to serve as concurrent biomarkers with the currently used clinical biomarker, CA19.9. Specifically for the screening of groups at high-risk for developing PDAC, i.e. those with a strong family history, genetic syndrome, or a pancreatic cystic lesion is primarily conducted *via* serial imaging and/or cystic fluid analysis (discussed in Chapter 1 of this thesis). Notably, CA19.9 has limited accuracy and therefore offers limited clinical advantage, especially for screening [492]. Not all patients express the appropriate fucosyltransferase enzyme required for CA19.9 synthesis [171] and this, combined with the fact that many other disease processes cause increase expression of CA19.9 [494, 495], has relegated its use mostly as a monitoring marker for PDAC recurrence after resection. Efforts have been made to increase the sensitivity and/or specificity of CA19.9 in the diagnostic setting [489, 490]. Unfortunately, to date, none have proven successful enough to become integrated into clinical practice. Combination screening could increase the diagnostic accuracy to a level amenable to high-risk population screening. This is quite

pertinent to this study since the low sensitivity precludes the use of the elucidated EV surface marker, EPHA2, from being used as a single agent biomarker, yet may provide a means of increasing the overall accuracy of CA19.9. For example, ruling out diseases other than PDAC, which also cause an increase in CA19.9 expression. Thus, further investigation into the concurrent assessment of EV surface EPHA2 and complete serum CA19.9 is warranted.

4B.5 Conclusions and future directions

In this study, we built upon the previous finding that EV surface analysis *via* surface-enhanced Raman spectroscopy is capable of discriminating between EVs isolated from healthy and PDAC patient serum, although with limited accuracy (discussed in part A of this chapter). This proof-of-concept study warranted further investigation into what specific molecular species of the EV surface contribute to the SERS spectral shifts.

We began by first elucidating a pool of cancer-specific proteins *via* EV surface shaving followed by LC-MS/MS analysis. Determination of the real-world significance of each marker was conducted by expression profiling, gene correlations, ROC curve assessment using data from TCGA as well as GSE27385 microarray datasets. This process allowed for the reduction of 229 possible proteins down eight target proteins: cluster of differentiation 151 (CD151), galectin-1 (LGALS1), cofilin (CFL1), tyrosine 3-monooxygenase/tryptophan 5-monooxygenase activation protein zeta (YWHAZ), extracellular matrix protein-1 (ECM1), ephrin A2 (EPHA2, integrin alpha 3 (ITGα3), and heat-shock protein family B (small) member-1 (HSPB1). All eight proteins were validated to be present in EVs via western blot, many of which were increased in EVs from cancer cells compared to normal immortalized human epithelial cells (HPDE). Four of these eight,

EPHA2, ECM1, CD151, and HSPB1, were able to be visualized on the surface of EVs *via* immunogold labeling and TEM imaging. TCGA expression and survival analysis of these four protein genes were assessed leading to the selection of EPHA2 to be used for subsequent experiments, due to the greatest difference in expression in cancer vs. normal tissue as well as the most significant impact on survival. ELISA conducted on EVs from PDAC cell lines and HPDE showed elevated expression of EPHA2 in PDAC EVs compared to match lysates as well as HPDE EVs. Additionally, EPHA2 was found to be elevated incomplete cancer patient serum compared to benign controls resulting in a diagnostic sensitivity of 76% and specificity of 62%. Finally, EV specific EPHA2 expression isolated from patient serum samples proved capable of identifying 25% of PDAC patients with 100% specificity.

Future studies will be undertaken in order to increase the diagnostic efficacy of EV surface characterization. Firstly, the other three protein markers that were immunogold validated to be on the surface of EVs: CD151, ECM1, and HSPB1 will be assessed in patient serum samples to determine if they offer any additive benefit to EPHA2, especially the low sensitivity (25%). Congruently, initial lectin array assessment identified four lectins that bound far more CD18/HPAF EVs than EVs from HPDE (AAL, Con A, EEL, and UEA-1) and one that preferentially bound with HPDE EVs (PNA) (**Figure 4B.15**). Thus, providing new targets to be used in multiparametric profiling of the EV surface. Finally, we have recently been able to analyze DNA isolated from EVs originating from Panc1 pancreatic cancer cell line and HPDE *via* digital droplet polymerase chain reaction (ddPCR), and detect PDAC associated mutation, KRAS G12D, in an accurate and

Figure 4B. 15 Preliminary lectin array of CD18/HPAF and HPDE EVs

Out of the 40 lectins analyzed as a part of the microarray, four were found to preferentially bind EVs isolated from CD18/HPAF: AAL, Con A, EEL, and UEA-1, as determined by relative fluorescence (red bars). Additionally, one lectin, PNA, bound HPDE EVs with greater avidity (black bars). This is meant to serve as the preliminary investigation into possible new surface markers to be used concomitantly with the elucidated protein markers in a multiparametric analysis.

Figure 4B.15

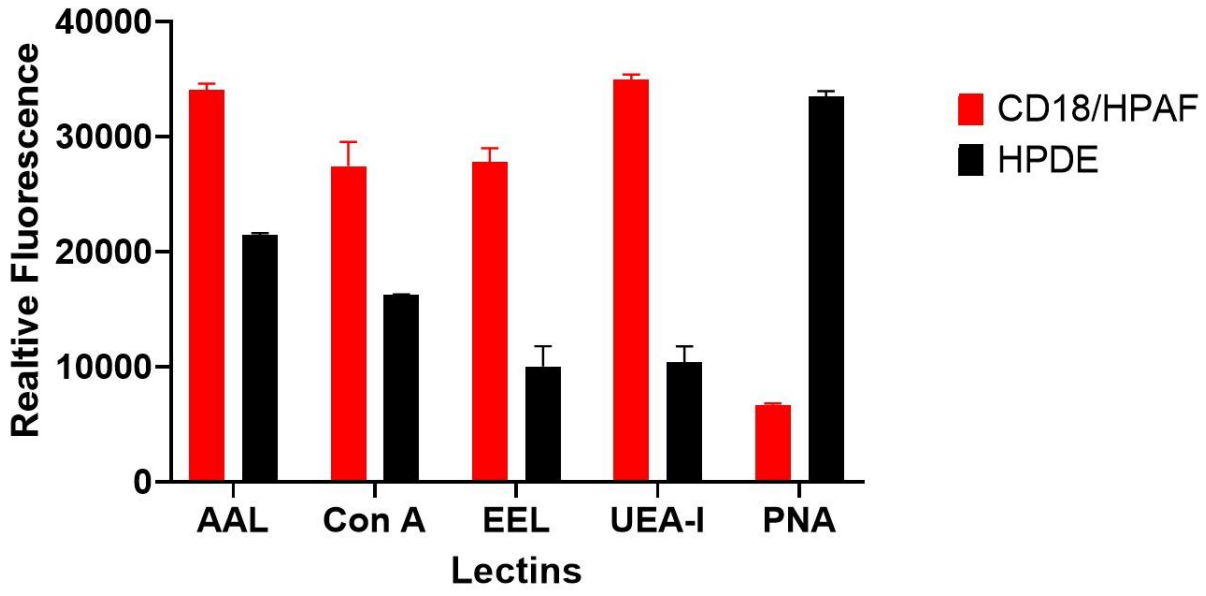
40000
30000
20000
10000
0
Realtive Fluorescence
AAL
Con A
EEL
UEA-I
PNA
Lectins
CD18/HPAF
HPDE

Figure 4B. 16 Digital droplet PCR analysis of cell line EVs

The detected KRAS G12D mutation (blue boxes) and KRAS WT (brown boxes) are presented in the graph as copy number/µl for each sample, which is enumerated above the boxes in the graph. DNA isolated from Panc1 EVs and HPDE EVs was combined in the following respective proportions: 1.0/0.0, .5/.5, .25/.75, .125/.875. and 0.0/1.0. As the proportion of Panc1 EV DNA decreases the amount of KRAS G12D mutation detected also decreases in a concentration-dependent manner. Importantly, no mutant KRAS is detected in the sample containing only HPDE EV DNA, thus supporting assay specificity.

Figure 4B.16

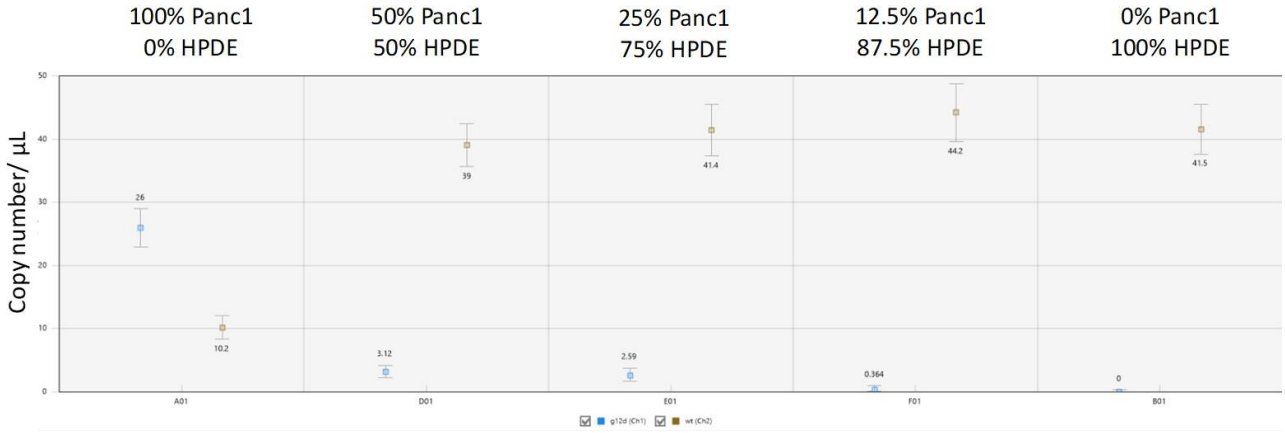
100% Panc1
0% HPDE
50% Panc1
50% HPDE
25% Panc1
75% HPDE
12.5% Panc1
87.5% HPDE
0% Panc1
100% HPDE
Copy number/ µL
50
40
30
20
10
0
26
10.2
3.12
39
2.59
41.4
0.364
44.2
0
41.5
A01
D01
E01
F01
B01
g12d (Ch1)
wt (Ch2)

concentration-dependent manner (**Figure 4B.16**). The detected copy number of the mutant KRAS decreases as the percentage of Panc1 EV DNA comprising the sample decreases. Future studies will combine this ddPCR technique with the identified EV surface proteins, in an effort to isolate and identify PDAC specific EVs from patient serum samples.

Chapter 5: Radiation Potentiation *via* Ferroptosis for the Improved Treatment of Pancreatic Ductal Adenocarcinoma

Chapter 5: Radiation potentiation *via* ferroptosis for the improved treatment of pancreatic ductal adenocarcinoma

5.1 Synopsis

Pancreatic ductal adenocarcinoma (PDAC) is one of the most lethal malignancies with an estimated 5-year survival rate of less than 9% [2]. A primary reason why PDAC is so deadly is because of ineffective standard treatment options including chemo and radiotherapy [215]. Therefore, in this study, we investigated the involvement of ferroptosis, a newly identified form of iron-dependent cell death [496], in radiation-induced cell death and further, if pharmaceutical induction of ferroptosis with the small molecule Erastin can potentiate the lethal effects of radiation. Analysis of PDAC samples in The Cancer Genome Atlas (TCGA) RNA sequencing database revealed GPX4 and system X_c (vis-à-vis SLC7A11) expression levels (two proteins integral in preventing ferroptosis) to be elevated in PDAC compared to healthy controls. Further, SLC7A11 expression was significantly correlated with worse overall survival in those who received radiation. IHC staining of patient tissue samples showed significantly higher SLC7A11 levels in PDAC and irradiated tissue compared to normal. Expression of GPX4 and SLC7A11 at the protein level were variable yet high in all cancer cell lines. Microarray analysis across multiple PDAC cell lines demonstrated increased GPX4 expression post-radiation, with 3 out of 4 showing GPX4 to be in the top 10 most upregulated genes. NRF2 phosphorylation and subsequent SLC7A11 protein expression increased in a time-dependent manner in CD18/HPAF, and Panc1 PDAC cells following 5Gy radiation treatment. Radiation was shown to increase the labile Fe^{2+} pool and the level of ROS in cells. Lipid peroxidation (the only known inducer of ferroptosis) was also increased with radiation and to a greater extent

with combination treatment. Combination treatment synergistically reduced cell and organoid viability, compared to RT alone. Finally, the combination of Erastin and radiation significantly reduced the size of tumors in xenograft mouse models.

5.2 Background and rationale

Surgical resection is the most effective treatment technique for PDAC [497]. Unfortunately, the vast majority of pancreatic cancer cases are detected in later stages, when resection is no longer a viable option [176]. Congruently, current chemotherapeutic options are either ineffective or extremely toxic and thus provide little added survival benefit [215]. Radiation therapy (RT) is primarily utilized in the neoadjuvant setting to shrink borderline resectable and unresectable non-metastatic tumors to a size amenable to resection [200, 201], with initial attempts recently being made to definitively treat those with nonresectable disease *via* stereotactic body radiation (SBRT) [203]. Unfortunately, many pancreatic tumors remain refractory to radiation treatment [208] (for more information regarding current PDAC therapies, see section 1.5 Therapeutic strategy, in Chapter 1 of this thesis). The combination of these factors has initiated the search for new treatment sensitizing agents to increase the effectiveness of current non-surgical treatments.

Ferroptosis is a recently discovered form of programmed cell death that requires labile intracellular ferrous iron (Fe^{2+}) [496, 498]. An abundance of reactive oxygen species (ROS) present within a cell, either endogenous or exogenous in origin, results in a lethal buildup of peroxidated lipid species, specifically phosphatidylethanolamine (PE), inducing ferroptosis [498]. Glutathione peroxidase 4 (GPX4) converts lethal PE peroxides to nontoxic lipid alcohols and this enzymatic activity of GPX4 is depended on the availability of glutathione (GSH) [499, 500]. One of the primary mechanisms of GSH synthesis requires the

import of extracellular cysteine into the cell *via* the cysteine-glutamate antiporter, System X_c (a complex of SLC3A2 and SLC7A11 proteins) [501]. Pharmacological inhibition of SLC7A11 with the small molecule Erastin, prevents the adequate production of GSH, thus inhibiting GPX4 enzymatic activity, which, in turn, causes the lethal lipid peroxides to accumulate, culminating in ferroptosis induction [502] (**Figure 5.1**).

This method of ferroptotic induction has become an increasingly popular area of study for use as a therapeutic adjuvant for a variety of cancer therapies including chemo [503] and radiation therapies [504, 505]. One of the advantages of targeting SLC7A11 is a degree of cancer specificity is offered by an increased level of ROS in the setting of cancer compared to normal and the inherent reliance on a variety of antioxidative mechanisms (including SLC7A11) [506-510]. Moreover, SLC7A11 CRISPR knock out does not affect the gestation or morphology of mice, thus implying systemic SLC7A11 blockade may be well tolerated [511]. Additionally, many cancers that have resistance to conventional cytotoxic chemotherapeutics seem sensitive to ferroptotic induction [503, 512, 513].

Radiation therapy is an excellent candidate for potentiation with ferroptosis as one of its primary mechanisms of inducing cell damage is mediated by the production of ROS [514]. With the advent of hypo fractionated SBRT, highly conformational large doses of radiation can be administered at a given time thereby producing higher levels of ROS at once, specifically within the tumor. These two therapeutic modalities are ideally suited to complement one another in their mechanisms of action where and increase in ROS generation is provided by radiation and a diminished capability of eliminating the associated lipid toxicity is provided by SLC7A11 inhibition. In accordance with this background and rationale, we hypothesize that in the setting of radiation, system X_c

Figure 5. 1 Schematic of Erastin induced ferroptosis

Erastin induction of ferroptosis is mediated by the blockade of SLC7A11, a component of the cystine-glutamate antiporter System X_c, thereby preventing glutathione (GSH) synthesis. GSH is required as a substrate for glutathione peroxidase 4 (GPX4) enzymatic conversion of toxic lipid hydro peroxides into non-toxic lipid alcohols. The build-up of lipid hydro peroxides culminates in ferroptotic death. NRF2, the transcription factor responsible for SLC7A11 and GPX4, is depicted. Cellular ferroptotic susceptibility is also determined by the availability of free ferrous iron (Fe^{2+}) and its ability to produce ROS *via* Fenton chemistry. The majority of iron existing in the ferritin bound non-ferrous form as depicted.

Figure 5.1

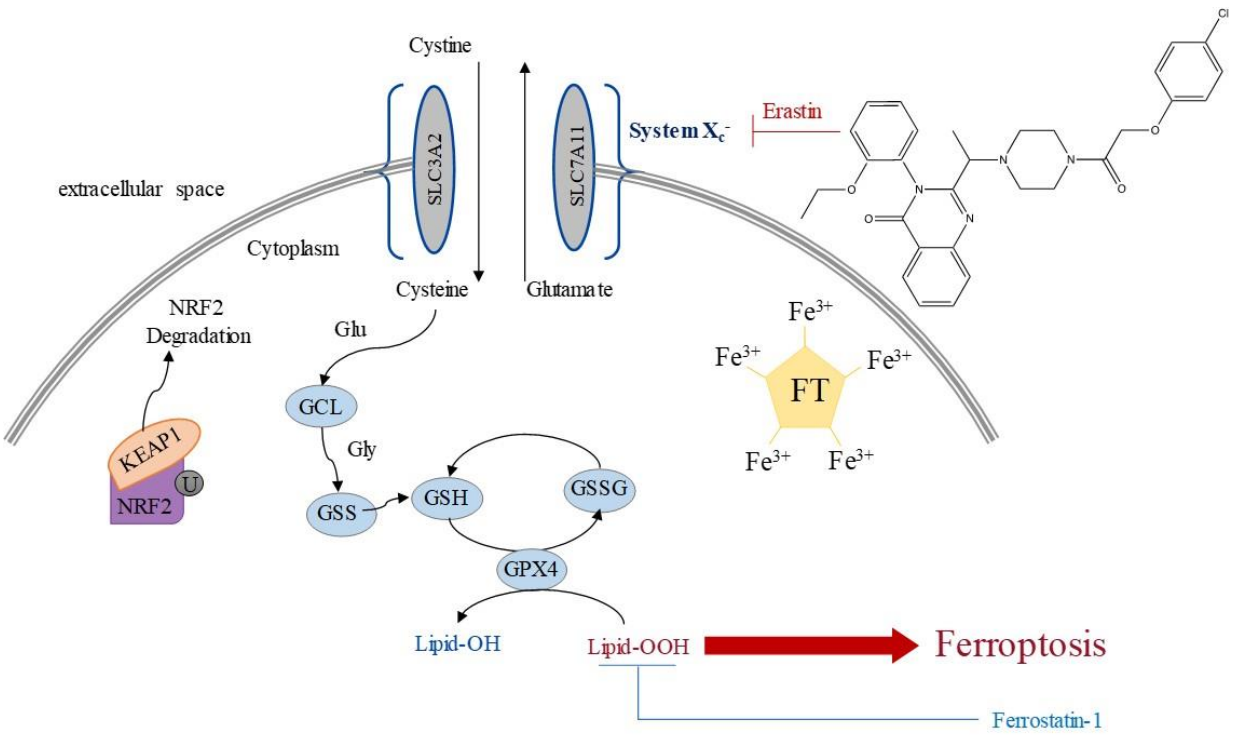
Cystine
SLC3A2
SLC7A11
System X_c^-
Erastin
extracellular space
Cytoplasm
Cysteine
Glutamate
NRF2
Degradation
Glu
GCL
Gly
GSS
GSH
GSSG
GPX4
KEAP1
U
NRF2
Fe^{3+}
FT
Lipid-OH
Lipid-OOH
Ferroptosis
Ferrostatin-1

inhibition with Erastin will facilitate ROS mediated lipid peroxidation and subsequent ferroptosis induction, thus increasing the lethal effect of radiation therapy in the setting PDAC.

5.3 Results

5.3.1 GPX4 and SLC7A11 are differentially expressed in pancreas cancer

As mentioned above, it is known that SLC7A11 and GPX4 act in concert as the primary mitigators of ferroptosis induction. As such, the expression levels of each protein were initially assessed through the Gepia and MiPanda Portals which both combine The Cancer Genome Atlas (TCGA) RNA sequencing data from patient tissue samples with the cell line genetic data found in the GTEx database. When both pancreas cancer tissues and cell line data are considered, GPX4 is present at far higher quantities as compared to healthy samples. **Figure 5.2A** displays the percentage of samples that have GPX4 expression levels >100 and 200 TPM in both cancer and healthy tissues. The difference between the percentage of samples with >100 TPM in cancer and healthy tissues can be better visualized in **Figure 5.2B**. Notably, the pancreas is one of the top three organs in terms of increased expression of GPX4 with 98% of cancer samples having a TPM >100 compared to only 8% of healthy samples. Congruently, the expression level of SLC7A11 in the combination TCGA and GTEx dataset is elevated in the setting of pancreas cancer as compared to healthy samples (**Figure 5.3**).

Interestingly, the expression of GPX4 was not found to be significantly altered in the setting of PDAC as compared to healthy tissue samples, nor did it have any significant effect on survival, when only considering patient samples in TCGA (**Figure 5.4A-B**).

Figure 5. 2 GPX4 expression in pancreas cancer compared to normal pancreas and relative to cancers of various origin

A. GPX4 expression is shown as transcripts per million (TPM) in cancer and normal tissues among a wide array of different organ types. The percentage of samples assayed with GPX4 expression >100 and >200 TPM are displayed as a heat map. Notably, the difference in expression in pancreas cancer and normal pancreas is one of the highest in both categories. **B.** Bar graph depiction of the difference between cancer and normal tissues with GPX4 expression >100 TPM. The pancreas is the third highest out of all tissue types with 98% of cancer and only 6% of normal tissue (92% difference) achieving this expression level. Notably, these data combine patient PDAC neuroendocrine samples (TCGA) and PDAC cell line (GTEx) data.

Figure 5.2

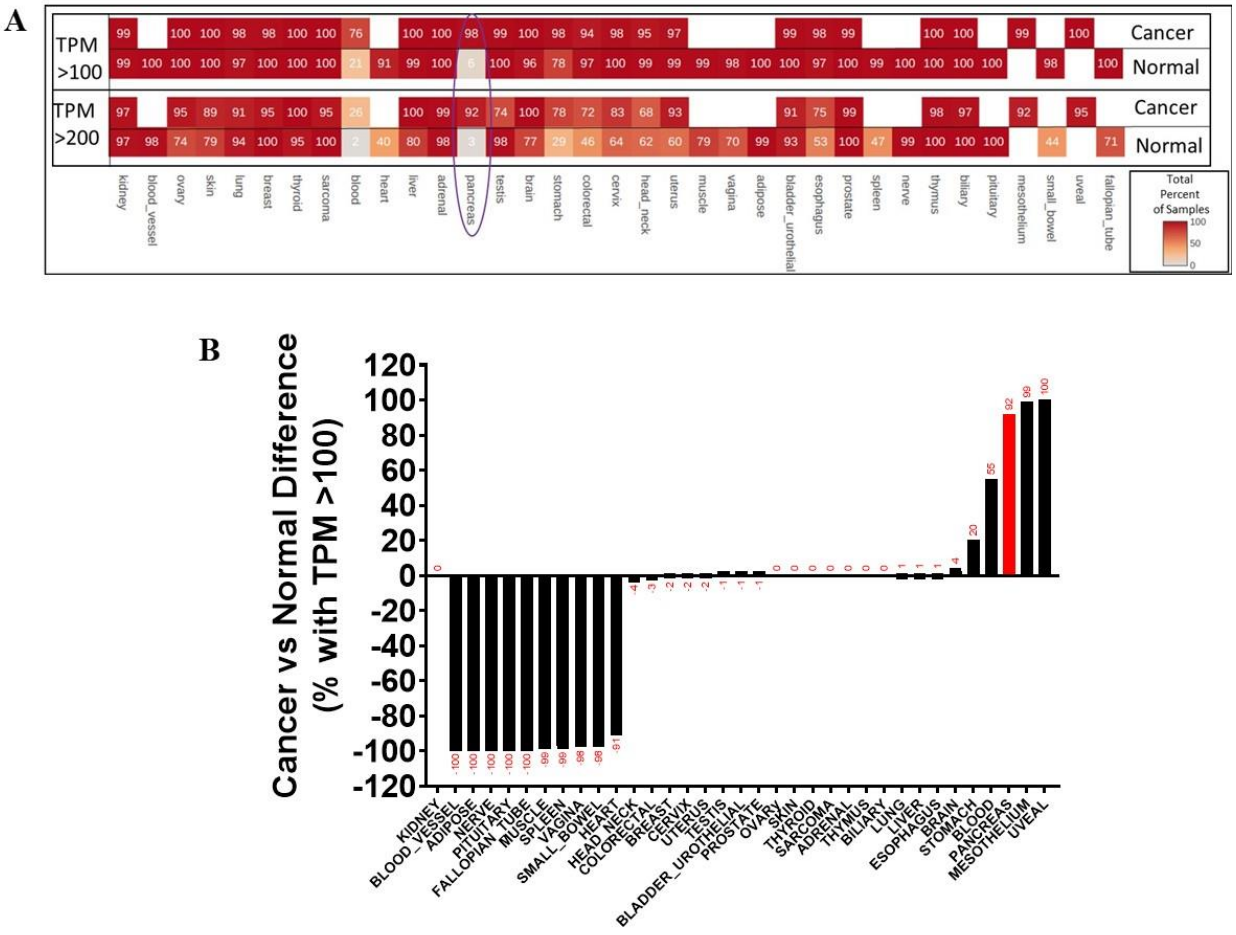
A
TPM >100
TPM >200
Cancer
Normal
kidney
blood_vessel
ovary
skin
lung
breast
thyroid
sarcoma
blood
heart
liver
adrenal
pancreas
testis
brain
stomach
colorectal
cervix
head_neck
uterus
muscle
vagina
adipose
bladder_urothelial
esophagus
prostate
spleen
nerve
thymus
biliary
pituitary
mesothelium
small_bowel
uveal
fallopian_tube
Total Percent of Samples
100
50
0
B
Cancer vs Normal Difference (% with TPM >100)
120
100
80
60
40
20
0
-20
-40
-60
-80
-100
-120
KIDNEY
BLOOD_VESSEL
ADIPOSE
NERVE
PITUITARY
FALLOPIAN_TUBE
MUSCLE
SPLEEN
VAGINA
SMALL_BOWEL
HEART
HEAD_NECK
COLORECTAL
BREAST
CERVIX
UTERUS
TESTIS
BLADDER_UROTHELIAL
PROSTATE
OVARY
SKIN
THYROID
SARCOMA
ADRENAL
THYMUS
BILIARY
LUNG
LIVER
ESOPHAGUS
BRAIN
STOMACH
BLOOD
PANCREAS
MESOTHELIUM
UVEAL

Figure 5. 3 SLC7A11 expression in pancreas cancer compared to normal pancreas and relative to cancers of various origin

The expression of SLC7A11 is shown as TPM. SLC7A11 is increased in cancer compared to normal in a wide array of tissue types. Specifically, it is increased over two-fold in pancreas cancer. Notably, these data combine patient PDAC neuroendocrine samples (TCGA) and PDAC cell line (GTEx) data.

Figure 5.3

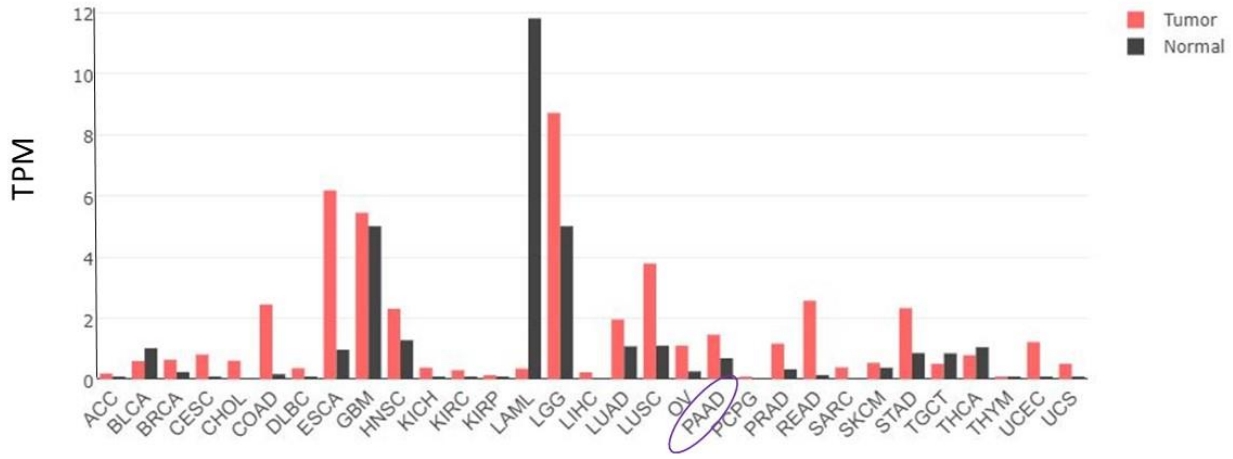
TPM
12
10
8
6
4
2
0
Tumor
Normal
ACC
BLCA
BRCA
CESC
CHOL
COAD
DLBC
ESCA
GBM
HNSC
KICH
KIRC
KIRP
LAML
LGG
LIHC
LUAD
LUSC
OV
PAAD
PCPG
PRAD
READ
SARC
SKCM
STAD
TGCT
THCA
THYM
UCEC
UCS

Conversely, SLC7A11 expression was indeed elevated in PDAC patients, yet also with no effect on survival (**Figure 5.4C-D**). Of note, the TCGA only has RNA sequencing data of four healthy pancreas tissue samples within the database, thus limiting its utility for PDAC vs healthy comparisons when used in isolation. Further, the pancreas cancer cohort is comprised of PDAC and pancreatic neuroendocrine tumor samples. The neuroendocrine samples have not been taken out of the datasets in the MiPanda and Gepia Portals and have been for our in house TCGA analysis to specifically discern the expression patterns in PDAC.

5.3.2 SLC7A11 protein expression is increased in the majority of PDAC cell lines compared to HPDE

The amount of GPX4 and SLC7A11 protein present in cell lines was next analyzed *via* western blot. This was conducted in many different PDAC cell lines that covered a wide mutational spectrum, differentiation statuses, as well as from primary and metastatic origins including CD18/HPAF, MiaPaCa, Colo357, AsPC1, Panc1, Capan1, T3M4, and BxPC3. Along with these, an immortalized human pancreatic epithelial cell lined, HPDE, was also assessed. GPX4 was present in roughly equal quantities across the PDAC cell lines as well as HPDE (**Figure 5.5**). Conversely, SLC7A11 expression was increased in five out of the eight PDAC cell lines assessed: CD18/HPAF, MiaPaCa, Panc1, T3M4, and BxPC3 (**Figure 5.5**). The increased expression of SLC7A11 in a majority of PDAC cell lines suggests an increased reliance on the cysteine import facilitated by System Xc and could prove to be an actionable target for the induction of ferroptosis.

Figure 5. 4 GPX4 and SLC7A11 expression and survival in the TCGA PDAC cohort

As mentioned prior, the previous figures showed data combining a wide variety of pancreas cancer specimens. PDAC specific expression was assessed in the TCGA dataset and is displayed as FPKM values. **A**. GPX4 expression in normal and tumor samples is not altered and survival is not impacted. **B.** SLC7A11 expression is higher in tumor samples as compared to normal but also does not have any correlation with overall survival. Of note, the limitation of the TCGA dataset is the presence of only four normal samples for comparison.

Figure 5.4

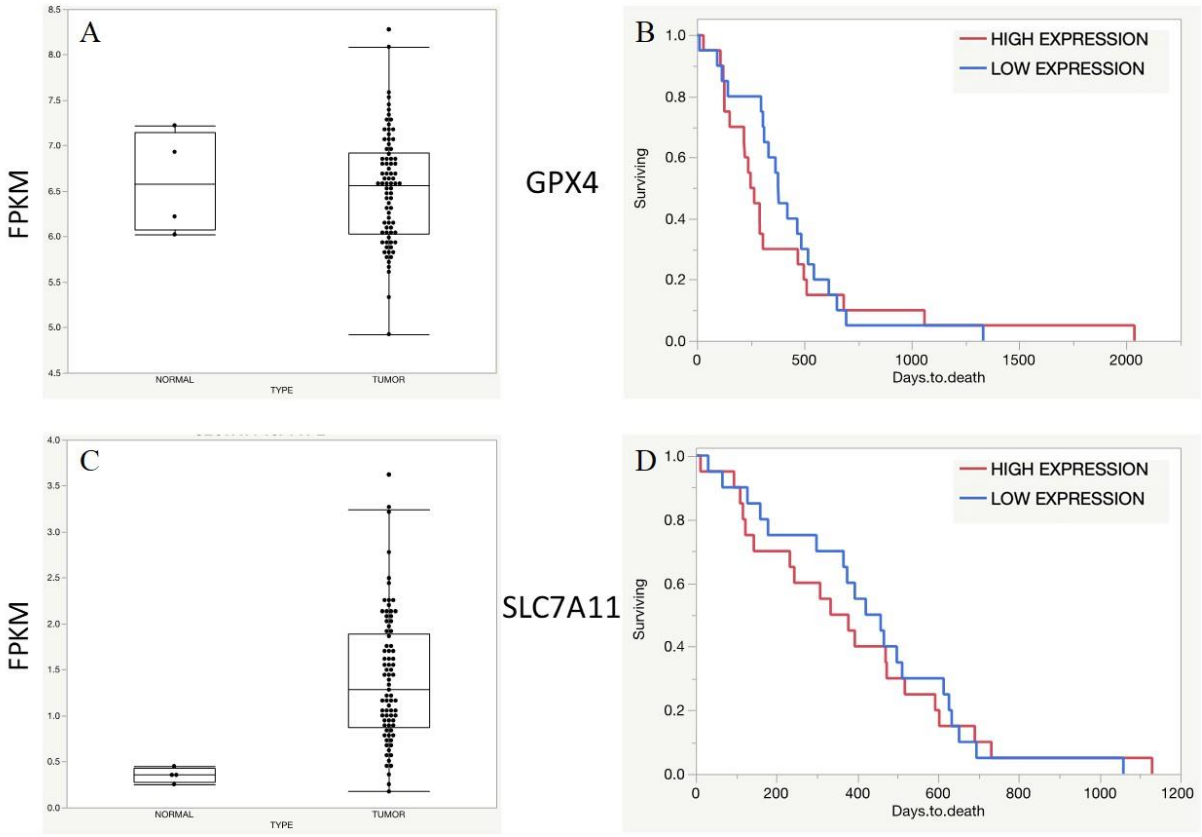
A
FPKM
NORMAL
TUMOR
TYPE
GPX4
B
HIGH EXPRESSION
LOW EXPRESSION
Surviving
Days.to.death
C
FPKM
NORMAL
TUMOR
TYPE
SLC7A11
D
HIGH EXPRESSION
LOW EXPRESSION
Surviving
Days.to.death

Figure 5. 5 GPX4 and SLC7A11 protein expression in PDAC cell lines

GPX4 and SCL7A11 protein expression were analyzed *via* western blot in CD18/HPAF, MiaPaCa, Colo357, AsPC1, Panc1, Capan1, T3M4, and BxPC3 PDAC cell lines and one immortalized normal human pancreatic ductal epithelium cell line, HPDE. There was no significant difference observed in GPX4 expression between the PDAC cell lines and HPDE. SLC7A11 protein level was increased in CD18/HPAF, MiaPaCa, Panc1, T3M4, and BxPC3 cell lines (5 out of 8).

Figure 5.5

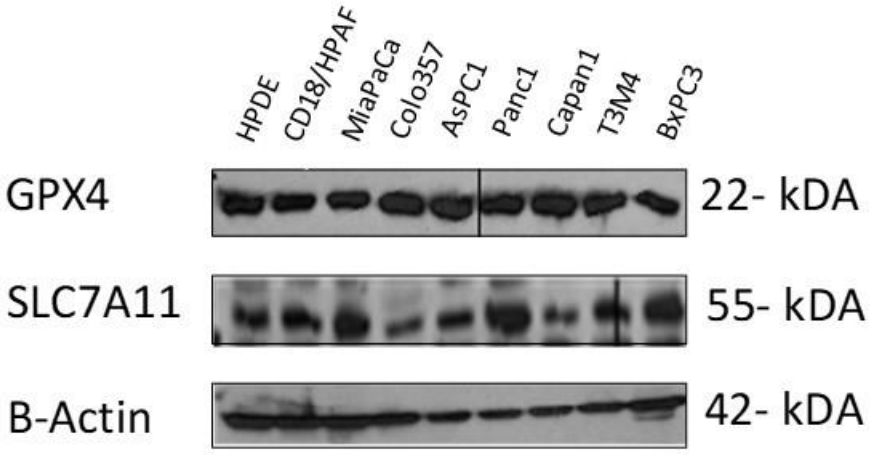
HPDE
CD18/HPAF
MiaPaCa
Colo357
AsPC1
Panc1
Capan1
T3M4
BxPC3
GPX4
22- kDA
SLC7A11
55- kDA
B-Actin
42- kDA

5.3.3 Most PDAC cell lines are more sensitive to Erastin than HPDE

Given these bioinformatics and protein data, we next sought to determine the efficacy of ferroptotic induction *via* pharmacological system X_c inhibition. Prior to the initiation of the *in vitro* experiments, the effect of SLC7A11 knockdown was queried in a publicly available RNAi screen conducted on 398 diverse cancer cell lines put forth by the Broad Institute called Project DRIVE [225]. This compendium was designed to elucidate dependencies and vulnerabilities associated with specific cancer types. Notably, five out of the top 25 most sensitivity cancer cell lines to SLC7A11 KD were PDAC and are highlighted by the red bars in **Figure 5.6**.

In vitro assessment of pharmaceutical inhibition of System X_c was conducted with Erastin, a small molecule inhibitor of SLC7A11 known to induce ferroptosis. The lethality of 0.312, 0.6125, 1.25, 2.5, 5, and 10 μM concentrations of Erastin in the eight PDAC cell lines, as well as HPDE, was measured by MTT assay at 24 and 48-hour time points. A non-linear fit of the MTT data allowed for the adjudication of the 48 hour IC50 values (**Figure 5.7A**). All but two of the PDAC cell lines (MiaPaCa and BxPC3) were more sensitive to ferroptotic induction *via* Erastin than HPDE cells. The 24 and 48-hour non-linear fit graphs are also presented for HPDE and the two cell lines that were used for the remainder of the studies (Panc1 and CD18/HPAF) in **Figure 5.7B**. Of note, HPDE is unaffected by Erastin treatment for 24 hours and the slope at 48 hours is not nearly a precipitous as the two PDAC cell lines. These data together suggest that PDAC cells are more sensitive to Erastin treatment that normal immortalized pancreatic epithelium.

Figure 5. 6 Project DRIVE analysis of RNAi SLC7A11 knockdown in PDAC cell lines

SLC7A11 RNAi screening of 398 cell lines from different cancer types showed that PDAC cell lines were 5 of the top 25 (including the 1st, 3rd, 8th, 20th, and 23rd) most susceptible cell lines. It is displayed here as the Project Drive susceptibility score. The more negative the score the more reliant upon SLC7A11 the cell line is. The PDAC cell lines are highlighted in red.

Figure 5.6

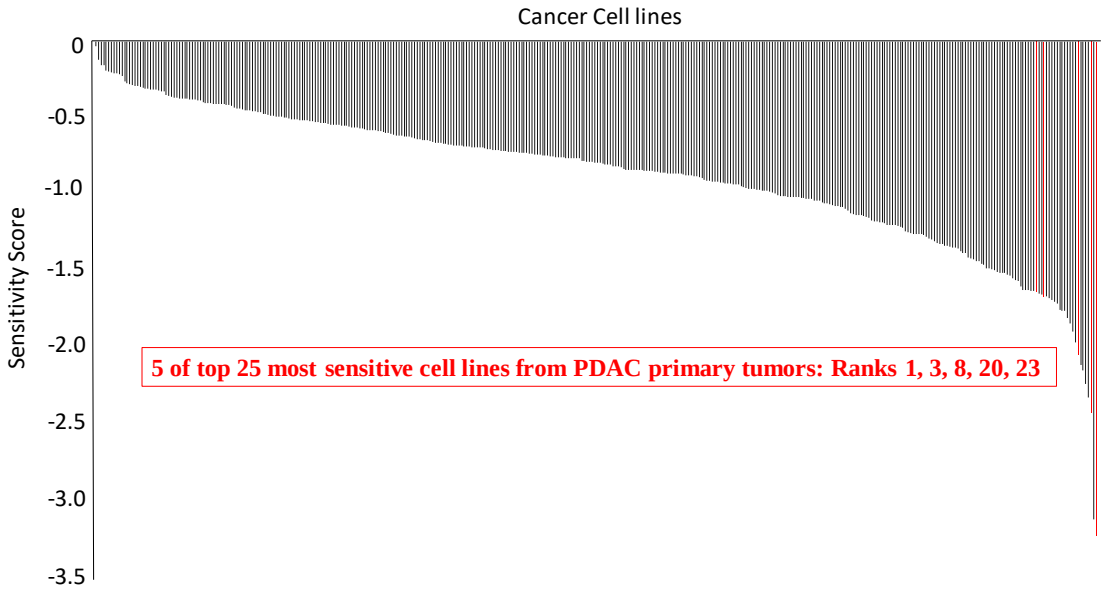
Cancer Cell lines
Sensitivity Score
0
-0.5
-1.0
-1.5
-2.0
-2.5
-3.0
-3.5
5 of top 25 most sensitive cell lines from PDAC primary tumors: Ranks 1, 3, 8, 20, 23

Figure 5. 7 Erastin MTT survival curves in PDAC cell lines and HPDE

Cell survival with different μM concentrations of Erastin (10, 5, 2.5, 1.25, 0.625, and 0.3125) was determined by MTT assay at 24 and 48-hour time points. It is displayed here as % viability relative to untreated control. A non-linear regression analysis was applied and IC50 concentrations elucidated **A**. The 48-hour survival curves of all the PDAC cell lines CD18/HPAF, MiaPaCa, Panc1, Colo357, T3M4, AsPC1, and BxPC3 along with the listed IC50 concentrations. **B.** 24 and 48-hour survival curves for HPDE as well as the two PDAC cell lines used in the remainder of the experiments, CD18/HPAF and Panc1. Of note, the normal cell line HPDE was far more resistant to Erastin induced cell death with no effect at 24 hours, even at 10 μM concentration and a far less steep slope at 48 hours compared to the PDAC cell lines.

Figure 5.7

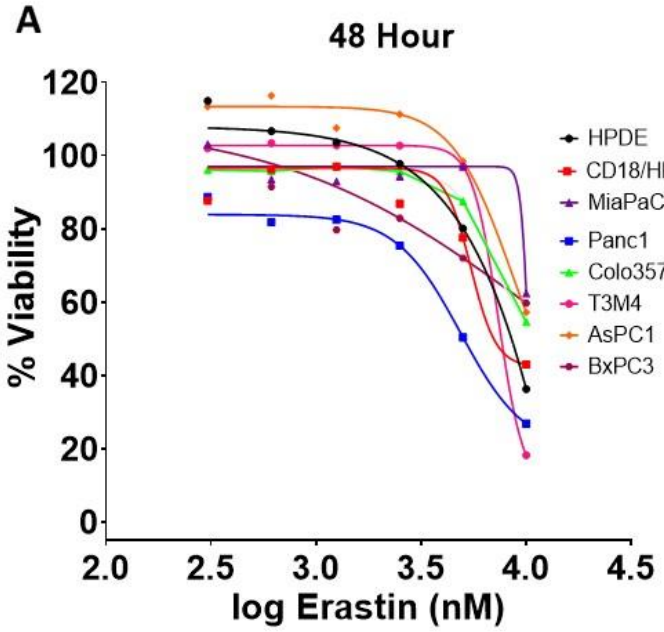

Cell line	IC50
HPDE	9.23
CD18/HPAF	8.45
MiaPaCa	10.34
Panc1	4.86
Colo357	6.89
T3M4	7.35
AsPC1	8.53
BxPC3	9.95

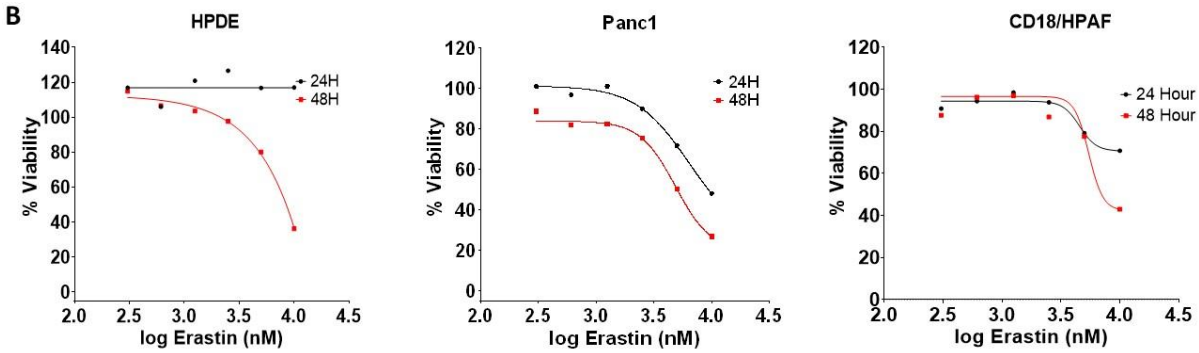

5.3.4 Erastin inhibits cellular migration

A scratch migration assay was conducted over the course of 72 hours on CD18/HPAF cells in the presence of various Erastin concentrations (1, 5, and 10 μM) to assess its functional ability to prevent cell migration. The area of the cruciform scratch was evaluated on day one and at 24, 48, and 72-hour time points with Image J software. The percent wound closure was calculated by dividing the measured area remaining at a given time point by the initial scratch area. Indeed, the wound closure percentage was decreased in a concentration-dependent manner at all three-time points (**Figure 5.8**).

5.3.5 Erastin treatment decreases intracellular GSH

The mechanism by which Erastin is said to induce ferroptosis is by preventing cysteine import required for GSH synthesis [515]. Thus, we next sought to verify that this was true by testing total glutathione levels after 24-hour treatment with Erastin in CD18/HPAF and Panc1 cancer cell lines. Treatment concentrations for each cell line were adjusted to below the projected 24 hour IC20 (as determined by the previous MTT assays) to 1 μM for Panc1 and 2 μM for CD18/HPAF (of note, these are the cell line-specific concentrations that will be used for the remainder of the experiments). Indeed, Erastin effectively reduced the total glutathione (GSH) concentrations to 61.7% of the untreated control in CD18/HPAF cells and 26.6% in Panc1 cells (**Figure 5.9**). Interestingly, even at the higher concentration, total GSH in CD18/HPAF was less effected by Erastin treatment, which mirrors the respective sensitivities to Erastin induced cell death as determined by MTT. These data suggest that CD18/HPAF may not have as much reliance upon SLC7A11 as Panc1 for the production of GSH and could be supported by an alternative pathway, i.e. transsulfuration.

Figure 5. 8 Erastin impact on CD18/HPAF migration

The ability of 1 µM, 5 µM, and 10 µM concentration of Erastin to reduce CD18/HPAF cell migration was assessed *via* scratch assay with images taken at 24, 48, and 72 hours. It is displayed here as the total percentage of wound closure at the given time. An impressive reduction in cellular migration was noticed at the 10 µM concentration at all times measured.

Figure 5.8

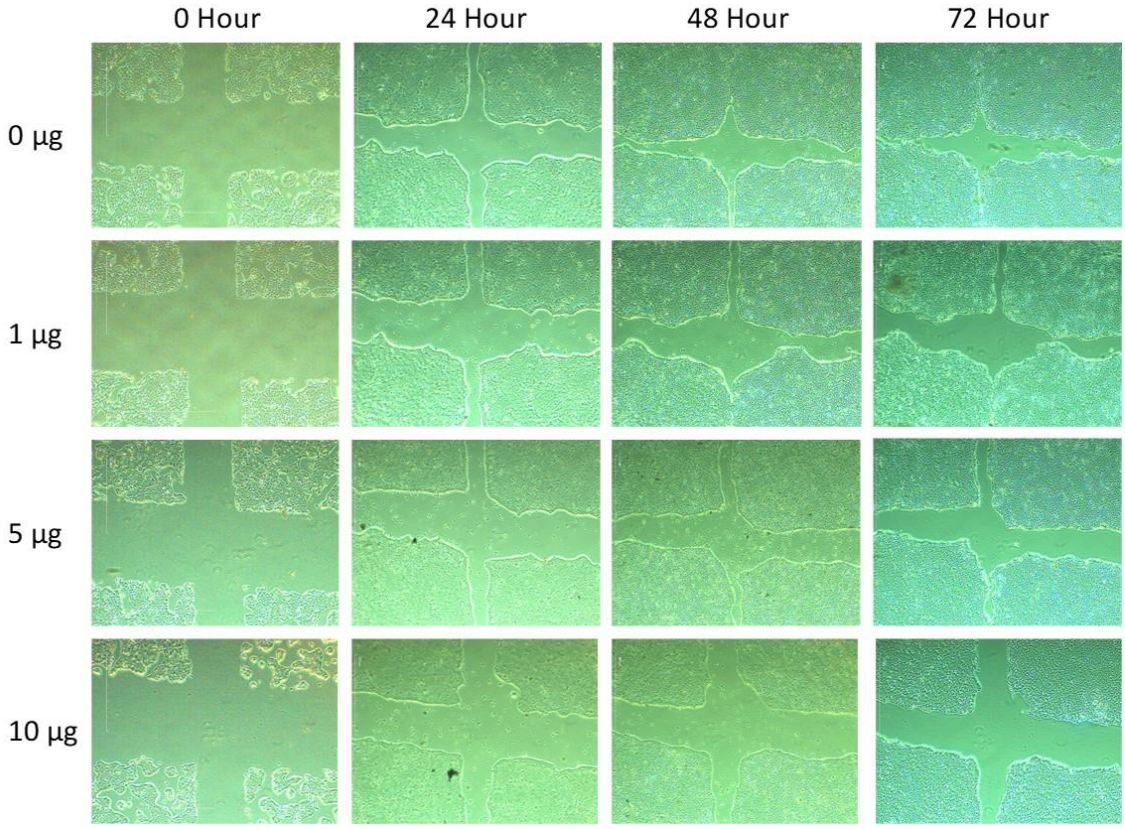
0 Hour
24 Hour
48 Hour
72 Hour
0 µg
1 µg
5 µg
10 µg

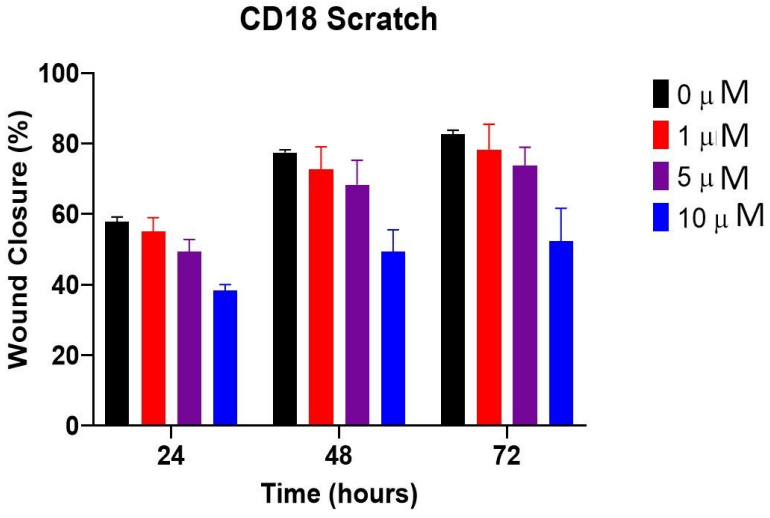
CD18 Scratch
Wound Closure (%)
100
80
60
40
20
0
24
48
72
Time (hours)
0 µM
1 µM
5 µM
10 µM

Figure 5. 9 Erastin depletion of glutathione

Panc1 was treated with 1 µM Erastin and CD18/HPAF with 2 µM Erastin for 24 hours at which point the total amount of glutathione present was determined. Erastin concentrations for each cell line were based on the IC20 values measured from the previous MTT experiments. Erastin treatment caused a 70% reduction and 40% reduction in proportion to the no treatment control in Panc1 and CD18/HPAF, respectively.

Figure 5.9

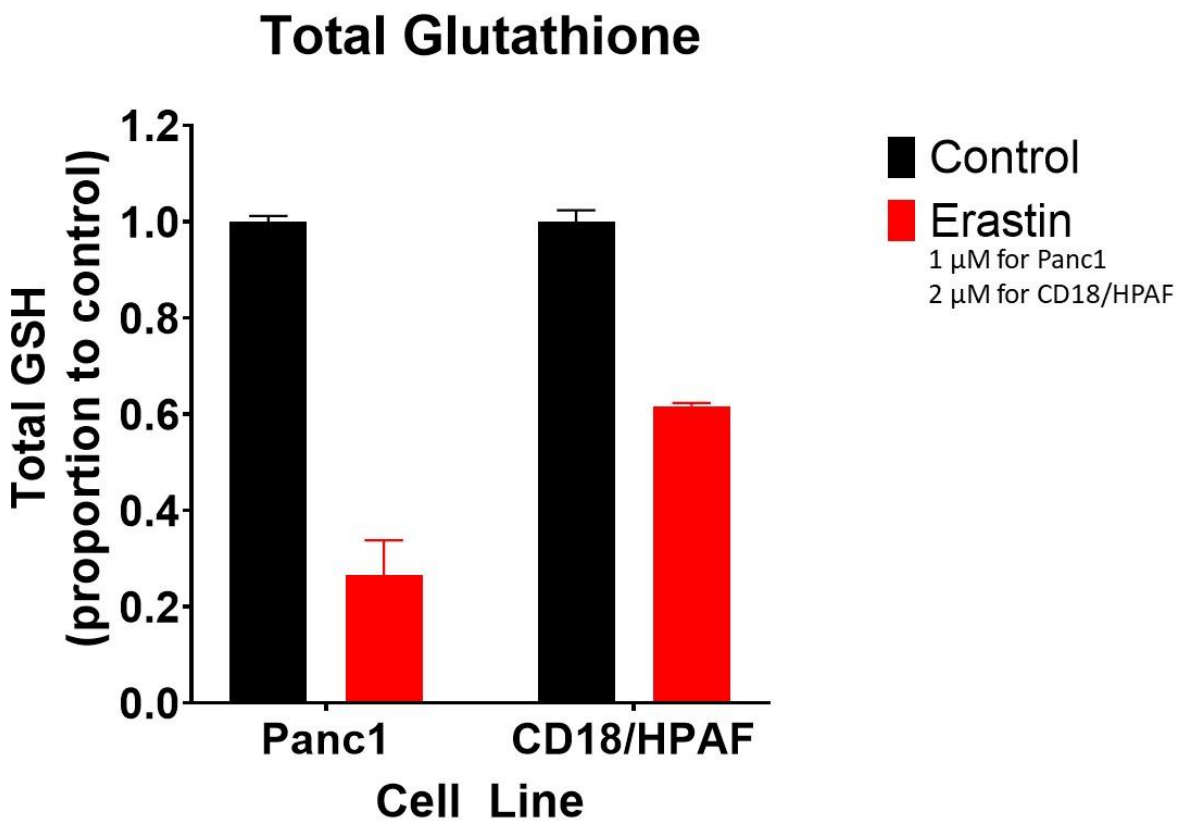
Total Glutathione
Total GSH
(proportion to control)
1.2
1.0
0.8
0.6
0.4
0.2
0.0
Panc1
CD18/HPAF
Cell Line
Control
Erastin
1 µM for Panc1
2 µM for CD18/HPAF

5.3.6 Radiation promotes GPX4, SLC7A11 expression and the phosphorylation of NRF2 *in vitro*

Publicly available microarray data of four PDAC cell lines (Panc1, AsPC1, MiaPaCa, and BxPC3) 6 hours after receiving a 2Gy dose of radiation was analyzed for our genes of interest. While SLC7A11 was not present in the microarray platform, GPX4 was highly upregulated in the irradiated cells compared to the non-radiated controls (**Figure 5.10A**). Specifically, GPX4 was the second most upregulated mRNA in both Panc1 and AsPC1, and the tenth and 111th most in MiaPaCa and BxPC3, respectively. Thus, suggesting an integral role of GPX4 in the response to radiation as well as the possibility of radiation-induced ferroptosis. Many genes involved in the induction of ferroptosis were down-regulated such as fatty acid-CoA ligase 4 (ACSL4/FACL4) [516], voltage-dependent anion channels (VDAC) 1-3 [517], and nuclear receptor coactivator 4 (NCOA4) (**Figure 5.10A**). Notably, NCOA4 is the known inducer of ferritinophagy (specific autophagy of iron-bound ferritin that releases free Fe^{2+}) thereby facilitating iron-mediated lipid peroxidation and eventual ferroptosis [518]. Concurrently, the iron sequestration molecule heat shock protein family B (small) member 1 (HSPB1) was upregulated (a known ferroptosis inhibitory molecule capable of binding free Fe^{2+} [519] as was glutathione synthetase (GSS) in the setting of radiation. Of not, GSS and GPX4 are transcribed by the transcription factor NRF2 [503].

Assessment of GPX4 and SLC7A11 at the protein level was conducted on Panc1 and CD18/HPAF cell lines at 6, 12, 24, 48, and 72 hour time points following the administration of 5Gy radiation. GPX4 expression was slightly increased in both cell lines though at an earlier time point in the Panc1 cell line compared to CD18/HPAF (**Figure**

5.10B). A more impressive increase was found in the time-dependent expression of SLC7A11 as well as the phosphorylation of NRF2 (the transcription factor responsible for GPX4, GSS, and SLC7A11 transcription [520]) in both cell lines (**Figure 5.10B**). Phosphorylation of NRF2 has been shown to increase nuclear localization and promotes transcription [521]. Taken together, these data suggest the importance of the SLC7A11-GSH-GPX4 axis in the response to radiation.

5.3.7 SLC7A11 is increased in PDAC and radiated patient tissues

The protein expression of GPX4 and SLC7A11 was next assessed via immunohistochemistry (IHC) staining in 8 healthy, 21 PDAC, and 12 irradiated PDAC patient tissue samples graciously provided by Dr. Chi Lin in the Department of Radiation Oncology at the University of Nebraska Medical Center. Slides were graded by a certified pathologist and H-scoring conducted as described in the methods chapter. GPX4 expression was not significantly different between the three cohorts (**Figure 5.11A**). SLC7A11 was relatively unchanged between the healthy and PDAC samples but significantly increased in the irradiated samples compared to both PDAC and healthy controls (**Figure 5.11B**).

5.3.8 SLC7A11 gene expression is significantly correlated with survival in radiated patients

Since SLC7A11 was increased so dramatically in the irradiated patient samples, we next determined its correlation with survival using the radiation patient PDAC cohort within the TCGA dataset. For those PDAC patients that underwent radiation treatment, SLC7A11 was significantly correlated with worse survival outcomes (Log-Rank test $p = 0.0344$, Wilcoxon test $p = 0.0478$, **Figure 5.12A**). The median survival time for patients

Figure 5. 10 mRNA and protein analysis of PDAC cell lines after radiation

A. A publicly available microarray dataset of mRNA analysis from 4 PDAC cell lines (Panc1, AsPC1, MiaPaCa, and BxPC3) exposed to 2Gy radiation and collected after 6 hours was used for this analysis. Radiation exposure caused an increase myriad molecules involved in ferroptosis including GPX4 and glutathione synthetase (GSS) (notably, both are transcription products of NRF2 transcription factor). Additionally, mRNA encoding the iron liberating protein implicated in ferroptosis, NCOA4, was decreased while that for HSPB1, an iron sequestration protein known to inhibit ferroptosis, was upregulated. **B.** GPX4 and SLC7A11 expression in Panc1 and CD18/HPAF cell lysates collected from cells at 6, 12, 24, 48, and 72 hours after 5Gy radiation exposure was measured via western blot. While GPX4 showed a marginal increase in both cell lines, SLC7A11 was dramatically increasing upon radiation exposure. Also, phosphorylation of NRF, a modification that has been shown to increase nuclear translocation and facilitate transcription, was increased after exposure to radiation. Of note, Along with GPX4 and GSS, NRF is responsible for the transcription of SLC7A11.

Figure 5.10

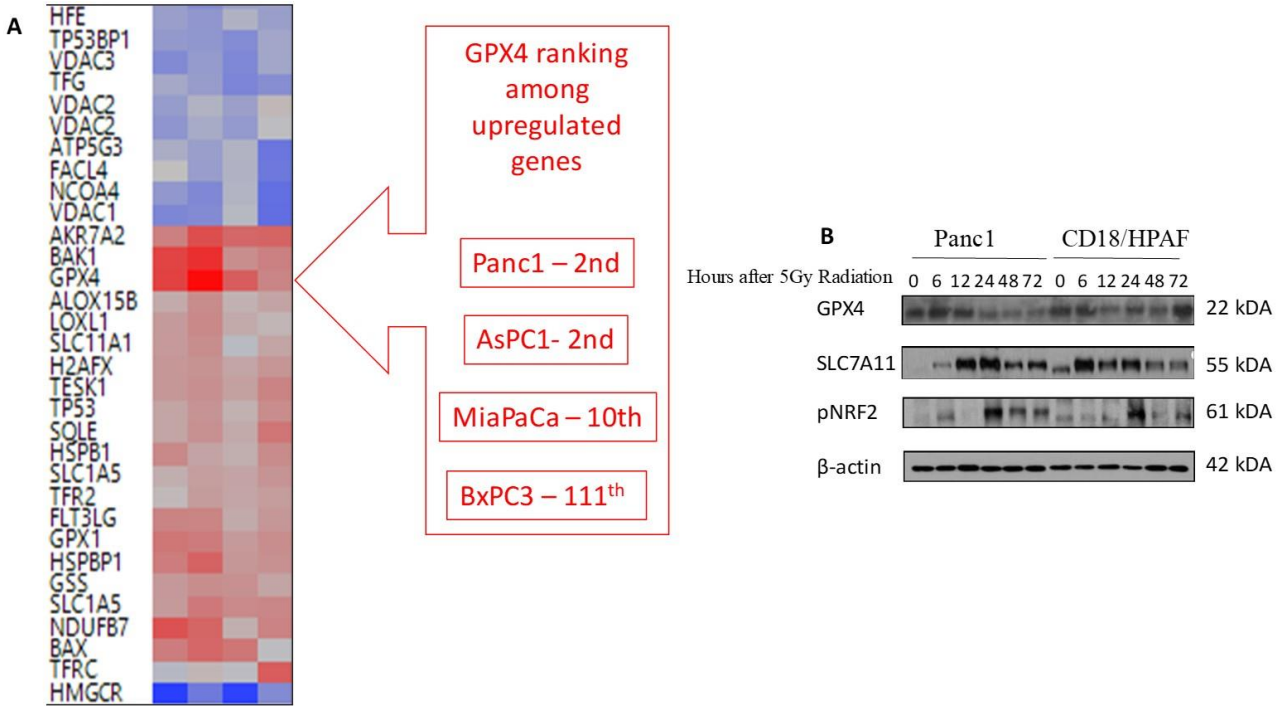
A
HFE
TP53BP1
VDAC3
TFG
VDAC2
VDAC2
ATP5G3
FACL4
NCOA4
VDAC1
AKR7A2
BAK1
GPX4
ALOX15B
LOXL1
SLC11A1
H2AFX
TESK1
TP53
SQLE
HSPB1
SLC1A5
TFR2
FLT3LG
GPX1
HSPBP1
GSS
SLC1A5
NDUFB7
BAX
TFRC
HMGCR
GPX4 ranking among upregulated genes
Panc1 – 2nd
AsPC1- 2nd
MiaPaCa – 10th
BxPC3 – 111th
B
Panc1
CD18/HPAF
Hours after 5Gy Radiation
0 6 12 24 48 72 0 6 12 24 48 72
GPX4
22 kDA
SLC7A11
55 kDA
pNRF2
61 kDA
β-actin
42 kDA

Figure 5. 11 GPX4 and SLC7A11 protein expression in patient tissue samples

Immunohistochemical (IHC) analysis was conducted on 8 healthy, 21 PDAC, and 12 irradiated PDAC patient samples to assess the levels of GPX4 and SLC7A11. The tissue level of each protein is presented as an H-score (for more on how H-scores were calculated see Chapter 2). **A.** No significant difference in tissue expression of GPX4 was observed between all three groups. **B.** SLC7A11 was significantly increased in irradiated samples compared to healthy ($p < 0.005$) and non-irradiated PDAC ($p < 0.005$).

Figure 5.11

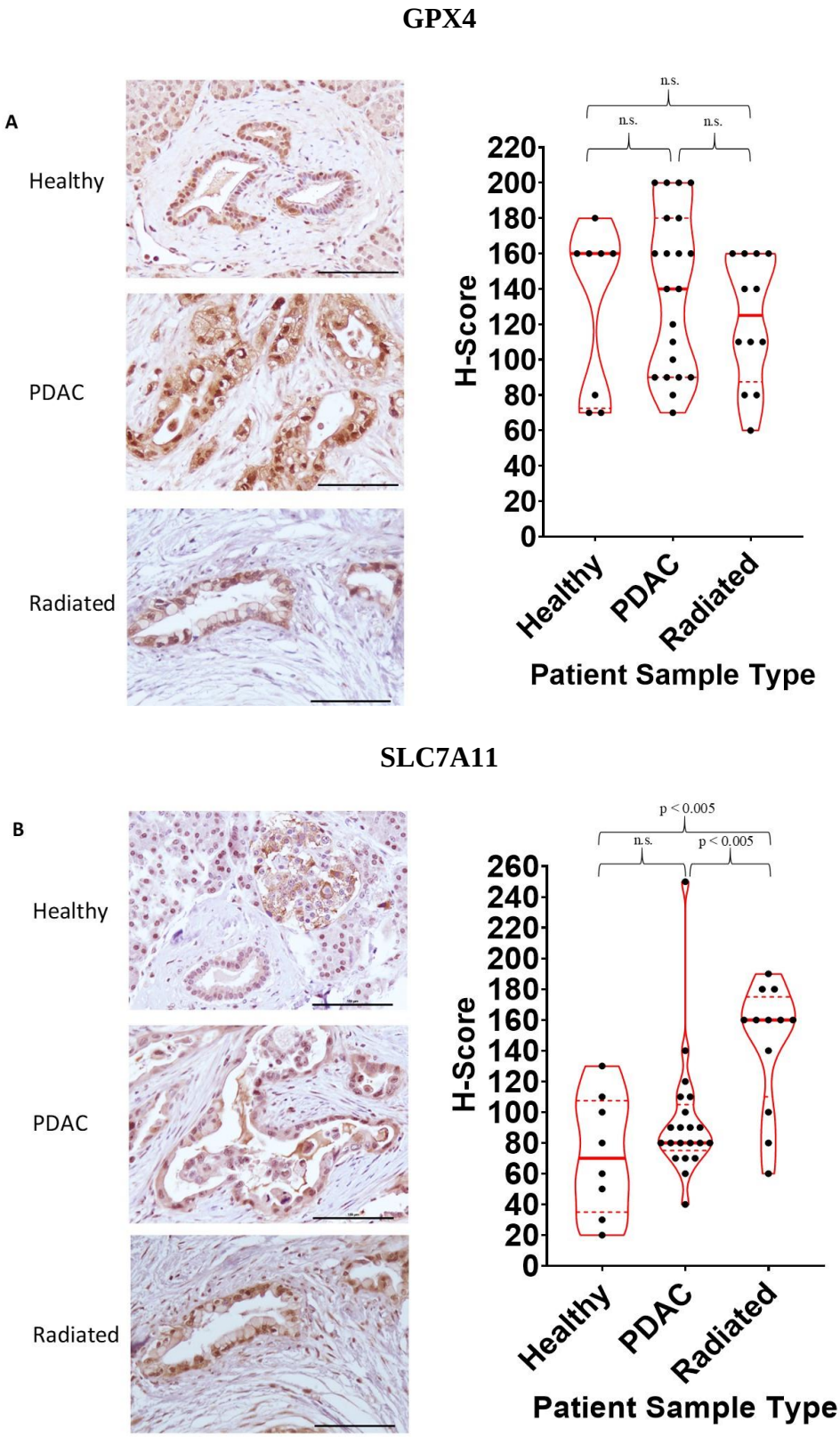
GPX4
A
Healthy
PDAC
Radiated
n.s.
n.s.
n.s.
H-Score
220
200
180
160
140
120
100
80
60
40
20
0
Healthy
PDAC
Radiated
Patient Sample Type
SLC7A11
B
Healthy
PDAC
Radiated
p < 0.005
n.s.
p < 0.005
H-Score
260
240
220
200
180
160
140
120
100
80
60
40
20
0
Healthy
PDAC
Radiated
Patient Sample Type

Figure 5. 12 SLC7A11 survival of radiated PDAC patients in TCGA

The PDAC patient RNA sequencing data in TCGA was revisited and the correlation between SLC7A11 expression and survival was assessed within the patient cohort that received radiation therapy. **A.** An impressive shift occurred from the survival analysis of SLC7A11 in the complete PDAC population. Its expression became significantly correlated with survival. A finding made all the more impressive by the fact that the total patients who received radiation and were analyzed were 12 (6 high and 6 low expressers). **B.** The previously presented SCL7A11 survival curve for the entire PDAC population provided for reference.

Figure 5.12

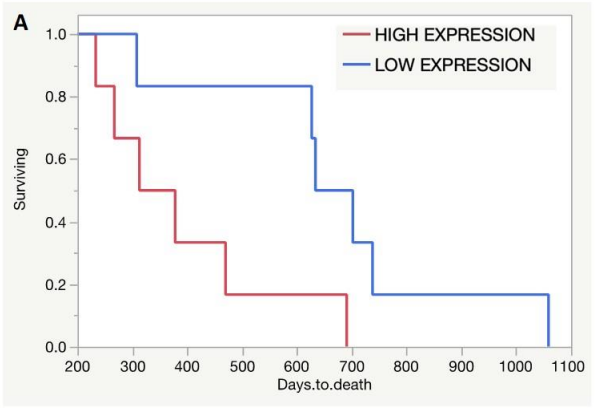

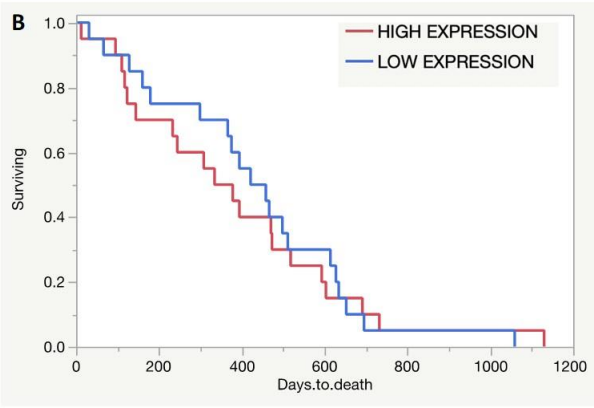

Test	ChiSquare	DF	Prob>ChiSq
Log-Rank	4.4759	1	0.0344*
Wilcoxon	3.9184	1	0.0478*

with low expression was 668 days while those with high expression were only 345.5 days. This is made even more interesting by the fact that no significant difference was observed in the entire PDAC patient cohort when considering SLC7A11 expression. The Kaplan-Meier curve presented at the beginning of this section is provided in panel B of this figure for reference (**Figure 5.12B**).

5.3.9 GPX4 knockdown sensitizes cells to radiation-induced cell death *in vitro*

Given the observed impact of radiation on GPX4 and SLC7A11 expression in cell lines and patient samples, we next evaluated the effect of GPX4 knockdown (KD) in the setting of radiation on cellular viability *in vitro*. 50 nmol GPX4 siRNA was transfected into CD18/HPAF and Panc1 PDAC cells using lipofectamine, allowed to incubate for 48 hours to achieve adequate KD, and clonogenic colony-forming assays conducted in the manner described in the methods chapter of this thesis. GPX4 KD had a dramatic effect in Panc1 by itself, resulting in almost zero colony formation (**Figure 5.13A**). This is not unexpected given the high sensitivity of the Panc1 cell line to Erastin. While GPX4 KD alone did affect the colony-forming capacity of CD18/HPAF, this was noticeably enhanced with the concurrent delivery of 5Gy radiation treatment (**Figure 5.13B**). Congruently, the combination treatment dramatically reduced the number of colonies as compared to radiation treatment alone.

5.3.10 Erastin and radiation synergistically induce cell death

To determine the radiation potentiation effect of pharmacological inhibition of System X_c with Erastin, colony-forming viability assays were next conducted on Panc1 and CD18/HPAF. Erastin effectively potentiated the lethality of radiation in a concentration depended manner, in both cell lines (**Figure 5.14A-B**). As can be seen in the

Figure 5. 13 Impact of GPX4 knockdown on CD18/HPAF and Panc1 survival in the setting of radiation

Colonies are presented on the left side of the panel and how the effect of GPX4 knockdown on the viability of cells with and without 5Gy radiation treatment. The quantification of colony number is presented as a proportion of the untreated control and is displayed on the right. **A.** Unfortunately, GPX4 knockdown in the Panc1 cell line proved too lethal to be able to assess any impact in the setting of radiation. This is not unexpected and is in line with our previous findings of Panc1 hypersensitivity to upstream GPX4 inhibition *via* Erastin treatment **B.** For CD18/HPAF GPX4 KD was able to sensitize cells to radiation treatment resulting in a greater proportion of cell death with the combination treatment.

Figure 5.13

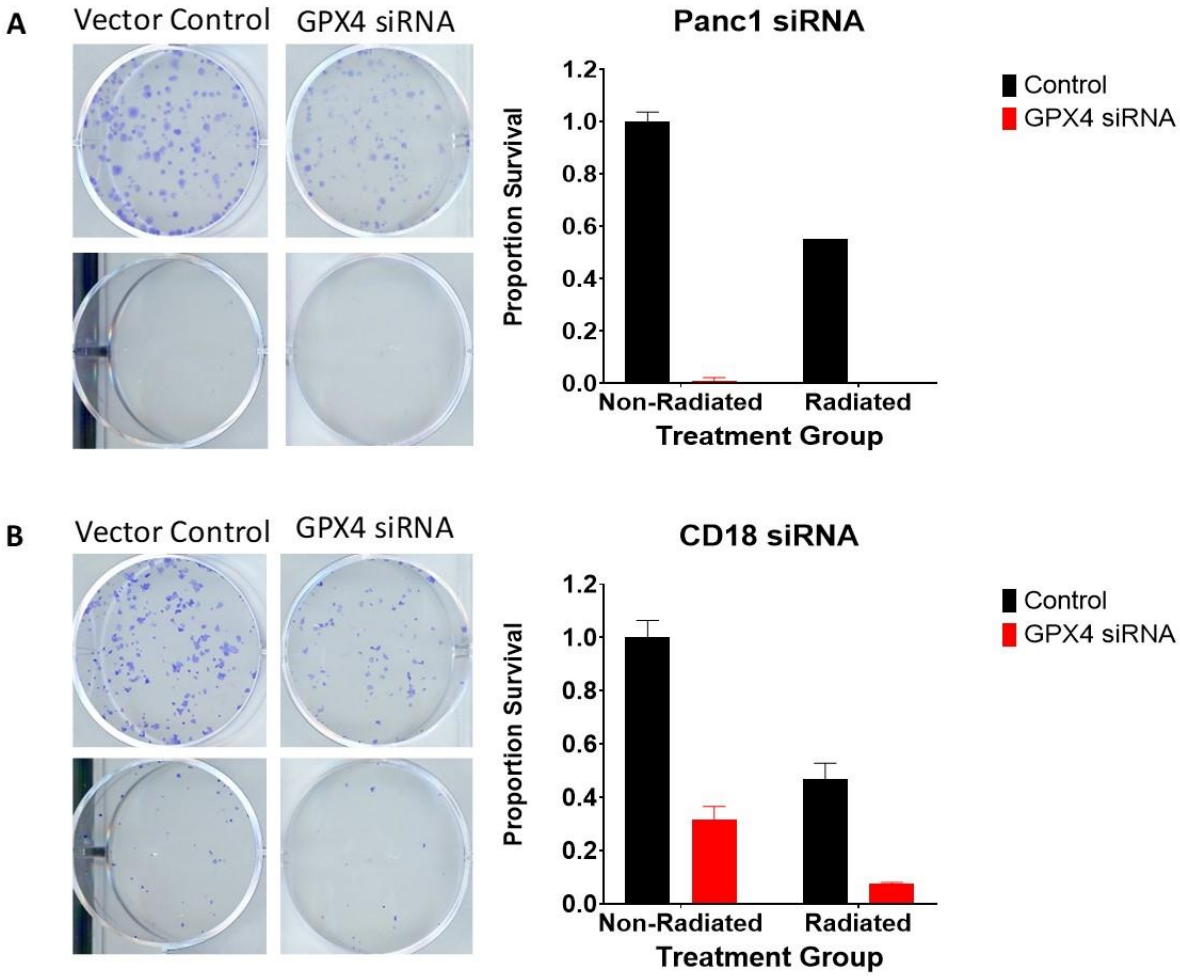
A
Vector Control
GPX4 siRNA
Panc1 siRNA
Proportion Survival
1.2
1.0
0.8
0.6
0.4
0.2
0.0
Non-Radiated
Radiated
Treatment Group
Control
GPX4 siRNA
B
Vector Control
GPX4 siRNA
CD18 siRNA
Proportion Survival
1.2
1.0
0.8
0.6
0.4
0.2
0.0
Non-Radiated
Radiated
Treatment Group
Control
GPX4 siRNA

graphical representation of the data, the highest concentration of Erastin tested, 2 μM, was required for adequate radiation potentiation in CD18/HPAF cells but was overtly lethal alone in Panc1 cells (this is directly in line with the previous MTT result for each cell line and their respective IC20 concentrations, **Figure 5.7**). A direct comparison of the survival of each cell line at 5Gy radiation is provided in **Figure 5.15**. In Panc1, 1 μM Erastin causes a significant reduction in survival at 5Gy while 2 μM is required to reach significance in CD18/HPAF. The difference in the respective radiation enhancement ratios (ER) for each concentration of Erastin are also presented to show the relative inter-concentration and individual cell efficacy, as determined by the Fertil linear quadratic method as described in Chapter 2 of this thesis (**Figure 5.14A-B**).

The online software Combenefit utilizes three individual synergy models, BLISS, Loewe, and HSA to determine if true synergism exists (and not merely additivity) between two treatments. The BLISS model takes into account the effect of each treatment independently and determines the level of synergism predicated on efficacy above the product of the combination lethality, i.e. $L_C < L_{T1}L_{T2}$; where L_c is the lethality of the combination treatment, and L_{T1} and L_{T1} are the lethality of treatment 1 and treatment 2, respectively. The Loewe model assumes linearity and is predicated on the IC50 values while the HSA model has the loosest definition for synergism where any death above single treatment is considered synergistic. Because of these reasons the BLISS model was chosen for subsequent analysis. The interpretation of BLISS synergy scores can be assumed as follows: < -10 is considered likely antagonism, 10 to 10 is considered likely additivity, and >10 is considered likely synergism.

Figure 5. 14 Response of CD18/HPAF and Panc1 to combination radiation and Erastin treatment

Colonies are presented on the left side of the panel and show the effect 0.0, 0.1, 0.5, 1.0, and 2.0 μM Erastin at 0, 1, 3, 5, and 7Gy radiation. The resultant survival curves are presented on the right as well as the associated radiation enhanced ratio (ER). Erastin displayed the ability to potentiate radiation induces cell death in a concentration-dependent manner in both cell lines **A & B**. Although, notable yet as expected, the 2 μM concentration was too high by itself in Panc1 leading to almost complete cell death by itself.

Figure 5.14

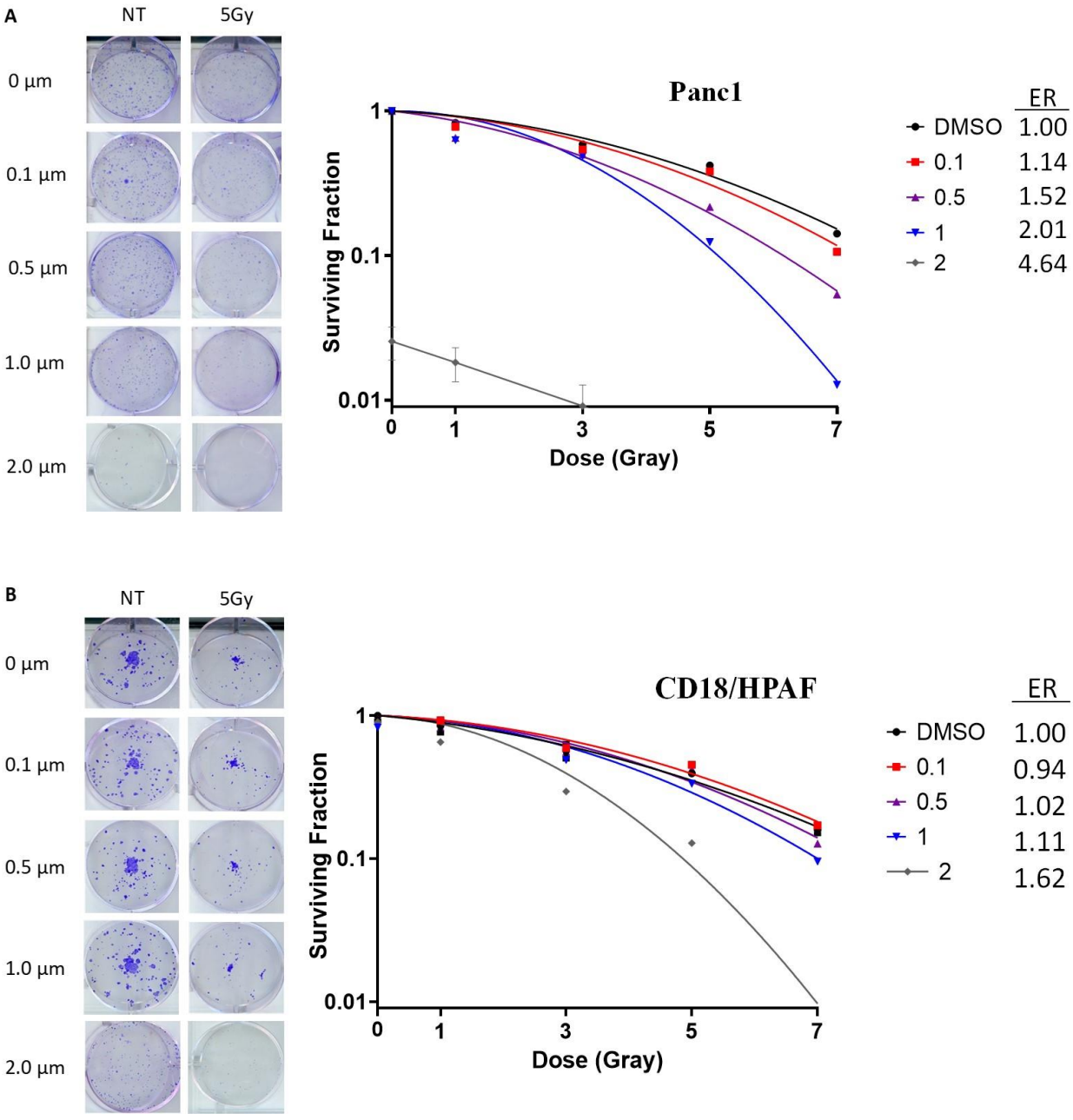
A
NT
5Gy
0 µm
0.1 µm
0.5 µm
1.0 µm
2.0 µm
Panc1
Surviving Fraction
1
0.1
0.01
0
1
3
5
7
Dose (Gray)
ER
DMSO 1.00
0.1 1.14
0.5 1.52
1 2.01
2 4.64
B
NT
5Gy
0 µm
0.1 µm
0.5 µm
1.0 µm
2.0 µm
CD18/HPAF
Surviving Fraction
1
0.1
0.01
0
1
3
5
7
Dose (Gray)
ER
DMSO 1.00
0.1 0.94
0.5 1.02
1 1.11
2 1.62

Figure 5. 15 Direct comparison between CD18/HPAF and Panc1 response to Erastin with 5Gy radiation treatment

Viability is presented as the proportional survival relative to untreated control. All treatment provides a significant reduction in cell viability as compared to control in both cell lines. However, 1 μM and 2 μM Erastin provide a significant increase in the level of cell death at 5Gy above that of radiation alone in Panc1 while only 2 μM Erastin treatment does so in CD18/HPAF.

Figure 5.15

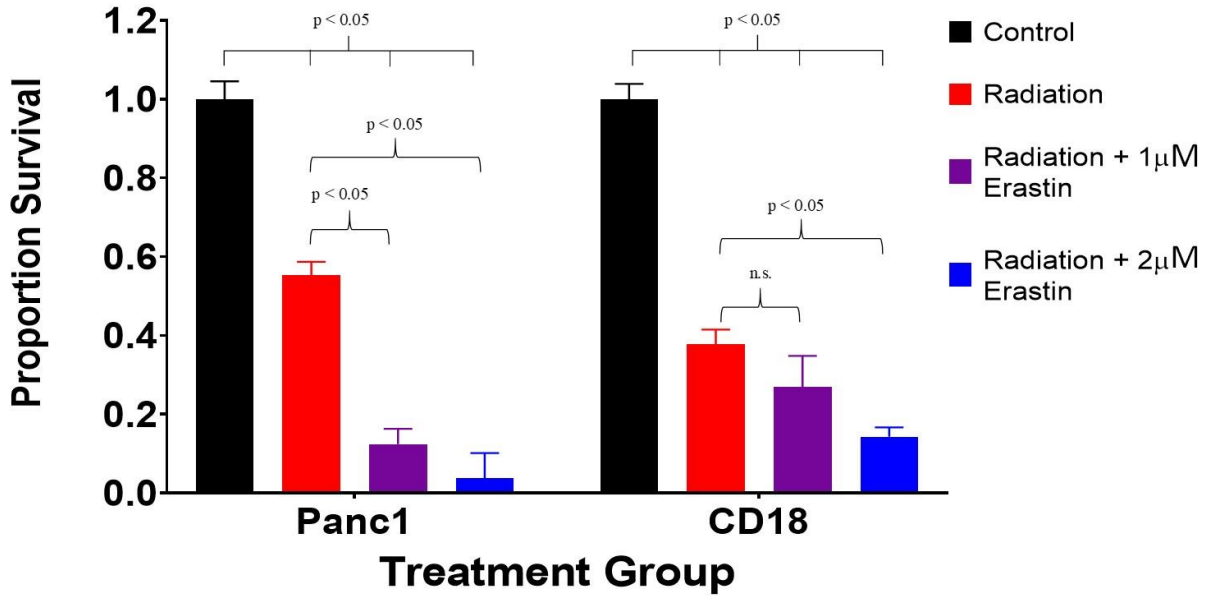
1.2
1.0
0.8
0.6
0.4
0.2
0.0
Proportion Survival
p < 0.05
p < 0.05
p < 0.05
p < 0.05
p < 0.05
n.s.
Panc1
CD18
Treatment Group
Control
Radiation
Radiation + 1μM Erastin
Radiation + 2μM Erastin

Our survival data was utilized to determine if any additive and/or synergistic lethality exist with combination Erastin and Radiation treatment, compared to either treatment alone. Indeed, a high degree of synergism was found with combination treatment in both CD18/HPAF and Panc1 cells, each attaining a BLISS score exceeding 40 (**Figure 5.16A-B)**. The percent decrease in viability is presented in the subpanel i of each panel and topographic representation of the BLISS scores as a function of treatment concentrations are presented in subpanels ii and iii. These are presented as a matrix in subpanel iv where one can see the actual numerical representation of the synergism present. Interestingly, a comparison between the CD18/HPAF matrix in **Figure 5.16Aiv** and the Panc1 matrix in **Figure 5.16Biv** brings to light the difference in the synergy pattern. Where the highest level of synergy occurs in CD18/HPAF at 2 μM Erastin and 3Gy radiation (BLISS score 42), the most efficient synergy observed in Panc1 occurs at 500 nM Erastin and 1Gy radiation. This is indicative of the relative sensitivities of each cell line to radiation as well as Erastin. Of not, synergy is observed (BLISS scores above 10) across a wide array of treatment combinations, though they are not as extreme.

5.3.11 Combination radiation and Erastin treatment-induced cell death is mitigated with the addition of Ferrostatin-1

In an effort to determine if the cell death resulting from the combination treatment is attributable to ferroptosis specifically, we repeated the colon forming assays (both cell lines with 5Gy radiation, CD18/HPAF with 2 μM Erastin and Panc1 with 1 μM Erastin) along with the addition of Ferrostatin-1 (Tocris), a lipophilic antioxidant that inhibits ferroptosis, Necroastain-1 (Sigma), a compound that binds RIPK and inhibits necroptosis, and Z-VAD-FMK (Tocris), a pan-caspase inhibitor and apoptosis inhibitor. The

Figure 5. 16 The lethal effects of radiation and Erastin combination are synergistic

Synergy scores predicated on the BLISS independence model were determined for both cell lines as a part of the online Combenefit Software package. The analysis of Panc1 and CD18/HPAF are presented in panels **A** and **B,** respectively. The subpanels are demarcated as follows: **i**- color map predicated on the percentage of the surviving cells in any given treatment condition, relative to the no treatment control. **ii**- color map of the BLISS synergy scores associated with each treatment condition. **iii**- topographical map depicting the percentage of cell death overlaid with the BLISS synergy score color map. **iv**- Matrix and numerical representation of the BLISS synergy scores associated with each specific treatment condition. The interpretation of BLISS synergy scores can be assumed as follows: < -10 is considered likely antagonism, 10 to 10 is considered likely additivity, and >10 is considered likely synergism.

Figure 5.16

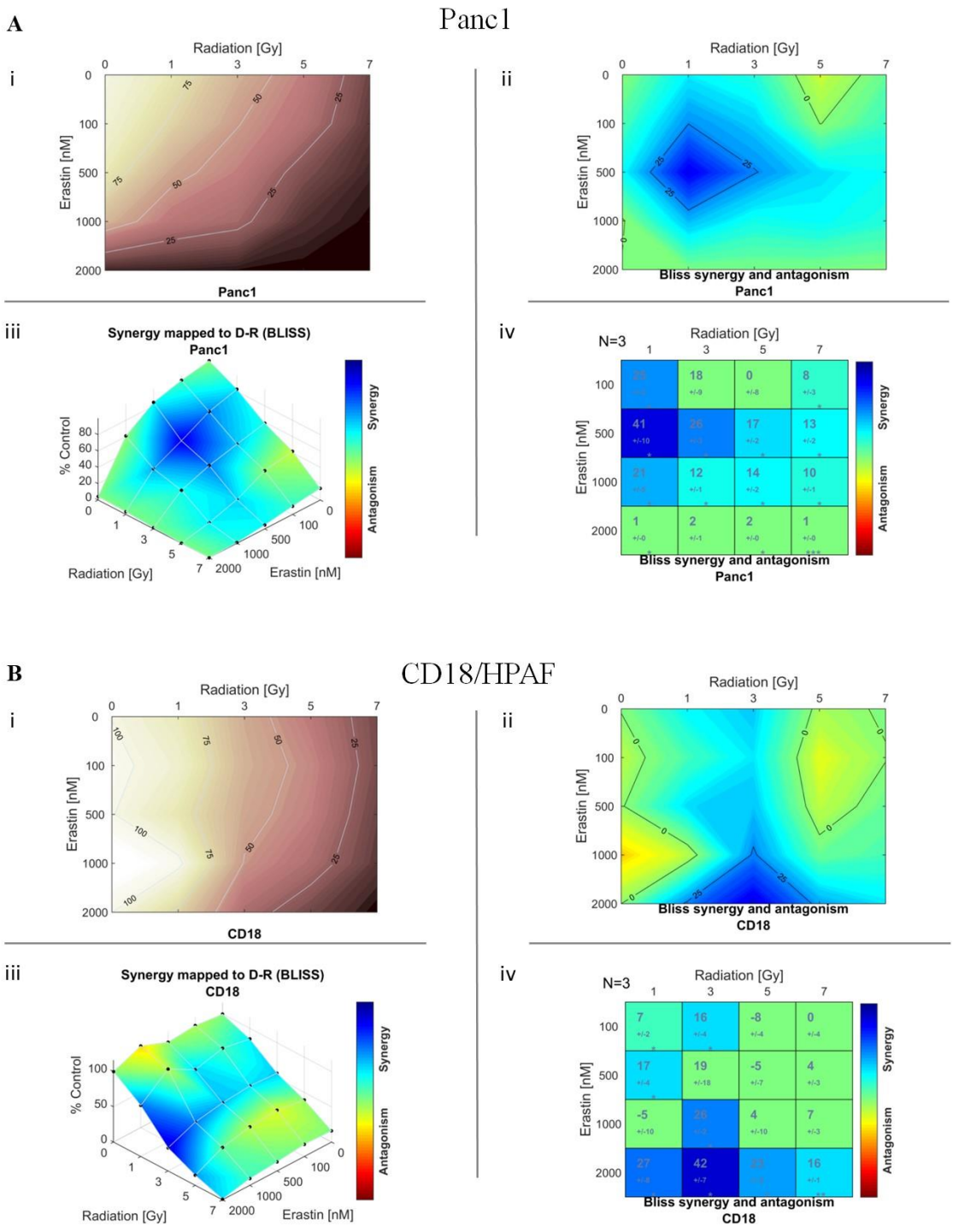
A
Panc1
i
Radiation [Gy]
Erastin [nM]
Panc1
ii
Bliss synergy and antagonism
Panc1
iii
Synergy mapped to D-R (BLISS)
Panc1
% Control
Synergy
Antagonism
iv
N=3
Bliss synergy and antagonism
Panc1
B
CD18/HPAF
CD18
Bliss synergy and antagonism
CD18
Synergy mapped to D-R (BLISS)
CD18

proportional survival with the inhibitors, relative to each treatment condition (i.e. radiation, Erastin, and radiation + Erastin) are shown in **Figure 5.17**. For CD18/HPAF, the lethality of radiation and Erastin alone was not diminished by any of the inhibitors but cell death produced by the combination treatment was partially rescued by the administration of ferrostatin-1 (**Figure 5.17A**). Alternatively, for Panc1, a partial rescue of treatment-induced cell death by ferrostatin-1 was observed in the radiation only and Erastin only groups, with a significant increase in cell viability in the combination treatment group (**Figure 5.17B**). The ability of ferrostatin-1 to abrogate cell death in both cell lines suggests that ferroptosis is a contributor to the overall cell death under combination treatment conditions.

5.3.12 Erastin potentiates radiation-induced cell death in patient-derived organoids

The next experimental evolution involved the transition from a cell monoculture to a patient-derived organoid culture, in order to more closely recapitulate real-world PDAC. Organoids derived from three separate PDAC patients were treated with 5Gy radiation, 5 μM Erastin, and a combination thereof and followed for 96 hours. Representative images of organoids (from a single patient) under the four different treatment conditions are provided in **Figure 5.18A**. While a noticeable increase in organoid size can be appreciated in the no treatment and single treatment groups, the combination treatment produced organoid shrinkage, increase opacity, and membrane dissolution which are common signs of death. The viability in each treatment group was determined by measuring the associated ATP levels with the CellTiterGlo 3D assay (Promega). The radiation and Erastin treatments alone produce a slight decrease in organoid ATP levels but the combination elicited a far more dramatic decrease that was near significant ($p = 0.06$, **Figure 5.18B**).

Figure 5. 17 Effect of combination treatment in the setting of apoptosis, necroptosis, or ferroptosis inhibition

Colonies are presented on the left side of the panel and show the effects 5Gy radiation, Erastin (1 μM for Panc1 and 2 μM for CD18/HPAF), and the combination treatment with the addition of Ferrostatin-1 (Tocris), a lipophilic antioxidant that inhibits ferroptosis, Necroastain-1 (Sigma), a compound that binds RIP1 and inhibits necroptosis, and Z-VAD-FMK (Tocris), a pan-caspase inhibitor and apoptosis inhibitor. The quantification of colony number is presented as a proportion of the treatment control (i.e. Radiation only, Erastin only, or the combination) and is displayed on the right. **A.** CD18/HPAF shows rescue of cell death with Ferrostatin-1 in combination treatment only **B.** Panc1 shows Ferrostatin-1 rescue of cell death in the single-agent treatment groups as well as in the combination arm.

Figure 5.17

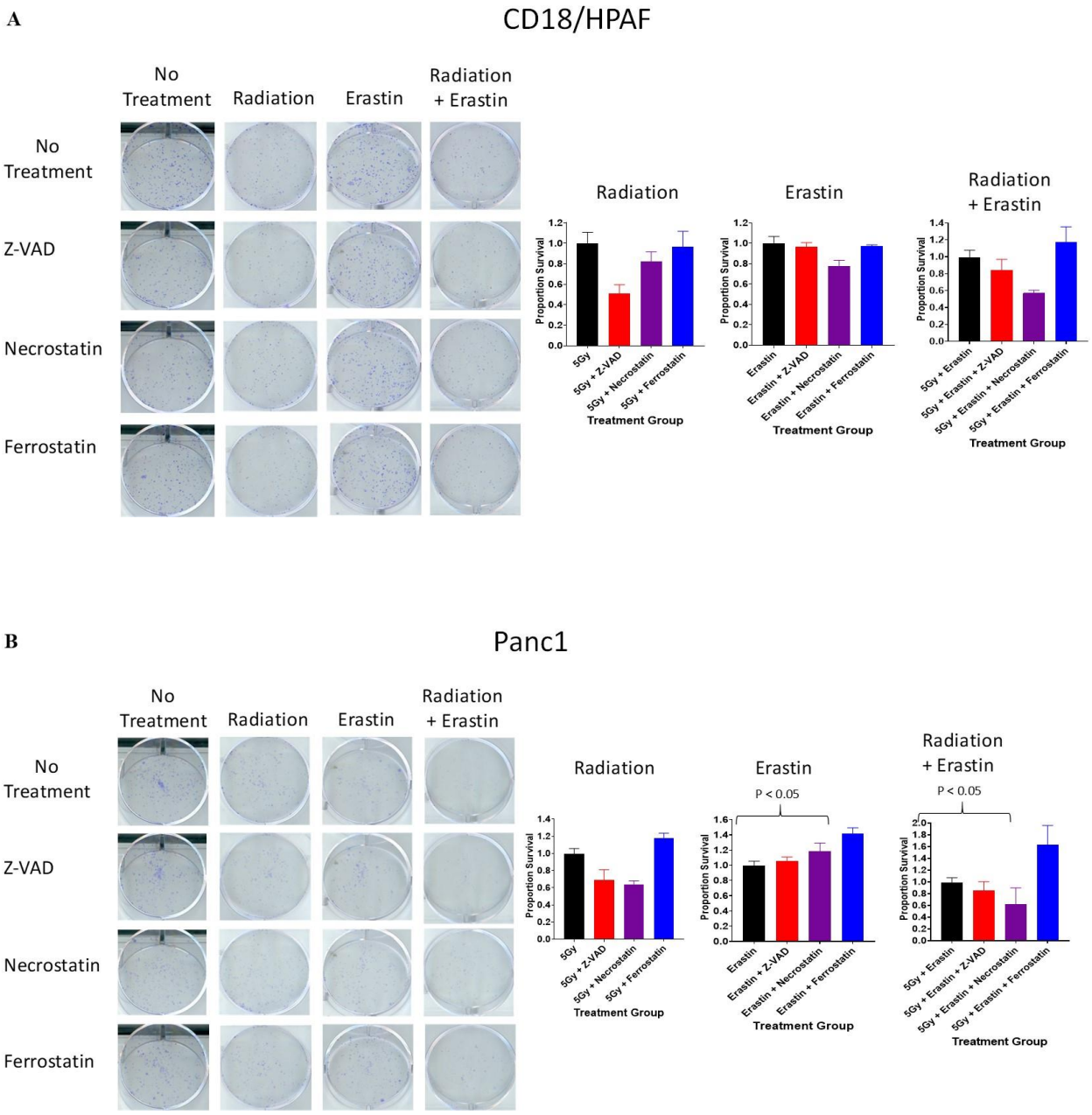
A
CD18/HPAF
No Treatment
Radiation
Erastin
Radiation + Erastin
No Treatment
Z-VAD
Necrostatin
Ferrostatin
Radiation
Erastin
Radiation + Erastin
Proportion Survival
5Gy
5Gy + Z-VAD
5Gy + Necrostatin
5Gy + Ferrostatin
Erastin
Erastin + Z-VAD
Erastin + Necrostatin
Erastin + Ferrostatin
5Gy + Erastin
5Gy + Erastin + Z-VAD
5Gy + Erastin + Necrostatin
5Gy + Erastin + Ferrostatin
Treatment Group
B
Panc1
P < 0.05

Figure 5.18C shows the individual measurements taken for each of the three patient-derived organoids to illustrate how the differences in response more closely resemble the true disease as encountered in patients.

5.3.13 Erastin potentiates radiation treatment *in vivo*

An orthotopic murine model of PDAC was generated by implanting CD18/HPAF cells modified with a luciferase vector into the pancreas of athymic nude mice. Mice were randomized into four groups that either received, no treatment, radiation, Erastin, or radiation + Erastin (the generation of the orthotopic model as well as the treatment schedule is discussed at length in Chapter 2 of this thesis). The luciferase positivity allowed for the *in vivo* visualization and monitoring of the implanted tumors using an IVIS imager *via* IP injection of luciferin and fluorescence measurements as a surrogate for tumor size. The combination of radiation and Erastin not only showed a reduction in tumor growth but produced tumor shrinkage between the last two IVIS imaging studies conducted eight days apart (**Figure 5.19A**). Since the tumor growth was merely slowed and not reversed in both of the single treatment arms, the difference in relative fluorescence intensity (R.F.I.) of the combination treatment group was the only on measurement significantly less than no treatment control on day 26 post-implantation ($p = 0.0317$). Importantly, the actual tumor size (as determined by weight after excision) was also significantly different between the control and combination groups ($p = 0.008$, **Figure 5.19B**).

5.3.14 Radiation increases intracellular reactive oxygen species (ROS)

To verify the production of reactive oxygen species (ROS) at the radiation doses being utilized in the majority of the experiments herein (5-7Gy), the ROS levels were measured in each cell line after treatment with 5Gy of radiation via DCF-DA assay.

Figure 5. 18 Response of patient-derived organoids to combination treatment

A. Images of patient-derived organoids at 0 and 96 Hours after no treatment, 5Gy radiation, 5 μM Erastin, or a combination thereof. Noticeably organoids in the no treatment and single-agent groups have increased in size while those in the combination group have shrunk, increase in opacity, and experienced membrane dissolution. **B.** The relative viability in each of the treatment conditions of a combination of three patient-derived organoids as determined by the relative ATP level. The combination treatment has a near significant reduction in viability with $p = 0.06$. **C.** Each of the three organoid experiments presented singly.

Figure 5.18

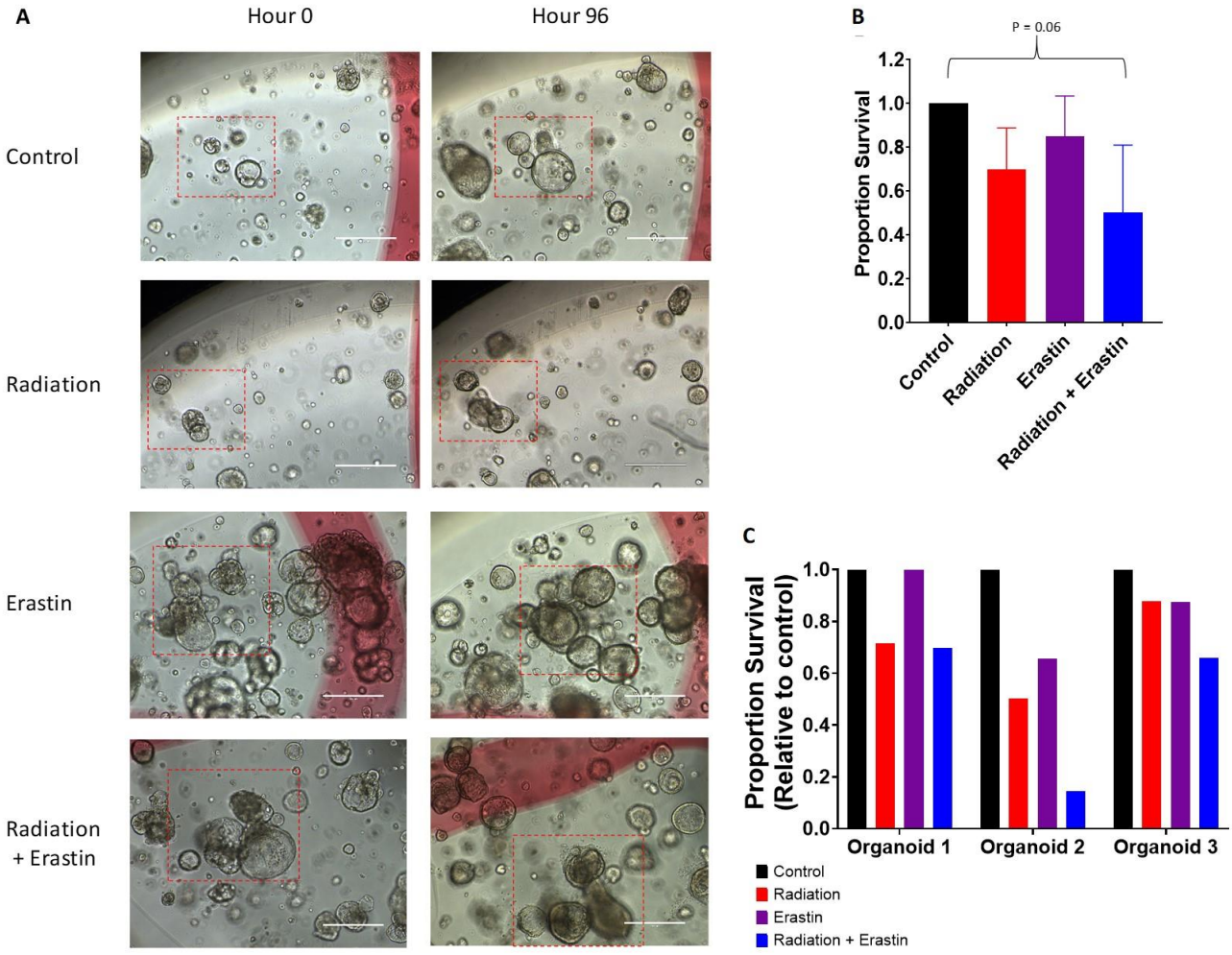
A
Hour 0
Hour 96
Control
Radiation
Erastin
Radiation + Erastin
B
P = 0.06
Proportion Survival
1.2
1.0
0.8
0.6
0.4
0.2
0.0
Control
Radiation
Erastin
Radiation + Erastin
C
Proportion Survival (Relative to control)
1.0
0.8
0.6
0.4
0.2
0.0
Organoid 1
Organoid 2
Organoid 3
Control
Radiation
Erastin
Radiation + Erastin

Figure 5. 19 Effect of Erastin and radiation in an orthotopic PDAC murine model

A. *In vivo* IVIS measurements of tumor size collected at days 10, 18, and 26 post-implantation. Presented as relative fluorescent intensity (R.F.I.). The difference in R.F.I. on day 26 between no treatment control and combination groups is significant with $p = 0.0317$. **B.** Images of excised tumors from each group are presented on the left with the quantification of their weights presented on the right side of the panel. Again, the only group to be significantly reduced from no treatment controls was the combination with $p = 0.008$.

Figure 5.19

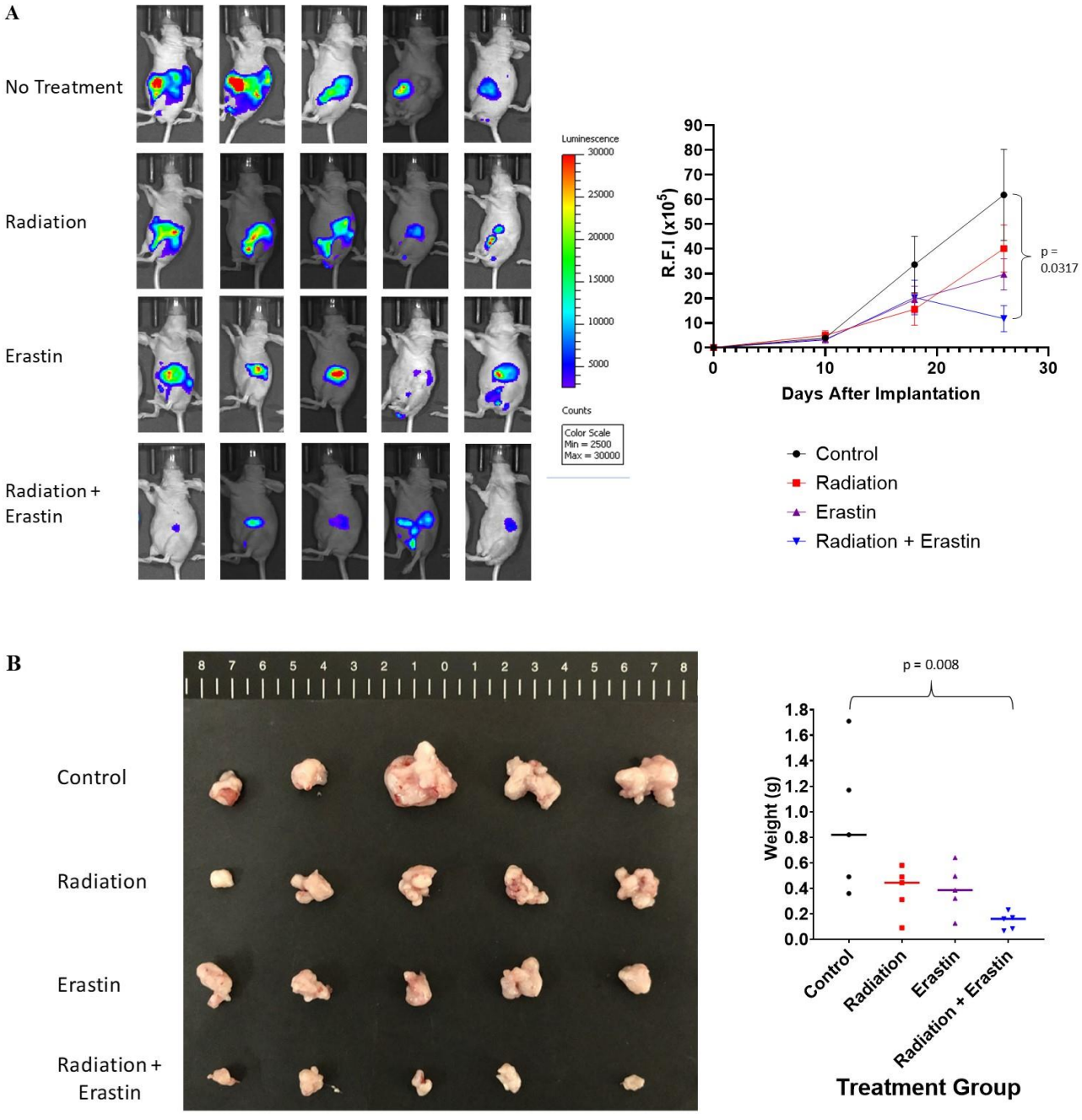
A
No Treatment
Radiation
Erastin
Radiation + Erastin
Luminescence
30000
25000
20000
15000
10000
5000
Counts
Color Scale
Min = 2500
Max = 30000
R.F.I (x10^5)
Days After Implantation
p = 0.0317
Control
Radiation
Erastin
Radiation + Erastin
B
Control
Radiation
Erastin
Radiation + Erastin
p = 0.008
Weight (g)
Treatment Group

Radiation alone increases the production of ROS by 1.5 to 2 fold compared to untreated controls (**Figure 5.20**). While the addition of Erastin interestingly did not increase the overall ROS levels, the lipophilic antioxidant Ferrostatin-1 did reduce total ROS measured (**Figure 5.20**).

5.3.15 Combination treatment causes lipid peroxidation *in vitro*

As mentioned early, the defining feature of ferroptosis is the requirement of a buildup of ROS mediated lipid hydro peroxides. With the observed increase in ROS, we next sought to determine the level of lipid peroxidation occurring in each treatment condition *via* C11-BODIPY 581/591 assay, which has previously been used for the elucidation of ferroptosis [231]. This is a dye that intercalates with lipids and the fluorescence changes predicated on the peroxidation state of the lipid: red if non-peroxidated and green if peroxidated, thus the relative level of peroxidation can be determined by the red/green ratio of the signal amplitudes. The lipid species in CD18/HPAF were resistant to peroxidation by radiation or Erastin monotherapy however a significant increase was observed when these were given in combination (**Figure 5.21**). On the other hand, Panc1, which we have shown to be more sensitive to radiation and Erastin, experiences a high level of lipid peroxidation with single-agent treatment as well as with the combination treatment (**Figure 5.22**). Also, the amount of lipid peroxidation was reduced back to normal levels in the setting of radiation when supplemented with Ferrostatin-1 (**Figure 5.22**).

5.3.16 Radiation increases intracellular free iron (Fe^{2+})

Given the requirement of free intracellular Fe^{2+} for the induction of ferroptosis, we determined its level using a FeRhoNox Assay. Rapidly after (3 hours) the administration

Figure 5. 20 Radiation production of reactive oxygen species (ROS)

DCF-DA fluorescent probe was utilized to detect the level of ROS in cells in the various treatment conditions. Representative images are provided on the left of each panel to allow a comparison between the relative level of fluorescence between the radiated and untreated controls. The quantification of ROS in each group is presented as a proportion of the total fluorescence measured in the untreated controls. **A.** Radiation-induced the expression of ROS nearly twofold that of untreated controls in Panc1 cells. **B.** Radiation-induced the expression of ROS nearly twofold that of untreated controls in CD18/HPAF cells.

Figure 5.20

Panc1

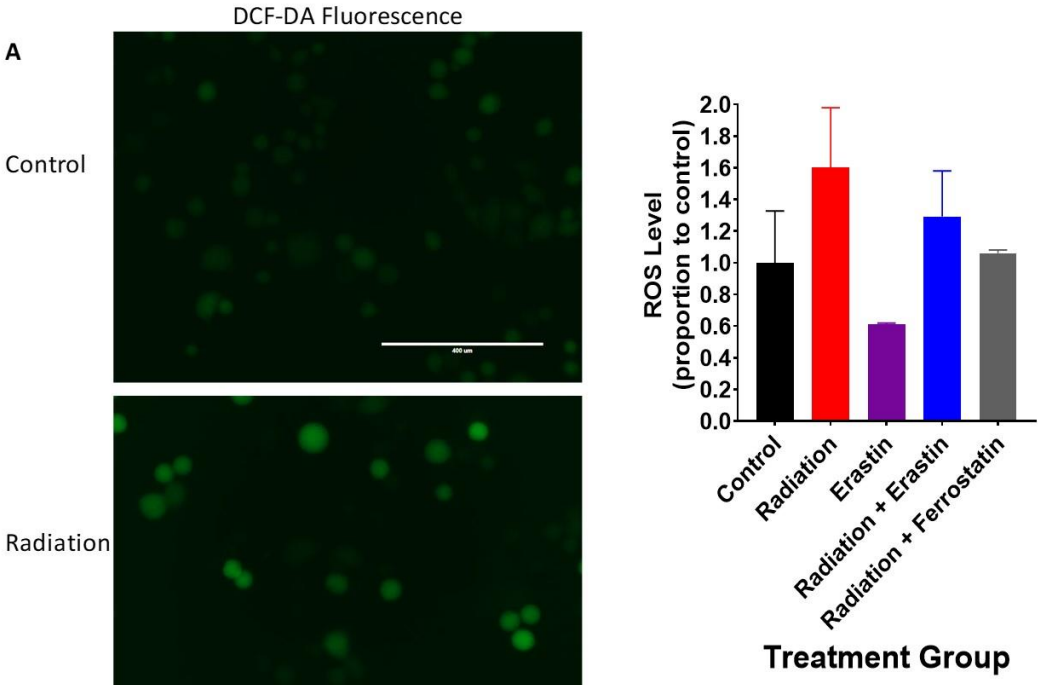

CD18/HPAF

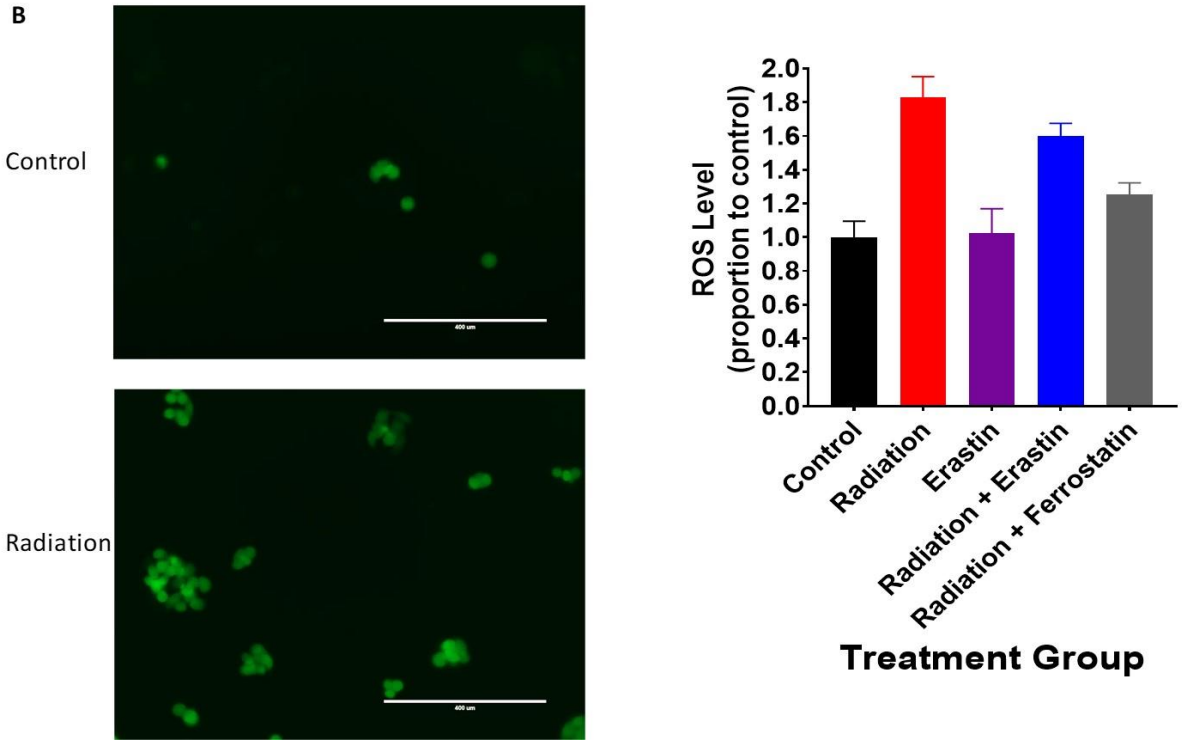

Figure 5. 21 Effect of combination therapy on lipid peroxidation in CD18/HPAF cells

C11-BODIPY 581/591 dye analysis was used to determine the relative level of lipid peroxidation in cells. This is a dye that intercalates with lipids and the fluorescence changes predicated on the peroxidation state of the lipid: red if non-peroxidated and green if peroxidated, thus the relative level of peroxidation can be determined by the red/green ratio of the signal amplitudes. The lipid species in CD18/HPAF were resistant to peroxidation by radiation or Erastin monotherapy however a significant increase was observed when these were given in combination as can be observed in the provided images and graphical representation of the fluorescence amplitude ratios.

Figure 5.21

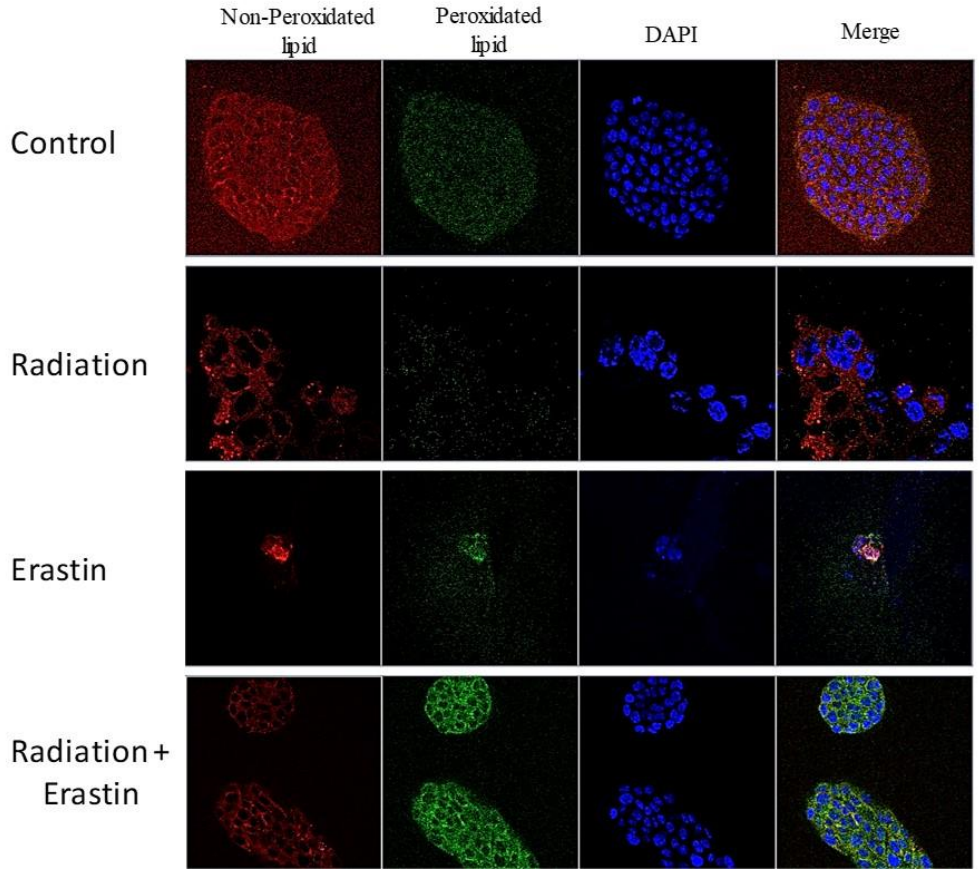
Non-Peroxidated lipid
Peroxidated lipid
DAPI
Merge
Control
Radiation
Erastin
Radiation + Erastin

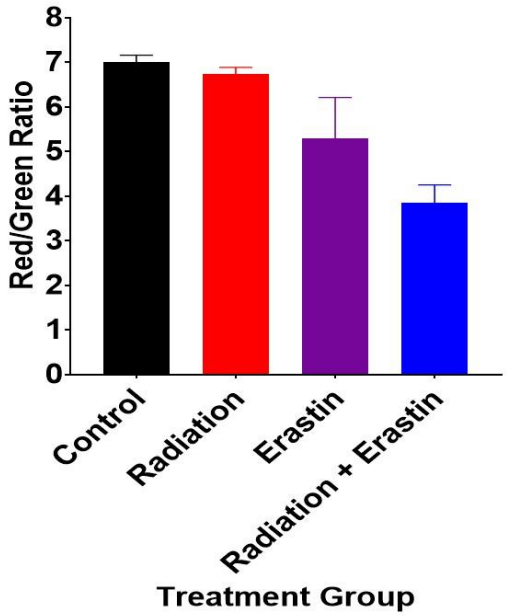
Red/Green Ratio
0
1
2
3
4
5
6
7
8
Control
Radiation
Erastin
Radiation + Erastin
Treatment Group

Figure 5. 22 Effect of combination therapy on lipid Peroxidation in Panc1 cells

C11-BODIPY 581/591 dye analysis was used to determine the relative level of lipid peroxidation in cells. This is a dye that intercalates with lipids and the fluorescence changes predicated on the peroxidation state of the lipid: red if non-peroxidated and green if peroxidated, thus the relative level of peroxidation can be determined by the red/green ratio of the signal amplitudes. Panc1, which we have shown to be more sensitive to radiation and Erastin, experiences a high level of lipid peroxidation with single-agent treatment as well as with the combination treatment and this phenotype was rescued with the addition of Ferrostatin-1 as can be observed in the provided images and graphical representation of the fluorescence amplitude ratios.

Figure 5.22

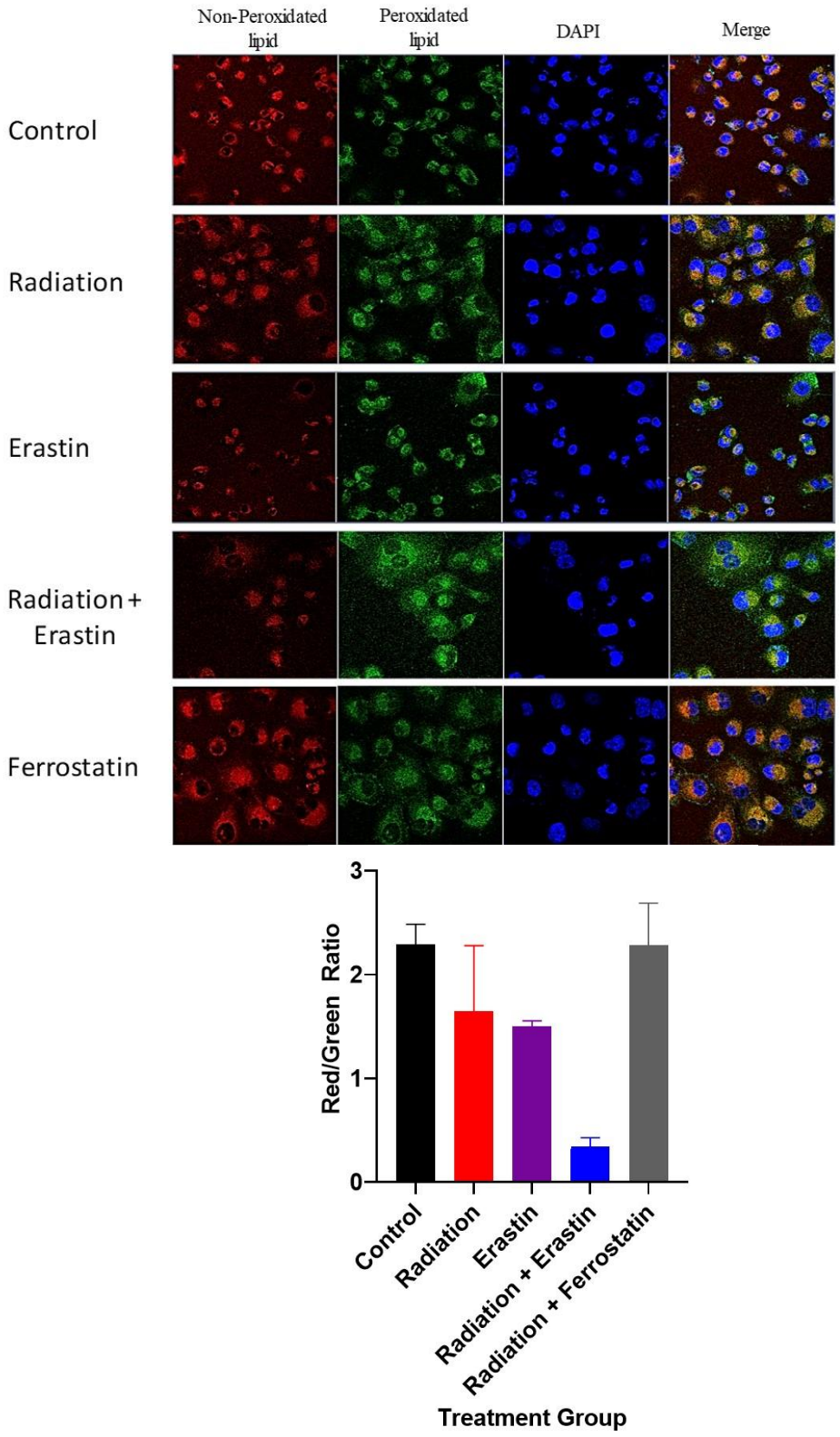
Non-Peroxidated lipid
Peroxidated lipid
DAPI
Merge
Control
Radiation
Erastin
Radiation + Erastin
Ferrostatin
Red/Green Ratio
0
1
2
3
Control
Radiation
Erastin
Radiation + Erastin
Radiation + Ferrostatin
Treatment Group

of 5Gy radiation, the level of unbound Fe^{2+} increases by 20-30% from pretreatment levels (**Figure 5.23**). Interestingly, this process was reversed in both cell lines and the amount of free Fe^{2+} reduced back down to or below, pretreatment level. Along with this, the addition of Erastin was shown to increase the free iron even further (**Figure 5.23**).

5.3.17 Lipid peroxidation can be measured in radiated PDAC patient serum samples

With the realization that ferroptosis contributes to the efficacy of radiation, circulating lipid peroxide metabolites, namely, malondialdehyde (MDA), offer a potential biomarker for the real-time monitoring of response to radiation therapy [522]. To test this, we analyzed malondialdehyde in 17 serum samples from patients that underwent radiation *via* TBARS assay. We found that not only was the level of malondialdehyde elevated after radiation treatment as compared to pretreatment (n = 8), but the addition of the radiation sensitizing agent zoledronic acid (an FDPS inhibitor that affects the mevalonate pathway [523]) showed comparatively higher levels (n = 9) (**Figure 5.24A**). *In vitro* C11-BODIPY analysis of zoledronic acid treatment and radiation found an increase in lipid peroxidation with the combination thus supporting the clinical sample results (**Figure 5.24B**). A likely reason for this is that the mevalonate pathway is the primary mechanism for CoQ10 synthesis [524]. Recently it was discovered that CoQ10 and its associated enzyme ferroptosis suppressor protein 1 (FSP1) are integral for the detoxification of lipid peroxides and ferroptosis inhibition [525]. Thus, the inhibition of the mevalonate pathway by zoledronic acid *via* FDPS, likely results in increased lipid peroxidation and a proclivity towards ferroptosis.

Figure 5. 23 Effect of treatment on intracellular free iron (Fe^{2+})

The relative amount of labile intracellular Fe^{2+} was assessed using a FeRhoNox Assay after 5Gy radiation, with Erastin, and the combination thereof. The values are presented as a proportion of the untreated control. **A.** The level of unbound Fe^{2+} increased in Panc1 cells by 30% when exposed to combination treatment over pretreatment levels, as depicted by the bar graph of measurements at the 3 hour time point. **B.** The level of unbound Fe^{2+} increased in CD18/HPAF cells by 20% when exposed to combination treatment over pretreatment levels, as depicted by the bar graph of measurements at the 3 hour time point. Interestingly, both cell lines experience increases in the free iron level with single-agent treatment. Additionally, these levels returned at or below pretreatment levels by hour six.

Figure 5.23

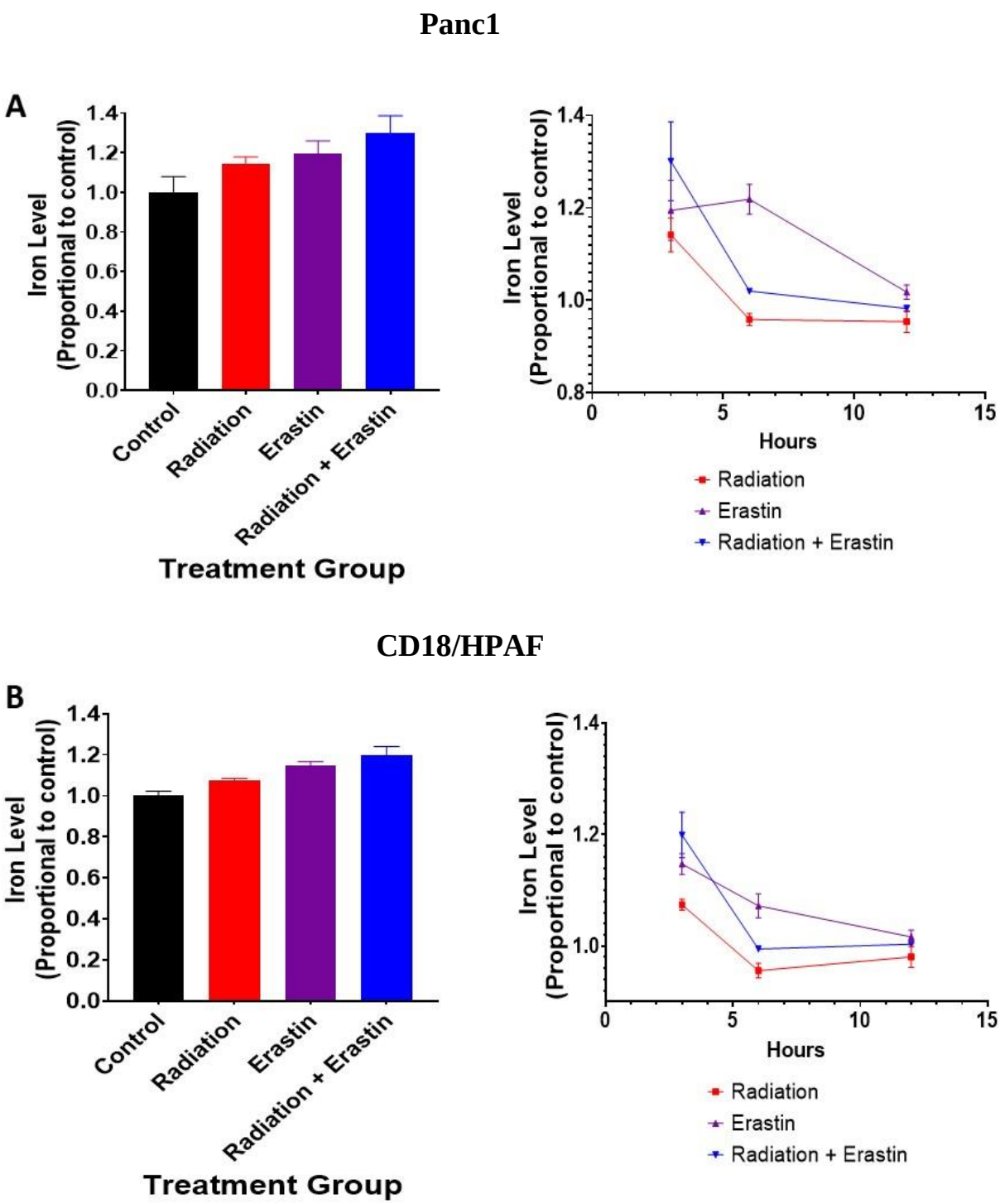
Panc1
A
Iron Level (Proportional to control)
1.4
1.2
1.0
0.8
0.6
0.4
0.2
0.0
Control
Radiation
Erastin
Radiation + Erastin
Treatment Group
Iron Level (Proportional to control)
1.4
1.2
1.0
0.8
0
5
10
15
Hours
Radiation
Erastin
Radiation + Erastin
CD18/HPAF
B
Iron Level (Proportional to control)
1.4
1.2
1.0
0.8
0.6
0.4
0.2
0.0
Control
Radiation
Erastin
Radiation + Erastin
Treatment Group
Iron Level (Proportional to control)
1.4
1.2
1.0
0
5
10
15
Hours
Radiation
Erastin
Radiation + Erastin

Figure 5. 24 Malondialdehyde (MDA) assessment in radiation patient samples

The level of Malondialdehyde in 17 serum samples from patients that underwent radiation was assessed *via* TBARS assay. **A.** We found that not only was the level of malondialdehyde elevated after radiation treatment as compared to pretreatment (n = 8), but the addition of the radiation sensitizing agent zoledronic acid (an FDPS inhibitor that affects the mevalonate pathway) showed comparatively higher levels (n = 9). This is presented as the proportion of pretreatment levels. **B.** *In vitro* C11-BODIPY analysis of zoledronic acid treatment and radiation found an increase in lipid peroxidation (decrease in red/green ratio) with combination treatment in CD18/HPAF cells.

Figure 5.24

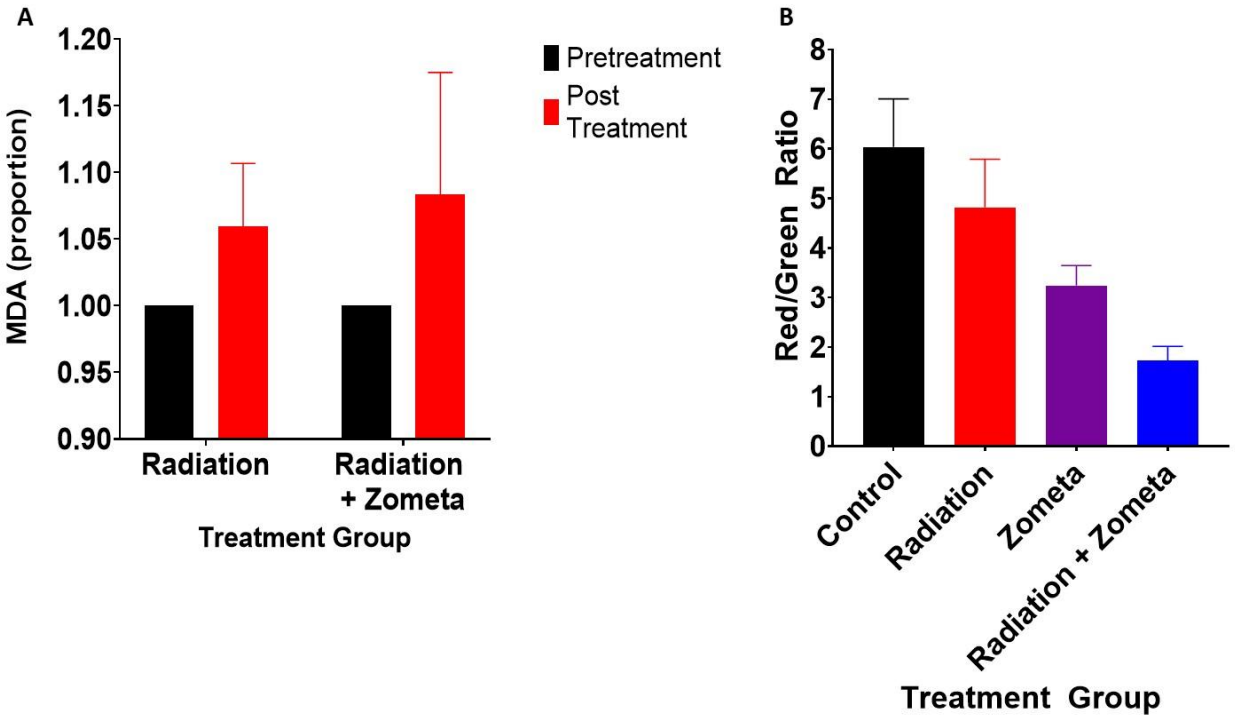
A
1.20
1.15
1.10
1.05
1.00
0.95
0.90
MDA (proportion)
Radiation
Radiation + Zometa
Treatment Group
Pretreatment
Post Treatment
B
8
7
6
5
4
3
2
1
0
Red/Green Ratio
Control
Radiation
Zometa
Radiation + Zometa
Treatment Group

5.4 Discussion

A major challenge in PDAC treatment is how to increase the efficacy of currently used therapeutic modalities to increase the survivorship of those diagnosed. Recent studies have reported PDAC specific sensitivity to Erastin induced ferroptosis [526]. Radiation therapy classically mediates cell death *via* double-stranded DNA breaks leading to mitotic catastrophe, however, studies have reported ferroptosis to be implicated in radiation-induced cell death [504, 505, 527]. By coupling these two treatment strategies together, we have been able to increase the ability of radiation to induce cellular death in vitro and in vivo, in this traditionally radiation-resistant cancer.

Herein we proposed a putative mechanism by which radiation and Erastin are inducing ferroptosis; the combination of lipid peroxidation mediated by radiation-induced ROS production and free ferrous iron (Fe^{2+}) release, coupled with Erastin mediated depletion of GSH. ROS is known to cause the disassociation of KEAP1 from NRF2, thereby preventing its degradation. Also of note, radiation was found to increase the phosphorylation of NRF2 along with a concomitant increase in its transcription products GPX4, GSS, and SLC7A11. Thus, Erastin blockade of SLC7A11 thwarts the cell's attempt at protecting itself from radiation leading to synergistic cell death. In other words, the Erastin synergism with radiation may not necessarily be the direct and simple result of increased ROS, but takes advantage of the increase in the ROS generated by radiation, coupled with GSH depletion provided by Erastin, and the prevention of NRF2 transcription products (i.e. GPX4, GSS, and SLC7A11) from actualizing their role in lipid deperoxidation. In so doing, combination therapy tips the balance towards a level of lipid peroxidation that triggers

Figure 5. 25 Schematic of the proposed mechanism of Erastin potentiation of radiation *via* ferroptosis

Radiation was found to increase ROS which causes KEAP1 to disassociated from NRF2 preventing its degradation. Along with this, radiation was shown to increase the phosphorylation of NRF2 along with a concomitant increase in its transcription products GPX4, GSS, and SLC7A11. SLC7A11 inhibition by Erastin nullifies any upregulated produced by NRF2 nuclear localization. Thus, Erastin blockade of SLC7A11 thwarts the cell's attempt at protecting itself from radiation leading to synergistic cell death. Along with this, radiation causes an increase in free Fe^{2+} and, in association with the concomitant production of ROS, Erastin prevents the synthesis of GSH thereby inhibiting the enzymatic conversion of lipid hydro peroxides to lipid alcohols by GPX4. In so doing, combination therapy tips the balance towards a level of lipid peroxidation that triggers ferroptosis.

Figure 5.25

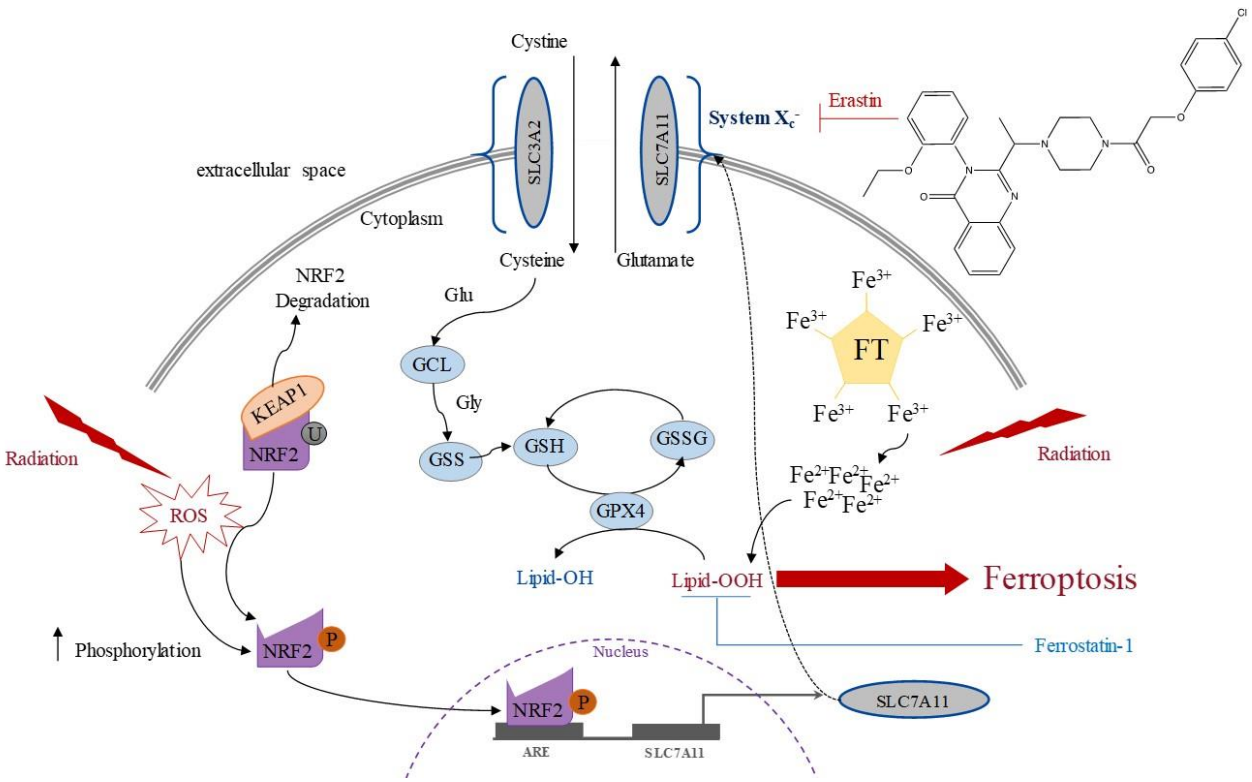
Cystine
SLC3A2
SLC7A11
System X_c^-
Erastin
extracellular space
Cytoplasm
Cysteine
Glutamate
NRF2
Degradation
Glu
GCL
Gly
GSS
GSH
GSSG
GPX4
KEAP1
NRF2
U
Radiation
ROS
Phosphorylation
NRF2
P
Nucleus
NRF2
P
ARE
SLC7A11
SLC7A11
Fe^{3+}
FT
Fe^{2+}
Radiation
Lipid-OH
Lipid-OOH
Ferroptosis
Ferrostatin-1

ferroptosis. A schematic representation of the overall mechanism is provided in **Figure. 5.25**.

5.5 Conclusions and future directions

Since the discovery of ferroptosis in 2012 [496] its role has been investigated in the setting of cancer and cancer treatments [508, 528]. The potential of ferroptosis as a therapeutic adjuvant has only just begun to be uncovered. Importantly, cancer cells seem to be far more susceptible to induced ferroptosis *via* SLC7A11 inhibition compared to normal cells, regardless of the organ of origin. A fact reiterated by the normal development of SLC7A11 knock out mice. The present study takes advantage of these observances and utilizes ferroptotic induction via SLC7A11 inhibition to potentiate cell death caused by radiation in the setting of PDAC. The significance of this lies in the elucidation of a novel sensitization mechanism that can increase RT efficacy, thereby increasing the importance of radiation in the PDAC treatment armamentarium.

While this study has provided valuable insight into the interplay between ferroptosis and radiation, many questions are still left unanswered and many new questions have arisen. Studies are planned to elucidate what kinases phosphorylation NRFs and where this occurs within the molecule to further elucidate the mechanism by which ferroptosis resistance arises with radiation. Further, given the recent insight that radiation and immunotherapies work together to induce ferroptosis in cancer cells [529], we will also repeat these experiments using a syngeneic immunocompetent mouse model to understand the local and distant immune effects of this therapy. Finally, the bioavailability of Erastin is very low and it is also not FDA approved. As such, we will investigate the utility of well-

tolerated FDA approved drugs known to block SLC7A11, such as Sulfasalazine and Sorafenib, as easily translatable radiation potentiation drugs.

Chapter 6: General conclusions and future directions

In this dissertation work, we sought to address the two primary causative challenges related to the high lethality of PDAC: the lack of an accurate early detection biomarker and the ineffectiveness of modern non-surgical therapeutic modalities. The first part of this dissertation investigated the use of the extracellular vesicle (EV) surface to serve as a PDAC biomarker. In the second part, we studied the implications of ferroptosis on radiation mediated cell death and tested whether radiation could be potentiated *via* pharmacologic ferroptotic induction. In this chapter, a summary and future directions for each of these aspects are provided.

A. Extracellular vesicle surfaceome characterization for the early detection of pancreatic ductal adenocarcinoma

The sole curative option for PDAC remains surgical resection. Unfortunately, patients often have late-stage disease at the time of initial when the primary tumor can no longer be resected or it has already metastasized. One of the reasons this is true is because of the lack of clinically useful diagnostic markers. The current gold standard marker, CA19.9, offers limited accuracy because it is also expressed in a variety of other diseases and some patients do not have the necessary fucosyltransferase enzyme to produce it. Over the past several decades there have been continuous efforts by our lab and many others to discover a PDAC biomarker that is capable of detecting early-stage resectable disease. However, the progress has been limited and a detection marker with the necessary sensitivity and specificity has yet to be found. Recently, many studies have begun to investigate the potential of extracellular vesicles (EVs) to serve as PDAC biomarkers.

All cell types and tissues in the human body produce and secrete EVs, 50-1000 nm diameter sized membranous-organelles. EVs harbor many biologically active molecules

including proteins, RNA species, DNA, and lipids. Inherent in their mechanism of creation is that the vesicular components mirror that of their cell of origin. These components are able to alter recipient cell functionality through the delivery of their cargo [279], target cell signaling initiation [280], and propagation of disease process [281]. Elucidation of their functions has prompted many investigations into their implications in cancer progression [282], metastasis [283, 284], and drug resistance [285]. Additionally, EVs are increased in the setting of cancer and are present in all biofluids including saliva, serum/plasma, urine, and ascitic fluid [473, 474]. Due to these many attributes, EVs are considered to be attractive targets to be used as cancer biomarkers.

Evaluation of the EV surface specifically holds several advantages for use as a cancer-specific biomarker. Firstly, surface evaluations can be conducted *via* a variety of label-free methods. Conversely, molecules present on the external surface are easily accessible and can be utilized for affinity-based isolation methods or high-throughput profiling techniques. EV surface biomarkers can also provide insight into their interaction with the immune system thereby dictating therapy choice as well as predict metastatic organ tropism. However, the majority of studies investigating EVs as potential biomarkers have focused on the entire vesicular contents and have neglected to separate the intravesicular and surface components. Towards this end, we have attempted to characterize the EV surface with a variety of methods for use as early detection PDAC biomarkers.

In the first part of this dissertation, we initially utilized a label-free technique for EV surface characterization called surface-enhanced Raman spectroscopy (SERS) and subsequent analysis by principal component discriminant function analysis (PC-DFA) to

identify PDAC EVs. Further attempts at identifying specific molecular contributors to observed SERS spectral variation were made *via* LC-MS/MS proteomics followed by bioinformatics and various surface profiling techniques. Our findings suggest a potential role for EV surface characterization as a PDAC biomarker but the limited accuracy requires further evaluation.

SERS holds many advantages for the profiling of EV surfaces in addition to being label-free. Namely, it is non-destructive, requires very small sample volume, is highly sensitive compared to traditional assays such as ELISA, and can produce a sample-specific Raman signature. Previous studies have proven the ability of SERS to determine if EVs originated from healthy or cancer cells. However, these experiments were only carried out on EVs purified from *in vitro* cultures and were not applied to EVs isolated from patient sera. We have been able to conduct a SERS based characterization on cell line EVs that was able to be applied to EVs isolated from patient serum samples. Isolation of EVs from two PDAC cell lines (CD18/HPAF and MiaPaCa) and an immortalized human pancreatic ductal epithelial cell line (HPDE) were isolated *via* density gradient ultracentrifugation. These EVs underwent multiparametric validation beginning with nanoparticle tracking analysis (NTA) to assess the quantity and size distribution of isolated EVs. Transmission electron microscopy (TEM) was used to visualize EVs with the characteristic cup shape and verify no morphological changes occurred during isolation. Western blot analysis was conducted to verify that the consensus EV markers, CD9 and CD63) were concentrated compared to whole cell lysates. Finally, atomic force microscopy (AFM) showed EVs to bind to the gold substrate and adequately distribute over the surface in a manner capable of undergoing SERS analysis.

We next conducted SERS measurements at Raman shift ranges of 719-1800 cm^{-1} on 33, 31, and 35 separate EV samples purified from CD18/HPAF, MiaPaCa, and HPDE, respectively. Variations in peaks (amplitude and Raman shift value) were noted both between the control and EV populations and also between the EV population samples themselves thus providing the foundation for differential characterization of the particles. Notably, these spectral shifts were found to be highly reproducible thus allowing for PC-DFA to discriminate differences across multiple measurements. The initial application of principal component analysis (PCA) to 1004 peaks in the SERS spectra collected from the cell line purified EVs efficiently reduced the total number of variables to 20 principal components (PCs). These PCs accounted for 88.2% of the total spectral variance. Specifically, principal component #1(PC #1) contained the most important data with 35.4% of the total variance. The next two PC #2 and PC #3 represented 14.4% and 6.6% of the total variance, respectively. The application of these three PCs was not able to isolated EVs into distinct populations predicated on the cells of origin. Thus, the PCs were used as the input independent variables for discriminant function analysis (DFA) to further separate the populations based on spectral shift. PC-DFA proved capable of accurately clustering SERS spectra from specific EV subpopulations. Thes formed discrete clusters and separated from each other as a function of the PC-DFA classifiers. This lead to a prediction sensitivity of 90.6% and a specificity of 97.1%.

Serum EVs were next isolated *via* ultracentrifugation from healthy, early PDAC (stage I-IIB), and late PDAC (stage III-IV) patients. The EV concentrations were found to be increased in the cancer patient serum as compared to healthy. Seromic EVs were assessed by NTA, TEM, and AFM just as cell line purified EVs. The PC-DFA algorithm

trained from the cell line SERS spectra was applied to 60 spectra collected from 4 different healthy patient serum EV isolations and 55 spectra collected from 4 different early PDAC serum EV isolations. This proved capable of predicting patient cancer status with 66.7% sensitivity and 67.3% specificity. This was a proof-of-concept study that displayed the possibility of label-free characterization of EVs for PDAC detection.

However, the limited overall accuracy of the label-free SERS PC-DFA algorithm required us to investigate the surface of EVs to discover specific molecular species that contribute to the observes variance and could also be used as specific biomarkers. We isolated EVs from four PDAC cell lines (CD18/HPAF, MiaPaCa, T3M4, and Capan1) and HPDE. We elucidated a pool of cancer-specific proteins *via* EV surface-specific liquid chromatography-tandem mass spectrometry (LC-MS/MS). Notably, Capan1 EVs were excluded from further analysis as evidence of cellular contamination was found. To determine the clinical significance of the identified markers we analyzed the gene expression pattern, correlations, and receiver operator characteristic (ROC) curve for each protein in the GSE27385 microarray datasets. This process allowed for the reduction of 229 possible proteins down eight target proteins: cluster of differentiation 151 (CD151), galectin-1 (LGALS1), cofilin (CFL1), tyrosine 3-monooxygenase/tryptophan 5-monooxygenase activation protein zeta (YWHAZ), extracellular matrix protein-1 (ECM1), ephrin A2 (EPHA2, integrin alpha 3 (ITGα3), and heat-shock protein family B (small) member-1 (HSPB1).

To validate the presence of these 8 targets, we analyzed EV isolates from each cell line by western blot. Indeed, all were present and enriched in EV samples compared to whole cell lysates and were increased in EVs from cancer cells compared to HPDE. Four

of these eight, EPHA2, ECM1, CD151, and HSPB1, were able to be visualized on the surface of EVs *via* immunogold labeling and TEM imaging. This was set as a requirement for subsequent analyses because this sufficiently proved the localization of each marker on the external surface of the EVs. Of note, immunogold staining requires much individual protocol standardization and because of this, immunogold was used to rule markers in and not out. Those that failed to be stained required further study.

The gene expression for the four selected markers along with survival analysis was conducted using data from TCGA. Among these four markers, EPHA2 was the most differentially regulated in cancer compared to normal and was the most significantly correlated with overall survival. To assess the ability of a high-throughput and sensitive screening modality detect EV surface EPHA2, we next conducted an ELISA on cell line EVs. Those from PDAC cell lines showed an elevated concentration of EPHA2 as compared to HPDE. The ELISA analysis was extended to complete serum samples from benign control patients, early PDAC, and late PDAC. EPHA2 was found to be elevated in cancer patient serum compared to benign controls resulting in a diagnostic sensitivity of 76% and specificity of 62%. Finally, EV specific EPHA2 expression isolated from patient serum samples proved capable of identifying 25% of PDAC patients with 100% specificity. While these results are promising, the generally low sensitivity requires continued evaluation of the EV surface.

Future directions

1. Development of a surface EV multimarker panel to be used in conjunction with CA19.9

A single marker will never be sensitive nor specific enough to be capable of identifying PDAC. The current accuracy provided by the SERS PC-DFA and EPHA2 analyses is too low to be clinically applicable. Therefore, we would like to continue our study of the identified EV surface markers (beginning with ECM1, CD151, and HSPB1) as well as investigate newly elucidated markers (glycans) to improve the sensitivity and specificity of our assay. Along with this, the current gold standard, CA19.9, is also not sufficient for the liquid biopsy-based detection of PDAC. Therefore, we would like to ascertain if our multimarker panel may provide an additive benefit when supplemented with CA19.9 assessment. The eventual aim would be the production of a multimarker panel capable of detecting PDAC at an early stage.

2. Determine the functional implications of the EV surfaceome

Many studies have found that the EV surface directly interacts and affects its surrounding environment. Further, interactions at the EV surface are capable of initiating signaling cascades, promoting receptor-mediated endocytosis, and effecting the immune milieu. Therefore, we would like to assess the functional implications associated with our identified surface proteins. These include studies such as determining if these proteins facilitate cellular uptake, initiate cancer-associated signaling pathways, impact local and distant immune cells, and if any of these functions can be blocked.

B. Erastin potentiates radiation therapy *via* the induction of ferroptosis in the setting of PDAC

Along with the inability to detect early-stage disease, another major reason why PDAC is so lethal is because of the lack of effective treatment options. As mentioned in section A of this chapter, the only curative therapeutic option is surgical resection of the

primary tumor. Most chemotherapy options provide little benefit or are extremely toxic thus only can only be given to the fittest patients. Radiation therapy is traditionally reserved for borderline resectable or locally advanced disease to try and shrink the tumor to a size amenable to resection. The recent progress of stereotactic body radiation therapy (SBRT) has improved response rates by administering highly conformational doses of radiation in fewer fractions with less off-target toxicity. However, many PDAC patients still remain refractory to radiation treatment. This has ignited the search for a potential means of enhancing radiation therapy efficacy for the treatment of PDAC.

Ferroptosis is a recently discovered non-apoptotic form of cell death. It is caused by the buildup of lipid hydro peroxides mediated by reactive oxygen species (ROS) and free ferrous iron (Fe^{2+}). Glutathione peroxidase 4 (GPX4) converts the toxic lipid hydro peroxides to non-toxic lipid alcohols, using glutathione (GSH) as a substrate. GSH synthesis requires cystine, which is transported into the cell *via* the cystine glutamate antiporter System X_c. System X_c inhibition facilitated by the blockade of one of its constituents, SLC7A11, is becoming a highly investigated area of study for use as a therapeutic adjuvant with a variety of cancer therapies including chemo and radiation. Many cancers that proved resistant to conventional cytotoxic therapies are susceptible to ferroptotic induction. Importantly, cancer cells seem to have an increased reliance on SLC7A11 expression compared to healthy cells, likely due to the higher levels of endogenous ROS. Along with this, whole-body SLC7A11 knock out does not affect the development of mice. Taken together, SLC7A11 may provide a cancer-selective means of inducing ferroptosis. One of the primary mechanisms that radiation induces cellular

damage is with the production of ROS. Thus, radiation therapy seems well suited for potentiation *via* ferroptosis induction.

These two therapeutic modalities are ideally suited to complement one another in their mechanisms of action, where an increase in ROS generation is provided by radiation and a diminished capability of eliminating the associated lipid toxicity is provided by SLC7A11 inhibition. Thus, in the second part of this dissertation, we investigated the involvement of ferroptosis, in radiation-induced cell death. Additionally, we tested if the pharmaceutical induction of ferroptosis with the small molecule Erastin (SLC7A11 blockade) can potentiate the lethal effects of radiation.

To determine the clinical viability of ferroptosis in the setting of pancreas cancer, we first analyzed the GPX4 and SLC7A11 expression in pancreas cancer samples in a combination of TCGA and GTEx dataset. Both GPX4 and SLC7A11 were found to be significantly upregulated in the setting of cancer compared to normal tissue as well as in comparison to cancers of various origin. This analysis was conducted on patient data from PDAC as well as neuroendocrine tumors in addition to cell line data. Since we are specifically interested in PDAC, we surveyed only the PDAC cohort within the TCGA dataset next. While GPX4 was not differentially expressed in PDAC compared to healthy tissue, SLC7A11 was. However, neither had a significant impact on survival. The protein expression of these two molecules was assessed *via* western blot in eight different PDAC cell lines: CD18/HPAF, MiaPaCa, Colo357, AsPC1, Panc1, Capan1, T3M4, and BxPC3 as well as the immortalized normal human pancreatic ductal epithelial cell line HPDE. Again, the expression of GPX4 was not observed to be different between PDAC cell lines and HPDE but SLC7A11 expression was increased in the majority of PDAC cell lines.

Project DRIVE, a database designed to provide insight into cancer dependencies based on RNAi screening, showed that 3 of the top 20 (including the top 2) cell lines most sensitive to SLC7A11 knockdown were PDAC line. We tested this finding by pharmaceutically inhibiting SLC7A11 *via* Erastin in all eight PDAC cell lines along with HPDE and measuring the viability *via* MTT assay. PDAC cell lines were observed to be more sensitive to SLC7A11 inhibition at 24 and 48 hours compared to HPDE. Of note, the cell lines selected for additional experiments based on these data were CD18/HPAF and Panc1. Additionally, Erastin treatment was able to inhibit the migration ability of CD18/HPAF cells and also resulted in a significant decrease in total GSH in both CD18/HPAF and Panc1 cell lines.

To determine the effects of radiation on genes important in ferroptosis, publicly available microarray data conducted on samples from PDAC cells (Panc1, MiaPaCa, AsPC1, and BxPC3) collected 6 hours after 2Gy radiation exposure was used. We found that many NRF2 transcription products including GPX4 and GSS are upregulated along with HSPB1, an iron sequestration protein known to inhibit ferroptosis. Concurrently, NCOA4, a protein involved in the release of free Fe^{2+} *via* ferritinophagy, was downregulated. Assessment at the protein level found GPX4 to be slightly increased in both CD18/HPAF and Panc1 but SLC7A11 and phosphorylation of NRF2 were dramatically increased in a time-dependent manner. Notably, NRF2 is also the transcription factor responsible for SLC7A11 production. A significant increase in SLC7A11 expression was also observed in irradiated patient PDAC tissue compared to non-radiated PDAC and healthy patient tissues. Following this result, survival analysis was conducted only on

patients who received radiation in the TCGA PDAC cohort, and SLC7A11 expression was significantly correlated with overall survival.

Next, the ability of GPX4 knockdown to potentiate radiation was assessed *via* clonogenic survival assay. GPX4 KD was able to enhance the lethal effects of radiation in CD18/HPAF but was not able to be assessed in Panc1 as the KD itself was lethal. This result is directly in line with Panc1 sensitivity to Erastin as determined by the MTT analysis. Congruently, SLC7A11 inhibition with Erastin was found to synergistically enhance the effects of radiation, as determined by the BLISS independent synergy model *in vitro*. The repetition of this experiment was conducted with the addition of Ferrostatin-1, a lipophilic antioxidant that inhibits ferroptosis, Necroastain-1, a compound that binds RIPK and inhibits necroptosis, and Z-VAD-FMK. This lead to the observation that cell death caused by combination treatment was abrogated by the addition of ferrostatin-1, which suggests that ferroptosis is at least a partial contributor to the overall lethality of the combination treatment. Additionally, the combination of Erastin and radiation decreased the viability of three individual patient-derived organoids. I*n vivo* assessment was carried out in an orthotopic xenograft mouse model of PDAC where tumor sizes were significantly reduced with combination treatment compared to no-treatment controls (single-agent treatment with radiation or Erastin alone was not significant).

To gain some mechanistic insight into how combination therapy is synergistically inducing cell death, we assessed the levels of ROS, intracellular free ferrous iron, and lipid peroxidation in untreated CD18/HPAF and Panc1 cells and those treated with radiation, Erastin, or a combination thereof. The relative level of ROS increases immediately after radiation administration (3 hours) compared to pre radiation levels and stays elevated for

at least 24 hours. On the other hand, free ferrous iron rises immediately after radiation (3 hours) and falls back to or below pre radiation levels by 6 hours. Finally, since lipid peroxidation is the initiator of ferroptosis, we measured its level with C11-BODIPY 581/581 dye. This is a lipophilic dye that intercalates with lipids and fluoresces red when interacting with a normal lipid and green when interacting with a peroxidated lipid. The red/green ratio can be thus be utilized to determine the relative amount of peroxidation between samples. Notably, Panc1 experiences a relative increase in lipid peroxidation in both single-agent treatment groups as well as the dramatic increase in the combination treatment group compared to no treatment control. For CD18/HPAF cells, an increase in the level of lipid peroxidation was only observed in the combination group.

With these results we propose a putative mechanism by which radiation and Erastin are inducing ferroptosis; the combination of lipid peroxidation mediated by radiation-induced ROS production and free ferrous iron (Fe^{2+}) release, coupled with Erastin mediated depletion of GSH. Radiation was found to increase the phosphorylation of NRF2 (a factor known to increase the nuclear localization and facilitate transcription) along with a concomitant increase in its transcription products GPX4, GSS, and SLC7A11. Thus, Erastin blockade of SLC7A11 thwarts the cell's attempt at protecting itself from radiation leading to synergistic cell death. In other words, the Erastin synergism with radiation may not necessarily be the direct and simple result of increased ROS, but takes advantage of the increase in the ROS generated by radiation, coupled with GSH depletion provided by Erastin, and the prevention of NRF2 transcription products (i.e. GPX4, GSS, and SLC7A11) from actualizing their role in lipid deperoxidation. In so doing, combination therapy tips the balance towards a level of lipid peroxidation that triggers ferroptosis.

Future directions

1. Elucidating the role of NRF2 phosphorylation in ferroptosis resistance

While this study has provided valuable insight into the interplay between ferroptosis and radiation, many questions are still left unanswered and many new questions have arisen. Phosphorylation of NRF2 can be facilitated by many different kinases (GSK-3β, AMPK, PKC, etc.). With this, the specific residue that is phosphorylated is integral to determining if it promotes or prevents nuclear translocation, e.g. serine 550 specific phosphorylation promotes translocation into the nucleus. Therefore, we hope to investigate what kinase phosphorylates NRF2 and where this occurs in the setting of radiation exposure. This could further be assessed in myriad other settings where ferroptosis may occur to determine the mechanism of resistance

2. Investigate FDA approved SLC7A11 inhibitors for possible radiation potentiation

The bioavailability of Erastin is quite low and it also is not an FDA approved drug, thus the translational utility of it is limited. With the success of Erastin at enhancing radiation lethality, it warrants the investigation of alternative drugs that block SLC7A11 as radiation potentiators. For example, Sulfasalazine (a commonly used anti-inflammatory) and Sorafenib (a pan kinase inhibitor) have been shown to inhibit SLC7A11. Therefore, we hope to assess the effectiveness of these compounds to be easily translatable radiation enhancing drugs.

3. Increase the bioavailability and targeted delivery of Erastin *via* EV loading

Importantly, these two aspects of early detection and treatment enhancement presented in this thesis merit union. A theranostic approach could be contrived whereby

PDAC specific EVs are isolated using one of our elucidated surface markers for diagnostic and prognostic purposes. These EVs could then be loaded with Erastin to increase its cellular uptake, bioavailability, and prevent degradation in circulation. The loaded EVs could then be used as an autologous means of radiation potentiation and tested *in vivo*. Conversely, we have observed that GPX4 is increased in EVs from Panc1 cells treated with radiation compared to untreated controls (data not shown). This finding merits further investigation into the role of EVs in ferroptosis resistance after radiation treatment.

Chapter 7: References

Chapter 7: References

1. Carmicheal J, Patel A, Dalal V, Atri P, Dhaliwal AS, Wittel UA, et al. Elevating pancreatic cystic lesion stratification: Current and future pancreatic cancer biomarker(s). Biochim Biophys Acta Rev Cancer. 2020;1873(1):188318.
2. Siegel RL, Miller KD, Jemal A. Cancer statistics, 2019. CA Cancer J Clin. 2019;69(1):7-34.
3. Rahib L, Smith BD, Aizenberg R, Rosenzweig AB, Fleshman JM, Matrisian LM. Projecting cancer incidence and deaths to 2030: the unexpected burden of thyroid, liver, and pancreas cancers in the United States. Cancer Res. 2014;74(11):2913-21.
4. Evans J, Chapple A, Salisbury H, Corrie P, Ziebland S. "It can't be very important because it comes and goes"--patients' accounts of intermittent symptoms preceding a pancreatic cancer diagnosis: a qualitative study. BMJ Open. 2014;4(2):e004215.
5. Lucenteforte E, La Vecchia C, Silverman D, Petersen GM, Bracci PM, Ji BT, et al. Alcohol consumption and pancreatic cancer: a pooled analysis in the International Pancreatic Cancer Case-Control Consortium (PanC4). Ann Oncol. 2012;23(2):374-82.
6. Bosetti C, Bravi F, Turati F, Edefonti V, Polesel J, Decarli A, et al. Nutrient-based dietary patterns and pancreatic cancer risk. Ann Epidemiol. 2013;23(3):124-8.
7. Genkinger JM, Kitahara CM, Bernstein L, Berrington de Gonzalez A, Brotzman M, Elena JW, et al. Central adiposity, obesity during early adulthood, and pancreatic cancer mortality in a pooled analysis of cohort studies. Ann Oncol. 2015;26(11):2257-66.
8. Whiteman DC, Webb PM, Green AC, Neale RE, Fritschi L, Bain CJ, et al. Cancers in Australia in 2010 attributable to modifiable factors: introduction and overview. Aust N Z J Public Health. 2015;39(5):403-7.
9. Bosetti C, Lucenteforte E, Silverman DT, Petersen G, Bracci PM, Ji BT, et al. Cigarette smoking and pancreatic cancer: an analysis from the International Pancreatic Cancer Case-Control Consortium (Panc4). Ann Oncol. 2012;23(7):1880-8.
10. McGuigan A, Kelly P, Turkington RC, Jones C, Coleman HG, McCain RS. Pancreatic cancer: A review of clinical diagnosis, epidemiology, treatment and outcomes. World journal of gastroenterology : WJG. 2018;24(43):4846-61.
11. Patel R, Ede J, Collins J, Willens D. Pancreatic cancer presenting as new-onset diabetes. Case Rep Oncol. 2014;7(1):171-4.
12. Canto MI, Harinck F, Hruban RH, Offerhaus GJ, Poley JW, Kamel I, et al. International Cancer of the Pancreas Screening (CAPS) Consortium summit on the management of patients with increased risk for familial pancreatic cancer. Gut. 2013;62(3):339-47.
13. Syngal S, Brand RE, Church JM, Giardiello FM, Hampel HL, Burt RW, et al. ACG clinical guideline: Genetic testing and management of hereditary gastrointestinal cancer syndromes. Am J Gastroenterol. 2015;110(2):223-62; quiz 63.
14. Chang MC, Wong JM, Chang YT. Screening and early detection of pancreatic cancer in high risk population. World journal of gastroenterology : WJG. 2014;20(9):2358-64.
15. Lynch HT, Brand RE, Deters CA, Shaw TG, Lynch JF. Hereditary pancreatic cancer. Pancreatology. 2001;1(5):466-71.

16. Wang L, Brune KA, Visvanathan K, Laheru D, Herman J, Wolfgang C, et al. Elevated cancer mortality in the relatives of patients with pancreatic cancer. Cancer Epidemiol Biomarkers Prev. 2009;18(11):2829-34.
17. Klein AP, Brune KA, Petersen GM, Goggins M, Tersmette AC, Offerhaus GJ, et al. Prospective risk of pancreatic cancer in familial pancreatic cancer kindreds. Cancer Res. 2004;64(7):2634-8.
18. McFaul CD, Greenhalf W, Earl J, Howes N, Neoptolemos JP, Kress R, et al. Anticipation in familial pancreatic cancer. Gut. 2006;55(2):252-8.
19. Brune KA, Lau B, Palmisano E, Canto M, Goggins MG, Hruban RH, et al. Importance of age of onset in pancreatic cancer kindreds. J Natl Cancer Inst. 2010;102(2):119-26.
20. Jones S, Hruban RH, Kamiyama M, Borges M, Zhang X, Parsons DW, et al. Exomic sequencing identifies PALB2 as a pancreatic cancer susceptibility gene. Science. 2009;324(5924):217.
21. Zhen DB, Rabe KG, Gallinger S, Syngal S, Schwartz AG, Goggins MG, et al. BRCA1, BRCA2, PALB2, and CDKN2A mutations in familial pancreatic cancer: a PACGENE study. Genet Med. 2015;17(7):569-77.
22. Roberts NJ, Norris AL, Petersen GM, Bondy ML, Brand R, Gallinger S, et al. Whole Genome Sequencing Defines the Genetic Heterogeneity of Familial Pancreatic Cancer. Cancer Discov. 2016;6(2):166-75.
23. Lal G, Liu G, Schmocker B, Kaurah P, Ozcelik H, Narod SA, et al. Inherited predisposition to pancreatic adenocarcinoma: role of family history and germ-line p16, BRCA1, and BRCA2 mutations. Cancer Res. 2000;60(2):409-16.
24. Middlebrooks CD, Stacey ML, Li Q, Snyder C, Shaw TG, Richardson-Nelson T, et al. Analysis of the CDKN2A Gene in FAMMM Syndrome Families Reveals Early Age of Onset for Additional Syndromic Cancers. Cancer Res. 2019;79(11):2992-3000.
25. Caldas C, Hahn SA, da Costa LT, Redston MS, Schutte M, Seymour AB, et al. Frequent somatic mutations and homozygous deletions of the p16 (MTS1) gene in pancreatic adenocarcinoma. Nat Genet. 1994;8(1):27-32.
26. de Snoo FA, Bishop DT, Bergman W, van Leeuwen I, van der Drift C, van Nieuwpoort FA, et al. Increased risk of cancer other than melanoma in CDKN2A founder mutation (p16-Leiden)-positive melanoma families. Clin Cancer Res. 2008;14(21):7151-7.
27. Bujanda L, Herreros-Villanueva M. Pancreatic Cancer in Lynch Syndrome Patients. J Cancer. 2017;8(18):3667-74.
28. Ligtenberg MJ, Kuiper RP, Chan TL, Goossens M, Hebeda KM, Voorendt M, et al. Heritable somatic methylation and inactivation of MSH2 in families with Lynch syndrome due to deletion of the 3' exons of TACSTD1. Nat Genet. 2009;41(1):112-7.
29. Giardiello FM, Allen JI, Axilbund JE, Boland CR, Burke CA, Burt RW, et al. Guidelines on genetic evaluation and management of Lynch syndrome: a consensus statement by the US Multi-society Task Force on colorectal cancer. Am J Gastroenterol. 2014;109(8):1159-79.
30. Kastrinos F, Mukherjee B, Tayob N, Wang F, Sparr J, Raymond VM, et al. Risk of pancreatic cancer in families with Lynch syndrome. JAMA. 2009;302(16):1790-5.

31. Gruber SB, Entius MM, Petersen GM, Laken SJ, Longo PA, Boyer R, et al. Pathogenesis of adenocarcinoma in Peutz-Jeghers syndrome. Cancer Res. 1998;58(23):5267-70.
32. Giardiello FM, Brensinger JD, Tersmette AC, Goodman SN, Petersen GM, Booker SV, et al. Very high risk of cancer in familial Peutz-Jeghers syndrome. Gastroenterology. 2000;119(6):1447-53.
33. van Lier MG, Wagner A, Mathus-Vliegen EM, Kuipers EJ, Steyerberg EW, van Leerdam ME. High cancer risk in Peutz-Jeghers syndrome: a systematic review and surveillance recommendations. Am J Gastroenterol. 2010;105(6):1258-64; author reply 65.
34. Raphael KL, Willingham FF. Hereditary pancreatitis: current perspectives. Clin Exp Gastroenterol. 2016;9:197-207.
35. Rebours V, Boutron-Ruault MC, Schnee M, Ferec C, Le Marechal C, Hentic O, et al. The natural history of hereditary pancreatitis: a national series. Gut. 2009;58(1):97-103.
36. Charnley RM. Hereditary pancreatitis. World journal of gastroenterology : WJG. 2003;9(1):1-4.
37. Howes N, Greenhalf W, Stocken DD, Neoptolemos JP. Cationic trypsinogen mutations and pancreatitis. Gastroenterol Clin North Am. 2004;33(4):767-87.
38. DiMagno MJ, DiMagno EP. Chronic pancreatitis. Curr Opin Gastroenterol. 2005;21(5):544-54.
39. Pfutzer RH, Barmada MM, Brunskill AP, Finch R, Hart PS, Neoptolemos J, et al. SPINK1/PSTI polymorphisms act as disease modifiers in familial and idiopathic chronic pancreatitis. Gastroenterology. 2000;119(3):615-23.
40. Lowenfels AB, Maisonneuve P, DiMagno EP, Elitsur Y, Gates LK, Jr., Perrault J, et al. Hereditary pancreatitis and the risk of pancreatic cancer. International Hereditary Pancreatitis Study Group. J Natl Cancer Inst. 1997;89(6):442-6.
41. Yamada M, Satoh T, Monden T, Murakami M, Iriuchijima T, Wilber JF, et al. Influences of hypothyroidism on TRH concentrations and preproTRH mRNA levels in rat hypothalamus: a simple and reliable method to detect preproTRH mRNA level. Neuroendocrinology. 1992;55(3):317-20.
42. Hruban RH, Takaori K, Klimstra DS, Adsay NV, Albores-Saavedra J, Biankin AV, et al. An illustrated consensus on the classification of pancreatic intraepithelial neoplasia and intraductal papillary mucinous neoplasms. Am J Surg Pathol. 2004;28(8):977-87.
43. Furukawa T, Fukushima N, Itoi T, Ohike N, Mitsuhashi T, Nakagohri T, et al. A Consensus Study of the Grading and Typing of Intraductal Papillary Mucinous Neoplasms of the Pancreas. Pancreas. 2019;48(4):480-7.
44. Zamboni G, Hirabayashi K, Castelli P, Lennon AM. Precancerous lesions of the pancreas. Best Pract Res Clin Gastroenterol. 2013;27(2):299-322.
45. Hruban RH, Adsay NV, Albores-Saavedra J, Compton C, Garrett ES, Goodman SN, et al. Pancreatic intraepithelial neoplasia: a new nomenclature and classification system for pancreatic duct lesions. Am J Surg Pathol. 2001;25(5):579-86.
46. Riva G, Pea A, Pilati C, Fiadone G, Lawlor RT, Scarpa A, et al. Histo-molecular oncogenesis of pancreatic cancer: From precancerous lesions to invasive ductal adenocarcinoma. World J Gastrointest Oncol. 2018;10(10):317-27.
47. Noe M, Brosens LA. Pathology of Pancreatic Cancer Precursor Lesions. Surg Pathol Clin. 2016;9(4):561-80.

48. Yokode M, Akita M, Fujikura K, Kim MJ, Morinaga Y, Yoshikawa S, et al. High-grade PanIN presenting with localised stricture of the main pancreatic duct: A clinicopathological and molecular study of 10 cases suggests a clue for the early detection of pancreatic cancer. Histopathology. 2018;73(2):247-58.
49. Nagata K, Horinouchi M, Saitou M, Higashi M, Nomoto M, Goto M, et al. Mucin expression profile in pancreatic cancer and the precursor lesions. J Hepatobiliary Pancreat Surg. 2007;14(3):243-54.
50. Basturk O, Khayyata S, Klimstra DS, Hruban RH, Zamboni G, Coban I, et al. Preferential expression of MUC6 in oncocytic and pancreatobiliary types of intraductal papillary neoplasms highlights a pyloropancreatic pathway, distinct from the intestinal pathway, in pancreatic carcinogenesis. Am J Surg Pathol. 2010;34(3):364-70.
51. Hruban RH, Goggins M, Parsons J, Kern SE. Progression model for pancreatic cancer. Clin Cancer Res. 2000;6(8):2969-72.
52. Decker GA, Batheja MJ, Collins JM, Silva AC, Mekeel KL, Moss AA, et al. Risk factors for pancreatic adenocarcinoma and prospects for screening. Gastroenterol Hepatol (N Y). 2010;6(4):246-54.
53. Mukewar SS, Sharma A, Phillip N, Gupta R, Aryal-Khanal A, de Pretis N, et al. Risk of Pancreatic Cancer in Patients With Pancreatic Cysts and Family History of Pancreatic Cancer. Clin Gastroenterol Hepatol. 2018;16(7):1123-30 e1.
54. Esposito I, Konukiewitz B, Schlitter AM, Kloppel G. Pathology of pancreatic ductal adenocarcinoma: facts, challenges and future developments. World journal of gastroenterology : WJG. 2014;20(38):13833-41.
55. Chernyak V, Flusberg M, Haramati LB, Rozenblit AM, Bellin E. Incidental pancreatic cystic lesions: is there a relationship with the development of pancreatic adenocarcinoma and all-cause mortality? Radiology. 2015;274(1):161-9.
56. Ohno E, Hirooka Y, Kawashima H, Ishikawa T, Kanamori A, Ishikawa H, et al. Natural history of pancreatic cystic lesions: A multicenter prospective observational study for evaluating the risk of pancreatic cancer. J Gastroenterol Hepatol. 2018;33(1):320-8.
57. Kim JR, Jang JY, Kang MJ, Park T, Lee SY, Jung W, et al. Clinical implication of serum carcinoembryonic antigen and carbohydrate antigen 19-9 for the prediction of malignancy in intraductal papillary mucinous neoplasm of pancreas. J Hepatobiliary Pancreat Sci. 2015;22(9):699-707.
58. de Jong K, Bruno MJ, Fockens P. Epidemiology, diagnosis, and management of cystic lesions of the pancreas. Gastroenterol Res Pract. 2012;147465(10):11.
59. Brugge WR. Diagnosis and management of cystic lesions of the pancreas. J Gastrointest Oncol. 2015;6(4):375-88.
60. Kimura W, Nagai H, Kuroda A, Muto T, Esaki Y. Analysis of small cystic lesions of the pancreas. Int J Pancreatol. 1995;18(3):197-206.
61. Gardner TB, Glass LM, Smith KD, Ripple GH, Barth RJ, Klibansky DA, et al. Pancreatic cyst prevalence and the risk of mucin-producing adenocarcinoma in US adults. Am J Gastroenterol. 2013;108(10):1546-50.
62. Tanaka M, Fernandez-Del Castillo C, Kamisawa T, Jang JY, Levy P, Ohtsuka T, et al. Revisions of international consensus Fukuoka guidelines for the management of IPMN of the pancreas. Pancreatology. 2017;17(5):738-53.
63. Farrell JJ. Prevalence, Diagnosis and Management of Pancreatic Cystic Neoplasms: Current Status and Future Directions. Gut Liver. 2015;9(5):571-89.

64. Capella C. SE, G. Pape K.I., Hruban R. H. Serous cystic neoplasms of the pancreas. In: SR Hamilton ALA, editor. World Health Organization Classification of Tumors. Lyon, France: IARC Press; 2000. p. 234-6.
65. Zamboni G KG, Hruban RH, Longnecker DS, Adler G. Mucinous cystic neoplasms of the pancreas. In: SR Hamilton AL, editor. World Health Organization Classification of Tumors. Lyon, France: IARC Press; 2000. p. 234-6.
66. Longnecker DS AG, Hruban RH. Intraductal papillarymucinous neoplasms of the pancreas. . In: SR Hamilton AL, editor. World Health Organization Classification of Tumors. Lyon, France: IARC Press; 2000. p. 237-41.
67. Compagno J, Oertel JE. Microcystic adenomas of the pancreas (glycogen-rich cystadenomas): a clinicopathologic study of 34 cases. Am J Clin Pathol. 1978;69(3):289-98.
68. Alpert LC, Truong LD, Bossart MI, Spjut HJ. Microcystic adenoma (serous cystadenoma) of the pancreas. A study of 14 cases with immunohistochemical and electron-microscopic correlation. Am J Surg Pathol. 1988;12(4):251-63.
69. Solcia E CC, Klöppel G: Tumors of the Pancreas. AFIP Atlas of Tumor Pathology, 3rd series, fasc 20. Washington, Armed Forces Institute of Pathology. Tumors of the Pancreas. AFIP Atlas of Tumor Pathology. fascicle 20. Washington. D.C.: Armed Forces Institutes of Pathology; 1997.
70. Egawa N, Maillet B, Schroder S, Mukai K, Kloppel G. Serous oligocystic and ill-demarcated adenoma of the pancreas: a variant of serous cystic adenoma. Virchows Arch. 1994;424(1):13-7.
71. Charville GW, Kao CS. Serous Neoplasms of the Pancreas: A Comprehensive Review. Arch Pathol Lab Med. 2018;142(9):1134-40.
72. Bogomoletz WV, Adnet JJ, Widgren S, Stavrou M, McLaughlin JE. Cystadenoma of the pancreas: a histological, histochemical and ultrastructural study of seven cases. Histopathology. 1980;4(3):309-20.
73. Brugge WR, Lewandrowski K, Lee-Lewandrowski E, Centeno BA, Szydlo T, Regan S, et al. Diagnosis of pancreatic cystic neoplasms: a report of the cooperative pancreatic cyst study. Gastroenterology. 2004;126(5):1330-6.
74. Al-Haddad M, Gill KR, Raimondo M, Woodward TA, Krishna M, Crook JE, et al. Safety and efficacy of cytology brushings versus standard fine-needle aspiration in evaluating cystic pancreatic lesions: a controlled study. Endoscopy. 2010;42(2):127-32.
75. Cizginer S, Turner BG, Bilge AR, Karaca C, Pitman MB, Brugge WR. Cyst fluid carcinoembryonic antigen is an accurate diagnostic marker of pancreatic mucinous cysts. Pancreas. 2011;40(7):1024-8.
76. Robinson SM, Scott J, Oppong KW, White SA. What to do for the incidental pancreatic cystic lesion? Surgical Oncology. (0).
77. Jais B, Rebours V, Malleo G, Salvia R, Fontana M, Maggino L, et al. Serous cystic neoplasm of the pancreas: a multinational study of 2622 patients under the auspices of the International Association of Pancreatology and European Pancreatic Club (European Study Group on Cystic Tumors of the Pancreas). Gut. 2016;65(2):305-12.
78. Yoshimi N, Sugie S, Tanaka T, Aijin W, Bunai Y, Tatematsu A, et al. A rare case of serous cystadenocarcinoma of the pancreas. Cancer. 1992;69(10):2449-53.

79. Hruban RH PM, Klimstra DS. Tumors of the pancreas. Atlas of Tumor Pathology. 6 ed. Washington, D.C.: American Registry of Pathology and Armed Forces Institute of Pathology; 2007.
80. Zamboni G, Scarpa A, Bogina G, Iacono C, Bassi C, Talamini G, et al. Mucinous cystic tumors of the pancreas: clinicopathological features, prognosis, and relationship to other mucinous cystic tumors. Am J Surg Pathol. 1999;23(4):410-22.
81. Sarr MG, Carpenter HA, Prabhakar LP, Orchard TF, Hughes S, van Heerden JA, et al. Clinical and pathologic correlation of 84 mucinous cystic neoplasms of the pancreas: can one reliably differentiate benign from malignant (or premalignant) neoplasms? Ann Surg. 2000;231(2):205-12.
82. Yamada M, Kozuka S, Yamao K, Nakazawa S, Naitoh Y, Tsukamoto Y. Mucin-producing tumor of the pancreas. Cancer. 1991;68(1):159-68.
83. Campbell F, Azadeh B. Cystic neoplasms of the exocrine pancreas. Histopathology. 2008;52(5):539-51.
84. Pittman ME, Rao R, Hruban RH. Classification, Morphology, Molecular Pathogenesis, and Outcome of Premalignant Lesions of the Pancreas. Arch Pathol Lab Med. 2017;141(12):1606-14.
85. Tanaka M, Chari S, Adsay V, Fernandez-del Castillo C, Falconi M, Shimizu M, et al. International consensus guidelines for management of intraductal papillary mucinous neoplasms and mucinous cystic neoplasms of the pancreas. Pancreatology. 2006;6(1-2):17-32.
86. Reddy RP, Smyrk TC, Zapiach M, Levy MJ, Pearson RK, Clain JE, et al. Pancreatic mucinous cystic neoplasm defined by ovarian stroma: demographics, clinical features, and prevalence of cancer. Clin Gastroenterol Hepatol. 2004;2(11):1026-31.
87. Li T, Chen ZQ, Meng ZX, Hong JG, Zhi XT. Calcified Cystic Lesion of the Pancreas. J Gastrointest Surg. 2016;20(6):1272-4.
88. Bosman FWHO, International Agency for Research on Cancer. WHO classification of tumours of the digestive system. 4 ed. Bosman F, editor. Lyon, France: IARC Press; 2010.
89. Crippa S, Salvia R, Warshaw AL, Dominguez I, Bassi C, Falconi M, et al. Mucinous cystic neoplasm of the pancreas is not an aggressive entity: lessons from 163 resected patients. Ann Surg. 2008;247(4):571-9.
90. Tanaka M. Intraductal Papillary Mucinous Neoplasm of the Pancreas as the Main Focus for Early Detection of Pancreatic Adenocarcinoma. Pancreas. 2018;47(5):544-50.
91. Valsangkar NP, Morales-Oyarvide V, Thayer SP, Ferrone CR, Wargo JA, Warshaw AL, et al. 851 resected cystic tumors of the pancreas: a 33-year experience at the Massachusetts General Hospital. Surgery. 2012;152(3 Suppl 1):S4-12.
92. Morohoshi T, Held G, Kloppel G. Exocrine pancreatic tumours and their histological classification. A study based on 167 autopsy and 97 surgical cases. Histopathology. 1983;7(5):645-61.
93. Madura JA, Wiebke EA, Howard TJ, Cummings OW, Hull MT, Sherman S, et al. Mucin-hypersecreting intraductal neoplasms of the pancreas: a precursor to cystic pancreatic malignancies. Surgery. 1997;122(4):786-92; discussion 92-3.
94. Choi SH, Park SH, Kim KW, Lee JY, Lee SS. Progression of Unresected Intraductal Papillary Mucinous Neoplasms of the Pancreas to Cancer: A Systematic Review and Meta-analysis. Clin Gastroenterol Hepatol. 2017;15(10):1509-20 e4.

95. Stark A, Donahue TR, Reber HA, Hines OJ. Pancreatic Cyst Disease: A Review. JAMA. 2016;315(17):1882-93.
96. Rosenblatt R, Dorfman V, Epelboym I, Poneros JM, Sethi A, Lightdale C, et al. Demographic features and natural history of intermediate-risk multifocal versus unifocal intraductal papillary mucinous neoplasms. Pancreas. 2015;44(3):478-83.
97. Monzen M, Shimizu K, Hatori T, Furukawa T, Shiratori K. Usefulness of cell block cytology for preoperative grading and typing of intraductal papillary mucinous neoplasms. Pancreatology. 2013;13(4):369-78.
98. Hisaka T, Horiuchi H, Uchida S, Ishikawa H, Kawahara R, Kawashima Y, et al. Potential usefulness of mucin immunohistochemical staining of preoperative pancreatic biopsy or juice cytology specimens in the determination of treatment strategies for intraductal papillary mucinous neoplasm. Oncol Rep. 2013;30(5):2035-41.
99. Yoon WJ, Daglilar ES, Mino-Kenudson M, Morales-Oyarvide V, Pitman MB, Brugge WR. Characterization of epithelial subtypes of intraductal papillary mucinous neoplasm of the pancreas with endoscopic ultrasound and cyst fluid analysis. Endoscopy. 2014;46(12):1071-7.
100. Furukawa T, Hatori T, Fujita I, Yamamoto M, Kobayashi M, Ohike N, et al. Prognostic relevance of morphological types of intraductal papillary mucinous neoplasms of the pancreas. Gut. 2011;60(4):509-16.
101. Tanaka M, Fernández-del Castillo C, Adsay V, Chari S, Falconi M, Jang J-Y, et al. International consensus guidelines 2012 for the management of IPMN and MCN of the pancreas. Pancreatology. 2012;12(3):183-97.
102. Luttges J, Zamboni G, Longnecker D, Kloppel G. The immunohistochemical mucin expression pattern distinguishes different types of intraductal papillary mucinous neoplasms of the pancreas and determines their relationship to mucinous noncystic carcinoma and ductal adenocarcinoma. Am J Surg Pathol. 2001;25(7):942-8.
103. Adsay NV, Merati K, Basturk O, Iacobuzio-Donahue C, Levi E, Cheng JD, et al. Pathologically and biologically distinct types of epithelium in intraductal papillary mucinous neoplasms: delineation of an "intestinal" pathway of carcinogenesis in the pancreas. Am J Surg Pathol. 2004;28(7):839-48.
104. Adsay NV, Adair CF, Heffess CS, Klimstra DS. Intraductal oncocytic papillary neoplasms of the pancreas. Am J Surg Pathol. 1996;20(8):980-94.
105. Law JK, Ahmed A, Singh VK, Akshintala VS, Olson MT, Raman SP, et al. A systematic review of solid-pseudopapillary neoplasms: are these rare lesions? Pancreas. 2014;43(3):331-7.
106. Yu PF, Hu ZH, Wang XB, Guo JM, Cheng XD, Zhang YL, et al. Solid pseudopapillary tumor of the pancreas: a review of 553 cases in Chinese literature. World journal of gastroenterology : WJG. 2010;16(10):1209-14.
107. Salvia R, Malleo G, Marchegiani G, Pennacchio S, Paiella S, Paini M, et al. Pancreatic resections for cystic neoplasms: from the surgeon's presumption to the pathologist's reality. Surgery. 2012;152(3 Suppl 1):S135-42.
108. Borhani AA, Fasanella KE, Iranpour N, Zureikat AH, Singhi AD, Furlan A, et al. Lymphoepithelial cyst of pancreas: spectrum of radiological findings with pathologic correlation. Abdom Radiol (NY). 2017;42(3):877-83.
109. Arumugam P, Fletcher N, Kyriakides C, Mears L, Kocher HM. Lymphoepithelial Cyst of the Pancreas. Case Rep Gastroenterol. 2016;10(1):181-92.

110. Moore PS, Missiaglia E, Antonello D, Zamo A, Zamboni G, Corleto V, et al. Role of disease-causing genes in sporadic pancreatic endocrine tumors: MEN1 and VHL. Genes Chromosomes Cancer. 2001;32(2):177-81.
111. Atiq M, Bhutani MS, Bektas M, Lee JE, Gong Y, Tamm EP, et al. EUS-FNA for pancreatic neuroendocrine tumors: a tertiary cancer center experience. Dig Dis Sci. 2012;57(3):791-800.
112. Habashi S, Draganov PV. Pancreatic pseudocyst. World journal of gastroenterology : WJG. 2009;15(1):38-47.
113. Braha J, Tenner S. Fluid Collections and Pseudocysts as a Complication of Acute Pancreatitis. Gastrointest Endosc Clin N Am. 2018;28(2):123-30.
114. Kloppel G, Maillet B. Pseudocysts in chronic pancreatitis: a morphological analysis of 57 resection specimens and 9 autopsy pancreata. Pancreas. 1991;6(3):266-74.
115. Ammann RW, Heitz PU, Kloppel G. Course of alcoholic chronic pancreatitis: a prospective clinicomorphological long-term study. Gastroenterology. 1996;111(1):224-31.
116. Matsubayashi H, Iwai T, Matsui T, Wada T, Kawata N, Ito H, et al. Pancreatic cystic lesions with atypical steroid response should be carefully managed in cases of autoimmune pancreatitis. J Gastroenterol Hepatol. 2016;31(1):270-6.
117. Brugge WR. Diagnosis and management of relapsing pancreatitis associated with cystic neoplasms of the pancreas. World journal of gastroenterology : WJG. 2008;14(7):1038-43.
118. Pezzilli R, Melzi d'Eril G, Barassi A. Can Serum Pancreatic Amylase and Lipase Levels Be Used as Diagnostic Markers to Distinguish Between Patients With Mucinous Cystic Lesions of the Pancreas, Chronic Pancreatitis, and Pancreatic Ductal Adenocarcinoma? Pancreas. 2016;45(9):1272-5.
119. Crippa S, Fernandez-Del Castillo C, Salvia R, Finkelstein D, Bassi C, Dominguez I, et al. Mucin-producing neoplasms of the pancreas: an analysis of distinguishing clinical and epidemiologic characteristics. Clin Gastroenterol Hepatol. 2010;8(2):213-9.
120. Hedayat AA, Lisovsky M, Suriawinata AA, Longnecker DS. Association of IgG4 response and autoimmune pancreatitis with intraductal papillary-mucinous neoplasms. Pancreatology. 2017;17(2):263-6.
121. Gomez D, Rahman SH, Won LF, Verbeke CS, McMahon MJ, Menon KV. Characterization of malignant pancreatic cystic lesions in the background of chronic pancreatitis. JOP. 2006;7(5):465-72.
122. Waddell N, Pajic M, Patch AM, Chang DK, Kassahn KS, Bailey P, et al. Whole genomes redefine the mutational landscape of pancreatic cancer. Nature. 2015;518(7540):495-501.
123. Witkiewicz AK, McMillan EA, Balaji U, Baek G, Lin WC, Mansour J, et al. Whole-exome sequencing of pancreatic cancer defines genetic diversity and therapeutic targets. Nat Commun. 2015;6:6744.
124. Wu J, Jiao Y, Dal Molin M, Maitra A, de Wilde RF, Wood LD, et al. Whole-exome sequencing of neoplastic cysts of the pancreas reveals recurrent mutations in components of ubiquitin-dependent pathways. Proc Natl Acad Sci U S A. 2011;108(52):21188-93.
125. Wood LD, Yurgelun MB, Goggins MG. Genetics of Familial and Sporadic Pancreatic Cancer. Gastroenterology. 2019;156(7):2041-55.

126. Hirai H, Okabe T, Anraku Y, Fujisawa M, Urabe A, Takaku F. Activation of the c-K-ras oncogene in a human pancreas carcinoma. Biochem Biophys Res Commun. 1985;127(1):168-74.
127. Barton CM, Staddon SL, Hughes CM, Hall PA, O'Sullivan C, Kloppel G, et al. Abnormalities of the p53 tumour suppressor gene in human pancreatic cancer. Br J Cancer. 1991;64(6):1076-82.
128. Hahn SA, Schutte M, Hoque AT, Moskaluk CA, da Costa LT, Rozenblum E, et al. DPC4, a candidate tumor suppressor gene at human chromosome 18q21.1. Science. 1996;271(5247):350-3.
129. Gisselsson D, Jonson T, Petersen A, Strombeck B, Dal Cin P, Hoglund M, et al. Telomere dysfunction triggers extensive DNA fragmentation and evolution of complex chromosome abnormalities in human malignant tumors. Proc Natl Acad Sci U S A. 2001;98(22):12683-8.
130. Distler M, Aust D, Weitz J, Pilarsky C, Grutzmann R. Precursor lesions for sporadic pancreatic cancer: PanIN, IPMN, and MCN. Biomed Res Int. 2014;2014:474905.
131. Campbell SL, Khosravi-Far R, Rossman KL, Clark GJ, Der CJ. Increasing complexity of Ras signaling. Oncogene. 1998;17(11 Reviews):1395-413.
132. Hezel AF, Kimmelman AC, Stanger BZ, Bardeesy N, Depinho RA. Genetics and biology of pancreatic ductal adenocarcinoma. Genes Dev. 2006;20(10):1218-49.
133. Lohr M, Kloppel G, Maisonneuve P, Lowenfels AB, Luttges J. Frequency of K-ras mutations in pancreatic intraductal neoplasias associated with pancreatic ductal adenocarcinoma and chronic pancreatitis: a meta-analysis. Neoplasia. 2005;7(1):17-23.
134. Shiroma N, Arihiro K, Oda M, Orita M. KRAS fluorescence in situ hybridisation testing for the detection and diagnosis of pancreatic adenocarcinoma. J Clin Pathol. 2018.
135. Chen PY, Muzumdar MD, Dorans KJ, Robbins R, Bhutkar A, Del Rosario A, et al. Adaptive and Reversible Resistance to Kras Inhibition in Pancreatic Cancer Cells. Cancer Res. 2018;78(4):985-1002.
136. Almoguera C, Shibata D, Forrester K, Martin J, Arnheim N, Perucho M. Most human carcinomas of the exocrine pancreas contain mutant c-K-ras genes. Cell. 1988;53(4):549-54.
137. Caldas C, Kern SE. K-ras mutation and pancreatic adenocarcinoma. Int J Pancreatol. 1995;18(1):1-6.
138. Tan MC, Basturk O, Brannon AR, Bhanot U, Scott SN, Bouvier N, et al. GNAS and KRAS Mutations Define Separate Progression Pathways in Intraductal Papillary Mucinous Neoplasm-Associated Carcinoma. J Am Coll Surg. 2015;220(5):845-54.
139. Satoh K, Shimosegawa T, Moriizumi S, Koizumi M, Toyota T. K-ras mutation and p53 protein accumulation in intraductal mucin-hypersecreting neoplasms of the pancreas. Pancreas. 1996;12(4):362-8.
140. Maitra A, Kern SE, Hruban RH. Molecular pathogenesis of pancreatic cancer. Best Pract Res Clin Gastroenterol. 2006;20(2):211-26.
141. Sato N, Mizumoto K, Nagai E, Tanaka M. Telomerase as a new target for pancreatic cancer treatment. J Hepatobiliary Pancreat Surg. 2002;9(3):322-7.
142. Clark SJ. Action at a distance: epigenetic silencing of large chromosomal regions in carcinogenesis. Hum Mol Genet. 2007;16 Spec No 1:R88-95.

143. House MG, Herman JG, Guo MZ, Hooker CM, Schulick RD, Lillemoe KD, et al. Aberrant hypermethylation of tumor suppressor genes in pancreatic endocrine neoplasms. Ann Surg. 2003;238(3):423-31; discussion 31-2.
144. Tan AC, Jimeno A, Lin SH, Wheelhouse J, Chan F, Solomon A, et al. Characterizing DNA methylation patterns in pancreatic cancer genome. Mol Oncol. 2009;3(5-6):425-38.
145. Sato N, Fukushima N, Hruban RH, Goggins M. CpG island methylation profile of pancreatic intraepithelial neoplasia. Mod Pathol. 2008;21(3):238-44.
146. Redston MS, Caldas C, Seymour AB, Hruban RH, da Costa L, Yeo CJ, et al. p53 mutations in pancreatic carcinoma and evidence of common involvement of homocopolymer tracts in DNA microdeletions. Cancer Res. 1994;54(11):3025-33.
147. Kern SE. p53: tumor suppression through control of the cell cycle. Gastroenterology. 1994;106(6):1708-11.
148. Schutte M, Hruban RH, Hedrick L, Cho KR, Nadasdy GM, Weinstein CL, et al. DPC4 gene in various tumor types. Cancer Res. 1996;56(11):2527-30.
149. Boschman CR, Stryker S, Reddy JK, Rao MS. Expression of p53 protein in precursor lesions and adenocarcinoma of human pancreas. Am J Pathol. 1994;145(6):1291-5.
150. Zauber P, Marotta SP, Sabbath-Solitare M. GNAS gene mutation may be present only transiently during colorectal tumorigenesis. Int J Mol Epidemiol Genet. 2016;7(1):24-31.
151. Safran H, Steinhoff M, Mangray S, Rathore R, King TC, Chai L, et al. Overexpression of the HER-2/neu oncogene in pancreatic adenocarcinoma. Am J Clin Oncol. 2001;24(5):496-9.
152. Korc M, Chandrasekar B, Yamanaka Y, Friess H, Buchier M, Beger HG. Overexpression of the epidermal growth factor receptor in human pancreatic cancer is associated with concomitant increases in the levels of epidermal growth factor and transforming growth factor alpha. J Clin Invest. 1992;90(4):1352-60.
153. Del Chiaro M, Segersvard R, Lohr M, Verbeke C. Early detection and prevention of pancreatic cancer: is it really possible today? World journal of gastroenterology : WJG. 2014;20(34):12118-31.
154. Rulyak SJ, Brentnall TA. Inherited pancreatic cancer: surveillance and treatment strategies for affected families. Pancreatology. 2001;1(5):477-85.
155. Costache MI, Costache CA, Dumitrescu CI, Tica AA, Popescu M, Baluta EA, et al. Which is the Best Imaging Method in Pancreatic Adenocarcinoma Diagnosis and Staging - CT, MRI or EUS? Curr Health Sci J. 2017;43(2):132-6.
156. Verna EC, Hwang C, Stevens PD, Rotterdam H, Stavropoulos SN, Sy CD, et al. Pancreatic cancer screening in a prospective cohort of high-risk patients: a comprehensive strategy of imaging and genetics. Clin Cancer Res. 2010;16(20):5028-37.
157. Vege SS, Ziring B, Jain R, Moayyedi P, Clinical Guidelines C, American Gastroenterology A. American gastroenterological association institute guideline on the diagnosis and management of asymptomatic neoplastic pancreatic cysts. Gastroenterology. 2015;148(4):819-22; quize12-3.
158. Dalal V, Carmicheal J, Dhaliwal A, Jain M, Kaur S, Batra SK. Radiomics in stratification of pancreatic cystic lesions: Machine learning in action. Cancer Lett. 2020;469:228-37.

159. Kauhanen S, Rinta-Kiikka I, Kemppainen J, Gronroos J, Kajander S, Seppanen M, et al. Accuracy of 18F-FDG PET/CT, Multidetector CT, and MR Imaging in the Diagnosis of Pancreatic Cysts: A Prospective Single-Center Study. J Nucl Med. 2015;56(8):1163-8.
160. England CG, Hernandez R, Eddine SB, Cai W. Molecular Imaging of Pancreatic Cancer with Antibodies. Mol Pharm. 2016;13(1):8-24.
161. van der Waaij LA, van Dullemen HM, Porte RJ. Cyst fluid analysis in the differential diagnosis of pancreatic cystic lesions: a pooled analysis. Gastrointestinal endoscopy. 2005;62(3):383-9.
162. Castellano-Megias VM, Andres CI, Lopez-Alonso G, Colina-Ruizdelgado F. Pathological features and diagnosis of intraductal papillary mucinous neoplasm of the pancreas. World J Gastrointest Oncol. 2014;6(9):311-24.
163. Suzuki R, Thosani N, Annangi S, Guha S, Bhutani MS. Diagnostic yield of EUS-FNA-based cytology distinguishing malignant and benign IPMNs: a systematic review and meta-analysis. Pancreatology. 2014;14(5):380-4.
164. Yoon WJ, Daglilar ES, Fernandez-del Castillo C, Mino-Kenudson M, Pitman MB, Brugge WR. Peritoneal seeding in intraductal papillary mucinous neoplasm of the pancreas patients who underwent endoscopic ultrasound-guided fine-needle aspiration: the PIPE Study. Endoscopy. 2014;46(5):382-7.
165. Vilas-Boas F, Macedo G. Pancreatic Cystic Lesions: New Endoscopic Trends in Diagnosis. J Clin Gastroenterol. 2018;52(1):13-9.
166. Zhao Q, Zhan T, Deng Z, Li Q, Liu Y, Yang S, et al. Glycan analysis of colorectal cancer samples reveals stage-dependent changes in CEA glycosylation patterns. Clin Proteomics. 2018;15:9.
167. Yoshikawa M, Morine Y, Ikemoto T, Imura S, Higashijima J, Iwahashi S, et al. Elevated Preoperative Serum CEA Level Is Associated with Poor Prognosis in Patients with Hepatocellular Carcinoma Through the Epithelial-Mesenchymal Transition. Anticancer Res. 2017;37(3):1169-75.
168. Talar-Wojnarowska R, Pazurek M, Durko L, Degowska M, Rydzewska G, Smigielski J, et al. Pancreatic cyst fluid analysis for differential diagnosis between benign and malignant lesions. Oncol Lett. 2013;5(2):613-6.
169. Wang W, Zhang L, Chen L, Wei J, Sun Q, Xie Q, et al. Serum carcinoembryonic antigen and carbohydrate antigen 19-9 for prediction of malignancy and invasiveness in intraductal papillary mucinous neoplasms of the pancreas: A meta-analysis. Biomed Rep. 2015;3(1):43-50.
170. Fritz S, Hackert T, Hinz U, Hartwig W, Buchler MW, Werner J. Role of serum carbohydrate antigen 19-9 and carcinoembryonic antigen in distinguishing between benign and invasive intraductal papillary mucinous neoplasm of the pancreas. Br J Surg. 2011;98(1):104-10.
171. Corvelo TC, de Loiola Rdo S, Aguiar DC, de Matos Gde C, de Brito DC. The Lewis histo-blood group system: molecular analysis of the 59T>G, 508G>A, and 1067T>A polymorphisms in an Amazonian population. PLoS One. 2013;8(7):e69908.
172. Hao C, Zhang G, Zhang L. Serum CEA levels in 49 different types of cancer and noncancer diseases. Prog Mol Biol Transl Sci. 2019;162:213-27.
173. Neoptolemos JP, Kleeff J, Michl P, Costello E, Greenhalf W, Palmer DH. Therapeutic developments in pancreatic cancer: current and future perspectives. Nat Rev Gastroenterol Hepatol. 2018.

174. Lynch SM, Vrieling A, Lubin JH, Kraft P, Mendelsohn JB, Hartge P, et al. Cigarette smoking and pancreatic cancer: a pooled analysis from the pancreatic cancer cohort consortium. Am J Epidemiol. 2009;170(4):403-13.
175. Kleeff J, Korc M, Apte M, La Vecchia C, Johnson CD, Biankin AV, et al. Pancreatic cancer. Nat Rev Dis Primers. 2016;2:16022.
176. Vincent A, Herman J, Schulick R, Hruban RH, Goggins M. Pancreatic cancer. Lancet. 2011;378(9791):607-20.
177. Khorana AA, Mangu PB, Berlin J, Engebretson A, Hong TS, Maitra A, et al. Potentially Curable Pancreatic Cancer: American Society of Clinical Oncology Clinical Practice Guideline Update. J Clin Oncol. 2017;35(20):2324-8.
178. Tempero MA. NCCN Guidelines Updates: Pancreatic Cancer. J Natl Compr Canc Netw. 2019;17(5.5):603-5.
179. Kalser MH, Ellenberg SS. Pancreatic cancer. Adjuvant combined radiation and chemotherapy following curative resection. Arch Surg. 1985;120(8):899-903.
180. Neoptolemos JP, Dunn JA, Stocken DD, Almond J, Link K, Beger H, et al. Adjuvant chemoradiotherapy and chemotherapy in resectable pancreatic cancer: a randomised controlled trial. Lancet. 2001;358(9293):1576-85.
181. Oettle H, Post S, Neuhaus P, Gellert K, Langrehr J, Ridwelski K, et al. Adjuvant chemotherapy with gemcitabine vs observation in patients undergoing curative-intent resection of pancreatic cancer: a randomized controlled trial. JAMA. 2007;297(3):267-77.
182. Neoptolemos JP, Palmer DH, Ghaneh P, Psarelli EE, Valle JW, Halloran CM, et al. Comparison of adjuvant gemcitabine and capecitabine with gemcitabine monotherapy in patients with resected pancreatic cancer (ESPAC-4): a multicentre, open-label, randomised, phase 3 trial. Lancet. 2017;389(10073):1011-24.
183. Philip PA, Buyse ME, Alistar AT, Rocha Lima CM, Luther S, Pardee TS, et al. A Phase III open-label trial to evaluate efficacy and safety of CPI-613 plus modified FOLFIRINOX (mFFX) versus FOLFIRINOX (FFX) in patients with metastatic adenocarcinoma of the pancreas. Future Oncol. 2019;15(28):3189-96.
184. Conroy T, Hammel P, Hebbar M, Ben Abdelghani M, Wei AC, Raoul JL, et al. FOLFIRINOX or Gemcitabine as Adjuvant Therapy for Pancreatic Cancer. N Engl J Med. 2018;379(25):2395-406.
185. Ghosn M, Kourie HR, El Rassy E, Haddad FG, Hanna C, El Karak F, et al. Where does chemotherapy stands in the treatment of ampullary carcinoma? A review of literature. World J Gastrointest Oncol. 2016;8(10):745-50.
186. Zhan HX, Xu JW, Wu D, Wu ZY, Wang L, Hu SY, et al. Neoadjuvant therapy in pancreatic cancer: a systematic review and meta-analysis of prospective studies. Cancer Med. 2017;6(6):1201-19.
187. Tachezy M, Gebauer F, Petersen C, Arnold D, Trepel M, Wegscheider K, et al. Sequential neoadjuvant chemoradiotherapy (CRT) followed by curative surgery vs. primary surgery alone for resectable, non-metastasized pancreatic adenocarcinoma: NEOPA- a randomized multicenter phase III study (NCT01900327, DRKS00003893, ISRCTN82191749). BMC Cancer. 2014;14:411.
188. Versteijne E, van Eijck CH, Punt CJ, Suker M, Zwinderman AH, Dohmen MA, et al. Preoperative radiochemotherapy versus immediate surgery for resectable and borderline resectable pancreatic cancer (PREOPANC trial): study protocol for a multicentre randomized controlled trial. Trials. 2016;17(1):127.

189. Varadhachary GR, Tamm EP, Abbruzzese JL, Xiong HQ, Crane CH, Wang H, et al. Borderline resectable pancreatic cancer: definitions, management, and role of preoperative therapy. Ann Surg Oncol. 2006;13(8):1035-46.
190. Sultana A, Smith CT, Cunningham D, Starling N, Neoptolemos JP, Ghaneh P. Meta-analyses of chemotherapy for locally advanced and metastatic pancreatic cancer. J Clin Oncol. 2007;25(18):2607-15.
191. Hurt CN, Falk S, Crosby T, McDonald A, Ray R, Joseph G, et al. Long-term results and recurrence patterns from SCALOP: a phase II randomised trial of gemcitabine- or capecitabine-based chemoradiation for locally advanced pancreatic cancer. Br J Cancer. 2017;116(10):1264-70.
192. Bockhorn M, Uzunoglu FG, Adham M, Imrie C, Milicevic M, Sandberg AA, et al. Borderline resectable pancreatic cancer: a consensus statement by the International Study Group of Pancreatic Surgery (ISGPS). Surgery. 2014;155(6):977-88.
193. Suker M, Beumer BR, Sadot E, Marthey L, Faris JE, Mellon EA, et al. FOLFIRINOX for locally advanced pancreatic cancer: a systematic review and patient-level meta-analysis. Lancet Oncol. 2016;17(6):801-10.
194. Hackert T, Sachsenmaier M, Hinz U, Schneider L, Michalski CW, Springfeld C, et al. Locally Advanced Pancreatic Cancer: Neoadjuvant Therapy With Folfirinox Results in Resectability in 60% of the Patients. Ann Surg. 2016;264(3):457-63.
195. Petrelli F, Coinu A, Borgonovo K, Cabiddu M, Ghilardi M, Lonati V, et al.. Pancreas. 2015;44(4):515-21.
196. Nitsche U, Wenzel P, Siveke JT, Braren R, Holzapfel K, Schlitter AM, et al. Resectability After First-Line FOLFIRINOX in Initially Unresectable Locally Advanced Pancreatic Cancer: A Single-Center Experience. Ann Surg Oncol. 2015;22 Suppl 3:S1212-20.
197. Murphy JE, Wo JY, Ryan DP, Jiang W, Yeap BY, Drapek LC, et al. Total Neoadjuvant Therapy With FOLFIRINOX Followed by Individualized Chemoradiotherapy for Borderline Resectable Pancreatic Adenocarcinoma: A Phase 2 Clinical Trial. JAMA Oncol. 2018;4(7):963-9.
198. Russo S, Ammori J, Eads J, Dorth J. The role of neoadjuvant therapy in pancreatic cancer: a review. Future Oncol. 2016;12(5):669-85.
199. Kim EJ, Ben-Josef E, Herman JM, Bekaii-Saab T, Dawson LA, Griffith KA, et al. A multi-institutional phase 2 study of neoadjuvant gemcitabine and oxaliplatin with radiation therapy in patients with pancreatic cancer. Cancer. 2013;119(15):2692-700.
200. Landry J, Catalano PJ, Staley C, Harris W, Hoffman J, Talamonti M, et al. Randomized phase II study of gemcitabine plus radiotherapy versus gemcitabine, 5-fluorouracil, and cisplatin followed by radiotherapy and 5-fluorouracil for patients with locally advanced, potentially resectable pancreatic adenocarcinoma. J Surg Oncol. 2010;101(7):587-92.
201. Talamonti MS, Small W, Jr., Mulcahy MF, Wayne JD, Attaluri V, Colletti LM, et al. A multi-institutional phase II trial of preoperative full-dose gemcitabine and concurrent radiation for patients with potentially resectable pancreatic carcinoma. Ann Surg Oncol. 2006;13(2):150-8.
202. Turrini O, Viret F, Moureau-Zabotto L, Guiramand J, Moutardier V, Lelong B, et al. Neoadjuvant 5 fluorouracil-cisplatin chemoradiation effect on survival in patients with

resectable pancreatic head adenocarcinoma: a ten-year single institution experience. Oncology. 2009;76(6):413-9.
203. Ruarus A, Vroomen L, Puijk R, Scheffer H, Meijerink M. Locally Advanced Pancreatic Cancer: A Review of Local Ablative Therapies. Cancers (Basel). 2018;10(1).
204. Jung J, Yoon SM, Park JH, Seo DW, Lee SS, Kim MH, et al. Stereotactic body radiation therapy for locally advanced pancreatic cancer. PLoS One. 2019;14(4):e0214970.
205. Zhu X, Shi D, Li F, Ju X, Cao Y, Shen Y, et al. Prospective analysis of different combined regimens of stereotactic body radiation therapy and chemotherapy for locally advanced pancreatic cancer. Cancer Med. 2018.
206. Wu G, Baine MJ, Zhao N, Li S, Li X, Lin C. Lymphocyte-sparing effect of stereotactic body radiation therapy compared to conventional fractionated radiation therapy in patients with locally advanced pancreatic cancer. BMC Cancer. 2019;19(1):977.
207. Herman JM, Chang DT, Goodman KA, Dholakia AS, Raman SP, Hacker-Prietz A, et al. Phase 2 multi-institutional trial evaluating gemcitabine and stereotactic body radiotherapy for patients with locally advanced unresectable pancreatic adenocarcinoma. Cancer. 2015;121(7):1128-37.
208. Baine MJ, Sleightholm R, Lin C. Incidence and Patterns of Locoregional Failure After Stereotactic Body Radiation Therapy for Pancreatic Adenocarcinoma. Pract Radiat Oncol. 2019;9(1):e29-e37.
209. Wagner M, Redaelli C, Lietz M, Seiler CA, Friess H, Buchler MW. Curative resection is the single most important factor determining outcome in patients with pancreatic adenocarcinoma. Br J Surg. 2004;91(5):586-94.
210. Patra KC, Bardeesy N, Mizukami Y. Diversity of Precursor Lesions For Pancreatic Cancer: The Genetics and Biology of Intraductal Papillary Mucinous Neoplasm. Clin Transl Gastroenterol. 2017;8(4):e86.
211. Poruk KE, Valero V, 3rd, He J, Ahuja N, Cameron JL, Weiss MJ, et al. Circulating Epithelial Cells in Intraductal Papillary Mucinous Neoplasms and Cystic Pancreatic Lesions. Pancreas. 2017;46(7):943-7.
212. Berger AW, Schwerdel D, Costa IG, Hackert T, Strobel O, Lam S, et al. Detection of Hot-Spot Mutations in Circulating Cell-Free DNA From Patients With Intraductal Papillary Mucinous Neoplasms of the Pancreas. Gastroenterology. 2016;151(2):267-70.
213. Melo SA, Luecke LB, Kahlert C, Fernandez AF, Gammon ST, Kaye J, et al. Glypican-1 identifies cancer exosomes and detects early pancreatic cancer. Nature. 2015;523(7559):177-82.
214. Goto T, Fujiya M, Konishi H, Sasajima J, Fujibayashi S, Hayashi A, et al. An elevated expression of serum exosomal microRNA-191, - 21, -451a of pancreatic neoplasm is considered to be efficient diagnostic marker. BMC Cancer. 2018;18(1):116.
215. Hall BR, Cannon A, Atri P, Wichman CS, Smith LM, Ganti AK, et al. Advanced pancreatic cancer: a meta-analysis of clinical trials over thirty years. Oncotarget. 2018;9(27):19396-405.
216. Prasanna A, Ahmed MM, Mohiuddin M, Coleman CN. Exploiting sensitization windows of opportunity in hyper and hypo-fractionated radiation therapy. J Thorac Dis. 2014;6(4):287-302.
217. Greening DW, Xu R, Ji H, Tauro BJ, Simpson RJ. A protocol for exosome isolation and characterization: evaluation of ultracentrifugation, density-gradient separation, and immunoaffinity capture methods. Methods Mol Biol. 2015;1295:179-209.

218. Shlyakhtenko LS, Gall AA, Filonov A, Cerovac Z, Lushnikov A, Lyubchenko YL. Silatrane-based surface chemistry for immobilization of DNA, protein-DNA complexes and other biological materials. Ultramicroscopy. 2003;97(1-4):279-87.
219. Huang X, Irmak S, Lu YF, Pipinos I, Casale G, Subbiah J. Spontaneous and coherent anti-Stokes Raman spectroscopy of human gastrocnemius muscle biopsies in CH-stretching region for discrimination of peripheral artery disease. Biomed Opt Express. 2015;6(8):2766-77.
220. Ashburner M, Ball CA, Blake JA, Botstein D, Butler H, Cherry JM, et al. Gene ontology: tool for the unification of biology. The Gene Ontology Consortium. Nat Genet. 2000;25(1):25-9.
221. Kaur S, Smith LM, Patel A, Menning M, Watley DC, Malik SS, et al. A Combination of MUC5AC and CA19-9 Improves the Diagnosis of Pancreatic Cancer: A Multicenter Study. Am J Gastroenterol. 2017;112(1):172-83.
222. Niknafs YS, Pandian B, Gajjar T, Gaudette Z, Wheelock K, Maz MP, et al. MiPanda: A Resource for Analyzing and Visualizing Next-Generation Sequencing Transcriptomics Data. Neoplasia. 2018;20(11):1144-9.
223. Tang Z, Li C, Kang B, Gao G, Li C, Zhang Z. GEPIA: a web server for cancer and normal gene expression profiling and interactive analyses. Nucleic Acids Res. 2017;45(W1):W98-W102.
224. Chatr-Aryamontri A, Oughtred R, Boucher L, Rust J, Chang C, Kolas NK, et al. The BioGRID interaction database: 2017 update. Nucleic Acids Res. 2017;45(D1):D369-D79.
225. McDonald ER, 3rd, de Weck A, Schlabach MR, Billy E, Mavrakis KJ, Hoffman GR, et al. Project DRIVE: A Compendium of Cancer Dependencies and Synthetic Lethal Relationships Uncovered by Large-Scale, Deep RNAi Screening. Cell. 2017;170(3):577-92 e10.
226. Fertil B, Dertinger H, Courdi A, Malaise EP. Mean inactivation dose: a useful concept for intercomparison of human cell survival curves. Radiat Res. 1984;99(1):73-84.
227. Di Veroli GY, Fornari C, Wang D, Mollard S, Bramhall JL, Richards FM, et al. Combenefit: an interactive platform for the analysis and visualization of drug combinations. Bioinformatics. 2016;32(18):2866-8.
228. Berenbaum MC. What is synergy? Pharmacol Rev. 1989;41(2):93-141.
229. Yadav B, Wennerberg K, Aittokallio T, Tang J. Searching for Drug Synergy in Complex Dose-Response Landscapes Using an Interaction Potency Model. Comput Struct Biotechnol J. 2015;13:504-13.
230. Loewe S. The problem of synergism and antagonism of combined drugs. Arzneimittelforschung. 1953;3(6):285-90.
231. Martinez AM, Kim A, Yang WS. Detection of Ferroptosis by BODIPY 581/591 C11. Methods Mol Biol. 2020;2108:125-30.
232. Fraga CG, Leibovitz BE, Tappel AL. Lipid peroxidation measured as thiobarbituric acid-reactive substances in tissue slices: characterization and comparison with homogenates and microsomes. Free Radic Biol Med. 1988;4(3):155-61.
233. Lasser C, Alikhani VS, Ekstrom K, Eldh M, Paredes PT, Bossios A, et al. Human saliva, plasma and breast milk exosomes contain RNA: uptake by macrophages. J Transl Med. 2011;9:9.

234. Hessvik NP, Llorente A. Current knowledge on exosome biogenesis and release. Cell Mol Life Sci. 2018;75(2):193-208.
235. Tricarico C, Clancy J, D'Souza-Schorey C. Biology and biogenesis of shed microvesicles. Small GTPases. 2017;8(4):220-32.
236. van Niel G, D'Angelo G, Raposo G. Shedding light on the cell biology of extracellular vesicles. Nat Rev Mol Cell Biol. 2018;19(4):213-28.
237. Jeppesen DK, Fenix AM, Franklin JL, Higginbotham JN, Zhang Q, Zimmerman LJ, et al. Reassessment of Exosome Composition. Cell. 2019;177(2):428-45 e18.
238. Zhang H, Freitas D, Kim HS, Fabijanic K, Li Z, Chen H, et al. Identification of distinct nanoparticles and subsets of extracellular vesicles by asymmetric flow field-flow fractionation. Nat Cell Biol. 2018;20(3):332-43.
239. Marzesco AM, Janich P, Wilsch-Brauninger M, Dubreuil V, Langenfeld K, Corbeil D, et al. Release of extracellular membrane particles carrying the stem cell marker prominin-1 (CD133) from neural progenitors and other epithelial cells. J Cell Sci. 2005;118(Pt 13):2849-58.
240. Hurley JH. ESCRTs are everywhere. EMBO J. 2015;34(19):2398-407.
241. Mathieu M, Martin-Jaular L, Lavieu G, Thery C. Specificities of secretion and uptake of exosomes and other extracellular vesicles for cell-to-cell communication. Nat Cell Biol. 2019;21(1):9-17.
242. Andreu Z, Yanez-Mo M. Tetraspanins in extracellular vesicle formation and function. Front Immunol. 2014;5:442.
243. Perez-Hernandez D, Gutierrez-Vazquez C, Jorge I, Lopez-Martin S, Ursa A, Sanchez-Madrid F, et al. The intracellular interactome of tetraspanin-enriched microdomains reveals their function as sorting machineries toward exosomes. J Biol Chem. 2013;288(17):11649-61.
244. van Niel G, Charrin S, Simoes S, Romao M, Rochin L, Saftig P, et al. The tetraspanin CD63 regulates ESCRT-independent and -dependent endosomal sorting during melanogenesis. Dev Cell. 2011;21(4):708-21.
245. McAndrews KM, Kalluri R. Mechanisms associated with biogenesis of exosomes in cancer. Mol Cancer. 2019;18(1):52.
246. Hsu C, Morohashi Y, Yoshimura S, Manrique-Hoyos N, Jung S, Lauterbach MA, et al. Regulation of exosome secretion by Rab35 and its GTPase-activating proteins TBC1D10A-C. J Cell Biol. 2010;189(2):223-32.
247. Ostrowski M, Carmo NB, Krumeich S, Fanget I, Raposo G, Savina A, et al. Rab27a and Rab27b control different steps of the exosome secretion pathway. Nat Cell Biol. 2010;12(1):19-30; sup pp 1-13.
248. Savina A, Fader CM, Damiani MT, Colombo MI. Rab11 promotes docking and fusion of multivesicular bodies in a calcium-dependent manner. Traffic. 2005;6(2):131-43.
249. Verweij FJ, Bebelman MP, Jimenez CR, Garcia-Vallejo JJ, Janssen H, Neefjes J, et al. Quantifying exosome secretion from single cells reveals a modulatory role for GPCR signaling. J Cell Biol. 2018;217(3):1129-42.
250. Trajkovic K, Hsu C, Chiantia S, Rajendran L, Wenzel D, Wieland F, et al. Ceramide triggers budding of exosome vesicles into multivesicular endosomes. Science. 2008;319(5867):1244-7.

251. Wei H, Malcor JM, Harper MT. Lipid rafts are essential for release of phosphatidylserine-exposing extracellular vesicles from platelets. Sci Rep. 2018;8(1):9987.
252. Skotland T, Sandvig K, Llorente A. Lipids in exosomes: Current knowledge and the way forward. Prog Lipid Res. 2017;66:30-41.
253. Skotland T, Hessvik NP, Sandvig K, Llorente A. Exosomal lipid composition and the role of ether lipids and phosphoinositides in exosome biology. J Lipid Res. 2019;60(1):9-18.
254. Record M, Silvente-Poirot S, Poirot M, Wakelam MJO. Extracellular vesicles: lipids as key components of their biogenesis and functions. J Lipid Res. 2018;59(8):1316-24.
255. Ghossoub R, Lembo F, Rubio A, Gaillard CB, Bouchet J, Vitale N, et al. Syntenin-ALIX exosome biogenesis and budding into multivesicular bodies are controlled by ARF6 and PLD2. Nat Commun. 2014;5:3477.
256. Skocaj M, Yu Y, Grundner M, Resnik N, Bedina Zavec A, Leonardi A, et al. Characterisation of plasmalemmal shedding of vesicles induced by the cholesterol/sphingomyelin binding protein, ostreolysin A-mCherry. Biochim Biophys Acta. 2016;1858(11):2882-93.
257. Colombo M, Raposo G, Thery C. Biogenesis, secretion, and intercellular interactions of exosomes and other extracellular vesicles. Annu Rev Cell Dev Biol. 2014;30:255-89.
258. Pan BT, Teng K, Wu C, Adam M, Johnstone RM. Electron microscopic evidence for externalization of the transferrin receptor in vesicular form in sheep reticulocytes. J Cell Biol. 1985;101(3):942-8.
259. Lynch S, Santos SG, Campbell EC, Nimmo AM, Botting C, Prescott A, et al. Novel MHC class I structures on exosomes. J Immunol. 2009;183(3):1884-91.
260. Raposo G, Nijman HW, Stoorvogel W, Liejendekker R, Harding CV, Melief CJ, et al. B lymphocytes secrete antigen-presenting vesicles. J Exp Med. 1996;183(3):1161-72.
261. Valadi H, Ekstrom K, Bossios A, Sjostrand M, Lee JJ, Lotvall JO. Exosome-mediated transfer of mRNAs and microRNAs is a novel mechanism of genetic exchange between cells. Nat Cell Biol. 2007;9(6):654-9.
262. Skliar M, Chernyshev VS, Belnap DM, Sergey GV, Al-Hakami SM, Bernard PS, et al. Membrane proteins significantly restrict exosome mobility. Biochem Biophys Res Commun. 2018;501(4):1055-9.
263. Thakur BK, Zhang H, Becker A, Matei I, Huang Y, Costa-Silva B, et al. Double-stranded DNA in exosomes: a novel biomarker in cancer detection. Cell Res. 2014;24(6):766-9.
264. Subra C, Laulagnier K, Perret B, Record M. Exosome lipidomics unravels lipid sorting at the level of multivesicular bodies. Biochimie. 2007;89(2):205-12.
265. Baietti MF, Zhang Z, Mortier E, Melchior A, Degeest G, Geeraerts A, et al. Syndecan-syntenin-ALIX regulates the biogenesis of exosomes. Nat Cell Biol. 2012;14(7):677-85.
266. Leca J, Martinez S, Lac S, Nigri J, Secq V, Rubis M, et al. Cancer-associated fibroblast-derived annexin A6+ extracellular vesicles support pancreatic cancer aggressiveness. J Clin Invest. 2016;126(11):4140-56.

267. Banfer S, Schneider D, Dewes J, Strauss MT, Freibert SA, Heimerl T, et al. Molecular mechanism to recruit galectin-3 into multivesicular bodies for polarized exosomal secretion. Proc Natl Acad Sci U S A. 2018;115(19):E4396-E405.
268. Kowal J, Arras G, Colombo M, Jouve M, Morath JP, Primdal-Bengtson B, et al. Proteomic comparison defines novel markers to characterize heterogeneous populations of extracellular vesicle subtypes. Proc Natl Acad Sci U S A. 2016;113(8):E968-77.
269. Figueroa JM, Skog J, Akers J, Li H, Komotar R, Jensen R, et al. Detection of wild-type EGFR amplification and EGFRvIII mutation in CSF-derived extracellular vesicles of glioblastoma patients. Neuro Oncol. 2017;19(11):1494-502.
270. Chen F, Chen J, Yang L, Liu J, Zhang X, Zhang Y, et al. Extracellular vesicle-packaged HIF-1alpha-stabilizing lncRNA from tumour-associated macrophages regulates aerobic glycolysis of breast cancer cells. Nat Cell Biol. 2019;21(4):498-510.
271. Ko J, Bhagwat N, Black T, Yee SS, Na YJ, Fisher S, et al. miRNA Profiling of Magnetic Nanopore-Isolated Extracellular Vesicles for the Diagnosis of Pancreatic Cancer. Cancer Res. 2018;78(13):3688-97.
272. Li Y, Zhao J, Yu S, Wang Z, He X, Su Y, et al. Extracellular Vesicles Long RNA Sequencing Reveals Abundant mRNA, circRNA, and lncRNA in Human Blood as Potential Biomarkers for Cancer Diagnosis. Clin Chem. 2019;65(6):798-808.
273. Kalluri R, LeBleu VS. Discovery of Double-Stranded Genomic DNA in Circulating Exosomes. Cold Spring Harb Symp Quant Biol. 2016;81:275-80.
274. Torralba D, Baixauli F, Villarroya-Beltri C, Fernandez-Delgado I, Latorre-Pellicer A, Acin-Perez R, et al. Priming of dendritic cells by DNA-containing extracellular vesicles from activated T cells through antigen-driven contacts. Nat Commun. 2018;9(1):2658.
275. Kahlert C, Melo SA, Protopopov A, Tang J, Seth S, Koch M, et al. Identification of double-stranded genomic DNA spanning all chromosomes with mutated KRAS and p53 DNA in the serum exosomes of patients with pancreatic cancer. J Biol Chem. 2014;289(7):3869-75.
276. Tkach M, Thery C. Communication by Extracellular Vesicles: Where We Are and Where We Need to Go. Cell. 2016;164(6):1226-32.
277. Lai CP, Kim EY, Badr CE, Weissleder R, Mempel TR, Tannous BA, et al. Visualization and tracking of tumour extracellular vesicle delivery and RNA translation using multiplexed reporters. Nat Commun. 2015;6:7029.
278. Takahashi A, Okada R, Nagao K, Kawamata Y, Hanyu A, Yoshimoto S, et al. Exosomes maintain cellular homeostasis by excreting harmful DNA from cells. Nat Commun. 2017;8:15287.
279. Haraszti RA, Miller R, Dubuke ML, Rockwell HE, Coles AH, Sapp E, et al. Serum Deprivation of Mesenchymal Stem Cells Improves Exosome Activity and Alters Lipid and Protein Composition. iScience. 2019;16:230-41.
280. Svensson KJ, Kucharzewska P, Christianson HC, Skold S, Lofstedt T, Johansson MC, et al. Hypoxia triggers a proangiogenic pathway involving cancer cell microvesicles and PAR-2-mediated heparin-binding EGF signaling in endothelial cells. Proc Natl Acad Sci U S A. 2011;108(32):13147-52.
281. Shah R, Patel T, Freedman JE. Circulating Extracellular Vesicles in Human Disease. N Engl J Med. 2018;379(10):958-66.

282. Al-Nedawi K, Meehan B, Micallef J, Lhotak V, May L, Guha A, et al. Intercellular transfer of the oncogenic receptor EGFRvIII by microvesicles derived from tumour cells. Nat Cell Biol. 2008;10(5):619-24.
283. Keklikoglou I, Cianciaruso C, Guc E, Squadrito ML, Spring LM, Tazzyman S, et al. Chemotherapy elicits pro-metastatic extracellular vesicles in breast cancer models. Nat Cell Biol. 2019;21(2):190-202.
284. Wortzel I, Dror S, Kenific CM, Lyden D. Exosome-Mediated Metastasis: Communication from a Distance. Dev Cell. 2019;49(3):347-60.
285. Zheng P, Chen L, Yuan X, Luo Q, Liu Y, Xie G, et al. Exosomal transfer of tumor-associated macrophage-derived miR-21 confers cisplatin resistance in gastric cancer cells. J Exp Clin Cancer Res. 2017;36(1):53.
286. Buzas EI, Toth EA, Sodar BW, Szabo-Taylor KE. Molecular interactions at the surface of extracellular vesicles. Semin Immunopathol. 2018;40(5):453-64.
287. Li X, Wang Y, Wang Q, Liu Y, Bao W, Wu S. Exosomes in cancer: Small transporters with big functions. Cancer Lett. 2018;435:55-65.
288. Bebelman MP, Smit MJ, Pegtel DM, Baglio SR. Biogenesis and function of extracellular vesicles in cancer. Pharmacol Ther. 2018;188:1-11.
289. Thery C, Amigorena S, Raposo G, Clayton A. Isolation and characterization of exosomes from cell culture supernatants and biological fluids. Curr Protoc Cell Biol. 2006;Chapter 3:Unit 3 22.
290. Konoshenko MY, Lekchnov EA, Vlassov AV, Laktionov PP. Isolation of Extracellular Vesicles: General Methodologies and Latest Trends. Biomed Res Int. 2018;2018:8545347.
291. Salih M, Zietse R, Hoorn EJ. Urinary extracellular vesicles and the kidney: biomarkers and beyond. Am J Physiol Renal Physiol. 2014;306(11):F1251-9.
292. Webber J, Clayton A. How pure are your vesicles? J Extracell Vesicles. 2013;2.
293. Onodi Z, Pelyhe C, Terezia Nagy C, Brenner GB, Almasi L, Kittel A, et al. Isolation of High-Purity Extracellular Vesicles by the Combination of Iodixanol Density Gradient Ultracentrifugation and Bind-Elute Chromatography From Blood Plasma. Front Physiol. 2018;9:1479.
294. Kosanovic M, Jankovic M. Isolation of urinary extracellular vesicles from Tamm-Horsfall protein-depleted urine and their application in the development of a lectin-exosome-binding assay. Biotechniques. 2014;57(3):143-9.
295. Monguio-Tortajada M, Galvez-Monton C, Bayes-Genis A, Roura S, Borras FE. Extracellular vesicle isolation methods: rising impact of size-exclusion chromatography. Cell Mol Life Sci. 2019;76(12):2369-82.
296. Nordin JZ, Lee Y, Vader P, Mager I, Johansson HJ, Heusermann W, et al. Ultrafiltration with size-exclusion liquid chromatography for high yield isolation of extracellular vesicles preserving intact biophysical and functional properties. Nanomedicine. 2015;11(4):879-83.
297. Santana SM, Antonyak MA, Cerione RA, Kirby BJ. Microfluidic isolation of cancer-cell-derived microvesicles from hetergeneous extracellular shed vesicle populations. Biomed Microdevices. 2014;16(6):869-77.
298. Davies RT, Kim J, Jang SC, Choi EJ, Gho YS, Park J. Microfluidic filtration system to isolate extracellular vesicles from blood. Lab Chip. 2012;12(24):5202-10.

299. Zhang H, Lyden D. Asymmetric-flow field-flow fractionation technology for exomere and small extracellular vesicle separation and characterization. Nat Protoc. 2019;14(4):1027-53.
300. Oksvold MP, Neurauter A, Pedersen KW. Magnetic bead-based isolation of exosomes. Methods Mol Biol. 2015;1218:465-81.
301. Balbi C, Bolis S, Vassalli G, Barile L. Flow Cytometric Analysis of Extracellular Vesicles from Cell-conditioned Media. J Vis Exp. 2019(144).
302. Tauro BJ, Greening DW, Mathias RA, Ji H, Mathivanan S, Scott AM, et al. Comparison of ultracentrifugation, density gradient separation, and immunoaffinity capture methods for isolating human colon cancer cell line LIM1863-derived exosomes. Methods. 2012;56(2):293-304.
303. Beekman P, Enciso-Martinez A, Rho HS, Pujari SP, Lenferink A, Zuilhof H, et al. Immuno-capture of extracellular vesicles for individual multi-modal characterization using AFM, SEM and Raman spectroscopy. Lab Chip. 2019;19(15):2526-36.
304. Ghosh A, Davey M, Chute IC, Griffiths SG, Lewis S, Chacko S, et al. Rapid isolation of extracellular vesicles from cell culture and biological fluids using a synthetic peptide with specific affinity for heat shock proteins. PLoS One. 2014;9(10):e110443.
305. Xu D, Esko JD. Demystifying heparan sulfate-protein interactions. Annu Rev Biochem. 2014;83:129-57.
306. Atai NA, Balaj L, van Veen H, Breakefield XO, Jarzyna PA, Van Noorden CJ, et al. Heparin blocks transfer of extracellular vesicles between donor and recipient cells. J Neurooncol. 2013;115(3):343-51.
307. Manandhar S, Park J, Kothandan VK, Lee J, Alam F, Jee JP, et al. Properties of Heparinoids Premixed with Tumor-Derived Extracellular Vesicles. Bioconjug Chem. 2018;29(11):3757-67.
308. Christianson HC, Svensson KJ, van Kuppevelt TH, Li JP, Belting M. Cancer cell exosomes depend on cell-surface heparan sulfate proteoglycans for their internalization and functional activity. Proc Natl Acad Sci U S A. 2013;110(43):17380-5.
309. Balaj L, Atai NA, Chen W, Mu D, Tannous BA, Breakefield XO, et al. Heparin affinity purification of extracellular vesicles. Sci Rep. 2015;5:10266.
310. Wan Y, Cheng G, Liu X, Hao SJ, Nisic M, Zhu CD, et al. Rapid magnetic isolation of extracellular vesicles via lipid-based nanoprobes. Nat Biomed Eng. 2017;1.
311. Wan Y, Maurer M, He HZ, Xia YQ, Hao SJ, Zhang WL, et al. Enrichment of extracellular vesicles with lipid nanoprobe functionalized nanostructured silica. Lab Chip. 2019;19(14):2346-55.
312. Yokota S, Kuramochi H, Okubo K, Iwaya A, Tsuchiya S, Ichiki T. Extracellular vesicles nanoarray technology: Immobilization of individual extracellular vesicles on nanopatterned polyethylene glycol-lipid conjugate brushes. PLoS One. 2019;14(10):e0224091.
313. Denecker G, Dooms H, Van Loo G, Vercammen D, Grooten J, Fiers W, et al. Phosphatidyl serine exposure during apoptosis precedes release of cytochrome c and decrease in mitochondrial transmembrane potential. FEBS Lett. 2000;465(1):47-52.
314. Kang YT, Purcell E, Palacios-Rolston C, Lo TW, Ramnath N, Jolly S, et al. Isolation and Profiling of Circulating Tumor-Associated Exosomes Using Extracellular Vesicular Lipid-Protein Binding Affinity Based Microfluidic Device. Small. 2019;15(47):e1903600.

315. Shih CL, Chong KY, Hsu SC, Chien HJ, Ma CT, Chang JW, et al. Development of a magnetic bead-based method for the collection of circulating extracellular vesicles. N Biotechnol. 2016;33(1):116-22.
316. Nakai W, Yoshida T, Diez D, Miyatake Y, Nishibu T, Imawaka N, et al. A novel affinity-based method for the isolation of highly purified extracellular vesicles. Sci Rep. 2016;6:33935.
317. Greening DW, Xu R, Gopal SK, Rai A, Simpson RJ. Proteomic insights into extracellular vesicle biology - defining exosomes and shed microvesicles. Expert Rev Proteomics. 2017;14(1):69-95.
318. Abramowicz A, Widlak P, Pietrowska M. Different Types of Cellular Stress Affect the Proteome Composition of Small Extracellular Vesicles: A Mini Review. Proteomes. 2019;7(2).
319. Nyman TA, Lorey MB, Cypryk W, Matikainen S. Mass spectrometry-based proteomic exploration of the human immune system: focus on the inflammasome, global protein secretion, and T cells. Expert Rev Proteomics. 2017;14(5):395-407.
320. Bandu R, Oh JW, Kim KP. Mass spectrometry-based proteome profiling of extracellular vesicles and their roles in cancer biology. Exp Mol Med. 2019;51(3):30.
321. Cvjetkovic A, Jang SC, Konecna B, Hoog JL, Sihlbom C, Lasser C, et al. Detailed Analysis of Protein Topology of Extracellular Vesicles-Evidence of Unconventional Membrane Protein Orientation. Sci Rep. 2016;6:36338.
322. Castillo J, Bernard V, San Lucas FA, Allenson K, Capello M, Kim DU, et al. Surfaceome profiling enables isolation of cancer-specific exosomal cargo in liquid biopsies from pancreatic cancer patients. Ann Oncol. 2018;29(1):223-9.
323. Hildonen S, Skarpen E, Halvorsen TG, Reubsaet L. Isolation and mass spectrometry analysis of urinary extraexosomal proteins. Sci Rep. 2016;6:36331.
324. Zou G, Benktander JD, Gizaw ST, Gaunitz S, Novotny MV. Comprehensive Analytical Approach toward Glycomic Characterization and Profiling in Urinary Exosomes. Anal Chem. 2017;89(10):5364-72.
325. Bai H, Pan Y, Qi L, Liu L, Zhao X, Dong H, et al. Development a hydrazide-functionalized thermosensitive polymer based homogeneous system for highly efficient N-glycoprotein/glycopeptide enrichment from human plasma exosome. Talanta. 2018;186:513-20.
326. Llorente A, Skotland T, Sylvanne T, Kauhanen D, Rog T, Orlowski A, et al. Molecular lipidomics of exosomes released by PC-3 prostate cancer cells. Biochim Biophys Acta. 2013;1831(7):1302-9.
327. Brzozowski JS, Jankowski H, Bond DR, McCague SB, Munro BR, Predebon MJ, et al. Lipidomic profiling of extracellular vesicles derived from prostate and prostate cancer cell lines. Lipids Health Dis. 2018;17(1):211.
328. Haraszti RA, Didiot MC, Sapp E, Leszyk J, Shaffer SA, Rockwell HE, et al. High-resolution proteomic and lipidomic analysis of exosomes and microvesicles from different cell sources. J Extracell Vesicles. 2016;5:32570.
329. Skotland T, Ekroos K, Kauhanen D, Simolin H, Seierstad T, Berge V, et al. Molecular lipid species in urinary exosomes as potential prostate cancer biomarkers. Eur J Cancer. 2017;70:122-32.

330. Akagi T, Kato K, Kobayashi M, Kosaka N, Ochiya T, Ichiki T. On-chip immunoelectrophoresis of extracellular vesicles released from human breast cancer cells. PLoS One. 2015;10(4):e0123603.
331. Vaidyanathan R, Naghibosadat M, Rauf S, Korbie D, Carrascosa LG, Shiddiky MJ, et al. Detecting exosomes specifically: a multiplexed device based on alternating current electrohydrodynamic induced nanoshearing. Anal Chem. 2014;86(22):11125-32.
332. He M, Zeng Y. Microfluidic Exosome Analysis toward Liquid Biopsy for Cancer. J Lab Autom. 2016;21(4):599-608.
333. Morales-Kastresana A, Jones JC. Flow Cytometric Analysis of Extracellular Vesicles. Methods Mol Biol. 2017;1545:215-25.
334. Suarez H, Gamez-Valero A, Reyes R, Lopez-Martin S, Rodriguez MJ, Carrascosa JL, et al. A bead-assisted flow cytometry method for the semi-quantitative analysis of Extracellular Vesicles. Sci Rep. 2017;7(1):11271.
335. Wiklander OPB, Bostancioglu RB, Welsh JA, Zickler AM, Murke F, Corso G, et al. Systematic Methodological Evaluation of a Multiplex Bead-Based Flow Cytometry Assay for Detection of Extracellular Vesicle Surface Signatures. Front Immunol. 2018;9:1326.
336. Yoshioka Y, Kosaka N, Konishi Y, Ohta H, Okamoto H, Sonoda H, et al. Ultra-sensitive liquid biopsy of circulating extracellular vesicles using ExoScreen. Nat Commun. 2014;5:3591.
337. Welsh JA, Holloway JA, Wilkinson JS, Englyst NA. Extracellular Vesicle Flow Cytometry Analysis and Standardization. Front Cell Dev Biol. 2017;5:78.
338. Morales-Kastresana A, Telford B, Musich TA, McKinnon K, Clayborne C, Braig Z, et al. Labeling Extracellular Vesicles for Nanoscale Flow Cytometry. Sci Rep. 2017;7(1):1878.
339. Groot Kormelink T, Arkesteijn GJ, Nauwelaers FA, van den Engh G, Nolte-'t Hoen EN, Wauben MH. Prerequisites for the analysis and sorting of extracellular vesicle subpopulations by high-resolution flow cytometry. Cytometry A. 2016;89(2):135-47.
340. Wang Y, Partridge A, Wu Y. In situ surface protein conjugation of small molecules for SPR immunoassays. Anal Biochem. 2017;539:149-51.
341. Defaus S, Aviles M, Andreu D, Gutierrez-Gallego R. Lectin-Binding Specificity of the Fertilization-Relevant Protein PDC-109 by Means of Surface Plasmon Resonance and Carbohydrate REcognition Domain EXcision-Mass Spectrometry. Int J Mol Sci. 2018;19(4).
342. Zhou C, Zou H, Sun C, Ren D, Chen J, Li Y. Signal amplification strategies for DNA-based surface plasmon resonance biosensors. Biosens Bioelectron. 2018;117:678-89.
343. Liu C, Zeng X, An Z, Yang Y, Eisenbaum M, Gu X, et al. Sensitive Detection of Exosomal Proteins via a Compact Surface Plasmon Resonance Biosensor for Cancer Diagnosis. ACS Sens. 2018;3(8):1471-9.
344. Rupert DL, Lasser C, Eldh M, Block S, Zhdanov VP, Lotvall JO, et al. Determination of exosome concentration in solution using surface plasmon resonance spectroscopy. Anal Chem. 2014;86(12):5929-36.
345. Gool EL, Stojanovic I, Schasfoort RBM, Sturk A, van Leeuwen TG, Nieuwland R, et al. Surface Plasmon Resonance is an Analytically Sensitive Method for Antigen Profiling of Extracellular Vesicles. Clin Chem. 2017;63(10):1633-41.

346. Unser S, Bruzas I, He J, Sagle L. Localized Surface Plasmon Resonance Biosensing: Current Challenges and Approaches. Sensors (Basel). 2015;15(7):15684-716.
347. Jiang Y, Shi M, Liu Y, Wan S, Cui C, Zhang L, et al. Aptamer/AuNP Biosensor for Colorimetric Profiling of Exosomal Proteins. Angew Chem Int Ed Engl. 2017;56(39):11916-20.
348. Bellassai N, D'Agata R, Jungbluth V, Spoto G. Surface Plasmon Resonance for Biomarker Detection: Advances in Non-invasive Cancer Diagnosis. Front Chem. 2019;7:570.
349. Thakur A, Qiu G, Ng SP, Guan J, Yue J, Lee Y, et al. Direct detection of two different tumor-derived extracellular vesicles by SAM-AuNIs LSPR biosensor. Biosens Bioelectron. 2017;94:400-7.
350. Wang Q, Zou L, Yang X, Liu X, Nie W, Zheng Y, et al. Direct quantification of cancerous exosomes via surface plasmon resonance with dual gold nanoparticle-assisted signal amplification. Biosens Bioelectron. 2019;135:129-36.
351. Wang Y, Irudayaraj J. Surface-enhanced Raman spectroscopy at single-molecule scale and its implications in biology. Philos Trans R Soc Lond B Biol Sci. 2013;368(1611):20120026.
352. Wang Z, Zong S, Wu L, Zhu D, Cui Y. SERS-Activated Platforms for Immunoassay: Probes, Encoding Methods, and Applications. Chem Rev. 2017;117(12):7910-63.
353. Carmicheal J, Hayashi C, Huang X, Liu L, Lu Y, Krasnoslobodtsev A, et al. Label-free characterization of exosome via surface enhanced Raman spectroscopy for the early detection of pancreatic cancer. Nanomedicine. 2019;16:88-96.
354. Stremersch S, Marro M, Pinchasik BE, Baatsen P, Hendrix A, De Smedt SC, et al. Identification of Individual Exosome-Like Vesicles by Surface Enhanced Raman Spectroscopy. Small. 2016;12(24):3292-301.
355. Fraire JC, Stremersch S, Bouckaert D, Monteyne T, De Beer T, Wuytens P, et al. Improved Label-Free Identification of Individual Exosome-like Vesicles with Au@Ag Nanoparticles as SERS Substrate. ACS Appl Mater Interfaces. 2019;11(43):39424-35.
356. Smolsky J, Kaur S, Hayashi C, Batra SK, Krasnoslobodtsev AV. Surface-Enhanced Raman Scattering-Based Immunoassay Technologies for Detection of Disease Biomarkers. Biosensors (Basel). 2017;7(1).
357. Kruglik SG, Royo F, Guigner JM, Palomo L, Seksek O, Turpin PY, et al. Raman tweezers microspectroscopy of circa 100 nm extracellular vesicles. Nanoscale. 2019;11(4):1661-79.
358. Carney RP, Hazari S, Colquhoun M, Tran D, Hwang B, Mulligan MS, et al. Multispectral Optical Tweezers for Biochemical Fingerprinting of CD9-Positive Exosome Subpopulations. Anal Chem. 2017;89(10):5357-63.
359. Sandfeld-Paulsen B, Jakobsen KR, Baek R, Folkersen BH, Rasmussen TR, Meldgaard P, et al. Exosomal Proteins as Diagnostic Biomarkers in Lung Cancer. J Thorac Oncol. 2016;11(10):1701-10.
360. Jin D, Yang F, Zhang Y, Liu L, Zhou Y, Wang F, et al. ExoAPP: Exosome-Oriented, Aptamer Nanoprobe-Enabled Surface Proteins Profiling and Detection. Anal Chem. 2018;90(24):14402-11.

361. Liu C, Zhao J, Tian F, Chang J, Zhang W, Sun J. lambda-DNA- and Aptamer-Mediated Sorting and Analysis of Extracellular Vesicles. J Am Chem Soc. 2019;141(9):3817-21.
362. Wu D, Yan J, Shen X, Sun Y, Thulin M, Cai Y, et al. Profiling surface proteins on individual exosomes using a proximity barcoding assay. Nat Commun. 2019;10(1):3854.
363. Echevarria J, Royo F, Pazos R, Salazar L, Falcon-Perez JM, Reichardt NC. Microarray-based identification of lectins for the purification of human urinary extracellular vesicles directly from urine samples. Chembiochem. 2014;15(11):1621-6.
364. Feng Y, Guo Y, Li Y, Tao J, Ding L, Wu J, et al. Lectin-mediated in situ rolling circle amplification on exosomes for probing cancer-related glycan pattern. Anal Chim Acta. 2018;1039:108-15.
365. Lewis JM, Vyas AD, Qiu Y, Messer KS, White R, Heller MJ. Integrated Analysis of Exosomal Protein Biomarkers on Alternating Current Electrokinetic Chips Enables Rapid Detection of Pancreatic Cancer in Patient Blood. ACS Nano. 2018;12(4):3311-20.
366. Cavallaro S, Horak J, Haag P, Gupta D, Stiller C, Sahu SS, et al. Label-Free Surface Protein Profiling of Extracellular Vesicles by an Electrokinetic Sensor. ACS Sens. 2019;4(5):1399-408.
367. Zhang H, Wang Z, Zhang Q, Wang F, Liu Y. Ti3C2 MXenes nanosheets catalyzed highly efficient electrogenerated chemiluminescence biosensor for the detection of exosomes. Biosens Bioelectron. 2019;124-125:184-90.
368. Liu C, Zhao J, Tian F, Cai L, Zhang W, Feng Q, et al. Low-cost thermophoretic profiling of extracellular-vesicle surface proteins for the early detection and classification of cancers. Nat Biomed Eng. 2019;3(3):183-93.
369. Kalluri R. The biology and function of exosomes in cancer. J Clin Invest. 2016;126(4):1208-15.
370. French KC, Antonyak MA, Cerione RA. Extracellular vesicle docking at the cellular port: Extracellular vesicle binding and uptake. Semin Cell Dev Biol. 2017;67:48-55.
371. Wang Q, Lu Q. Plasma membrane-derived extracellular microvesicles mediate non-canonical intercellular NOTCH signaling. Nat Commun. 2017;8(1):709.
372. Tang X, Chang C, Guo J, Lincoln V, Liang C, Chen M, et al. Tumour-Secreted Hsp90alpha on External Surface of Exosomes Mediates Tumour - Stromal Cell Communication via Autocrine and Paracrine Mechanisms. Sci Rep. 2019;9(1):15108.
373. Menck K, Scharf C, Bleckmann A, Dyck L, Rost U, Wenzel D, et al. Tumor-derived microvesicles mediate human breast cancer invasion through differentially glycosylated EMMPRIN. J Mol Cell Biol. 2015;7(2):143-53.
374. Gabison EE, Hoang-Xuan T, Mauviel A, Menashi S. EMMPRIN/CD147, an MMP modulator in cancer, development and tissue repair. Biochimie. 2005;87(3-4):361-8.
375. Elinav E, Nowarski R, Thaiss CA, Hu B, Jin C, Flavell RA. Inflammation-induced cancer: crosstalk between tumours, immune cells and microorganisms. Nat Rev Cancer. 2013;13(11):759-71.
376. Hinshaw DC, Shevde LA. The Tumor Microenvironment Innately Modulates Cancer Progression. Cancer Res. 2019;79(18):4557-66.
377. Yang X, Li Y, Zou L, Zhu Z. Role of Exosomes in Crosstalk Between Cancer-Associated Fibroblasts and Cancer Cells. Front Oncol. 2019;9:356.

378. Han L, Lam EW, Sun Y. Extracellular vesicles in the tumor microenvironment: old stories, but new tales. Mol Cancer. 2019;18(1):59.
379. Cerezo-Magana M, Bang-Rudenstam A, Belting M. The pleiotropic role of proteoglycans in extracellular vesicle mediated communication in the tumor microenvironment. Semin Cancer Biol. 2019.
380. Shelke GV, Yin Y, Jang SC, Lasser C, Wennmalm S, Hoffmann HJ, et al. Endosomal signalling via exosome surface TGFbeta-1. J Extracell Vesicles. 2019;8(1):1650458.
381. Antonyak MA, Li B, Boroughs LK, Johnson JL, Druso JE, Bryant KL, et al. Cancer cell-derived microvesicles induce transformation by transferring tissue transglutaminase and fibronectin to recipient cells. Proc Natl Acad Sci U S A. 2011;108(12):4852-7.
382. Tang MKS, Yue PYK, Ip PP, Huang RL, Lai HC, Cheung ANY, et al. Soluble E-cadherin promotes tumor angiogenesis and localizes to exosome surface. Nat Commun. 2018;9(1):2270.
383. Takasugi M, Okada R, Takahashi A, Virya Chen D, Watanabe S, Hara E. Small extracellular vesicles secreted from senescent cells promote cancer cell proliferation through EphA2. Nat Commun. 2017;8:15729.
384. Manini I, Ruaro ME, Sgarra R, Bartolini A, Caponnetto F, Ius T, et al. Semaphorin-7A on Exosomes: A Promigratory Signal in the Glioma Microenvironment. Cancers (Basel). 2019;11(6).
385. Chanda D, Otoupalova E, Hough KP, Locy ML, Bernard K, Deshane JS, et al. Fibronectin on the Surface of Extracellular Vesicles Mediates Fibroblast Invasion. Am J Respir Cell Mol Biol. 2019;60(3):279-88.
386. Shtam T, Naryzhny S, Samsonov R, Karasik D, Mizgirev I, Kopylov A, et al. Plasma exosomes stimulate breast cancer metastasis through surface interactions and activation of FAK signaling. Breast Cancer Res Treat. 2019;174(1):129-41.
387. Pickup MW, Mouw JK, Weaver VM. The extracellular matrix modulates the hallmarks of cancer. EMBO Rep. 2014;15(12):1243-53.
388. Sanderson RD, Bandari SK, Vlodavsky I. Proteases and glycosidases on the surface of exosomes: Newly discovered mechanisms for extracellular remodeling. Matrix Biol. 2019;75-76:160-9.
389. Harkonen K, Oikari S, Kyykallio H, Capra J, Hakkola S, Ketola K, et al. CD44s Assembles Hyaluronan Coat on Filopodia and Extracellular Vesicles and Induces Tumorigenicity of MKN74 Gastric Carcinoma Cells. Cells. 2019;8(3).
390. Yue S, Mu W, Erb U, Zoller M. The tetraspanins CD151 and Tspan8 are essential exosome components for the crosstalk between cancer initiating cells and their surrounding. Oncotarget. 2015;6(4):2366-84.
391. Bandari SK, Purushothaman A, Ramani VC, Brinkley GJ, Chandrashekar DS, Varambally S, et al. Chemotherapy induces secretion of exosomes loaded with heparanase that degrades extracellular matrix and impacts tumor and host cell behavior. Matrix Biol. 2018;65:104-18.
392. Costa-Silva B, Aiello NM, Ocean AJ, Singh S, Zhang H, Thakur BK, et al. Pancreatic cancer exosomes initiate pre-metastatic niche formation in the liver. Nat Cell Biol. 2015;17(6):816-26.

393. Hoshino A, Costa-Silva B, Shen TL, Rodrigues G, Hashimoto A, Tesic Mark M, et al. Tumour exosome integrins determine organotropic metastasis. Nature. 2015;527(7578):329-35.
394. Zhao K, Wang Z, Hackert T, Pitzer C, Zoller M. Tspan8 and Tspan8/CD151 knockout mice unravel the contribution of tumor and host exosomes to tumor progression. J Exp Clin Cancer Res. 2018;37(1):312.
395. Jimenez L, Yu H, McKenzie AJ, Franklin JL, Patton JG, Liu Q, et al. Quantitative Proteomic Analysis of Small and Large Extracellular Vesicles (EVs) Reveals Enrichment of Adhesion Proteins in Small EVs. J Proteome Res. 2019;18(3):947-59.
396. Karasu E, Eisenhardt SU, Harant J, Huber-Lang M. Extracellular Vesicles: Packages Sent With Complement. Front Immunol. 2018;9:721.
397. Chaput N, Thery C. Exosomes: immune properties and potential clinical implementations. Semin Immunopathol. 2011;33(5):419-40.
398. Sagini K, Costanzi E, Emiliani C, Buratta S, Urbanelli L. Extracellular Vesicles as Conveyors of Membrane-Derived Bioactive Lipids in Immune System. Int J Mol Sci. 2018;19(4).
399. Park SJ, Kim JM, Kim J, Hur J, Park S, Kim K, et al. Molecular mechanisms of biogenesis of apoptotic exosome-like vesicles and their roles as damage-associated molecular patterns. Proc Natl Acad Sci U S A. 2018;115(50):E11721-E30.
400. Genschmer KR, Russell DW, Lal C, Szul T, Bratcher PE, Noerager BD, et al. Activated PMN Exosomes: Pathogenic Entities Causing Matrix Destruction and Disease in the Lung. Cell. 2019;176(1-2):113-26 e15.
401. Nair RR, Mazza D, Brambilla F, Gorzanelli A, Agresti A, Bianchi ME. LPS-Challenged Macrophages Release Microvesicles Coated With Histones. Front Immunol. 2018;9:1463.
402. Chauhan S, Danielson S, Clements V, Edwards N, Ostrand-Rosenberg S, Fenselau C. Surface Glycoproteins of Exosomes Shed by Myeloid-Derived Suppressor Cells Contribute to Function. J Proteome Res. 2017;16(1):238-46.
403. Schaper F, van Spriel AB. Antitumor Immunity Is Controlled by Tetraspanin Proteins. Front Immunol. 2018;9:1185.
404. Oksvold MP, Kullmann A, Forfang L, Kierulf B, Li M, Brech A, et al. Expression of B-cell surface antigens in subpopulations of exosomes released from B-cell lymphoma cells. Clin Ther. 2014;36(6):847-62 e1.
405. Chen G, Huang AC, Zhang W, Zhang G, Wu M, Xu W, et al. Exosomal PD-L1 contributes to immunosuppression and is associated with anti-PD-1 response. Nature. 2018;560(7718):382-6.
406. Ricklefs FL, Alayo Q, Krenzlin H, Mahmoud AB, Speranza MC, Nakashima H, et al. Immune evasion mediated by PD-L1 on glioblastoma-derived extracellular vesicles. Sci Adv. 2018;4(3):eaar2766.
407. Poggio M, Hu T, Pai CC, Chu B, Belair CD, Chang A, et al. Suppression of Exosomal PD-L1 Induces Systemic Anti-tumor Immunity and Memory. Cell. 2019;177(2):414-27 e13.
408. Muller L, Simms P, Hong CS, Nishimura MI, Jackson EK, Watkins SC, et al. Human tumor-derived exosomes (TEX) regulate Treg functions via cell surface signaling rather than uptake mechanisms. Oncoimmunology. 2017;6(8):e1261243.

409. Siravegna G, Marsoni S, Siena S, Bardelli A. Integrating liquid biopsies into the management of cancer. Nat Rev Clin Oncol. 2017;14(9):531-48.
410. Advancing Cancer Screening with Liquid Biopsies. Cancer Discov. 2018;8(3):256.
411. Osti D, Del Bene M, Rappa G, Santos M, Matafora V, Richichi C, et al. Clinical Significance of Extracellular Vesicles in Plasma from Glioblastoma Patients. Clin Cancer Res. 2019;25(1):266-76.
412. Lee J, McKinney KQ, Pavlopoulos AJ, Niu M, Kang JW, Oh JW, et al. Altered Proteome of Extracellular Vesicles Derived from Bladder Cancer Patients Urine. Mol Cells. 2018;41(3):179-87.
413. Wang X. Isolation of Extracellular Vesicles from Breast Milk. Methods Mol Biol. 2017;1660:351-3.
414. Vojtech L, Zhang M, Dave V, Levy C, Hughes SM, Wang R, et al. Extracellular vesicles in human semen modulate antigen-presenting cell function and decrease downstream antiviral T cell responses. PLoS One. 2019;14(10):e0223901.
415. Yokoi A, Yoshioka Y, Yamamoto Y, Ishikawa M, Ikeda SI, Kato T, et al. Malignant extracellular vesicles carrying MMP1 mRNA facilitate peritoneal dissemination in ovarian cancer. Nat Commun. 2017;8:14470.
416. Carnino JM, Lee H, Jin Y. Isolation and characterization of extracellular vesicles from Broncho-alveolar lavage fluid: a review and comparison of different methods. Respir Res. 2019;20(1):240.
417. Alvarez-Erviti L, Seow Y, Yin H, Betts C, Lakhal S, Wood MJ. Delivery of siRNA to the mouse brain by systemic injection of targeted exosomes. Nat Biotechnol. 2011;29(4):341-5.
418. Vallabhajosyula P, Korutla L, Habertheuer A, Yu M, Rostami S, Yuan CX, et al. Tissue-specific exosome biomarkers for noninvasively monitoring immunologic rejection of transplanted tissue. J Clin Invest. 2017;127(4):1375-91.
419. Sandfeld-Paulsen B, Aggerholm-Pedersen N, Baek R, Jakobsen KR, Meldgaard P, Folkersen BH, et al. Exosomal proteins as prognostic biomarkers in non-small cell lung cancer. Mol Oncol. 2016;10(10):1595-602.
420. Belov L, Matic KJ, Hallal S, Best OG, Mulligan SP, Christopherson RI. Extensive surface protein profiles of extracellular vesicles from cancer cells may provide diagnostic signatures from blood samples. J Extracell Vesicles. 2016;5:25355.
421. Melo SA, Luecke LB, Kahlert C, Fernandez AF, Gammon ST, Kaye J, et al. Glypican-1 identifies cancer exosomes and detects early pancreatic cancer. Nature. 2015;523(7559):177-82.
422. Indira Chandran V, Welinder C, Mansson AS, Offer S, Freyhult E, Pernemalm M, et al. Ultrasensitive Immunoprofiling of Plasma Extracellular Vesicles Identifies Syndecan-1 as a Potential Tool for Minimally Invasive Diagnosis of Glioma. Clin Cancer Res. 2019;25(10):3115-27.
423. Xu R, Greening DW, Chen M, Rai A, Ji H, Takahashi N, et al. Surfaceome of Exosomes Secreted from the Colorectal Cancer Cell Line SW480: Peripheral and Integral Membrane Proteins Analyzed by Proteolysis and TX114. Proteomics. 2019;19(8):e1700453.
424. Logozzi M, De Milito A, Lugini L, Borghi M, Calabro L, Spada M, et al. High levels of exosomes expressing CD63 and caveolin-1 in plasma of melanoma patients. PLoS One. 2009;4(4):e5219.

425. Tian Y, Ma L, Gong M, Su G, Zhu S, Zhang W, et al. Protein Profiling and Sizing of Extracellular Vesicles from Colorectal Cancer Patients via Flow Cytometry. ACS Nano. 2018;12(1):671-80.
426. Yang KS, Im H, Hong S, Pergolini I, Del Castillo AF, Wang R, et al. Multiparametric plasma EV profiling facilitates diagnosis of pancreatic malignancy. Sci Transl Med. 2017;9(391).
427. Liang K, Liu F, Fan J, Sun D, Liu C, Lyon CJ, et al. Nanoplasmonic Quantification of Tumor-derived Extracellular Vesicles in Plasma Microsamples for Diagnosis and Treatment Monitoring. Nat Biomed Eng. 2017;1.
428. Pinho SS, Reis CA. Glycosylation in cancer: mechanisms and clinical implications. Nat Rev Cancer. 2015;15(9):540-55.
429. Drake RR. Glycosylation and cancer: moving glycomics to the forefront. Adv Cancer Res. 2015;126:1-10.
430. Costa J. Glycoconjugates from extracellular vesicles: Structures, functions and emerging potential as cancer biomarkers. Biochim Biophys Acta Rev Cancer. 2017;1868(1):157-66.
431. Sakaue T, Koga H, Iwamoto H, Nakamura T, Ikezono Y, Abe M, et al. Glycosylation of ascites-derived exosomal CD133: a potential prognostic biomarker in patients with advanced pancreatic cancer. Med Mol Morphol. 2019;52(4):198-208.
432. Surman M, Hoja-Lukowicz D, Szwed S, Drozdz A, Stepien E, Przybylo M. Human melanoma-derived ectosomes are enriched with specific glycan epitopes. Life Sci. 2018;207:395-411.
433. Vermassen T, D'Herde K, Jacobus D, Van Praet C, Poelaert F, Lumen N, et al. Release of urinary extracellular vesicles in prostate cancer is associated with altered urinary N-glycosylation profile. J Clin Pathol. 2017;70(10):838-46.
434. Goldbloom R, Battista RN, Haggerty J. Periodic health examination, 1989 update: 1. Introduction [corrected]. CMAJ. 1989;141(3):205-7.
435. Shin H, Jeong H, Park J, Hong S, Choi Y. Correlation between Cancerous Exosomes and Protein Markers Based on Surface-Enhanced Raman Spectroscopy (SERS) and Principal Component Analysis (PCA). ACS Sens. 2018;3(12):2637-43.
436. Park J, Hwang M, Choi B, Jeong H, Jung JH, Kim HK, et al. Exosome Classification by Pattern Analysis of Surface-Enhanced Raman Spectroscopy Data for Lung Cancer Diagnosis. Anal Chem. 2017;89(12):6695-701.
437. Ferreira N, Marques A, Aguas H, Bandarenka H, Martins R, Bodo C, et al. Label-Free Nanosensing Platform for Breast Cancer Exosome Profiling. ACS Sens. 2019;4(8):2073-83.
438. Lee W, Nanou A, Rikkert L, Coumans FAW, Otto C, Terstappen L, et al. Label-Free Prostate Cancer Detection by Characterization of Extracellular Vesicles Using Raman Spectroscopy. Anal Chem. 2018;90(19):11290-6.
439. Vader P, Mol EA, Pasterkamp G, Schiffelers RM. Extracellular vesicles for drug delivery. Adv Drug Deliv Rev. 2016;106(Pt A):148-56.
440. Didiot MC, Haraszti RA, Aronin N, Khvorova A. Loading of Extracellular Vesicles with Hydrophobically Modified siRNAs. Methods Mol Biol. 2018;1740:199-214.
441. S ELA, Mager I, Breakefield XO, Wood MJ. Extracellular vesicles: biology and emerging therapeutic opportunities. Nat Rev Drug Discov. 2013;12(5):347-57.

442. Charoenviriyakul C, Takahashi Y, Morishita M, Nishikawa M, Takakura Y. Role of Extracellular Vesicle Surface Proteins in the Pharmacokinetics of Extracellular Vesicles. Mol Pharm. 2018;15(3):1073-80.
443. Rana S, Yue S, Stadel D, Zoller M. Toward tailored exosomes: the exosomal tetraspanin web contributes to target cell selection. Int J Biochem Cell Biol. 2012;44(9):1574-84.
444. Stanisic A, Kries H. Adenylation Domains in Nonribosomal Peptide Engineering. Chembiochem. 2019;20(11):1347-56.
445. Li Y, Gao Y, Gong C, Wang Z, Xia Q, Gu F, et al. A33 antibody-functionalized exosomes for targeted delivery of doxorubicin against colorectal cancer. Nanomedicine. 2018;14(7):1973-85.
446. Kim MS, Haney MJ, Zhao Y, Mahajan V, Deygen I, Klyachko NL, et al. Development of exosome-encapsulated paclitaxel to overcome MDR in cancer cells. Nanomedicine. 2016;12(3):655-64.
447. Zhang YF, Shi JB, Li C. Small extracellular vesicle loading systems in cancer therapy: Current status and the way forward. Cytotherapy. 2019;21(11):1122-36.
448. Kooijmans SAA, Schiffelers RM, Zarovni N, Vago R. Modulation of tissue tropism and biological activity of exosomes and other extracellular vesicles: New nanotools for cancer treatment. Pharmacol Res. 2016;111:487-500.
449. Si Y, Kim S, Zhang E, Tang Y, Jaskula-Sztul R, Markert JM, et al. Targeted Exosomes for Drug Delivery: Biomanufacturing, Surface Tagging, and Validation. Biotechnol J. 2020;15(1):e1900163.
450. Yerneni SS, Lathwal S, Shrestha P, Shirwan H, Matyjaszewski K, Weiss L, et al. Rapid On-Demand Extracellular Vesicle Augmentation with Versatile Oligonucleotide Tethers. ACS Nano. 2019;13(9):10555-65.
451. Suk JS, Xu Q, Kim N, Hanes J, Ensign LM. PEGylation as a strategy for improving nanoparticle-based drug and gene delivery. Adv Drug Deliv Rev. 2016;99(Pt A):28-51.
452. Kooijmans SA, Aleza CG, Roffler SR, van Solinge WW, Vader P, Schiffelers RM. Display of GPI-anchored anti-EGFR nanobodies on extracellular vesicles promotes tumour cell targeting. J Extracell Vesicles. 2016;5:31053.
453. Zheng Z, Li Z, Xu C, Guo B, Guo P. Folate-displaying exosome mediated cytosolic delivery of siRNA avoiding endosome trapping. J Control Release. 2019;311-312:43-9.
454. Tan A, De La Pena H, Seifalian AM. The application of exosomes as a nanoscale cancer vaccine. Int J Nanomedicine. 2010;5:889-900.
455. Delcayre A, Estelles A, Sperinde J, Roulon T, Paz P, Aguilar B, et al. Exosome Display technology: applications to the development of new diagnostics and therapeutics. Blood Cells Mol Dis. 2005;35(2):158-68.
456. Hartman ZC, Wei J, Glass OK, Guo H, Lei G, Yang XY, et al. Increasing vaccine potency through exosome antigen targeting. Vaccine. 2011;29(50):9361-7.
457. Horrevorts SK, Stolk DA, van de Ven R, Hulst M, van Het Hof B, Duinkerken S, et al. Glycan-Modified Apoptotic Melanoma-Derived Extracellular Vesicles as Antigen Source for Anti-Tumor Vaccination. Cancers (Basel). 2019;11(9).
458. Carney RP, Hazari S, Rojalin T, Knudson A, Gao T, Tang Y, et al. Targeting Tumor-Associated Exosomes with Integrin-Binding Peptides. Adv Biosyst. 2017;1(5).
459. Cai Z, Yang F, Yu L, Yu Z, Jiang L, Wang Q, et al. Activated T cell exosomes promote tumor invasion via Fas signaling pathway. J Immunol. 2012;188(12):5954-61.

460. Sohal DP, Mangu PB, Laheru D. Metastatic Pancreatic Cancer: American Society of Clinical Oncology Clinical Practice Guideline Summary. J Oncol Pract. 2017;13(4):261-4.
461. Chang JC, Kundranda M. Novel Diagnostic and Predictive Biomarkers in Pancreatic Adenocarcinoma. Int J Mol Sci. 2017;18(3).
462. Kowal J, Tkach M, Thery C. Biogenesis and secretion of exosomes. Curr Opin Cell Biol. 2014;29:116-25.
463. Chen Y, Pfeifer A. Brown Fat-Derived Exosomes: Small Vesicles with Big Impact. Cell Metab. 2017;25(4):759-60.
464. Shrivastava S, Devhare P, Sujijantarat N, Steele R, Kwon YC, Ray R, et al. Knockdown of Autophagy Inhibits Infectious Hepatitis C Virus Release by the Exosomal Pathway. J Virol. 2016;90(3):1387-96.
465. Maybruck BT, Pfannenstiel LW, Diaz-Montero M, Gastman BR. Tumor-derived exosomes induce CD8(+) T cell suppressors. J Immunother Cancer. 2017;5(1):65.
466. Liu Y, Cao X. Organotropic metastasis: role of tumor exosomes. Cell Res. 2016;26(2):149-50.
467. Soung YH, Nguyen T, Cao H, Lee J, Chung J. Emerging roles of exosomes in cancer invasion and metastasis. BMB Rep. 2016;49(1):18-25.
468. Moravec R, Divi R, Verma M. Detecting circulating tumor material and digital pathology imaging during pancreatic cancer progression. World J Gastrointest Oncol. 2017;9(6):235-50.
469. Jin H, Wu Y, Tan X. The role of pancreatic cancer-derived exosomes in cancer progress and their potential application as biomarkers. Clin Transl Oncol. 2017;19(8):921-30.
470. Madhavan B, Yue S, Galli U, Rana S, Gross W, Muller M, et al. Combined evaluation of a panel of protein and miRNA serum-exosome biomarkers for pancreatic cancer diagnosis increases sensitivity and specificity. Int J Cancer. 2015;136(11):2616-27.
471. Zhao K, Liang G, Sun X, Guan le L. Comparative miRNAome analysis revealed different miRNA expression profiles in bovine sera and exosomes. BMC Genomics. 2016;17(1):630.
472. Huang X, Yuan T, Tschannen M, Sun Z, Jacob H, Du M, et al. Characterization of human plasma-derived exosomal RNAs by deep sequencing. BMC Genomics. 2013;14:319.
473. Sun Y, Liu S, Qiao Z, Shang Z, Xia Z, Niu X, et al. Systematic comparison of exosomal proteomes from human saliva and serum for the detection of lung cancer. Anal Chim Acta. 2017;982:84-95.
474. Butz H, Nofech-Mozes R, Ding Q, Khella HWZ, Szabo PM, Jewett M, et al. Exosomal MicroRNAs Are Diagnostic Biomarkers and Can Mediate Cell-Cell Communication in Renal Cell Carcinoma. Eur Urol Focus. 2016;2(2):210-8.
475. Auner GW, Koya SK, Huang C, Broadbent B, Trexler M, Auner Z, et al. Applications of Raman spectroscopy in cancer diagnosis. Cancer Metastasis Rev. 2018;37(4):691-717.
476. Carey PR, Heidari-Torkabadi H. New techniques in antibiotic discovery and resistance: Raman spectroscopy. Ann N Y Acad Sci. 2015;1354:67-81.
477. Etchegoin PG, Le Ru EC. A perspective on single molecule SERS: current status and future challenges. Phys Chem Chem Phys. 2008;10(40):6079-89.

478. Li L, Hutter T, Steiner U, Mahajan S. Single molecule SERS and detection of biomolecules with a single gold nanoparticle on a mirror junction. Analyst. 2013;138(16):4574-8.
479. Lee C, Carney RP, Hazari S, Smith ZJ, Knudson A, Robertson CS, et al. 3D plasmonic nanobowl platform for the study of exosomes in solution. Nanoscale. 2015;7(20):9290-7.
480. Noble JM, Roberts LM, Vidavsky N, Chiou AE, Fischbach C, Paszek MJ, et al. Direct comparison of optical and electron microscopy methods for structural characterization of extracellular vesicles. J Struct Biol. 2020:107474.
481. Singh SP, Deshmukh A, Chaturvedi P, Krishna CM. Raman spectroscopy in head and neck cancers: toward oncological applications. J Cancer Res Ther. 2012;8 Suppl 1:S126-32.
482. Wang H, Wang X, Wang J, Fu W, Yao C. A SPR biosensor based on signal amplification using antibody-QD conjugates for quantitative determination of multiple tumor markers. Sci Rep. 2016;6:33140.
483. Arya SK, Zhurauski P, Jolly P, Batistuti MR, Mulato M, Estrela P. Capacitive aptasensor based on interdigitated electrode for breast cancer detection in undiluted human serum. Biosens Bioelectron. 2018;102:106-12.
484. Makler A, Asghar W. Exosomal biomarkers for cancer diagnosis and patient monitoring. Expert Rev Mol Diagn. 2020.
485. Fan Y, Duan X, Zhao M, Wei X, Wu J, Chen W, et al. High-sensitive and multiplex biosensing assay of NSCLC-derived exosomes via different recognition sites based on SPRi array. Biosens Bioelectron. 2020;154:112066.
486. Cho S, Yang HC, Rhee WJ. Simultaneous multiplexed detection of exosomal microRNAs and surface proteins for prostate cancer diagnosis. Biosens Bioelectron. 2019;146:111749.
487. Daassi D, Mahoney KM, Freeman GJ. The importance of exosomal PDL1 in tumour immune evasion. Nat Rev Immunol. 2020.
488. Pace KR, Dutt R, Galileo DS. Exosomal L1CAM Stimulates Glioblastoma Cell Motility, Proliferation, and Invasiveness. Int J Mol Sci. 2019;20(16).
489. Jahan R, Ganguly K, Smith LM, Atri P, Carmicheal J, Sheinin Y, et al. Trefoil factor(s) and CA19.9: A promising panel for early detection of pancreatic cancer. EBioMedicine. 2019;42:375-85.
490. Zhang J, Wang Y, Zhao T, Li Y, Tian L, Zhao J, et al. Evaluation of serum MUC5AC in combination with CA19-9 for the diagnosis of pancreatic cancer. World J Surg Oncol. 2020;18(1):31.
491. van Manen L, Groen JV, Putter H, Vahrmeijer AL, Swijnenburg RJ, Bonsing BA, et al. Elevated CEA and CA19-9 serum levels independently predict advanced pancreatic cancer at diagnosis. Biomarkers. 2020:1-8.
492. Ballehaninna UK, Chamberlain RS. The clinical utility of serum CA 19-9 in the diagnosis, prognosis and management of pancreatic adenocarcinoma: An evidence based appraisal. J Gastrointest Oncol. 2012;3(2):105-19.
493. Ozawa PMM, Vieira E, Lemos DS, Souza ILM, Zanata SM, Pankievicz VC, et al. Identification of miRNAs Enriched in Extracellular Vesicles Derived from Serum Samples of Breast Cancer Patients. Biomolecules. 2020;10(1).

494. Giron F, Alcantar D. Looks can be Deceiving: A Case Report on the Clinical Value of CA 19-9 in Obstructive Jaundice. Cureus. 2020;12(1):e6637.
495. Kato S, Honda K. CA19-9 as a therapeutic target in pancreatitis. Ann Transl Med. 2019;7(Suppl 8):S318.
496. Dixon SJ, Lemberg KM, Lamprecht MR, Skouta R, Zaitsev EM, Gleason CE, et al. Ferroptosis: an iron-dependent form of nonapoptotic cell death. Cell. 2012;149(5):1060-72.
497. Neoptolemos JP, Kleeff J, Michl P, Costello E, Greenhalf W, Palmer DH. Therapeutic developments in pancreatic cancer: current and future perspectives. Nat Rev Gastroenterol Hepatol. 2018;15(6):333-48.
498. Stockwell BR, Friedmann Angeli JP, Bayir H, Bush AI, Conrad M, Dixon SJ, et al. Ferroptosis: A Regulated Cell Death Nexus Linking Metabolism, Redox Biology, and Disease. Cell. 2017;171(2):273-85.
499. Yang WS, SriRamaratnam R, Welsch ME, Shimada K, Skouta R, Viswanathan VS, et al. Regulation of ferroptotic cancer cell death by GPX4. Cell. 2014;156(1-2):317-31.
500. Forcina GC, Dixon SJ. GPX4 at the Crossroads of Lipid Homeostasis and Ferroptosis. Proteomics. 2019;19(18):e1800311.
501. Wang L, Liu Y, Du T, Yang H, Lei L, Guo M, et al. ATF3 promotes erastin-induced ferroptosis by suppressing system Xc(). Cell Death Differ. 2020;27(2):662-75.
502. Hajdinak P, Czobor A, Szarka A. The potential role of acrolein in plant ferroptosis-like cell death. PLoS One. 2019;14(12):e0227278.
503. Roh JL, Kim EH, Jang HJ, Park JY, Shin D. Induction of ferroptotic cell death for overcoming cisplatin resistance of head and neck cancer. Cancer Lett. 2016;381(1):96-103.
504. Lei G, Zhang Y, Koppula P, Liu X, Zhang J, Lin SH, et al. The role of ferroptosis in ionizing radiation-induced cell death and tumor suppression. Cell Res. 2020;30(2):146-62.
505. Ye LF, Chaudhary KR, Zandkarimi F, Harken AD, Kinslow CJ, Upadhyayula PS, et al. Radiation-Induced Lipid Peroxidation Triggers Ferroptosis and Synergizes with Ferroptosis Inducers. ACS Chem Biol. 2020;15(2):469-84.
506. Yang H, Villani RM, Wang H, Simpson MJ, Roberts MS, Tang M, et al. The role of cellular reactive oxygen species in cancer chemotherapy. J Exp Clin Cancer Res. 2018;37(1):266.
507. Malla JA, Umesh RM, Yousf S, Mane S, Sharma S, Lahiri M, et al. A Glutathione Activatable Ion Channel Induces Apoptosis in Cancer Cells by Depleting Intracellular Glutathione Levels. Angew Chem Int Ed Engl. 2020.
508. Yang H, Xiang S, Kazi A, Sebti SM. The GTPase KRAS suppresses the P53 tumor suppressor by activating the NRF2-regulated antioxidant defense system in cancer cells. J Biol Chem. 2020.
509. Hu K, Li K, Lv J, Feng J, Chen J, Wu H, et al. Suppression of the SLC7A11/glutathione axis causes synthetic lethality in KRAS-mutant lung adenocarcinoma. J Clin Invest. 2019.
510. Koppula P, Zhang Y, Zhuang L, Gan B. Amino acid transporter SLC7A11/xCT at the crossroads of regulating redox homeostasis and nutrient dependency of cancer. Cancer Commun (Lond). 2018;38(1):12.

511. Gu Y, Albuquerque CP, Braas D, Zhang W, Villa GR, Bi J, et al. mTORC2 Regulates Amino Acid Metabolism in Cancer by Phosphorylation of the Cystine-Glutamate Antiporter xCT. Mol Cell. 2017;67(1):128-38 e7.
512. Hassannia B, Wiernicki B, Ingold I, Qu F, Van Herck S, Tyurina YY, et al. Nano-targeted induction of dual ferroptotic mechanisms eradicates high-risk neuroblastoma. J Clin Invest. 2018;128(8):3341-55.
513. Viswanathan VS, Ryan MJ, Dhruv HD, Gill S, Eichhoff OM, Seashore-Ludlow B, et al. Dependency of a therapy-resistant state of cancer cells on a lipid peroxidase pathway. Nature. 2017;547(7664):453-7.
514. Chatterjee A, Kosmacek EA, Oberley-Deegan RE. MnTE-2-PyP Treatment, or NOX4 Inhibition, Protects against Radiation-Induced Damage in Mouse Primary Prostate Fibroblasts by Inhibiting the TGF-Beta 1 Signaling Pathway. Radiat Res. 2017;187(3):367-81.
515. Cao JY, Dixon SJ. Mechanisms of ferroptosis. Cell Mol Life Sci. 2016;73(11-12):2195-209.
516. Cheng J, Fan YQ, Liu BH, Zhou H, Wang JM, Chen QX. ACSL4 suppresses glioma cells proliferation via activating ferroptosis. Oncol Rep. 2020;43(1):147-58.
517. Yang Y, Luo M, Zhang K, Zhang J, Gao T, Connell DO, et al. Nedd4 ubiquitylates VDAC2/3 to suppress erastin-induced ferroptosis in melanoma. Nat Commun. 2020;11(1):433.
518. Gao M, Monian P, Pan Q, Zhang W, Xiang J, Jiang X. Ferroptosis is an autophagic cell death process. Cell Res. 2016;26(9):1021-32.
519. Sun X, Ou Z, Xie M, Kang R, Fan Y, Niu X, et al. HSPB1 as a novel regulator of ferroptotic cancer cell death. Oncogene. 2015;34(45):5617-25.
520. Habib E, Linher-Melville K, Lin HX, Singh G. Expression of xCT and activity of system xc(-) are regulated by NRF2 in human breast cancer cells in response to oxidative stress. Redox Biol. 2015;5:33-42.
521. Joo MS, Kim WD, Lee KY, Kim JH, Koo JH, Kim SG. AMPK Facilitates Nuclear Accumulation of Nrf2 by Phosphorylating at Serine 550. Mol Cell Biol. 2016;36(14):1931-42.
522. Yoo MH, Gu X, Xu XM, Kim JY, Carlson BA, Patterson AD, et al. Delineating the role of glutathione peroxidase 4 in protecting cells against lipid hydroperoxide damage and in Alzheimer's disease. Antioxid Redox Signal. 2010;12(7):819-27.
523. Souchek JJ, Baine MJ, Lin C, Rachagani S, Gupta S, Kaur S, et al. Unbiased analysis of pancreatic cancer radiation resistance reveals cholesterol biosynthesis as a novel target for radiosensitisation. Br J Cancer. 2014;111(6):1139-49.
524. Lee SQ, Tan TS, Kawamukai M, Chen ES. Cellular factories for coenzyme Q10 production. Microb Cell Fact. 2017;16(1):39.
525. Bersuker K, Hendricks JM, Li Z, Magtanong L, Ford B, Tang PH, et al. The CoQ oxidoreductase FSP1 acts parallel to GPX4 to inhibit ferroptosis. Nature. 2019;575(7784):688-92.
526. Chen G, Guo G, Zhou X, Chen H. Potential mechanism of ferroptosis in pancreatic cancer. Oncol Lett. 2020;19(1):579-87.
527. Zhang X, Xing X, Liu H, Feng J, Tian M, Chang S, et al. Ionizing radiation induces ferroptosis in granulocyte-macrophage hematopoietic progenitor cells of murine bone marrow. Int J Radiat Biol. 2020:1-12.

528. Shi ZZ, Fan ZW, Chen YX, Xie XF, Jiang W, Wang WJ, et al. Ferroptosis in Carcinoma: Regulatory Mechanisms and New Method for Cancer Therapy. Onco Targets Ther. 2019;12:11291-304.
529. Lang X, Green MD, Wang W, Yu J, Choi JE, Jiang L, et al. Radiotherapy and Immunotherapy Promote Tumoral Lipid Oxidation and Ferroptosis via Synergistic Repression of SLC7A11. Cancer Discov. 2019;9(12):1673-85.

Publications

1. Ryckman JM, Baine M, **Carmicheal J**, Osayande F, Sleightholm R, Samson K, Zheng D, Zhen W, Lin C, Zhang C. *Correlation of dosimetric factors with the development of symptomatic radiation pneumonitis in stereotactic body radiotherapy.* **Radiation Oncology,** 2020 Feb 13;15(1):33.

2. **Carmicheal J***, Atri P*, Sharma S*, Sushil Kumar Ph.D., Ramakanth Chirravuri Venkata Ph.D., Prakash Kulkarni Ph.D., Ravi Salgia M.D., Ph.D., Dario Ghersi Ph.D., Sukhwinder KaurPh.D., Surinder K. Batra Ph.D. *Presence and structure-activity relationship of intrinsically disordered regions across mucins.* **FASEB Journal,** 2020 Feb;34(2):1939-1957. (*Equal contributions)

3. **Carmicheal J**, Asish Patel, Vipin Dalal, Pranita Atri, Amaninder S. Dhaliwal, Uwe A. Wittel, Mokenge P. Malafa, Geoffrey Talmon, Benjamin J. Swanson, Shailender Singh, Maneesh Jain, Sukhwinder Kaur, and Surinder K. Batra. *Elevating pancreatic cystic lesion stratification: Current and future pancreatic cancer biomarker(s).* **Biochimica et Biophysica Acta (BBA) Reviews on Cancer,** 2020 Jan;1873(1):188318.

4. Dalal V, **Carmicheal J**, Dhaliwal A, Jain M, Kaur S, Batra SK. *Radiomics in stratification of pancreatic cystic lesions: Machine learning in action.* **Cancer Letters,** 2020 Jan 28;469:228-237.

5. Jahan R, Ganguly K, Smith LM, Atri P, **Carmicheal J**, Sheinin Y, Rachagani S, Natarajan G, Brand RE, Macha MA, Grandgenett PM, Kaur S, Batra SK. *Trefoil factor(s) and CA19.9: A promising panel for early detection of pancreatic cancer.* **EBiomedicine,** 2019 Apr;42:375-385.

6. **Carmicheal J*,** Hiyashi C*, Huang X*, Liu L, Yao Lu, Krosnoslobotstev A, Lushnikov A, Patel A, Lu Y, Kaur S, Batra SK**.** *Label free exosome characterization via surface enhanced Raman spectroscopy for the early detection of pancreatic cancer.* **Nanomedicine: Nanotechnology, Biology and Medicine,** 2019 Feb;16:88-96. (*Equal contributions)

7. Verma I, Ganguly K, Sharma S, **Carmicheal J**, Kaur S, Batra SK, Bhasin MK. *Systems Biology Approach to Identify Novel Genomic Determinants for Pancreatic Cancer Pathogenesis*, **Scientific Reports,** 2019 Jan 15;9(1):123.

8. **Carmicheal J,** Kaur S, Batra SK, Ganti A. *Hunting for transcription factors: STAT3 decoy in non-small cell lung cancer.* **Translational Lung Cancer Research,** 2018 Sep;7(Suppl 3):S254-S257.

Articles near submission

1. **Carmicheal J,** Atri P, Seas A, Satyanarayana R, Seshacharyulu P, Souchek J, Rauth S, Leon F, Prajapati D, Reid W, Talmon GA, Li S, Lin C, Ponnusamy MP, Kaur S, Batra SK. *Radiation potentiation via SLC7A11 inhibition induced ferroptosis in pancreatic ductal adenocarcinoma*. (**Near submission**)

2. **Carmicheal J**, Hiyashi C, Atri P, Kaur S, Batra SK. *Extracellular vesicle surfaceome characterization for the early detection of pancreatic ductal adenocarcinoma.* (**Near submission**)

3. **Carmicheal J,** Kaur S, Batra SK. *Judging a vesicle by its cover: Investigations of the extracellular vesicle surfaceome.* (**Near submission**).

4. File N[*], **Carmicheal J[*]**, Krosnoslobotstev A, Kshirsagar P, Junker W, Japp N, Chakravarty S, Kaur S, Batra SK, *Raman reporter molecule selection predicated on inductive effect and Hammett constant.* (*Equal contributions, **Near submission)**

5. Lakshmanan I, Gupta R, Seshacharyulu P, Vengoji R, Rachagani S, **Carmicheal J**, Jahan R, Atri P, Venkata Ramakanth C, Marimuthu S, Perumal N, Rauth S, Kaur S, Smith LM, Lele SM, Ponnusamy MP, Ganti AK, Batra SK. *ST6GalNAc-I alters MUC5AC Sialylation to promote lung cancer liver metastasis.* **(Near submission)**